ELECTROLYTIC TRANSPORT, ELECTRIC FIELDS, AND THE PROPENSITY FOR CHARGE DENSITY IN ELECTROLYTES

A Thesis Submitted to the College of

Graduate Studies and Research

In Partial Fulfillment of the Requirements

For the Degree of Doctor of Philosophy

In the Department of Chemical Engineering

University of Saskatchewan

Saskatoon

By

GLYN F. KENNELL

© Copyright Glyn F. Kennell, September, 2011. All rights reserved.

PERMISSION TO USE

In presenting this thesis in partial fulfilment of the requirements for a Postgraduate degree from the University of Saskatchewan, I agree that the Libraries of this University may make it freely available for inspection. I further agree that permission for copying of this thesis in any manner, in whole or in part, for scholarly purposes may be granted by the professor or professors who supervised my thesis work or, in their absence, by the Head of the Department or the Dean of the College in which my thesis work was done. It is understood that any copying or publication or use of this thesis or parts thereof for financial gain shall not be allowed without my written permission. It is also understood that due recognition shall be given to me and to the University of Saskatchewan in any scholarly use which may be made of any material in my thesis.

Requests for permission to copy or to make other use of material in this thesis in whole or part should be addressed to:

Head of the Department of Chemical and Biological Engineering

University of Saskatchewan

Saskatoon, Saskatchewan S7N 5A9

ABSTRACT

This research presents a universal characterization of the electric field coupled with a non-isotropic electrolyte conducting an electric current. Also presented is a reorganization of Maxwell's fundamental equations for the case where multiple forms of charge density may be created, such as in an electrolyte. This thesis suggests that the electric field does not balance charge density, but that it balances the strength of the phenomena causing charge density, and names this strength: the propensity for charge density.

Also presented in this thesis are models and research that corroborate each other and this reorganization of Maxwell's equations. A one-dimensional transport model was used to model crevice corrosion. It couples the two schools of crevice corrosion theory: the critical crevice solution theory and the IR drop crevice corrosion theory. Simulations showed the correct scaling law for the corroding crevices examined should be: L^2/G. Also, a tendency for cathodic reactions occurring towards the tip of the crevices was numerically observed. This one-dimensional transport model incorporates a simplified one-dimensional version of the universal characterization of the electric field and supports the theory of the propensity for charge density.

A universal multi-dimensional electrolyte model was developed incorporating the universal characterization of the electric field. It was shown how this model simulates different systems incorporating complex and different phenomena using the same governing equations and the same boundary conditions; the only parameters changed

between multi-dimensional simulations were the initial concentrations and diffusion coefficients, system geometry, and the positions and rates of spatially distinct anodic and cathodic reactions. It was demonstrated that this model could predict current distributions for multi-dimensional liquid-junctions, a system containing a moving liquid-boundary, and a charging plasticized lithium-ion cell. For the lithium-ion cell, it was shown how this model predicts a phenomenon that was not reported by numerical simulations based on classical dilute solution theory, but was experimentally observed.

The numerical results presented in this thesis are important because they support the theory of the propensity for charge density. The theory of the propensity for charge density clarifies theory pertaining to an electric field coupled to an electrochemical system.

ACKNOWLEDGMENTS

I would like to acknowledge the support provided by my supervisor and friend Prof. Evitts. Not only did Prof. Evitts support me in my endeavors to publish unconventional ideas, but he also encouraged me in the face of strong criticism from researchers who were invested in conventional methodologies.

I would also like to acknowledge the members of my supervisory committee: Prof. Phoenix, Prof. Nemati, Prof. Oguocha, Prof. Hill, and Prof. Hwang. I appreciate the valuable advice I have received from this committee. I also acknowledge the time and advice given freely by additional members of the research community: Prof. Bourassa, Dr. Heppner, and Prof. Kelly who acted as my external examiner.

I would like to thank my wife and my best friend, Ammy Murray, for her many years of unwavering support. It was Ammy who first encouraged me to start following my dream and obtain my G.E.D. at 26 years of age. She has been encouraging me ever since, even with the additional challenges of being a student herself and raising our two children, Fraser and Ebyn. I would like to thank the many friends I made during my graduate studies who are too numerous to mention here.

Scholarship support for my Ph.D. was provided by the Natural Sciences and Engineering Research Council (NSERC) through an Alexander Graham Bell Canada Graduate Doctoral Scholarship and by the University of Saskatchewan through a Dean's Scholarship and computational facilities.

To all those who are different, may you embrace and utilize your anomalies.

TABLE OF CONTENTS

page

LIST OF TABLES

LIST OF FIGURES

NOMENCLATURE

Symbol	Definition	Units
A	Constant of integration	
$\mathbf{B}$	Magnetic field	$V \cdot s/m^2$
C	Concentration	mol/m^3
C_s	Solid phase lithium concentration	mol/m^3
C_t	Solid phase maximum lithium concentration	mol/m^3
D	Diffusion coefficient	m^2/s
D^{eff}	Effective diffusion coefficient	m^2/s
$\mathbf{D}$	Electric displacement field	C/m^2
$\mathbf{D}_0$	Time independent electric displacement	C/m^2
$\mathbf{E}$	Electric field	V/m
E^0	Reversible potential	V
E_{corr}	Corrosion potential	V
E_{crit}	Critical potential	V
F	Faraday's constant	96,487 C/equiv
$\mathbf{F}$	Force vector	N
$\mathbf{H}$	Magnetizing field	A/m
i	Current density	A/m^2

$\mathbf{i}$	Current density vector	A/m^2
i_o	Exchange current density	A/m^2
i_{Li}	Current density of lithium insertion or dissolution	A/m^2
i_p	Passive current density	A/m^2
I_{set}	Applied current density	A/m^2
J	Diffusive flux of chemical species	$mol/m^2 \cdot s$
K	Equilibrium constant	
K_{MT}	Mass Transfer Coefficient	m/s
l	Length	m
m	Molality of species	mol/kg
n	Number of electrons involved in electrode reaction	
$\mathbf{N}$	Species flux	$mol/m^2 \cdot s$
$\mathbf{P}$	Polarization vector	C/m^2
Q	Reaction quotient	
R	Universal gas constant	8.3143 J/mol·K
s	Displacement	m
$\mathbf{s}$	Displacement vector	m
$\mathbf{s}_0$	Time independent displacement vector	m
S	Reaction source or sink	$mol/m^3 \cdot s$
t	Time	s
T	Temperature	K
T_S	Tafel slope	V/decade

u	Mobility	$m^2 \cdot mol/J \cdot s$
U	Equilibrium potential	V
$\mathbf{v}$	Velocity of species	m/s
$\mathbf{V}$	Fluid velocity	m/s
y	Spatial coordinate	m
X	Extent of reaction	
z	Charge number	

Greek letters

α	Transfer coefficient	
β	Volume fraction	
δ	Charge density	C/m^3
ε	Permittivity	C/Vm
ε_0	Permittivity of free space	C/Vm
ε_r	Relative permittivity	C/Vm
Φ	Electric potential	V
γ	Activity coefficient	
η	Surface overpotential	V
κ	Conductivity	$\Omega^{-1}m^{-1}$
ν	Stoichiometric coefficient	
ρ	Free charge density	C/m^3

ρ_M	Mobile charge density	C/m^3
ρ_N	Charge density due to non-isotropic properties	C/m^3
ρ_P	Bound charge density	C/m^3
ρ_S	Static charge density	C/m^3
ρ_T	Total charge density	C/m^3
τ	Time period	s
ω	Relaxation factor	
Δx	Width of control volume	m
Δy	Distance between bulk fluid and bold surface	m
Δz	Height of control volume	m

Subscripts/superscripts

a	Anode
c	Cathode
H	Hydrogen evolution reaction
i	Species
j	Index/electrode
mouth	Crevice Mouth
last_Node	Last node on bold surface
O_2	Oxygen
θ	Standard / reference

1. INTRODUCTION

Theory and mathematical models must accompany experimental advances. Without theory, experimental observations are meaningless and without experimental observations theories are abstract. This thesis presents the development of a new theory of electrolytic transport and the coupled electric field that clarifies previous electrochemical theory.

1.1 General Summary

Electrolytic transport and the coupled electric field are important to many systems, including electrochemical cells. However, a universal characterization of the electric field corresponding to a non-isotropic electrolyte that may be conducting an electric current has remained elusive since the inception of Maxwell's equations in 1862. This thesis develops this characterization, applies it to engineering systems, and presents an underlying theory. Then, this thesis presents a reorganization of Maxwell's equations for the case where, in addition to the bound charge density theorized by Maxwell, other forms of charge density may also be present. The resulting equations accompany a unifying theory that explains electric fields as being due to the *propensity for charge density*.

This thesis contains portions of works that have been published in the open literature, accepted for publication, and are currently under review. Chapter 2 of this thesis presents conventional theory of electrolytic transport and the accompanying electric field. Chapters 3 and 4 investigate the numerical simulation of crevice corrosion. The majority of the content of Chapters 3 and 4 is reproduced from the journals of Corrosion Science (Kennell et al., 2008) and Electrochimica Acta (Kennell and Evitts, 2009), respectively, with permission from Elsevier. The models of crevice corrosion use a simplified one-dimensional characterization of the electric field developed from dilute solution theory. Chapter 5 develops a universal multi-dimensional characterization of the electric field (the Inherent Charge Density Model). Chapter 6 presents a universal electrolyte model that builds on the simpler model first presented by Kennell and Evitts (2010a). The universal electrolyte model incorporates the Inherent Charge Density Model developed in Chapter 5. Chapter 6 deals mainly with the validation of the universal electrolyte model against both experimental and numerical data from different systems containing different phenomena. Chapter 7 presents applications of the universal electrolyte model to different systems and investigates the advantages of including the charge density and concentration gradient effects on the electric field. Chapter 7 is based on a manuscript accepted for publication by the Canadian Journal of Chemical Engineering (Kennell and Evitts, 2011). Chapter 8 demonstrates multi-dimensional current distributions in charging lithium-ion cells and investigates the relationship between these current distributions and equilibrium potentials gradients caused by lithium concentration gradients within the electrodes. Chapter 9 presents a theory for the propensity for charge density that accompanies a reorganization of

Maxwell's equations for the case where multiple forms of charge density may be present, such as within a non-isotropic electrolyte conducting electric current. For all of the papers incorporated into this thesis, the author of this thesis was the main investigator, wrote the drafts of the papers, and corrected the drafts.

1.2 Significance of Contributions

Classical electrochemical theory (as presented in Chapter 2) does not present a universal characterization of the electric field coupled with an electrolyte. Instead, there are different equations describing effects on the electric field that incorporate different phenomena. These equations include: Ohm's law, Laplace's equation, Poisson's equation, and the Nernst equation, to name just a few. One complexity facing an electrochemical modeler is: which phenomena can be neglected and which effects on the electric field are important? In fact, Newman and Thomas-Alyea state that "no quantitative characterization or measure of the difference of electrical state of two phases has yet been given when the phases are of different chemical composition" (2004). In other words, a complete and quantitative characterization of the electric potential in an electrolyte has remained incomplete. This research presents the first such characterization of the electric potential field that accounts for all of the phenomena incorporated in the aforementioned equations, and additional phenomena, and developed from Maxwell's concept of the Electric Displacement Field. The incorporation of these multiple phenomena in a single equation results in a universal electrolyte model. When using this model it is no longer necessary to neglect important effects on the electric field. Instead, the new theory developed in this thesis presents a framework within which to compare the effects of different phenomena on the electric field. Furthermore,

this framework may be used to identify a single trend evident in the different phenomena: the *propensity for charge density*.

This research also presents models for predicting specific systems: a localized corrosion cell, a lithium-ion battery, and a dynamic liquid-junction. The model used for simulating the localized corrosion cell was developed prior to the universal electrolyte model; however, all models presented in this research build on the concept that an electrolyte transport equation not only describes the transport of ions, but a transport equation also inherently represents the relationship between a non-isotropic electrolyte and the coupled electric field.

1.3 Research Objective

The objective of this research was to develop a new multi-dimensional universal electrolyte model. The model must account for the effects of electric force interactions between ions, concentration gradients (including liquid-junctions), spatially separated anodic and cathodic reactions, and charge density. This model must not require the prescription of current distributions or the assumption of electroneutrality. Poisson's equation should not be directly incorporated to avoid a numerically stiff equation. This model must be capable of predicting current distributions, charge density distributions, concentration fields, and electric fields, and should require the prescription of a single transport property: the Fickian Diffusion Coefficient. A further objective of this research is to find a method of solving this model using a personal computer. Simulations for various systems should validate the model and provide theoretical insight.

2. CLASSICAL THEORY FOR ELECTROLYTIC TRANSPORT

Electrolytic transport covers a range of scientific topics. Some of the topics included in electrolytic transport theory, and utilized in this thesis, include: electrochemical circuits, electrochemical reaction kinetics, charge and mass transport, and the electric potential. This chapter will provide a brief review of classical theory covering the topics listed above. More information on these topics and other fields of theory that may affect electrolytic transport, but are not covered in this thesis, are presented by Newman and Thomas-Alyea (2004). Section 2.4.2 demonstrates how the multiple characterizations of the electric field available in the open literature are at a disadvantage when compared with the possibility for a single universal characterization. However, later chapters in this thesis build on this classical theory to present a universal characterization of the electric field and a new theory pertaining to the *propensity for charge density*.

2.1 Electrochemical Circuits

Electrolytic transport is often important for systems where the electrolyte forms part of an electrochemical circuit. Figure 2.1 shows an electrochemical circuit consisting of an electrolyte contained in a beaker, two electrodes, and a wire connecting the electrodes. Figure 2.1 also shows half reactions occurring at each electrode. For this discussion the nature of the half reactions are unimportant. It is sufficient to state that

the two half reactions form an electrochemical reaction and that current flows between the spatially distinct half reactions. The current flows from one electrode through the wire to the second electrode and then back to the original electrode through the electrolyte. In this manner, a complete electrochemical circuit is formed. The current through the wire takes the form of the transport of electrons and the current through the electrolyte takes the form of ionic transport. Since the net sum of electric potential gradients around any electric circuit (including an electrochemical circuit) is zero, the electric gradients in the electrolyte must be balanced with the electric gradients at all other locations in the electrochemical circuit.

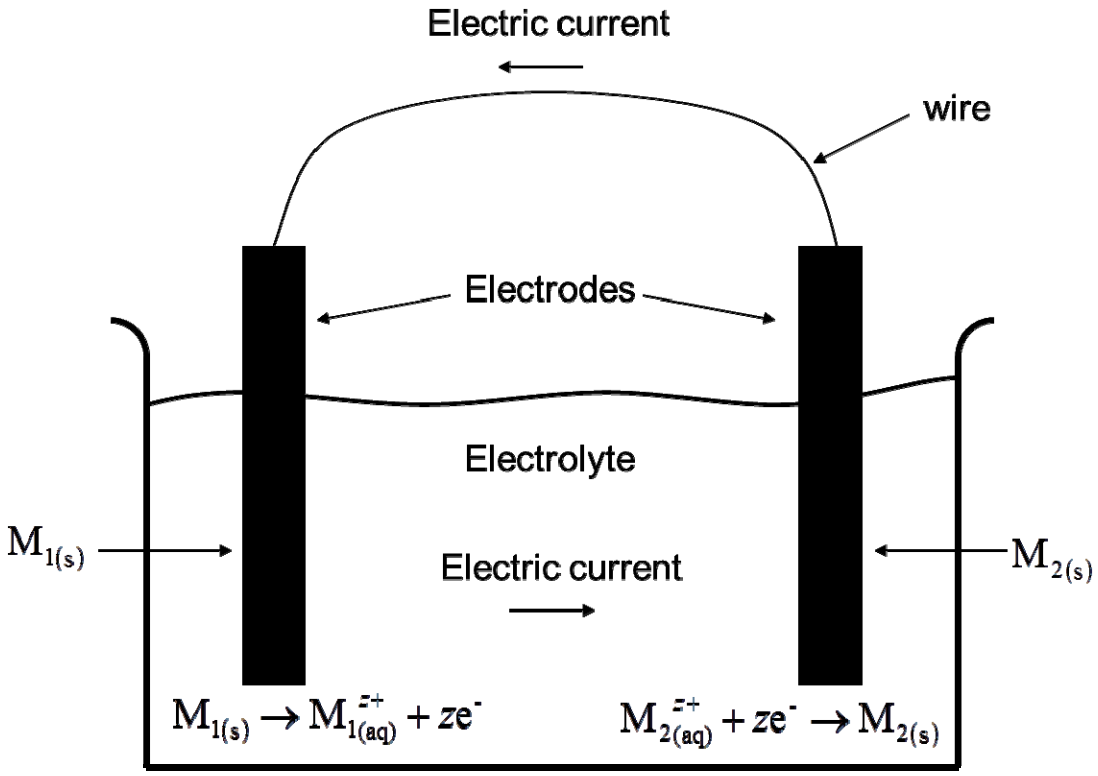

Figure 2.1. Electrochemical circuit.

To enhance understanding of electrochemical circuits, electric potential gradients are often attributed to different phenomena. For example, a potential gradient called the *surface overpotential* is often associated with the rate of half reactions occurring at electrodes and occurs very close to the electrolyte surface. The effect of this overpotential on the rate of electrochemical reactions will be further explored in Section 2.2. *Concentration overpotentials* are associated with concentration gradients that occur at larger distances from the electrode. If there is a concentration gradient with no flow of electric current, and if activity coefficients are equal to 1, then concentration overpotentials may be described via the Nernst equation. For the case where the electrodes are inserted into solutions of different molalities, the open circuit potential is given:

$$U = U^{\theta} - \frac{RT}{nF}\ln\left(\prod_i m_i^s\right)_{right} + \frac{RT}{nF}\ln\left(\prod_i m_i^s\right)_{left} \tag{2.1}$$

where the subscripts *left* and *right* correspond to the two different electrodes. If an electric current flows through the electrolyte and electrodes then Equation (2.1) is not valid. In this case, instead of Equation (2.1) other phenomena such as *Ohmic potential gradients* may be significant. Ohmic potential gradients are caused by the flow of electric current through the electrolyte. In the absence of concentration gradients the potential gradient associated with the electric current may be described by Ohm's Law (Newman and Thomas-Alyea, 2004):

$$\mathbf{i} = -\kappa\nabla\Phi \tag{2.2}$$

One difficulty in classical electrochemical theory is the ability to relate the multiple definitions of electric potential described above and in Section 2.4. In Chapter 9 of this thesis it will be proposed that a single phenomenon affects the electric potential

gradient, that of the *propensity for charge density*, and that the multiple phenomena listed above and the phenomenon incorporated in the concept of relative permittivity and described in Section 2.4.1 are simply different symptoms or manifestations of the *propensity for charge density*.

2.2 Electrochemical Reaction Kinetics

Electrochemical reactions may occur across an electrolyte-substrate interface. As described in Section 2.1, the rate of electrochemical reactions typically depends strongly on the surface overpotential, η. A commonly used relationship between the surface overpotential and reaction rate is the Butler-Volmer equation, which has terms that represent both the forward and reverse reactions:

$$i = i_0 \left[\exp\left(\frac{\alpha_a F}{RT} \eta \right) - \exp\left(-\frac{\alpha_c F}{RT} \eta \right) \right] \tag{2.3}$$

The Butler-Volmer equation can be simplified under some reaction conditions. The Tafel equation can be used when either the forward or reverse reaction can be neglected:

$$i = -i_0 \exp\left(-\frac{\alpha_c F}{RT} \eta \right) \tag{2.4}$$

This thesis does not utilize any aspect of electrochemical reaction kinetics more detailed than those already presented in this section. However, there is one aspect of electrochemical reaction kinetic theory that may be useful for a subsequent comparison with theories developed in this thesis: the electric double layer. The electric double layer may contribute significantly to the surface overpotential. A simple model of the double layer explains this contribution to surface overpotential as being due to a non-homogeneous distribution of ions close to the interface. The ionic distribution close to

the interface may not be homogenous because some ions have a greater tendency to get very close to the interface when compared with other ions in solution. In the case of a metal at the electrolyte interface, this tendency may be impacted by any electric charge on the metal. The non-homogenous distribution of ions in the electrolyte may cause localized charge density very close to the electrolyte (up to approximately 1 nm to 10 nm) (Newman and Thomas-Alyea, 2004). The aspect of this theory that compares favorably with theories developed in this thesis is that the relative movement, or tendency for ions to be located in a specific location, can cause charge density.

2.3 Charge and Mass Transport

2.3.1 Dilute Solution Theory

Dilute solution theory consists of infinitely dilute solution theory and moderately dilute solution theory (Newman and Thomas-Alyea, 2004). Moderately dilute solution theory is similar to infinitely dilute solution theory but considers effects of activity coefficients and is thus applicable to electrolytes of stronger concentrations. Newman (1973) presented a method for modeling current distribution and mass transfer in electrochemical systems that is very widely referenced in academic papers and in electrochemical text books. The method is based on the four principal equations from infinitely dilute solution theory (Equations (2.5) to (2.8)). The first equation describes the flux of a solute species due to electro-migration, diffusion, and convection:

$$\mathbf{N}_i = -z_i u_i F C_i \nabla \Phi - D_i \nabla C_i + \mathbf{V} C_i \tag{2.5}$$

where the fluid velocity, $\mathbf{V}$, may be determined from the Navier-Stokes equation and the continuity equation. The second equation is obtained from a material balance that leads to the differential conservation law:

$$\frac{\partial C_i}{\partial t} = -\nabla \cdot \mathbf{N}_i + S_i \tag{2.6}$$

The third equation presented by Newman states that the electrolyte is electrically neutral:

$$\sum_i z_i C_i = 0 \tag{2.7}$$

Newman states that Equation (2.7) is correct for the bulk electrolyte "to a very good approximation," when reactions are limited to the surfaces of electrodes (1973). This assumption is based on an argument made using Poisson's equation. This theory used Poisson's equation to show that "any initial charge density would be neutralized very rapidly or would rapidly flow to the boundaries of the solution" (Newman, 1973). The rapid transport of charge density to electrolyte boundaries is reasonable, but the compatibility of Poisson's equation with macroscopic transport equations for electrolytes will be explored in Chapter 5. The fourth equation presented by Newman describes the current density in an electrolyte as being due to the motion of charged species (1973):

$$\mathbf{i} = F \sum_i z_i \mathbf{N}_i \tag{2.8}$$

A fifth equation is identified by Newman for describing the potential in the bulk electrolyte when concentration gradients can be ignored is Laplace's equation (1973):

$$\nabla^2 \Phi = 0 \tag{2.9}$$

The method outlined by Newman uses Equations (2.5) to (2.9) to model current distribution and mass transfer in the bulk electrolyte. Phenomena occurring within a small layer of electrolyte in contact with the electro active area are accounted for through implementation of various boundary conditions. Some possible boundary conditions are when the electrolyte contacts an insulator into which no current is transported, where (Newman, 1973):

$$\frac{\partial \Phi}{\partial y} = 0 \tag{2.10}$$

and for current across the boundary:

$$i = 0 \tag{2.11}$$

or the electrolyte contacts an electro active area into which significant charge is transported across the boundary:

$$i = f(\eta_s, C_i) \tag{2.12}$$

For the case where the electrolyte contacts an electro active area and significant charge is transported between the electrolyte and substrate (and Equation (2.12) is used) the surface overpotential must also be calculated such that it balances with the overall potential drop caused by transport through the electrolyte (Newman, 1973):

$$\eta = V - \Phi \tag{2.13}$$

During computation, balancing the various electric potentials and currents in the system of equations may be accomplished via iteration. However, further assumptions are often made that simplify solving the system of equations. These assumptions depend on the type of system being analyzed and the magnitudes of various potential drops expected to occur within the system. For example, a Primary Current Distribution is expected when the potential drop due to Ohmic considerations is much larger than the

potential drop caused by surface and concentration overpotentials. Also, a Secondary Current Distribution is expected when Ohmic potential drops and surface overpotentials may be considered significant, but concentration overpotentials are not considered to be significant.

This brief review of Newman's model for current distribution and mass transfer in electrochemical systems (based on infinitely dilute solution theory) is not intended to be a complete literature review of current papers in the genre. Instead, the fundamentals of the approach presented by Newman are highlighted. There are three basic issues to modeling current distributions using the method based on classical dilute solution theory:

1. The model only applies to the electrically neutral bulk fluid. Therefore, for many applications additional models must be incorporated to model the diffuse boundary layer and results from these models incorporated into the bulk electrolyte model as boundary conditions.

2. Electrical interaction forces are neglected. Dilute solution theory does not account for the electrical interaction forces between various solute species. Therefore, Dilute Solution Theory "promotes circular or incorrect reasoning [when applied to] the question of liquid-junction potentials" (Newman and Thomas-Alyea, 2004).

3. Modeling electric fields requires drastic assumptions. The use of Laplace's equation to model the electric field requires the assumption of insignificant concentration gradients. The use of Poisson's equation to model the electric field creates a very stiff system of equations. This stiffness, the use of Poisson's equation, and an alternative equation will be explored in the Chapter 5.

In light of these issues there are scenarios for which dilute solution theory and the model for current distribution and mass transfer in electrochemical systems (based on dilute solution theory) may not suffice.

2.3.2 Concentrated Solution Theory

Concentrated solution theory may be used for multi-component transport where force interactions between the solute-solute and solute-solvent species are important. Concentrated solution theory deals with some of the issues pertaining to dilute solution theory by replacing Equation (2.5) with:

$$C_i \nabla \mu_i = RT \sum_j \frac{C_i C_j}{C_T D_{ij}} \left(\mathbf{v}_j - \mathbf{v}_i \right) \tag{2.14}$$

Equation (2.14) utilizes the gradient of electrochemical potential as the mass transfer driving force for diffusion and migration. It also uses a coefficient for the interaction between pairs of species. However, concentrated solution theory does not solve the problem of inter-species interactions without utilizing additional data to calculate the interaction coefficients; solutions of a single salt are characterized by three transport properties: the conductivity, the diffusion coefficient, and the transference number. Dilute solution theory utilizes only one transport property for each solute species: the diffusion coefficient. The difficulty of acquiring sufficient information to model plastic lithium ion cells using concentrated solution theory was stated by Doyle and Newman: "Unfortunately, very little of this information is available. In fact, the experimental methodology required to measure these properties has not yet even been developed. Thus, a full description of the electrolyte phase does not exist" (Doyle and Newman, 1996).

2.4 Electric Potential

2.4.1 Maxwell's Equations

In 1864 James Maxwell presented nine equations summarizing all known laws on electricity and magnetism (Maxwell, 1997). These equations have been shown to apply to a wide range of systems (Siegel, 1991). These equations may be presented in a number of different forms. These forms differ in the manner in which the materials are considered. The oldest and most widely used form was presented by Minkowski in 1908 (Rothwell and Cloud, 2009). Minkowski's form of Maxwell's equations consists of four field equations along with the continuity equation, referred to as the Maxwell-Minkowski equations. The four field equations are (Rothwell and Cloud, 2009):

$$\nabla \times \mathbf{E} = -\frac{\partial}{\partial t}\mathbf{B} \tag{2.15}$$

$$\nabla \times \mathbf{H} = \mathbf{i} + \frac{\partial}{\partial t}\mathbf{D} \tag{2.16}$$

$$\nabla \cdot \mathbf{D} = \rho \tag{2.17}$$

$$\nabla \cdot \mathbf{B} = 0 \tag{2.18}$$

The continuity equation is (Rothwell and Cloud, 2009):

$$\nabla \cdot \mathbf{i} = -\frac{\partial}{\partial t}\rho \tag{2.19}$$

For a linear isotropic material the Electric Displacement Field is (Rothwell and Cloud, 2009):

$$\mathbf{D} = \varepsilon_0 \mathbf{E} + \varepsilon_0 (\varepsilon_r - 1)\mathbf{E} \tag{2.20}$$

where, in the Maxwell-Boffi equations (Boffi, 1957), the second term on the right-hand-side is the polarization vector, $\mathbf{P}$. The polarization vector represents a response of bulk

molecules to an applied electromagnetic field. The polarization or distortion of these molecules creates an electric field that opposes the applied electric field. Equation (2.20) can be re-written (Rothwell and Cloud, 2009):

$$\mathbf{D} = \varepsilon_0 \mathbf{E} + \mathbf{P} \tag{2.21}$$

The bound charge density that is created by the polarization of molecules may be defined (Rothwell and Cloud, 2009):

$$\rho_P = -\nabla \cdot \mathbf{P} \tag{2.22}$$

Therefore, the only actual displacement of charge described by Equation (2.20) is described by the second term on the right-hand-side (RHS). The first term on RHS of Equation (2.20) describes an apparent displacement of charge that occurs whether or not a polarizable material is present. Equation (2.20) can be simplified (Rothwell and Cloud, 2009):

$$\mathbf{D} = \varepsilon \mathbf{E} \tag{2.23}$$

If the linear isotropic material is conductive Ohm's Law is applicable (Rothwell and Cloud, 2009):

$$\mathbf{i} = \kappa \mathbf{E} \tag{2.24}$$

At a given location and time Equations (2.17) and (2.23) may be combined:

$$\nabla \cdot (\varepsilon \mathbf{E}) = \rho \tag{2.25}$$

Electric potential is defined:

$$\mathbf{E} = -\nabla \Phi \tag{2.26}$$

Combining Equations (2.25) and (2.26) gives Poisson's equation:

$$\nabla \cdot (\varepsilon \nabla \Phi) = -\rho \tag{2.27}$$

This form of expressing Maxwell's equations and Poisson's equation are applicable at an instant in time. Poisson's equation relates the electric potential with charge density, the permittivity of free space and the effect of bound charge density created due to the polarization and reorganization of molecules. This polarization of molecules may be represented as a bound charge density (Equation (2.22)) and as a displacement of charge in the Electric Displacement Field (Equation (2.21)).

2.4.2 Multiple Characterizations of Electric Potential

In Sections 2.1 and 2.4.1 several characterizations of the electric field have already been given. Section 2.4.1 characterizes the electric field for a linear isotropic material using Poisson's equation (Equation (2.27)). A common assumption in the open literature is to assume Poisson's equation is applicable to non-isotropic electrolytes and Newman and Thomas-Alyea make this assumption in their famous argument when they use Poisson's equation to prove that the electroneutrality assumption is a good assumption for electrolytes (2004). However, Newman and Thomas-Alyea also offer some skepticism regarding electrostatics and Poisson's equation: "the concepts developed in electrostatic theory are not directly applicable to energetic relationships within condensed phases" (2004). As expressed in Section 2.1, there are a number of different electric potentials associated with different phenomena occurring within a condensed phase and often referred to as overpotentials. One of the characterizations given in Section 2.1 was derived from empirical observations: Ohm's Law (Equation (2.2)). An additional characterization of the electric field given in Section 2.1 and associated with a non-uniform electrolyte was the famous Nernst equation. Another version of this equation may be developed from the Nernst-Planck transport equation at

steady-state. The Nernst-Planck equation at steady-state is Equation (2.5) with convection neglected, and with the overall species flux equal to zero:

$$0 = -z_i u_i F C_i \nabla\Phi - D_i \nabla C_i \tag{2.28}$$

Rearranging Equation (2.28), incorporating the Nernst-Einstein equation, and integrating in one-dimension for a single species gives another version of the Nernst Equation:

$$\Phi^2 - \Phi^1 = -\frac{RT}{zF} \ln\left(\frac{C^2}{C^1}\right) \tag{2.29}$$

The Nernst Equation may be expressed in different forms than Equation (2.29) and may be developed from different theories. However, the method used here is based on transport of ionic species and this is the main theme investigated in this thesis.

Many other expressions describing the electric field as a function of ionic transport through an electrolyte have been presented in the open literature. One common characterization, for use when the current distribution is known, is given by Newman and Thomas-Alyea (2004):

$$\nabla\Phi = -\frac{\mathbf{i}}{\kappa} - \frac{F}{\kappa}\sum_i z_i D_i \nabla C_i \tag{2.30}$$

Similar to the Nernst Equation, Equation (2.30) can be developed from the Nernst-Planck equation. Equation (2.30) is used in the development of the mass transport model developed by Watson and Postlethwaite (1990a) and used in the crevice corrosion models of Chapters 3 and 4. Equation (2.30) and the other equations discussed in this section are just a few of the characterizations of the electric field that may be found in the open literature. Each characterization includes some effects on the electric field and neglects others. Newman and Thomas-Alyea state: “Much of the electrochemical

literature is written in terms of electrical potentials of various kinds, and it is necessary to set our minds straight on these matters and to investigate how potentials might be used in electrochemistry. Much of the confusion in electrochemistry arises from uncertainty in the use of these concepts" (2004). This thesis develops one equation that describes all of these effects in the separate equations mentioned in this chapter, and provides an accompanying explanatory theory that removes the confusion previously incorporated in electrochemical theory.

3. THE PATH TO A NEW THEORY – PART I: A CRITICAL CREVICE SOLUTION AND IR DROP CREVICE CORROSION MODEL

Sections 3.1 through 3.4 of this chapter constitute a reproduction from Corrosion Science, 50, of the paper: Glyn F. Kennell, Richard W. Evitts, Kevin L. Heppner, "A Critical Crevice Solution and IR Drop Crevice Corrosion Model", 1716-1725, (2008), with permission from Elsevier. The author of this thesis contributed to this paper in the following capacities: main investigator, conducted numerical modeling, analyzed results, wrote initial drafts of manuscript, and corrected drafts with editorial contributions made by Prof. Evitts and Dr. Heppner.

This chapter presents a numerical model for the simulation of crevice corrosion. Because models based on conventional dilute solution theory (as described in Chapter 2) have difficulties in modeling all of the aspects of corroding crevices, different approaches to crevice corrosion modeling have been developed to augment conventional theory. These different approaches emphasize the importance of different phenomena on the initiation and propagation of crevice corrosion. Many different approaches have been presented in the open literature. However, it may be possible to classify many models as belonging to one of two schools of theory: Critical Crevice Solution Theory emphasizes the importance of the chemical composition of the electrolyte within the crevice and IR Drop Theory emphasizes the importance of the electric potential drop (caused by Ohmic considerations) along the crevice. This chapter represents a first step

in the development of theory that is completed in later chapters. This chapter utilizes a characterization of the electric field that is a simplification of the Inherent Charge Density Model developed in later chapters. This one-dimensional characterization of the electric field was developed from the transport equation from dilute solution theory.

3.1 Introduction

Crevice corrosion is an especially important from of corrosion due to its nature of being difficult to detect whilst potentially destroying the structural integrity of metals that do not corrode under normal circumstances. Since crevices that cause this form of corrosion can be readily created, for example, through the gap in a flange or under a deposit, catastrophic structural failure can occur in situations that corrosion may have otherwise been unexpected. In these situations crevice corrosion may also go completely undetected until failure. Mathematical models help to understand the fundamental mechanisms underlying crevice corrosion and improve our ability to predict crevice corrosion.

Crevice corrosion has three stages: incubation, initiation, and propagation. The duration of each stage depends on geometric, metallurgical and environmental situations and thus the time to attain any given stage can vary significantly. In other words, a crevice may almost immediately move to a stage of initiation, meaning high rates of corrosion, or else a crevice may indefinitely remain in a stage of incubation, meaning crevice corrosion never initiates. The first stage of crevice corrosion is incubation. Two theories exist describing the processes occurring during incubation that determine the possibility of initiation: Critical Crevice Solution Theory (CCST) and IR Drop Theory

(IRDT). The particulars of each of these two theories are discussed below after an explanation of the fundamental processes similar to both.

Both CCST and IRDT state that during incubation very low levels of corrosion occur on the surface of passive metals in contact with an electrolyte which is manifested as a small leakage current, often called the passive current. This process occurs both within the crevice and on the bold surface (metal surface exterior to the crevice). Dependent upon the geometry of the crevice, oxygen may become depleted within the crevice. Oxygen will be depleted in the crevice if it is consumed faster than it is able to diffuse into the crevice through the crevice mouth. The depletion of oxygen suppresses cathodic reactions within the crevice; however, cathodic reactions on the bold surface may maintain the anodic reactions in the crevice. Anodic regions in the crevice couple with cathodic regions on the bold surface through the transportation of charge via electrons through the metal and ions through the solution, as shown in Figure 3.1. Hydrolysis of the metal ions resulting from dissolution will lower the pH of the crevice solution. The current flowing in the solution, along with the electroneutrality constraint, will cause an influx of anions into the crevice.

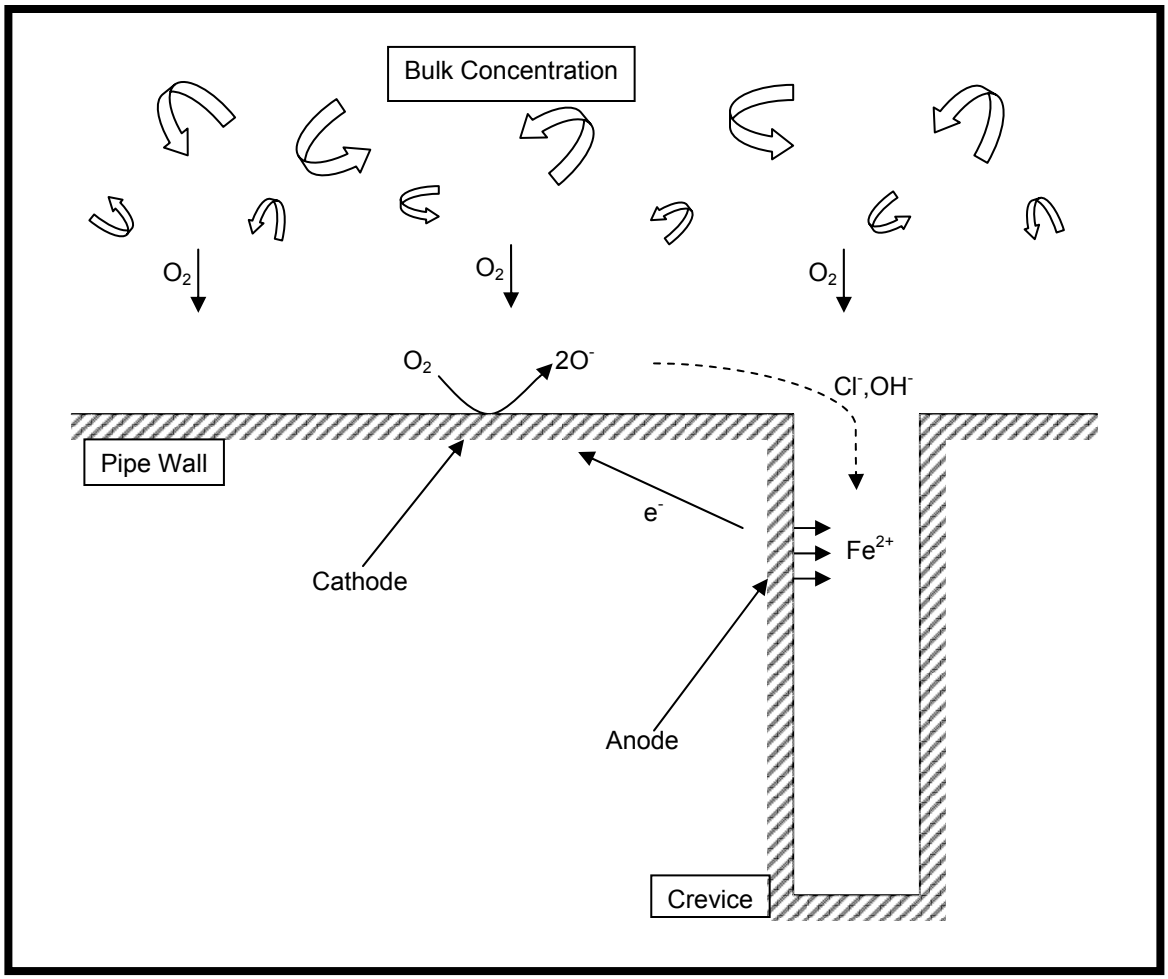

Figure 3.1. Idealized corroding crevice (unrealistic crevice aspect ratio)

3.1.1 Critical Crevice Solution Theory

When the pH and chloride ion concentration in the crevice solution cause disruption of the passive film the solution is said to have reached a critical state and crevice corrosion will have initiated. This is the onset of the active stage of crevice corrosion with high rates of corrosion occurring in the crevice. The anodic sites within the crevice are coupled with cathodic sites upon the bold surface as shown in Figure 3.1. During this stage the rate of the anodic reactions may increase causing a further reduction in pH

and an increase in the rate of influx of anions into the crevice. This stage causes rapid deterioration of the metal within the crevice, with possible structural failure of the metal.

3.1.2 IR Drop Theory

The IR drop mechanism was first published by Pickering (1986), who stated that crevice corrosion would abruptly start when the potential difference between the crevice mouth and interior was large enough to cause the anodic potentials to become active. This difference is caused by the iR drop in the solution, the magnitude of which is due to factors such as concentration gradients, composition and geometry. Figure 3.2 shows the effect of the iR drop on reaction kinetics. In Figure 3.2, the cathodic polarization curve is shown without any iR effects. This curve only cuts the anodic polarization curve within the passive region, resulting in a very low corrosion current. The cathodic polarization curve with iR effects is shown to cut the anodic polarization curve below the critical potential, in the active region, resulting in significantly greater magnitudes of corrosion current.

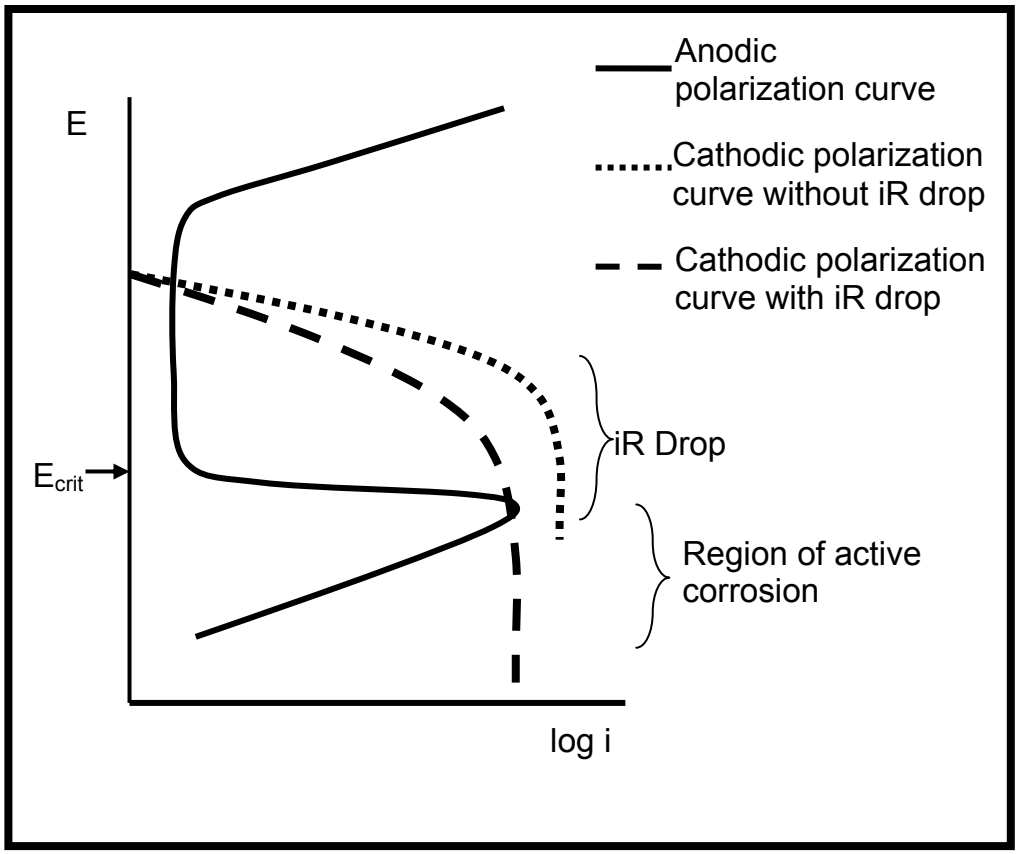

Figure 3.2. Idealized kinetic corrosion diagram for a passive metal

3.1.3 Modelling Studies for Crevice Corrosion

Oldfield and Sutton (1978) developed a CCST model that predicted the crevice corrosion incubation period for stainless steels. They assumed that there were no concentration gradients within the crevice, with mass transport occurring solely between the crevice and bulk fluid. Galvele (1976, 1981), and Galvele and Gravano (1984) developed three CCST pitting corrosion models culminating in a model that considered diffusion, migration, and electroneutrality. The authors demonstrated that the pH within the pit was significantly lower than the bulk pH, with the major change occurring at the pit mouth. Turnbull and Ferris (1986) developed a steady state model, including convection, describing the chemical composition of corrosion fatigue cracks in

cathodically protected steel in sea water. The reduction of oxygen was assumed negligible and the decomposition of water was assumed to be the cathodic reaction. Some results agreed well with experimental data while other results did not. Sharland and Tasker (1988) simulated the initiation of crevice corrosion and determined the solution chemistry and potential within the crevice using CCST. They assumed negligible hydrogen reduction and constant passive current. Ion production, transport, and chemical equilibrium were decoupled in the model, with electroneutrality subsequently imposed. Results were in reasonable agreement with experimental data. The IRDT model produced by Walton et al. (1996) accounted for transport in moderately concentrated solution by diffusion and electromigration. The simulation, conducted for stainless steel, assumed passive current independent of potential in the crevice. Results were in approximate agreement with the experimental data of Alavis and Cottis (1987) for AISI 304 stainless steel. Engelhardt et al. (1999) combined a boiling crevice model with a coupled environment fracture model to create a model describing transport processes in a pressurized water reactor. The coupling was implemented using the principle of charge conservation and considered the influence of convection, diffusion, and electromigration. Results showed that after an initial period concentration gradients exist at the crevice mouth whilst further into the crevice no concentration gradients exist. Cui et al. (2005) used the computational code CREVICER to model the net current supplied from the cathode while maintaining an anodic crevice at the repassivation potential. The size of the cathode was limited by the size the electrolyte, which was considered to be a thin layer of water from atmospheric moisture with dissolved ions. Conductivity was assumed to be constant. The net

current was found to be influenced by water layer thickness, size of cathode, chloride ion concentration, kinetic parameters, and repassivation potential. The potential was found to approach the corrosion potential and the cathodic current decreased as the distance from the crevice increased. White et al. (2000) numerically simulated variations in solution chemistry in the crevice using CCST. Their simulations examined the initiation period for bulk solutions of near neutral pH. They predicted that the pH within the crevice did not fall below the critical pH of 2.1 for AISI 304 stainless steel when predicting the experiment of Alavi and Cottis (1987). Subsequently, by considering potential drops in the crevice and using a semi-empirical correlation with parameters chosen to match model current densities with experimental current densities, pH profiles were predicted that approximated the experimental data of Alavis and Cottis. Watson and Postlethwaite (1990a, 1990b, 1991) created a CCST model with few empirical limitations describing the incubation period of a crevice, and solved Poisson's Equation for electroneutrality. Heppner et al. (2002a, 2002b) subsequently developed this model into a generic model for different types of metals and electrolytes. The model described the chemistry within the crevice rigorously.

The research presented within this chapter is a significant extension of the Heppner et al. (2002a, 2002b) model. The current model maintains the rigorous chemical description of the crevice solution, and develops a method to augment the CCST model with a model that considers the potential differences between anodic sites in the crevice and cathodic sites on the bold surface.

3.2 Mathematical Model Development

The mass transport model and models for chemical reactions and electroneutrality used in this research were previously developed and validated (Heppner et al., 2002a; Heppner et al., 2002b; Heppner and Evitts, 2005; Heppner and Evitts, 2006). However, they will be briefly discussed here for clarity. A new method for determining the rate of electrochemical reactions and coupling the crevice with the bold surface, by combining Crtitical Crevice Solution Theory and iR Drop Theory, is the main focus of this chapter.

3.2.1 Mass Transport Mechanisms within the Crevice

Within the crevice the fluid is assumed to be completely stagnant. Thus, mass transport is due only to concentration or activity and electric potential gradients. The mass transport model developed by Watson and Postlethwaite (1990a, 1990b, 1991) is used in this model and it considers diffusion, electromigration, diffusion potential, charge density constraints, and a source or sink of chemical species due to chemical reactions. It is given as Equation 3.1:

$$\frac{\partial C_i}{\partial t} = -\frac{z_i u_i F^2 C_i}{\varepsilon}\sum_j z_j C_j - \frac{z_i u_i \nabla C_i}{F\sum_j z_j^2 u_j C_j} i - \frac{z_i u_i \nabla C_i}{\sum_j z_j^2 u_j C_j}\sum_{j=1}^{k} z_j D_j \nabla C_j + D_i \nabla^2 C_i + S \quad (3.1)$$

For reasons given in the next section describing electroneutrality, the first term in this equation describing charge density is solved independently, resulting in:

$$\frac{\partial C_i}{\partial t} = -\frac{z_i u_i \nabla C_i}{F\sum_j z_j^2 u_j C_j} i - \frac{z_i u_i \nabla C_i}{\sum_j z_j^2 u_j C_j}\sum_{j=1}^{k} z_j D_j \nabla C_j + D_i \nabla^2 C_i + S \quad (3.2)$$

This equation was discretized using a one-dimensional finite difference grid, shown in Figure 3.3, with two fictitious nodes and a hybrid Crank-Nicolson method (Heppner and

Evitts, 2005). Boundary conditions for the numerical solution of the crevice mass transport model were zero flux at the crevice tip and bulk solution concentration at the fictitious node outside the crevice mouth. (Bulk solution concentration used in the prediction of the Alavi and Cottis (1987) experiment was 0.6 M NaCl solution). The values for the diffusion coefficients and mobilities used in the model are found elsewhere (Heppner et al., 2002b).

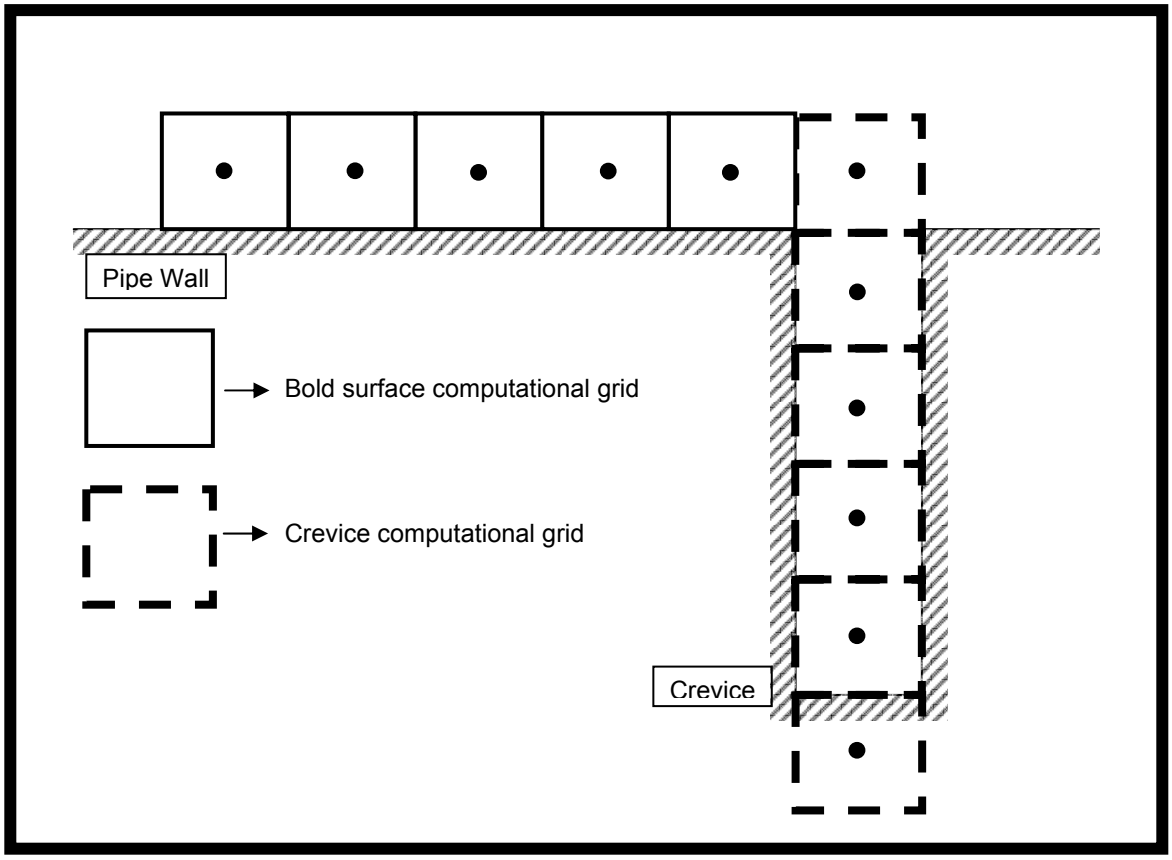

Figure 3.3. Computational grid used in current model.

3.2.2 Treatment of Electroneutrality

Providing the system does not deviate significantly from electroneutrality the charge density term in Equation (3.1) has little influence on the rate of mass transport and it can

be neglected. This reduces the stiffness of Equation (3.1) and produces Equation (3.2) which is numerically less stiff than Equation (3.1). However, in order to maintain the system in a state that is close to electroneutrality Equation (3.1) is reapplied to the solution using time steps of the order of 10^{-10} s. The effect is to reduce Equation (3.1) to Equation (3.3), since over such a small time step transport processes other than by electroneutrality are negligible. It is the solution of Equation (3.3) that maintains the system close to electroneutrality.

$$\frac{\partial C_i}{\partial t} = -\frac{z_i u_i F^2 C_i}{\varepsilon} \sum_j z_j C_j \tag{3.3}$$

Equation (3.3) is solved using the algebraic correction method of Heppner and Evitt (2006):

$$C_i = C_i^{old} - z_i u_i C_i \frac{F\delta}{\kappa} \tag{3.4}$$

This algebraic equation is derived from Poisson's Equation for charge density. Use of this method provides a numerical solution for a concentration field that is free of net electrical charge at less computational expense than alternative methods by avoiding the direct solution of Poisson's equation (Heppner and Evitts, 2006).

3.2.3 Chemical and Electrochemical Reactions

Chemical and electrochemical reactions are represented by the source term, *S*, in Equation (3.1). For chemical reactions kinetic behaviour is neglected, giving (Heppner et al., 2002a):

$$\prod_j C_j^{v_{ij}} - K_i = 0 \tag{3.5}$$

where C_j is the equilibrated concentration of the jth species occurring in the ith chemical reaction, and K is the equilibrium constant. For electrochemical reactions a similar equation can be written (Heppner et al., 2002a):

$$\prod_j C_j^{v_{ij}} - Q_i = 0 \tag{3.6}$$

where:

$$Q_i = \exp\left(\frac{\left(E^0 - E\right)z_i F}{RT}\right) \tag{3.7}$$

where E^0 is the reversible potential and E is the potential. A mass balance equation can also be written for each species involved (Heppner et al., 2002a):

$$C_j = C_j^{init} + \sum_{i=1}^{n} X_i v_{ji} \tag{3.8}$$

The mass balance equations for both the chemical and electrochemical reactions are combined providing a guaranteed non-singular matrix, solution of which is achieved by the Newton-Raphson method.

3.2.4 Bulk Solution Mass Transport Model

A mass transport model was developed to model the aerated electrolyte for the cathode used by Alavi and Cottis (1987). Since practically no information pertaining to the dynamic state of the electrolyte for the cathode was given by Alavi and Cottis, some variables were estimated for this part of the model. However, the estimated variables have little effect on the final results presented in this chapter because the numerical solution of the cathode only provides the values of the potential drop and cathodic current that are used during the numerical solution of the anode (this is further explained

in a later section of this chapter). This potential drop is small and does not greatly affect the final numerical solution of the anode.

Transport of species to the bold surface was modeled by using a grid of control volumes, shown in Figure 3.3, stretching from the mouth of the crevice outwards along the bold surface. This grid was assumed one dimensional due to the absence of convection in the Alavis and Cottis electrolyte. It was assumed that three phenomena could exist that would affect the concentration of species in the bold surface computational domain: diffusive transport of species between control volumes due to a concentration gradient along the bold surface, transport of species between the bold surface and bulk fluid, and depletion of species due to electrochemical reactions at the bold surface.

Diffusive transport of species from a neighbouring control volume was calculated using Fick's Law:

$$J = -D\frac{\partial C}{\partial x} \tag{3.9}$$

where J is the amount of species transported, and D is the diffusion coefficient. Transport of oxygen from the bulk fluid into each control volume is assessed using the relation:

$$S = \frac{K_{MT}}{\Delta y}\left([Bulk]-[Surface]\right) \tag{3.10}$$

where C is concentration, t is time, Δy is the distance of the bulk fluid from the top of the control volumes, [] indicates concentration, and K_{MT} is the mass transport coefficient estimated to be $5.5 \times 10^{-8} m^2/s$ (this includes estimated aeration effects). The bulk concentration of oxygen at atmospheric pressure was calculated to be 2.6535×10^{-4}

mol/l. Consumption of oxygen from each control volume was considered proportional to the corrosion current in that control volume:

$$S = -\frac{i}{\Delta z F z} \tag{3.11}$$

where i is the current density. Thus the transport of the species is described by:

$$\frac{\partial C}{\partial t} = D\frac{\partial^2 C}{\partial x^2} + \frac{K_{MT}}{\Delta y}\left([Bulk] - [Surface]\right) - \frac{i}{\Delta z F z} \tag{3.12}$$

This equation was solved implicitly using backward time and central space discretization and two fictitious nodes at the crevice mouth and far from the crevice where the bold surface is unaffected by the crevice. The initial condition was bulk concentration in all control volumes. It was assumed that there are no concentration gradients at the crevice mouth and concentration for the control volume furthest from the crevice is constant.

3.2.5 Anodic Corrosion Current

At the start of the simulation oxygen is assumed depleted in the crevice and the passive current flows from metal into solution in the crevice. The magnitude of the passive current is determined by modifying a reference current for pH effects by a Freundlich adsorption equation (Shreir et al., 1994):

$$\log(i_P) = \log(k) - n\text{pH} \tag{3.13}$$

At the start of the simulation the conductivity of the solution in the crevice is relatively low. The passive current causes anions (including chloride ions) to be drawn into the crevice and the pH within the crevice to drop. This increase of chloride ion concentration and decrease in pH within the crevice attacks the passive film and causes

the conductivity of the crevice solution to increase. The attack on the passive film reduces the protectiveness of the film and, generally, the corrosion current (whether passive or active) will increase. The increase in corrosion current, concentration of species within the crevice, and conductivity between the anodic and cathodic sites on the metal surface changes the potential difference between the sites. This change in potential difference affects the overpotential at the anode as explained in a later section of this chapter. If the overpotential is shifted from the passive into the active region, the crevice would be active at those anodic sites. In that case, for the active portions within the crevice, the current is calculated assuming Tafel behaviour:

$$i = i_{0,a} \cdot 10^{\left(T_S\left(E_a - E_{0,a}\right)\right)} \tag{3.14}$$

where, $i_{0,a}$ is the exchange current density for the anodic reactions, T_S is the Tafel slope, E_a is the anodic surface overpotential, and $E_{0,a}$ is the reversible potential of AISI 304 stainless steel. A portion of crevice is assumed active if its potential falls between the critical potential, E_{crit}, and the reversible potential, $E_{0,a}$. Values for all of these parameters were estimated from experimental data from a number of sources (Shreir et al, 1994; Majidi and Streicher , 1984; Matsushima et al., 1978; Oldfield, 1980; Sridhar and Dunn, 1994). Oldfield (1980) observed that the logarithm of active peak height for AISI 304 stainless steel varied linearly with a change in solution pH. Oldfield found this slope to be 2 over a small pH range. By observing more of the data covering a larger pH range presented in Oldfield's (1980) paper, and also the effect of pH and chloride ion concentration on the anodic polarization curve presented by Matsushima et al. (1978), the dependence of $i_{0,a}$ on pH was determined for the present study. These values of all of the above parameters are presented in Table (3.1).

Table 3.1. Values for parameters used in mathematical model.

Anode	$i_{0,a}$	$E_{0,a}$	T_S	E_{crit}
	$1\times10^{-3\text{-pH}}$ A/cm^2	-0.259 V/SHE	0.1 V/dec	-0.009 V/SHE
Cathode	$i_{0,c}$*	$E_{0,c}$*	T_S *	E_{corr}
	1×10^{-9} A/cm^2	0.191 V/SHE	0.1 V/dec	0.1 V/SHE

* (Cui et al., 2005)

3.2.6 Anodic Surface Overpotential

Cell potential is composed of three parts: the ohmic potential drop in the solution; a potential loss due to concentration variations; and a surface overpotential caused by the electrochemical reactions (Newman, 1973). If the potential drop across the metal connecting the anode with the cathode is also considered, a complete circuit of electrical potential drops is achieved and the total potential drop for the circuit must be zero. The complete circuit can be seen in Figure 3.4, showing potential drops in solution, at the surface of each electro-active site, and through the metal. For situations where the solution contains concentration gradients, for an infinitely dilute solution, the potential drop in the solution due to ohmic and concentration effects is (Newman, 1973):

$$\nabla\Phi = -\frac{\mathbf{i}}{\kappa} - \frac{F}{\kappa}\sum_j z_j D_j \nabla C_j \tag{3.15}$$

where **i** is the current, κ is the conductivity of the solution, F is Faraday's constant, z is the charge of the species, D is the diffusion coefficient, and ∇C is the concentration gradient. The resistance to the flow of electrons through the metal is extremely small compared to the other potential drops being considered; therefore, the electrical resistance of the metal is assumed to be zero. To complete the circuit the surface overpotentials are still required. The anodic surface overpotential is calculated by:

$$\eta_a = E_{mouth} + \nabla\Phi \tag{3.16}$$

where E_{mouth} is the potential at the mouth of the crevice, which is determined by balancing the potentials at the anodic and cathodic sites as described in a subsequent section in this chapter.

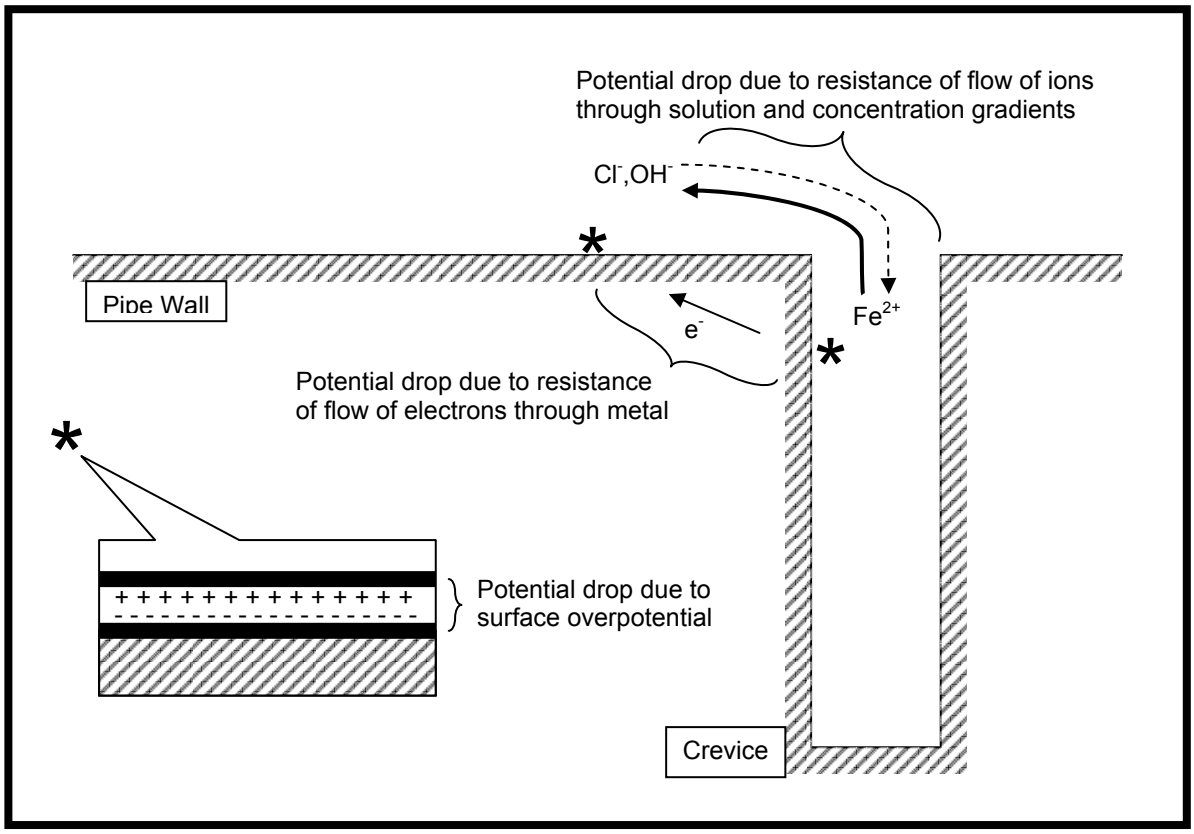

Figure 3.4. Electrochemical circuit of corroding crevice after depletion of oxygen in the crevice.

3.2.7 Cathodic Current and Surface Overpotential

At the bold surface the cathodic current is calculated with the assumption that the reaction undergoes Tafel kinetics:

$$i = i_{0,c} \cdot 10^{\left(T_S\left(E_{0,c} - E_c\right)\right)} - i_p \tag{3.17}$$

where $i_{0,c}$ is the cathode exchange current density, $E_{0,c}$ is the cathode reversible potential, E is the surface overpotential, i_p is the passive current being consumed by anodic reactions occurring on the bold surface. Values for the cathodic reversible potential and exchange current density can be found in Table (3.1) (Cui et al., 2005). The potential, $E_{cathode}$, is calculated in a similar manner to the anode potential, but increasing with distance from the crevice mouth because node potentials are solved for in the same direction as the flow of corrosion current:

$$\eta_c = E_{mouth} - \nabla\Phi \tag{3.18}$$

where $\nabla\Phi$ is calculated via Equation (3.19):

$$\nabla\Phi = -\frac{\mathbf{i}}{\kappa} - \frac{RT}{2F}\ln\left(\frac{[O_2]_{mouth}}{[O_2]}\right) \tag{3.19}$$

3.2.8 Numerical Solution and Balancing of Anodic and Cathodic Currents

The equations used to mathematically describe the corroding crevice and supporting bold area have been given in the previous sections of this chapter. This section describes the manner in which these equations are solved. The electrode kinetics for the model are separated into two distinct parts: the anode within the crevice, and the cathode at the bold surface. These two parts are solved sequentially then balanced. The approach taken to balance the anode and cathode first considers the current produced at the anode and the current produced at the cathode separately. Then these two currents are balanced by finding the potential at the interface between the two that causes equal cathodic and anodic currents. In this model the interface is assumed to be the crevice mouth. Figure 3.5 illustrates the locations of variable and fixed potentials in the crevice

corrosion system. This type of balance is somewhat different than the technique of Engelhardt et al. (1999) who balanced a system of transport equations and the current produced in a boiling crevice with Laplace's equation in the external environment by iterating to find the correct potential at the crevice mouth.

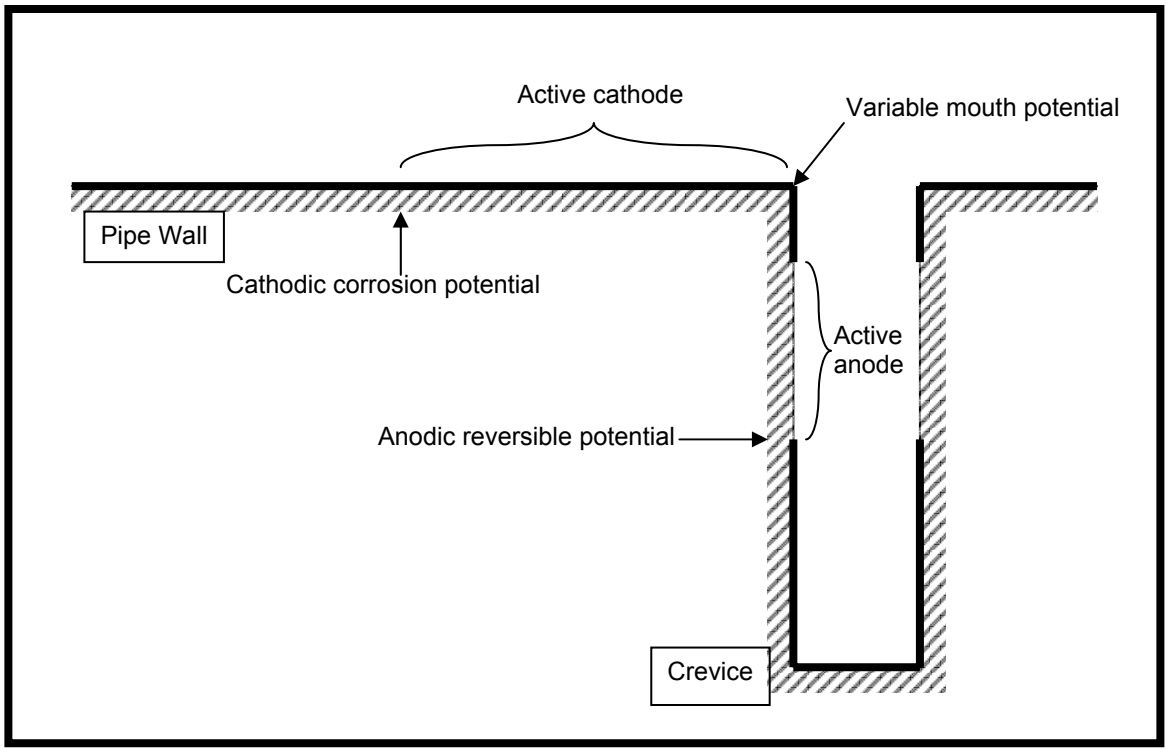

Figure 3.5. Locations of variable and fixed potential differences.

In the model presented in this chapter, if the potential at the crevice mouth increases, then potentials along the anode, which are calculated relative to the potential at the crevice mouth, also increase. For an active-state anodic site, this increase in potential increases the total current produced at the site. Conversely, an increase in potential at the crevice mouth increases the potential along the cathode. This decreases the cathodic current produced by the electrochemical reactions along the cathode because they are

assumed to follow Tafel behaviour. This process is akin to the balancing of electrochemical potential in the system.

Figure 3.6 is a flow sheet of the current model that focuses on the balancing of charge and current between the anode and cathode and neglects some of the procedures implemented in other aspects of the overall model and that have been previously published. As shown in Figure 3.6, at each time step the current is determined at each node, starting at the crevice mouth, using Equation (3.13) or Equation (3.14), depending on whether the node is in the active state or not. Equation (3.14) is solved using a simple root searching technique. For each iteration in the search the potential field in the crevice is determined and this updates the prediction of the anodic current. When solving Equation (3.14) the root searching technique does not solve for current densities that would cause the surface overpotential to be below the reversible potential of AISI 304 stainless steel. In the case where solving Equation (3.14) for the specified solution conditions and corrosion densities from neighbouring nodes would lead to a surface overpotential less than the reversible potential, the root solving technique returns the current density that causes the surface overpotential to be the reversible potential at that node. When the electric potential drops in the crevice solution become equal to the reversible potential of AISI 304 stainless steel at some location within the crevice, it is assumed that any node deeper into the crevice is unable to couple with the bold surface. These nodes are said to be extinct and no net current is produced from these nodes.

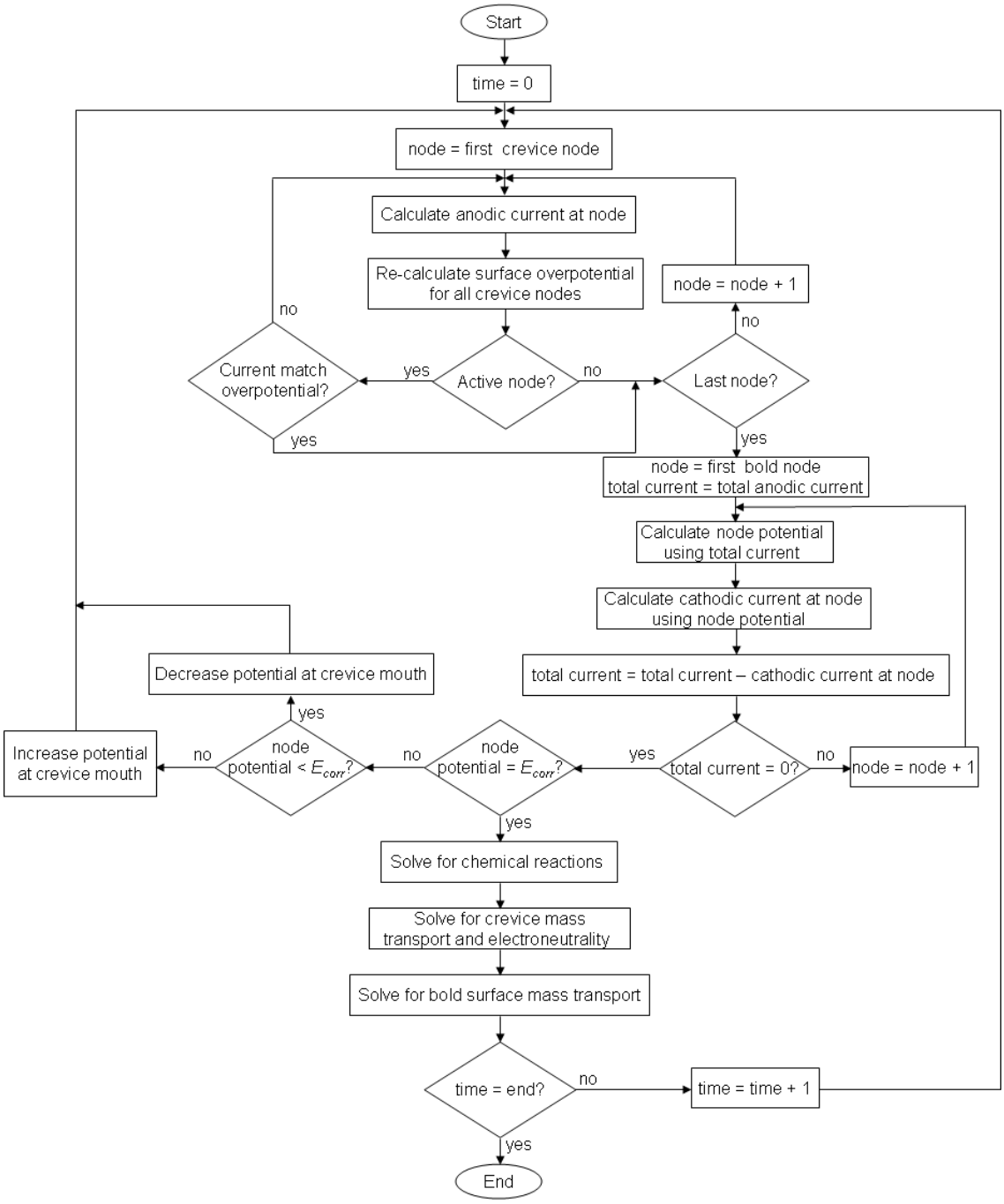

Figure 3.6. Flow chart showing the order of operations for the current model. The flowchart focuses more on the operations pertaining to the balancing of potential and current at anode and cathode.

The cathodic corrosion currents along the bold surface are found starting at the node closest to the crevice mouth and progressing away from the mouth. The current flowing

into the first node will be the total current exiting the crevice. This current, **i**, can be used to solve Equation (3.19) for the electrical potential drop and then Equation (3.18) for the surface overpotential for the first node. Subsequently, the cathodic current produced by the first cathodic node can be calculated using Equation (3.17). The current flowing through the next node will be the total current from the crevice minus the cathodic current produced by the first cathodic node. In this manner the current density produced along the bold surface nodes can be solved until the final node is determined . The final node is deemed to be a node with a potential that is equal to, or above, the corrosion potential, E_{corr} , or else if the current produced at the cathode exceeds the current produced at the anode, the node that causes this excess current. Dependent upon whether the cathode is producing too much current, or has too little cathodic overpotential (not enough current), the crevice mouth potential is changed. After a change in crevice mouth potential new corrosion current densities are determined at all anodic and cathodic sites. This process continues until the potential at the final node on the bold surface is equal to the corrosion potential and the total cathodic current is equal to the total anodic current. The potential at the crevice mouth is changed according to:

$$E_{mouth} = E_{mouth} + \left(E_{corr} - E_{Last\_Node}\right) \cdot \omega \tag{3.20}$$

where E_{Last_Node} is the potential of the last active cathodic node, ω is a relaxation factor, and E_{mouth} is initially arbitrarily set to zero. This balancing algorithm may seem computationally expensive. However, the total current produced by either the anodic or cathodic regions does not change significantly between time steps, except during crevice

initiation. In fact, this technique does not result in a large amount of computation expense.

3.3 Results and Discussion

The model presented in this chapter was validated against the experimental data of Alavi and Cottis (1987). In their experiment Alavi and Cottis studied a crevice of 90 ± 10 μm gap, 2.5 cm width, and 8 cm depth. The crevice walls were made from AISI 304 stainless steel and were coupled to a cathode made from AISI 304 stainless steel situated in aerated bulk electrolyte under free corrosion conditions. The electrolyte consisted of 0.6 M NaCl solution. The temperature of the electrolyte was 23 ± 1°C.

Figure 3.7 shows the validation of the current model against the experimental data of Alavi and Cottis (1987) and five of the leading published crevice corrosion models that were also used to simulate the Alavi and Cottis experiment. It is evident from the figure that the current model is a significant improvement over the other models. The model is the only one that also correctly predicts the shape of the pH profile along the length of the crevice. It predicts a pH at the tip, which is higher than the pH at the mouth, which is strikingly similar to that of the experimental data. The model also displays a minimum of pH that is about 1 cm from the crevice mouth, which also corresponds quite well to the experimental data.

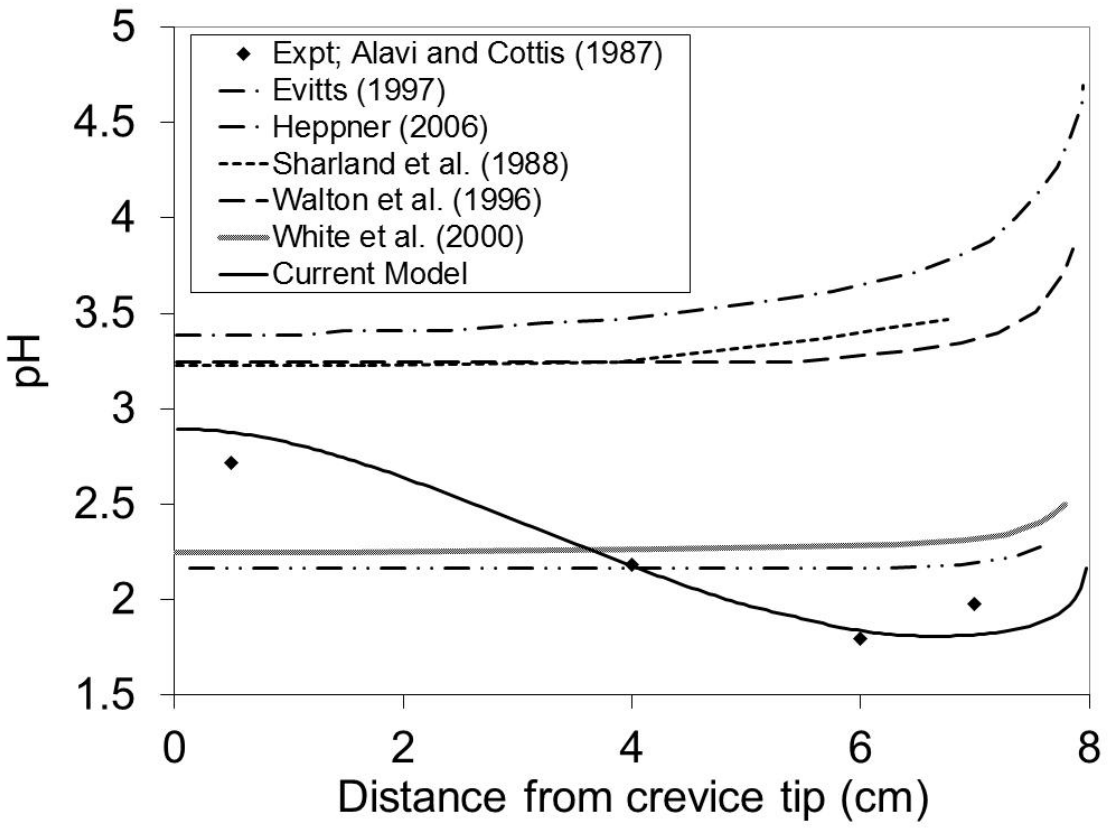

Figure 3.7. Comparison of published models and experimental data for a corroding AISI 304 stainless steel crevice.

The current model does not only correctly predict the steady-state pH profile in the crevice, but the predicted pH profile also has a reasonable correspondence to the dynamic behaviour found in the experiment of Alavi and Cottis (1987). Predicted pH profiles at different time intervals are shown in Figures 3.8 to 3.10. This dynamic behaviour can be broken down into three phases that explain the model predictions shown in Figures 3.8 to 3.10: the total corrosion phase, the dynamic phase, and the quasi steady-state phase.

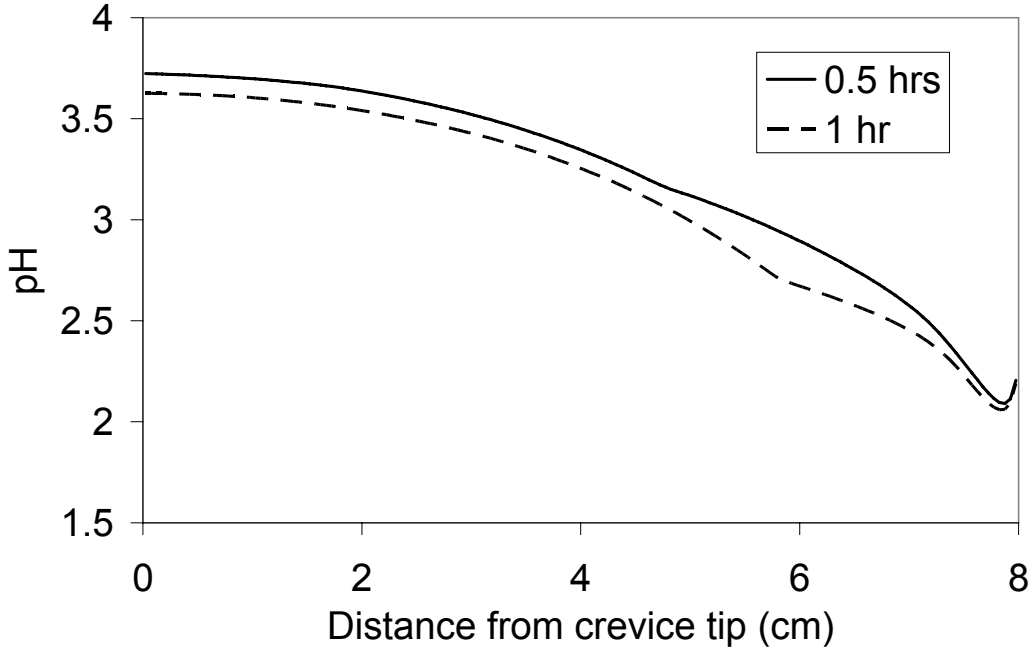

Figure 3.8. Predicted pH profiles in a corroding crevice during the total corrosion phase.

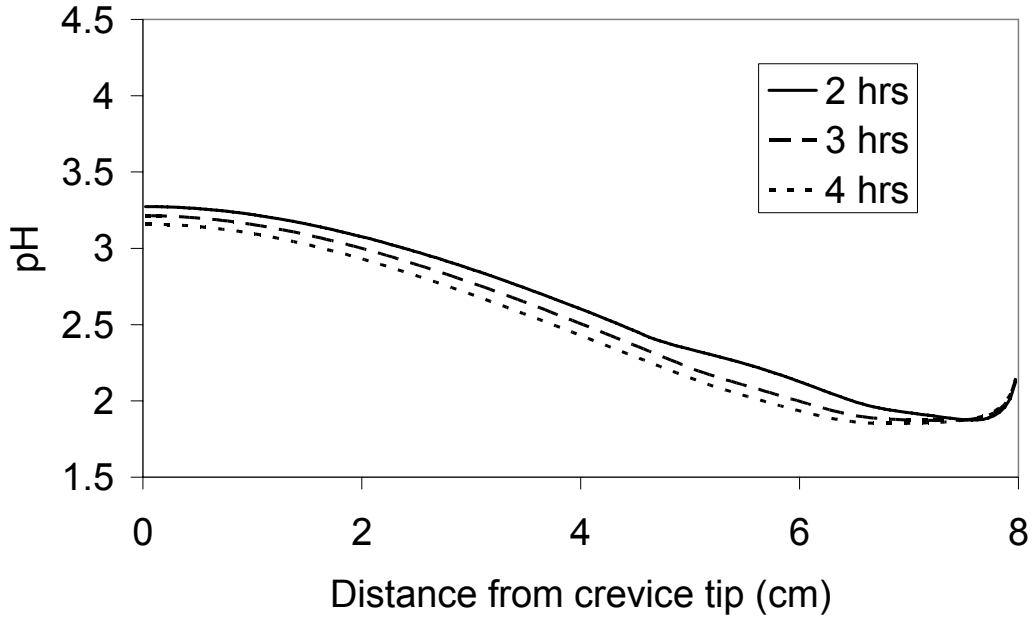

Figure 3.9. Predicted pH profiles in a corroding crevice during the dynamic phase.

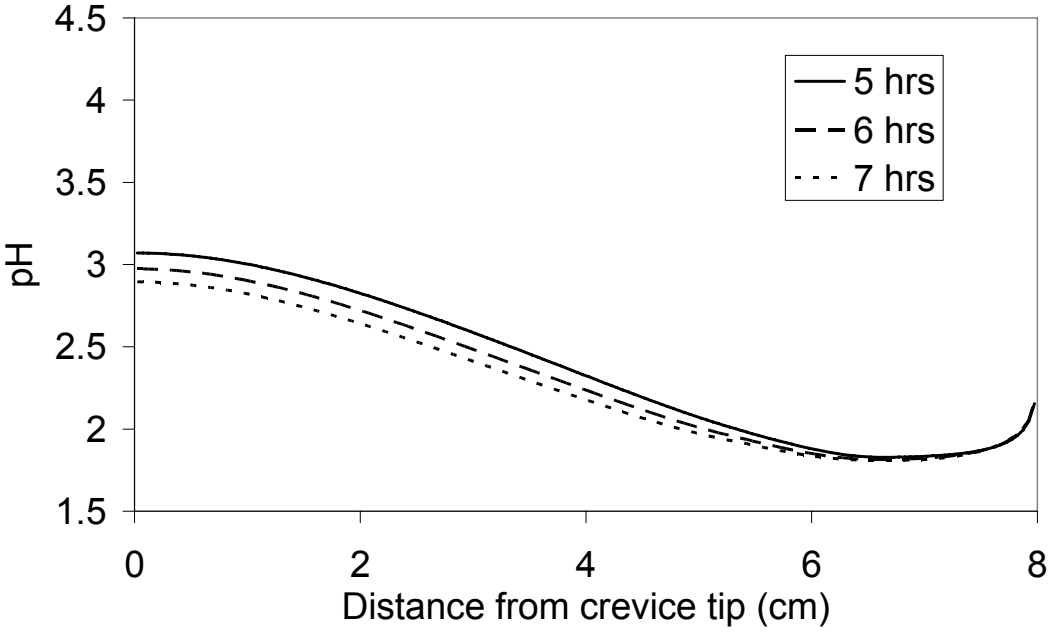

Figure 3.10. Predicted pH profiles in a corroding crevice during the quasi steady-state phase.

The total corrosion phase occurs first and is characterized by corrosion, including either passive or active corrosion, at any node in the crevice from mouth to tip. This phase includes the incubation, initiation, and propagation of crevice corrosion, although, in the case currently being studied the incubation period only lasts for approximately five minutes. The incubation period ends when the combination of concentration, concentration gradients and passive current, which manifests as current flow in the solution, cause the electric potential in the crevice to fall below the critical potential at some point in the crevice (normally at the crevice tip). This causes the nodes with potential less than the critical potential to become active and under Tafel control. Then, as more species diffuse into the crevice, increasing the conductivity of the solution, and metal cations are released into the solution, the active area within the crevice will

increase in size. As this process continues the metal cations will move towards the crevice mouth. These cations also undergo rapid hydrolysis which lowers the pH, which in turn increases the corrosion current at both active and passive regions. This increase in passive current towards the crevice mouth decreases the electric potential of the solution (and surface overpotential) at the crevice tip due to Ohmic considerations, decreasing current produced at active areas at the tip, because they are under Tafel control. Ultimately, the whole crevice becomes active with the highest levels of corrosion occurring closer to the crevice mouth, caused by the higher surface overpotentials seen in Figure 3.11.

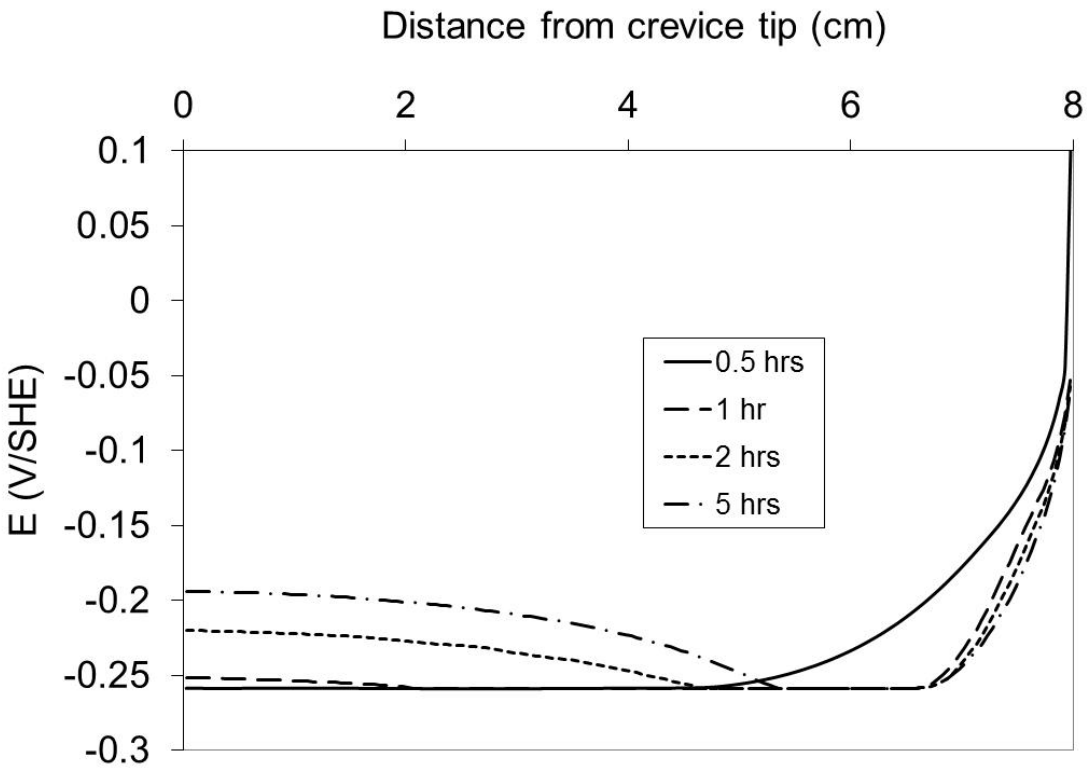

Figure 3.11. Predicted surface overpotentials.

The dynamic phase starts when the electric potential at some point (likely the tip) reaches the reversible potential. If the active current or concentration of cations then continues to increase, the surface overpotential at the tip will be further decreased past the reversible potential. This pushes the area of the crevice that has a surface overpotential equal to the reversible potential closer to the crevice mouth. Essentially, the region of the crevice at the reversible potential will move closer to the crevice mouth. The area deeper into the crevice than the area at the reversible potential is unable to couple with cathodic regions on the bold surface. These areas will become inactive. The inactivity of these areas means that corrosion currents that were previously originating from the tip area and flowing to the crevice mouth, decreasing the potential in each of these regions in the crevice due to Ohmic considerations, no longer exist and are no longer causing a decrease in the potentials in other regions located closer to the crevice mouth. This increase in potential towards the crevice mouth increases the active corrosion current in these areas. The increase in corrosion current increases the rate of migration to these areas, further decreasing the pH and increasing the chloride concentration in these areas, which in turn further increases the corrosion current to these areas. Migration is no longer occurring for regions of the crevice deeper than the region of the crevice at the reversible potential, leaving only diffusion to transport species to these areas. This causes the change in shape of the pH profile towards the crevice tip from the curve seen in the model prediction at one hour in Figure 3.8 to the diffusion dominated regions shown in Figure 3.10. It is due to this movement of regions at the reversible potential up the crevice from the tip and towards the mouth, which causes this dynamic pH behaviour.

The final phase demonstrated by the model is the quasi steady state phase. This occurs when the electric potentials in the solution stop changing. At this point the corrosion currents in the crevice that are dependent upon potential drops caused by Ohmic and concentration gradients, are balanced with changes in the anodic exchange current density (the exchange current density is determined as a function of pH and chloride ion concentration). During this phase potentials in the crevice relative to the bold surface are steady.

3.4 Conclusions

The model presented in this chapter accurately predicts the experimental data of Alavi and Cottis (1987) by combining Critical Crevice Solution Theory with iR Drop Theory. This is accomplished by coupling anodic sites within the crevice with cathodic areas on the bold surface and accounting for the potential drops between these areas. Three new phases of crevice corrosion are also theorized. These are the total corrosion phase, the dynamic phase, and the quasi-steady state phase. These three phases illuminate how the corrosion in the crevice changes from a uniform passive current to an actively corroding region near the crevice mouth with an extinct region near the crevice tip. The extinct region is unable to couple with the bold surface exterior to the crevice due to the electric potential difference between it and the bold surface. The extinct region therefore creates no net corrosion current.

3.5 Recommendations

The numerical solution procedure for the model presented in this chapter is complex, especially when the electric potential in the electrolyte approaches the reversible

potential. This is because the numerical procedure must balance areas not producing current (and below the reversible potential) with areas assumed to be electroactive and undergoing Tafel kinetics. A simplification of this procedure would be achieved by assuming Butler-Volmer kinetics. The inclusion of Butler-Volmer kinetics would also enable the investigation of cathodic reactions within the crevice.

4. THE PATH TO A NEW THEORY – PART II: CREVICE CORROSION CATHODIC REACTIONS AND CREVICE SCALING LAWS

Sections 4.1 through 4.5 of this chapter constitute a reproduction from Electrochimica Acta, 54, of the paper: Glyn F. Kennell, Richard W. Evitts, "Crevice Corrosion Cathodic Reactions and Crevice Scaling Laws", 4696-4703, (2009), with permission from Elsevier. The author of this thesis contributed to this paper in the following capacities: main investigator, conducted numerical modeling, analyzed results, wrote initial drafts of manuscript, and corrected drafts with editorial contributions made by Prof. Evitts.

This chapter presents an improved model of crevice corrosion, when compared with the model from Chapter 3. The main model improvement is the inclusion of both the forward and reverse electrochemical reactions, instead of utilizing only the Tafel equation. This simplifies the numerical solution process considerably and allows for a more detailed examination of processes occurring within the crevice that are not only affected by the electric field, but also impact the electric field. This chapter provides a second step towards an understanding of electric fields coupled with electrochemical systems, and how a transport equation from dilute solution theory not only describes transport, but can also provide a characterization of the electric field.

4.1 Introduction

Crevice corrosion is a localized form of corrosion that can cause considerable damage. It can occur on passive metals under conditions that do not normally cause high levels of uniform corrosion. These facts, combined with the fact that crevice corrosion can be difficult to detect, may lead to situations where the structural integrity of equipment is challenged by crevice corrosion under conditions that corrosion was not expected. The damage presented by crevice corrosion creates the need for a detailed understanding of the complex phenomena causing this type of corrosion. This understanding would help enable the prediction and prevention of crevice corrosion, as well as provide insight into related forms of localized corrosion, such as stress corrosion cracking.

Crevice corrosion occurs in occluded spaces, possibly caused by a flange or under sediment deposited on the inside of a pipe. In a crevice a micro environment may form in which the concentrations of species may be considerably different from those in the bulk electrolyte. A concentration gradient between the crevice and bulk electrolyte can be caused by a very low rate of corrosion that manifests as a small leakage or passive current, which is always present with passive metals. A passive current density is often much less than 1 $\mu A/cm^2$.

For metal surfaces exposed to the bulk electrolyte, the build-up of species due to the passive current is overwhelmed by mass transfer of the species away from the surface. Therefore, the concentrations of species in proximity to the metal are similar to bulk electrolyte concentrations. However, for a stagnant electrolyte within a crevice, mass transfer is limited by the width and gap of the crevice mouth through which all species must traverse. This mass transfer limitation allows the buildup and depletion of species

in the crevice electrolyte due to the passive current. The oxygen in the crevice may become depleted if oxygen reduction occurs faster than the transport rate of oxygen through the crevice mouth. Depletion of oxygen in a crevice is the first stage of crevice corrosion and this may be followed by an incubation period during which the crevice acidifies due to metal ion hydrolysis. At the end of the incubation period the passive film on the crevice will be damaged. Conversely an infinite incubation corresponds to an absence of crevice corrosion.

After the oxygen in the crevice becomes depleted the reduction of oxygen continues on the bold surface and anodic reactions may still occur in the crevice if they are supported by bold surface cathodic reactions. Cathodic reactions can support crevice anodic reactions if ions and electrons can move between the cathodic and anodic areas. A complete electrical circuit is developed with aqueous ionic charge transfer and electronic conduction in the solid phase. The conduction of charged ions through the electrolyte may cause a significant drop in potential, commonly referred to as the iR drop (Pickering, 1986).

Chloride anions also migrate into the crevice, attracted to the anodic metal surface. The increased concentrations of hydrogen and chloride ions in the crevice attack the passive film protecting the metal and cause the passive current to increase. An increase of corrosion current through the crevice increases the potential drop into the crevice if the change in conductivity of the electrolyte is negligible. With this decrease in potential some regions in the crevice may be at an electric potential that causes significantly higher rates of corrosion, viz for a passive metal this potential may be below the critical potential at some regions in the crevice. These regions would be in a

state of active crevice corrosion and significant corrosion within the crevice may be occurring.

An actively corroding crevice undergoes corrosion at rates that can be several magnitudes larger than when the metal is in the passive state. These high rates of corrosion can further increase concentrations gradients within the crevice and change the dimensions of the crevice. These changes may cause the rate of active corrosion to change and relocate or expand the active region. These changes occur during the propagation phase of crevice corrosion.

During the propagation phase, rates of corrosion near the crevice mouth may become very large. These large rates of corrosion cause large electric potential drops in the electrolyte close to the crevice mouth mainly due to larger current flow in the solution. If the potential drop near the crevice mouth becomes too large, cations produced at active anodic areas deeper in the crevice will be less likely to traverse this large potential barrier and exit the crevice. Under these circumstances electroactive regions deeper into the crevice may cease to produce a net anodic current. This would result in no net metal dissolution at these deeper regions, whilst regions close to the crevice mouth may undergo high levels of corrosion. These phenomena are explored in the model presented in this chapter through the explicit representation of forward and reverse reactions for the corrosion of AISI 304 stainless steel and the hydrogen evolution reaction.

Crevice corrosion can be classified due to its ability to initiate with or without an induction period. Crevice corrosion can therefore be referred to as immediate or delayed crevice corrosion (Al-Zahrani and Pickering, 2005). Immediate crevice

corrosion occurs when the potential at some area in the crevice is immediately forced below the crevice corrosion critical potential upon oxygen depletion. For this to occur, the passive current density generated in the crevice must generate a large iR drop in the solution at bulk pH and chloride ion concentrations to cause the potential of the metal to fall in the active region. For the situations where an incubation period occurs before active corrosion, higher levels of hydrogen and chloride ions will build up in the crevice. These species will attack the passive film and cause a higher passive current density, which in turn will increase the iR drop in the crevice.

4.2 Mathematical Models of Crevice Corrosion

A number of models describing crevice corrosion have previously been presented in the literature. The first model was developed by Oldfield and Sutton (1978). It was a general model of crevice corrosion that predicted the incubation period of crevice corrosion. This model considered diffusion and migration and used empiricisms that simplified aspects of the simulation, including the mass transport of species into the crevice. The model assumed the determining factor for initiation of active crevice corrosion was the aggressive levels of pH and chloride ion concentration in the crevice attacking the passive film. This theory is commonly called Critical Crevice Solution Theory (CCST). The iR drop mechanism was first published by Pickering (1986), who claimed that the initiation of crevice corrosion was dependent upon the potential drop between anodic active regions in the crevice and cathodic regions on the bold surface. Xu and Pickering (1992) developed a model that focused upon the difference in potential between the bold and interior crevice surfaces. This model predicted electrical effects inside the crevice without modeling any mass transfer or concentration effects

other than the conductivity of the electrolyte. This model was used to simulate an iron crevice immersed in an ammoniacal electrolyte. Results from simulations indicated that the potential applied to the bold surface influences the potential and current distributions within the crevice. Watson and Postlethwaite (1990a) developed a new CCST model for mass transport processes occurring in a crevice and applied it to simulating the incubation period of crevice corrosion of stainless steels. This represented a more rigorous representation of the transport processes occurring in the crevice based on infinitely dilute solution theory. Walton et al. (1996) developed a transient general model for crevice corrosion. This model included the influence of iR effects on the transport of species in the electrolyte; however, electric potential effects on the rates of electrochemical reactions were not considered when they simulated the experiment conducted by Alavis and Cottis (1987), as a passive current was assumed. The predicted pH was close to the average pH seen experimentally, but the experimental pH profile was not predicted. Englehardt et al. (1999) developed a model for crevice corrosion in a Pressurized Water Reactor Steam Generator that considered mass transport due to diffusion, migration, and convection. This model considered iR drops inside and exterior to the crevice; however, electrochemical reactions for the dissolution of the metal were considered independent of potential inside the crevice, with the corrosion current empirically related to the pH of the electrolyte. The interior of the crevice was coupled with the exterior of the crevice using the principle of charge conservation. White et al. (2000) used CCST to determine the onset of active crevice corrosion for the Alavi and Cottis (1987) experiment. Potential differences were calculated using the Nernst-Planck equation and were assumed fixed throughout the simulation. The crevice

was numerically coupled to a spherical external environment which was assumed to have zero gradients of concentration and potential. Passive current independent of electric potential was assumed within the crevice. The model did not predict a pH in the crevice that would cause active crevice corrosion. However, an empirical correlation was determined that described the corrosion current within the crevice and this provided results that better fit the experimental results of Alavi and Cottis (1987). Since the empirical correlation was based on Tafel behaviour, White et al (2000) concluded that the corrosion current within a corroding crevice may be described using Tafel-like dissolution kinetics. Cui et al. (2005) developed a mathematical model describing the cathodic area supplying a net cathodic current to a corroding crevice with an electric potential at the crevice mouth equal to the repassivation potential. Potential gradients were calculated using Laplace's equation. The cathodic current was assessed using Tafel-kinetics with mass transfer limitations. Heppner (2006) developed a crevice corrosion model that rigorously described the transport of species within a corroding crevice by utilizing Pitzer's ionic interaction model. Chemical reactions occurring in the crevice were also rigorously modeled through the implementation of a large number of chemical equilibria. Simulations were conducted for the experiment of Alavi and Cottis (1987), and the average experimental pH was accurately predicted, but the pH profile was not. Kennell et al. (2008) presented a model for crevice corrosion that combined CCST and iR drop theories. It considered the mass transport of species and the electric potential drops both interior and exterior to the crevice. The two environments were coupled using the principle of charge conservation. Mass transport inside the crevice was based on infinitely dilute solution theory and considered transport

due to diffusion, migration, and electroneutrality. Electrochemical reactions for the dissolution of the alloy and reduction of oxygen were considered dependent upon the electric field close to the metal surface. The reactions were modeled using Tafel kinetics. The experiment of Alavi and Cottis (1987) was simulated and the experimental results, including the pH profile along the length of the crevice, were predicted very well. However, Tafel kinetics for metal dissolution poorly represented the phenomena occurring towards the crevice tip, where the potential approached the reversible potential of the alloy and the reverse reaction became significant. Other cathodic reactions that were neglected include the hydrogen evolution reaction.

4.3 Theory

A mechanistic model is presented that describes a metallic crevice in various stages of corrosion. At the beginning of the simulation it is assumed that there are no concentration gradients in the electrolyte in the crevice or in the bulk solution. The passive current that exists at the prescribed initial conditions is assumed to exist along all metal surfaces and causes the depletion of oxygen in the crevice. During the incubation period, changes in concentration gradients, passive currents, and electric potentials are predicted. If active corrosion is predicted the model determines the rate of active corrosion within the crevice. During the propagation phase the IR drop may cause the potential drop between anodic crevice areas and cathodic bold areas to increase. If this potential drop becomes too great some anodic regions in the crevice will decouple from cathodic areas on the bold surface. It is assumed (and verified in the Results and Discussion section of this chapter), that decoupled anodic regions do not produce a net anodic current that is transported to the bold surface. This model

presented here is unique as it is capable of a) describing the phenomena occurring during the decoupling process, and b) possible cathodic (and anodic) reactions occurring at decoupled regions. This includes the possibility for net cathodic reactions occurring at decoupled regions towards the crevice tip.

4.3.1 Mathematical Model Development

Some aspects of the overall model that have been previously published will be briefly presented here for completeness. Kennell et al. (2008) describe in detail the development of an earlier version of the model presented in this chapter. The model presented here calculates the corrosion current in the crevice by considering both the forward and reverse electrochemical reactions, instead of assuming simple Tafel kinetics. This greatly simplifies the numerical solution of the mathematical model because a continuous function is now used to describe the rate of substrate dissolution rather than the Tafel equation which was not assumed valid at potentials less than the reversible potential in the previous model. This also increases the flexibility of the model as the assumption of zero current at decoupled regions is no longer applied (Kennell et al., 2008). This allows for an inspection analysis of the decoupling process of anodic sites in the crevice from cathodic sites on the bold surface. The model also includes a method for representing the hydrogen evolution reaction (HER).

Mass transport within the crevice is determined using the Equations 4.1 and 4.2. Equation 4.1 describes the transport of species due to convection, diffusion, diffusion potential, and electromigration (Watson and Postlethwaite, 1990a):

$$\frac{\partial C_i}{\partial t} = -\frac{z_i u_i \nabla C_i}{F\sum_j z_j^2 u_j C_j} i - \frac{z_i u_i \nabla C_i}{\sum_j z_j^2 u_j C_j} \sum_{j=1}^{k} z_j D_j \nabla C_j + D_i \nabla^2 C_i + S \tag{4.1}$$

Equation 4.1 was solved over a one dimensional grid using a hybrid Crank-Nicolson method (Heppner and Evitts, 2005). The boundary conditions associated with this equation were zero flux at the crevice tip and bulk solution concentration outside the crevice mouth. The values for diffusion coefficients and mobilities are found elsewhere (Heppner et al., 2002b). Near electroneutrality of the electrolyte in the crevice is modeled by applying the algebraic correction term developed by Heppner and Evitts (2006) to Equation 4.1:

$$C_i = C_i^{old} - z_i u_i C_i \frac{F\delta}{\kappa} \tag{4.2}$$

The source term, S, in Equation 4.1 represents species produced or depleted by chemical reactions. For chemical reactions kinetic behaviour is neglected (Heppner et al., 2002a):

$$\prod_j C_j^{v_{ij}} - K_i = 0 \tag{4.3}$$

where C_j is the equilibrated concentration of the *j*th species occurring in the *i*th chemical reaction, and *K* is the equilibrium constant. A mass balance equation can be written for each species involved in chemical reactions (Heppner et al., 2002a):

$$C_j = C_j^{init} + \sum_{i=1}^{n} X_i v_{ji} \tag{4.4}$$

The mass balance equations are combined to provide a guaranteed non-singular matrix. This matrix was solved using the Newton-Raphson method.

Mass transport exterior to the crevice was modeled using the equation developed by Kennell et al. (2008) for an oxygenated, convection-free electrolyte:

$$\frac{\partial C}{\partial t} = D\frac{\partial^2 C}{\partial x^2} + \frac{K_{MT}}{\Delta y}\left([Bulk]-[Surface]\right) - \frac{i}{\Delta z F z} \tag{4.5}$$

Equation 4.5 considers the diffusion of oxygen parallel to the bold surface, the transfer of oxygen between the bulk electrolyte and bold surface and the consumption of oxygen at the bold surface due to electrochemical reactions. This equation was solved implicitly over a one dimensional grid parallel to the bold metal surface using central space discretization. The initial condition was bulk concentration at all nodes and boundary conditions were zero concentration gradient at the crevice mouth and bulk concentration at the node furthest from the crevice. The diffusion coefficient of oxygen was assumed to be $5.5 \times 10^{-8} m^2/s$ and the electrolyte was assumed to be under atmospheric conditions.

For oxygen depleted areas in the crevice with surface overpotential greater than the crevice corrosion critical potential the passive current was determined by modifying a reference current for pH using a Freundlich adsorption equation (Shreir et al., 1994):

$$\log(i_P) = \log(k) - n\text{pH} \tag{4.6}$$

For all crevice areas with a surface overpotential less than the critical potential the rate of corrosion was determined by considering both the forward and reverse reactions:

$$i = i_{0,a} \cdot \left(10^{(T_S(\eta_a - E_{0,a}))} - 10^{(T_S(E_{0,a} - \eta_a))}\right) \tag{4.7}$$

The critical potential, the Tafel slope, the reversible potentials and exchange current density are given in Table 4.1.

Table 4.1. Values for parameters used in mathematical model.

Anode	$i_{0,a}$	$E_{0,a}$	T_S	E_{crit}
	$1\times10^{-2\text{-pH}}$ A/cm^2	-0.259 V/SHE	0.03 V/dec	-0.009 V/SHE
Cathode	$i_{0,c}$ *	$E_{0,c}$ *	T_S *	E_{corr}
	1×10^{-9} A/cm^2	0.191 V/SHE	0.1 V/dec	0.1 V/SHE

* (Cui et al., 2005)

The electric potential gradient was calculated in the crevice (Newman and Thomas-Alyea, 2004):

$$\nabla\Phi = -\frac{\mathbf{i}}{\kappa} - \frac{F}{\kappa}\sum_j z_j D_j \nabla C_j \tag{4.8}$$

and the surface overpotentials were determined with reference to the potential at the crevice mouth (Kennell et al., 2008):

$$\eta_a = E_{mouth} + \nabla\Phi \tag{4.9}$$

The electric potential gradient parallel to the bold surface was calculated using (Kennell et al., 2008):

$$\nabla\Phi = -\frac{\mathbf{i}}{\kappa} - \frac{RT}{2F}\ln\left(\frac{[O_2]_{mouth}}{[O_2]}\right) \tag{4.10}$$

where the reduction of oxygen was assumed to adhere to Tafel behaviour and the oxidation of metal was assumed to occur in the passive region (i_p) and calculated via Equation 6 (Kennell et al., 2008):

$$i = i_{0,c}\cdot 10^{\left(T_S\left(E_{0,c}-\eta_c\right)\right)} - i_p \tag{4.11}$$

The values for the exchange current density and reversible potential can be found in Table 4.1. The surface overpotential was again determined by using the potential at the crevice mouth as a reference (Kennell et al., 2008):

$$\eta_c = E_{mouth} - \nabla\Phi \tag{4.12}$$

The hydrogen evolution reaction was considered for some of the simulations conducted and the contribution to the current density determined by:

$$i_H = i_{0,H} \times 10^{\left(10\left(E_{0,H} - \eta_a\right)\right)} \tag{4.13}$$

where the exchange current density for the hydrogen reaction was assumed to be equal to that on iron and given by (Shrier, 1979)

$$i_{0,H} = -1 \times 10^{-5.9}\left(10^{-pH}\right)^{0.5} \tag{4.14}$$

and the reversible potential was calculated using the Nernst equation:

$$E_{0,H} = -0.0591\text{pH} \tag{4.15}$$

4.3.2 Numerical Solution

The numerical solution of the mathematical model is similar to the method employed by Kennell et al. (2008); however, the implementation of Equation (4.7) in the current model instead of simple Tafel behaviour simplifies the numerical solution and at the same time makes the model more realistic.

The mathematical model is solved by initially assuming a value for the potential at the crevice mouth and solving the appropriate electrochemical equations for the crevice and bold surface separately. (The numerical solution of the electrochemical equations is described below). If the total cathodic current produced along the bold surface is not equal in magnitude to the total anodic current produced in the crevice, the potential at the crevice mouth is modified. In addition, the potential at the outer edge of the cathodic region must be equal to the corrosion potential. By reducing the value of potential at the crevice mouth all of the surface overpotentials along the bold surface and

in the crevice are reduced via Equations 4.9 and 4.12. Such a reduction in potential would decrease the crevice anodic current and increase the bold surface cathodic current. These changes in anodic and cathodic currents are modeled by Equations 4.7 and 4.11 respectively. In other words, a potential gradient along the bold surface and into the crevice is ultimately calculated, including the potential at the crevice mouth. This potential gradient balances all transport and electrochemical production or depletion of species.

The electrochemical equations relevant to the crevice are Equations 4.6, 4.7, 4.8, 4.9, and 4.13. These equations were solved in series and then iterated until convergence was achieved. The electrochemical equations describing the bold surface are Equations 4.10, 4.11, and 4.12. These equations were explicitly solved since the potential at the crevice mouth and the total anodic current from the crevice are known (Kennell et al., 2008).

4.4 Results and Discussion

The model presented in this chapter is first validated without incorporating the hydrogen evolution reaction, and then used to examine critical crevice scaling laws. A subsequent validation and a number of numerical simulations were then conducted for the case where the hydrogen evolution reaction is considered to be significant after an electric field has been established within the crevice. These results were compared with the experimental data of Alavis and Cottis (1987).

4.4.1 Model simulations without HER

The model was compared against the experimental data of Alavi and Cottis (1987). Alavi and Cottis studied a crevice of 2.5 cm width, 90 ± 10 μm gap, and 8 cm depth. A

crevice with walls made from AISI 304 stainless steel was coupled to a cathode made from AISI 304 stainless steel situated in aerated bulk electrolyte under free corrosion conditions. The electrolyte was 0.6 M NaCl solution that was at a temperature of 23 ± 1°C. Figure 4.1 shows the pH profile predicted by the model presented in this chapter compared with the experimental data of Alavi and Cottis and predictions made by other published models that were also compared with the experimental data of Alavi and Cottis (1987). Figure 4.1 shows that the model presented in this chapter more closely predicts the pH profile in the corroding crevice than any other model prediction displayed in Figure 4.1; however, this validation is very similar to the model of Kennell et al. (2008).

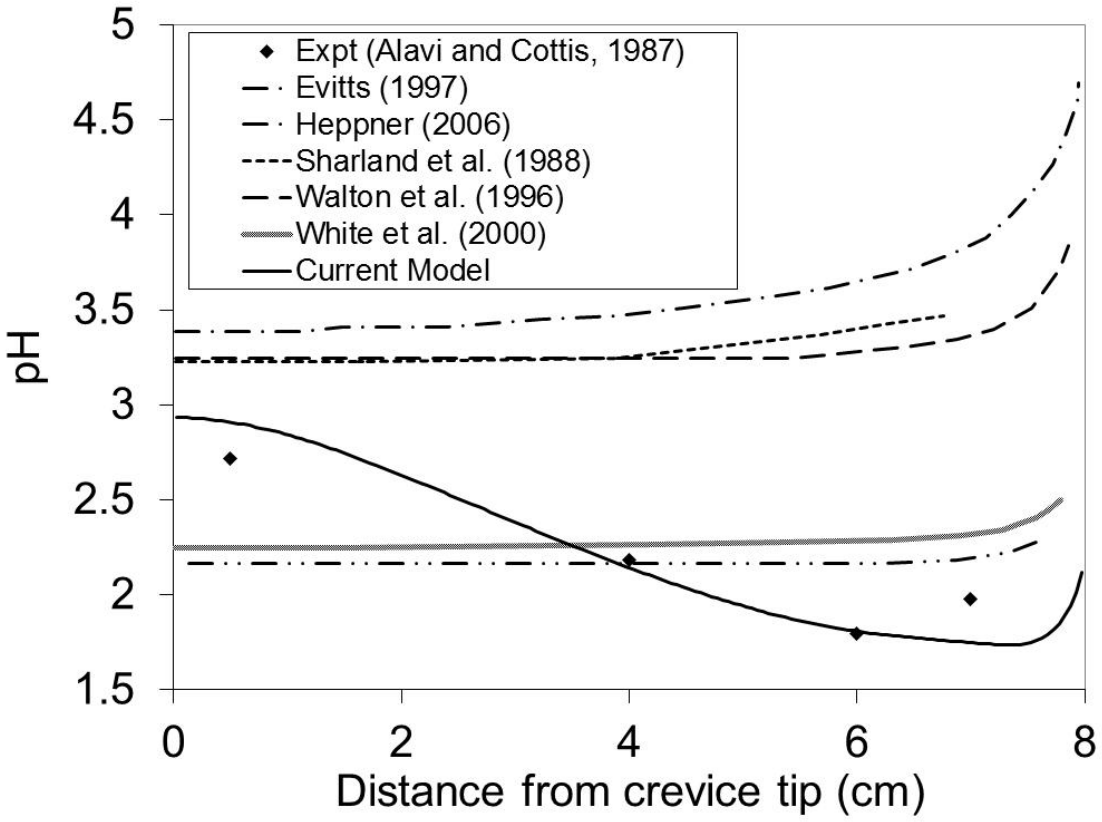

Figure 4.1. Model predictions (without HER).

The new model described in this chapter was used to determine an applicable critical crevice corrosion scaling law. The model was used to predict the corrosion currents and electric potential fields for a variety of AISI 304 stainless steel crevices with the same electrolyte and physical setup as was used for model validation. Only the prescribed length and gap of the crevice was altered for each simulation. If the potential within the crevice at any point at any time was predicted to be below the critical potential, that crevice was deemed to become active. If the potential at some point in the crevice was below the critical potential immediately upon deoxygenation of the crevice, the crevice was deemed "active upon oxygen depletion." Otherwise, an active crevice was deemed "active after incubation." These results can be seen in Figure 4.2, where crevice dimensions predicted to become active after oxygen depletion are indicated via solid diamond shapes, and crevice dimensions predicted to become active after a period of incubation are indicated via solid squares. Also shown in Figure 4.2 are the crevices dimensions in which the metal remained in the passive state, indicated as solid triangles. Also shown in Figure 4.2 are shaded zones that represent a range of crevice dimensions assumed to be in one of the particular categories outlined above. The corrosion processes for many of these passive crevices were modeled for extended periods of time, during which the potential drop into the crevice reached a maximum and then decreased due to an increased conductivity of the electrolyte in the crevice.

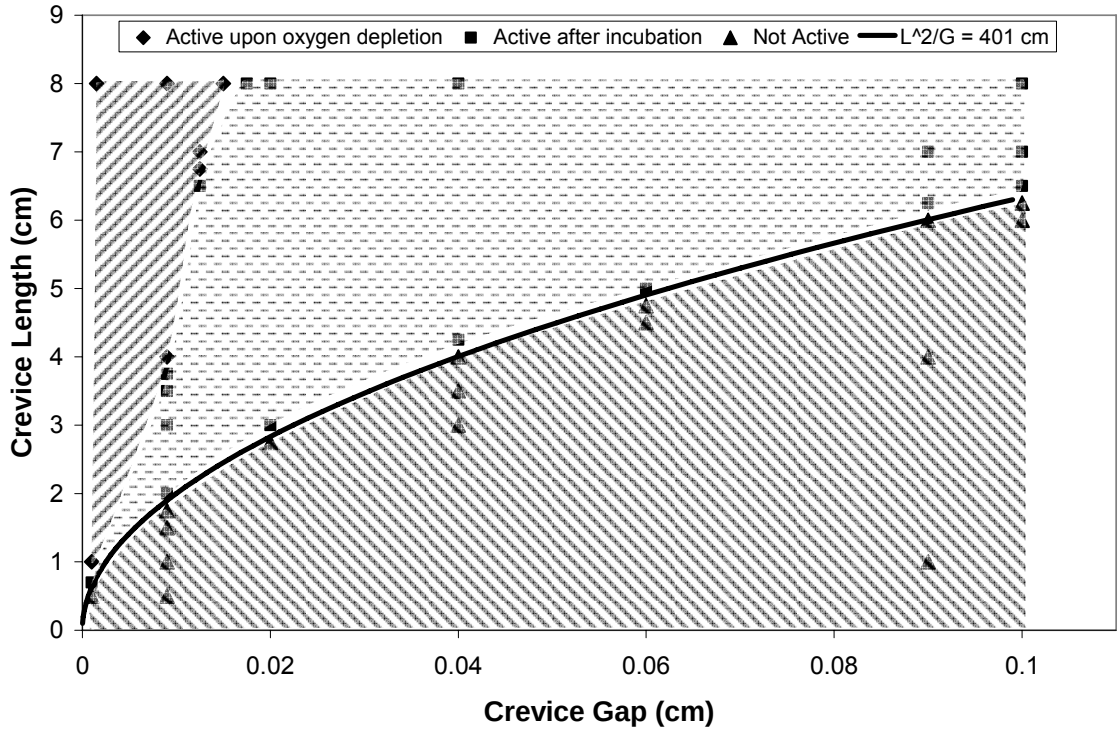

Figure 4.2. Critical aspect ratio for crevice corrosion.

The critical aspect ratio fell between the active crevice and not active crevice zones shown in Figure 4.2. Two scaling factors from the literature were fitted to this data by assuming the midpoint between the active and not active crevice dimensions was the critical dimension for crevice corrosion. These two scaling factors were L/G (Xu and Pickering, 1993) and L^2/G (Turnbull and Thomas, 1982). The first scaling factor tested, L/G, did not fit the data. The second scaling factor, L^2/G, fit the data well. In fact, Figure 4.2 shows that the scaling factor L^2/G delimits the active and non-active zones shown in the figure very well when of $L^2/G = 401$.

Interesting observations pertaining to cathodic reactions during several of the predictions from Figure 4.2 can be made. Several of the predictions from Figure 4.2

show low amounts of metal deposition at the crevice tip during some periods of the simulation. The predicted deposition is several orders of magnitude smaller than the amounts that would be deposited for cathodic currents of the order of the passive current density, which equates to approximately a total depostition of 3 ng. Figure 4.3 shows the predicted net corrosion current for the crevice of 2.5 cm width, 90 μm gap, and 8 cm depth, which is the model validation prediction. The figure shows the development of the net corrosion current along the crevice at different times during the simulation. As the simulation proceeds, the net anodic currents towards the mouth of the crevice become greater as do the concentration gradients towards the crevice mouth. This changes the electric potential gradient and decreases the potential at the crevice tip due to Ohmic and electrochemical considerations, as shown in Figure 4.4, which is a plot of potential distance along the crevice. The potential inside the crevice is calculated with respect to the bold surface. After five hours the predicted electric potential at the crevice tip is equal to the reversible potential of the metal at these conditions. However, as the electric potential drop approximately half a centimeter into the crevice mouth continues to drop due to increasing anodic current and Ohmic considerations, the potential drop approximately two centimeters into the crevice also continues to drop due to the diffusion potential and changing concentration gradient of the electrolyte. This combination of potential drops causes the potential at the tip of the crevice to fall below the reversible potential estimated for this metal, causing very low levels of net metal deposition. Figure 4.3 shows predicted currents for the case involving low levels of deposition after 9 hours. It should be noted that this prediction only considers the cathodic reaction of metal deposition and other cathodic reactions that may occur

preferentially, such as the hydrogen evolution reaction, are not considered. Therefore, for the situation not considering the hydrogen evolution reaction, an important cause of metal deposition is the diffusion potential in the crevice electrolyte. The discovery of possible net cathodic reactions at the crevice tip highlights the importance of modeling both the forward and reverse reactions for types of localized corrosion similar to crevice corrosion.

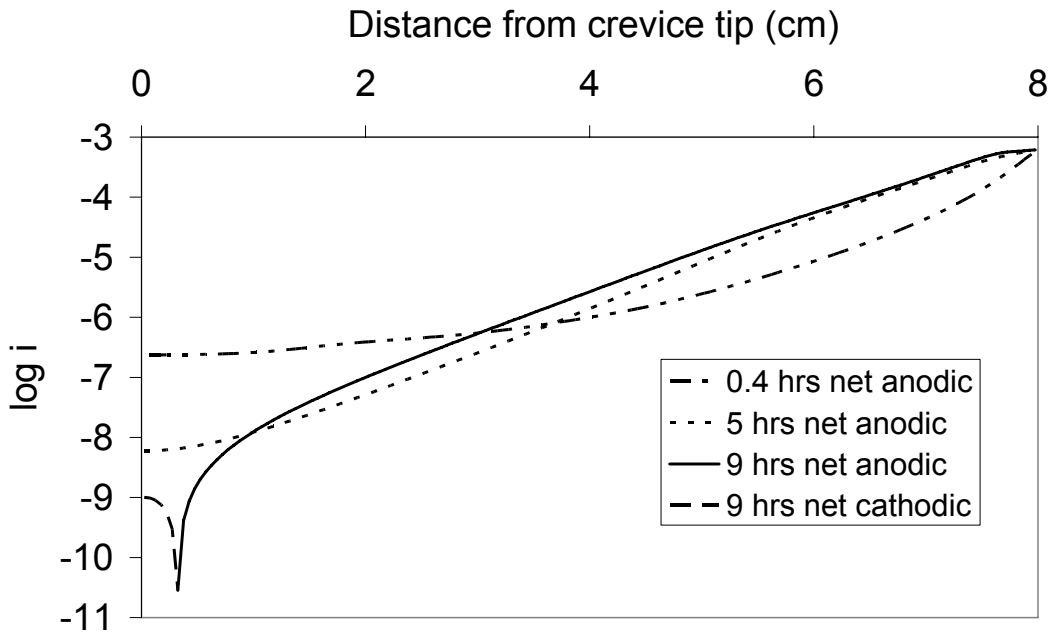

Figure 4.3. Predicted net currents for the Alavi and Cottis (1987) experimental parameters without considering the possibility for the hydrogen evolution reaction.

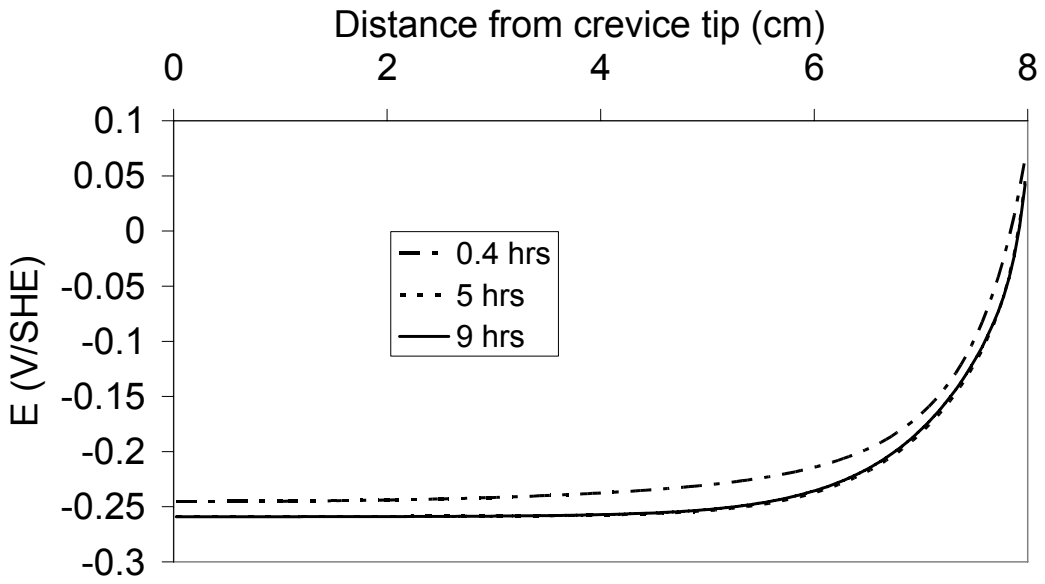

Figure 4.4. Predicted electric potentials for the Alavi and Cottis (1987) experimental parameters.

4.4.2 Model Incorporating HER

Hydrogen evolution would naturally occur prior to the deposition of metal at the crevice tip. However, hydrogen evolution will only occur after the crevice has become active and considerable concentration and potential gradients have been established. The lack of incorporation of the hydrogen evolution reaction during the examination of the critical crevice scaling laws in the previous section of this chapter is not an important factor due to the lack of established potential drops into the crevice prior to the initiation of active crevice corrosion. Simulations of crevice corrosion incorporating the hydrogen evolution reaction were conducted for the analysis of electrochemical phenomena occurring in the crevice after a prolonged period of active crevice corrosion. The validation of the model including the hydrogen evolution reaction, shown in Figure 4.5, fits the experimental data a slightly worse than the validation without the hydrogen

evolution reaction shown in Figure 4.1. However, the numerical representation of the hydrogen evolution reaction in the current model allows for the possible explanation of a peculiar phenomenon displayed in the experimental data of Alavi and Cottis (1987).

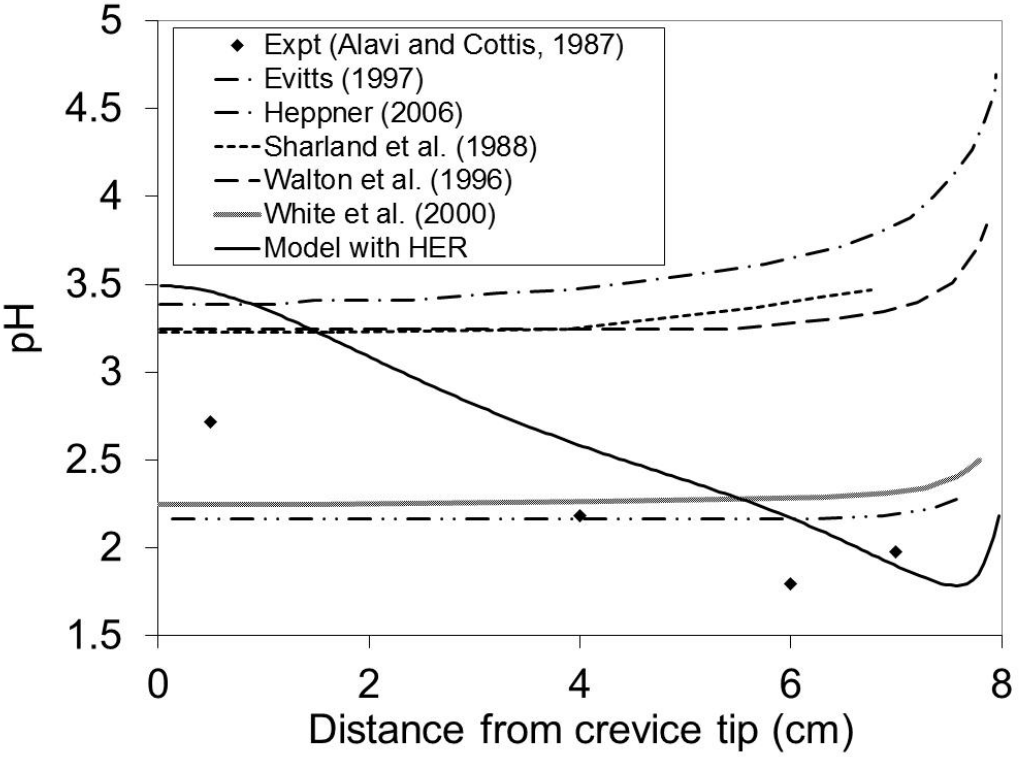

Figure 4.5. Model validation with hydrogen evolution reaction.

During the initial period of the Alavi and Cottis (1987) experiment the pH at the crevice tip falls to approximately 4.4, then rises to about 4.6, and then falls for the rest of the experiment. During this initial period, the pH at other locations in the crevice decreases continuously. One explanation for this increase-decrease may be experimental errors/scatters; however, the numerical simulation including the hydrogen evolution reaction explains provides an alternate explanation of why this change in pH

might have occurred. Figure 4.6 shows the predicted pH in the crevice at various times. It can be seen that after 0.4 hours the pH at the tip of the crevice is approximately 4. The pH then rises to about 4.1, then the pH decreases for the rest of the numerical simulation. Although this predicted increase in pH is not excellent when compared with the experimental data of Alavi and Cottis (1987), no similar increase in pH was seen at the crevice tip for simulations conducted without considering the hydrogen evolution reaction. This increase in pH at the crevice tip may be explained as follows. Upon initiation of active crevice corrosion high levels of anodic current are produced near the crevice mouth that produce a large iR drop in the solution. The large iR drop causes the potential at the crevice tip to be reduced relative to the bold surface. This decrease in potential increases the rate of hydrogen evolution along the crevice (especially at the crevice tip). The evolution of hydrogen at the tip causes an increase in the pH at the tip. The pH continues to rise until a new quasi-steady state is achieved and the evolution of hydrogen is balanced with the production (via hydrolysis) and diffusion of hydrogen ions into the tip region. Then, the pH at the crevice tip continues to decrease along with the decreasing pH in the remainder of the crevice.

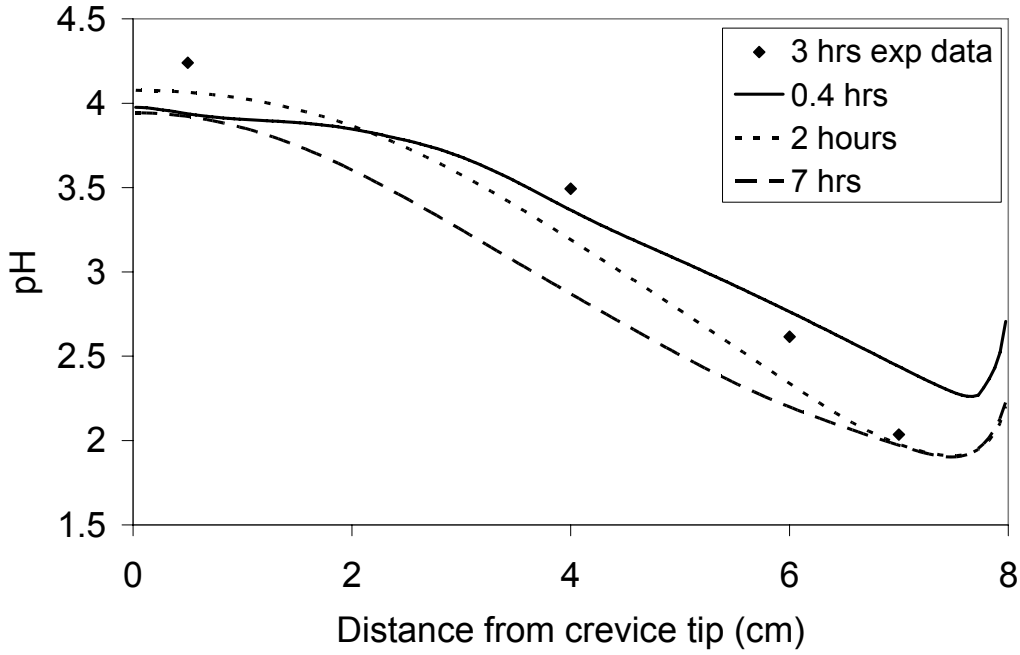

Figure 4.6. pH predicted by model considering hydrogen evolution compared with the experimental data of Alavi and Cottis (1987).

It can be surmised that the rise in pH seen experimentally may be due to the hydrogen evolution reaction occurring only after an increase in the potential drop inside the crevice (due to iR drop caused by active corrosion). This further justifies the assumption that the hydrogen evolution reaction is only significant after active crevice corrosion initiates causing larger potential drops within the crevice. Figure 4.7 shows the net current at the crevice wall with depth into the crevice. At the early time periods of 0.5 hours and 2 hours corrosion is predicted to occur along the entire length of the crevice; however, the current emanating from the crevice wall closer to the mouth increases from 0.5 hours to 2 hours, causing a larger potential drop, and reducing the current emanating from the crevice tip (due to Ohmic considerations). Figure 4.7 shows that after 5 hours the predicted anodic current at the crevice wall closer to the mouth has

increased, whilst a net anodic current is no longer predicted to occur towards the tip. Net cathodic reactions are predicted to occur towards the tip due mainly to the hydrogen evolution reaction. By the 9th hour the anodic current towards the crevice mouth is predicted to continue increasing whilst the cathodic current towards the tip is predicted to increase in magnitude over a smaller area of the crevice.

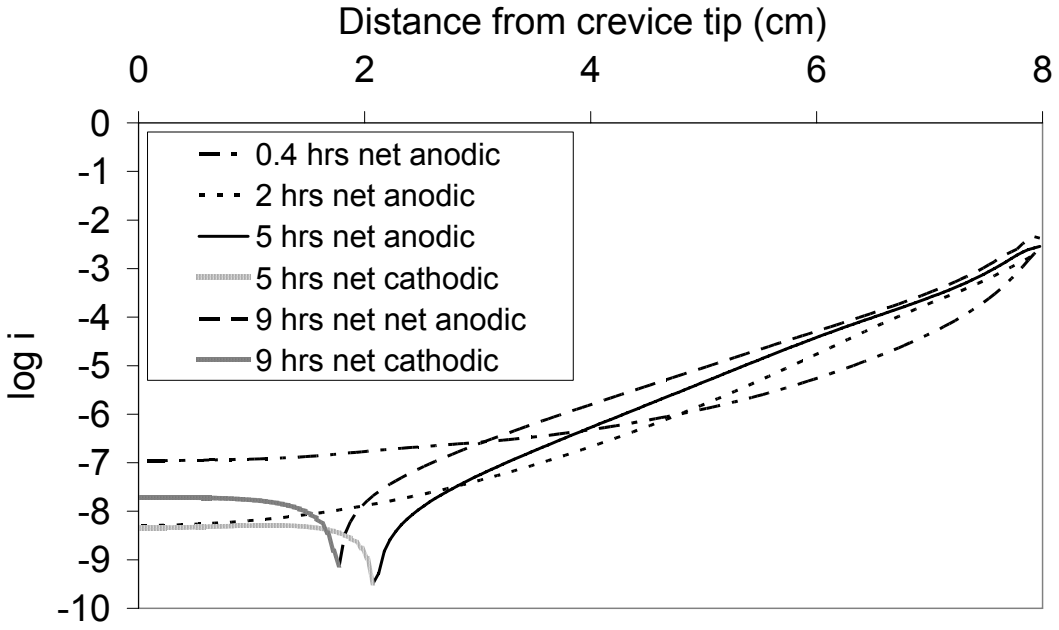

Figure 4.7. Predicted net currents for the Alavi and Cottis (1987) experimental parameters considering the possibility for the hydrogen evolution reaction.

Hydrogen evolution had originally been neglected in the model presented in this chapter because no hydrogen evolution was reported by Alavi and Cottis (1987) for their stainless steel crevice experiment. The maximum current due to the hydrogen evolution reaction predicted at the crevice tip during the first ten simulated hours was approximately 1×10^{-8} A/cm^2. This corresponds to approximately 5×10^{-7} mL/min of

hydrogen produced in the deepest part of the crevice, where the crevice volume is 1.8 $\times 10^{-3}$ mL. This amount of hydrogen production may go unobserved, but has an impact on the numerical simulation of the crevice pH. Also, the evolution of hydrogen at the tip may be the cause of the steady state concentration gradient of hydrogen ions in the experimental data of Alavi and Cottis (1987). This pH gradient towards the crevice tip can be seen in Figure 4.5.

Due to repeated numerical and experimental indications that cathodic reactions may occur towards the crevice tip for 304 stainless steel crevices, a theoretical mechanism was constructed describing a second cathodic area at the crevice tip, in addition to the main cathodic area on the bold surface exterior to the crevice. Important aspects from this mechanism are shown in Figure 4.8. Figure 4.8 shows the main cathodic reactions occurring on the bold surface as the reduction of oxygen molecules into hydroxide molecules. The passage of ions from the cathodic area and bulk electrolyte into the crevice are illustrated by chloride and hydroxide along the dotted arrow to the main anodic area close to the crevice mouth. Electrons are shown travelling from this anodic area to the main cathodic area exterior to the crevice, and positive charge exiting the crevice towards the main cathodic area is shown as positive metal ions along the dotted arrow. Collectively, the transport of these various charges completes one electrochemical circuit. Electrons are also shown travelling from the main anodic area close to the crevice mouth towards the crevice tip, where a minor cathodic area may occur. The cathodic reactions occurring towards the crevice tip are illustrated as the hydrogen evolution reaction. This reaction is more likely to occur as a large potential drop becomes established. This large potential drop may be largely due to the iR drop

caused by the transport of charged ions between the main cathodic area and main anodic area, but may also be influenced by concentration gradients. Completing the electrochemical circuit between the crevice tip cathodic area and the crevice mouth anodic area is the transport of positive ions towards the crevice tip. This is illustrated in Figure 4.8 as protons along the dotted arrow. It is unknown if the hydrogen produced in the crevice tip forms small bubbles and exits the crevice, or if the hydrogen penetrates into the metal walls. An important reaction occurring in the crevice, the hydrolization of water by metal ions, is also shown in Figure 4.8. This mechanism of a second cathodic area would explain the steady state pH profiles demonstrated in the experimental data of Alavi and Cottis (1987).

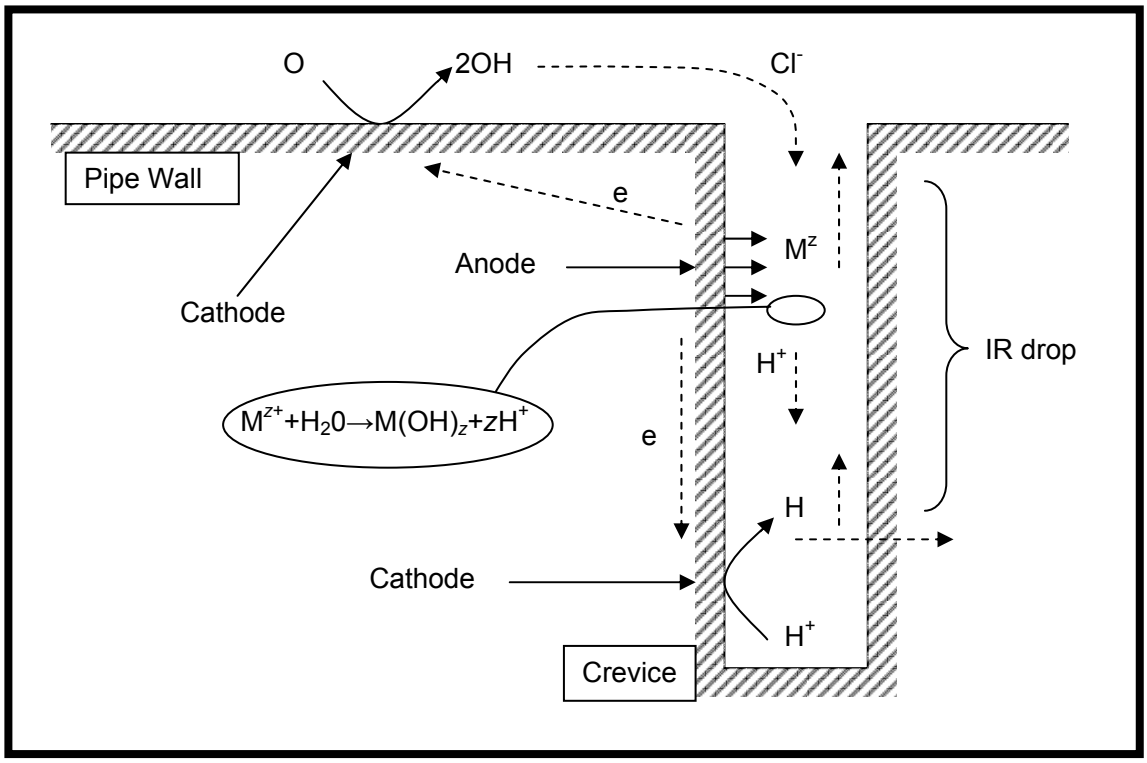

Figure 4.8. Idealized description of second cathodic area at crevice tip.

4.5 Conclusions

The numerical model of crevice corrosion presented in this chapter (without considering the hydrogen evolution reaction) predicts the pH profile seen in the experimental data of Alavi and Cottis (1987). This model demonstrates the importance of modeling both the forward and reverse reactions of metal dissolution when modeling localized corrosion. When the hydrogen evolution reaction was not considered it was found that conditions may exist within a corroding crevice that may cause a net deposition of metal at the crevice tip. This deposition would be due to an overall potential drop caused by a combination of an iR drop coupled with a diffusion potential drop. However, this deposition is unlikely since HER would occur prior to metal deposition.

Simulations were used to find a critical crevice corrosion scaling law. The scaling law that fit the results was found to be L^2/G. From data predicted by the current model it was observed that the critical crevice geometric dimensions were described when $L^2/G = 401$.

Due to the observed importance of cathodic reactions within a corroding crevice after establishment of a significant potential drop into the crevice (due to the iR-drop), further simulations were conducted that incorporated the hydrogen evolution reaction within the crevice. It was predicted that the hydrogen evolution reaction occurs in the crevice after concentration and potential gradients have become significant due to active crevice corrosion. Due to the delay in the establishment of larger concentration and potential gradients, the initiation of hydrogen evolution within the crevice is delayed. This delay was responsible for an increase in the pH at the crevice tip during the numerical simulation of the Alavi and Cottis (1987) experiment. An actual delayed increase in the

pH at the crevice tip that was recorded in the experimental data of Alavi and Cottis (1987) may be also be caused by these factors. A new theory is also developed that illustrates some of the important factors in crevice corrosion, including the development of a second cathodic area towards the crevice.

4.6 Recommendations

Further circumstantial evidence for the mechanism of cathodic reactions inside the crevice described in this chapter may be found in the paper of Kennell and Evitts (2009b). This paper shows how the mechanism described in this chapter may also be responsible for the initiation of the Reverse Crevice Corrosion of Copper, after a period of regular crevice corrosion.

The model presented in this chapter is successful in explaining a number of experimentally observed phenomena; however, the model has three main disadvantages: the model neglects phenomena, the model requires either the prescription of a current distribution or else the assumption of a one-dimensional system, and the numerical procedure required to solve the model is complex and cumbersome. To overcome these disadvantages and simultaneously simplify the numerical solution procedure, new fundamental equations are needed that better describe electrolytes and the corresponding electric fields. This thesis solves this problem in Chapters 5 and 6 by presenting the first characterization of the electric field coupled with a non-isotropic electrolyte conducting electric current. Similar to the characterization utilized in this chapter, this new characterization may be developed from the transport equation described by dilute solution theory.

5. THE KEYSTONE TO A NEW THEORY: THE INHERENT CHARGE DENSITY MODEL

Chapters 3 and 4 presented models for crevice corrosion that utilized a characterization of the electric field developed from the transport equation of dilute solution theory. This characterization presented limitations because it required the prescription of the current distribution and it neglected phenomena. Also, the numerical procedure necessary to solve this set of equations was complex and cumbersome. This chapter seeks to develop an improved characterization of the electric field, also from the transport equation described by dilute solution theory. This improved characterization will be multi-dimensional and it will not neglect any phenomena already described by dilute solution theory. An analysis of Maxwell's equations will demonstrate this characterization to be fundamentally correct. Also, the relationship between this new characterization and Poisson's equation will be explored.

5.1 Charge Density in Electrolytes

Electrolytes conduct electrical current through the transport of ions. The influence of an electric potential gradient causes anions and cations to migrate in opposite directions. Also, anions and cations may be transported due to phenomena other than the electric field, such as diffusion. If the propensity is for anions to diffuse faster than cations, such as across some liquid-junctions, charge density may form in the electrolyte that is

not represented by Poisson's equation. This charge density may be due to macroscopic tendencies for the transport of charge, and not the polarization of atoms. In this section the possibility for different forms of charge density to occur simultaneously in an electrolyte will be explored, including the bound charge density incorporated in Poisson's equation.

5.1.1 Poisson's Equation and Steady-state Non-isotropic Electrolytes

Poisson's equation was developed in Section 2.4.1 this thesis. Another form of Poisson's equation that uses a different expression for the charge density and assumes uniform dielectric constant is shown in Equation (5.1) (Newman and Thomas-Alyea, 2004):

$$\nabla^2 \Phi = -\frac{F}{\varepsilon} \sum_i z_i C_i \tag{5.1}$$

If the assumption of uniform dielectric constant is not made:

$$\nabla \cdot \left(\varepsilon \nabla \Phi \right) = -F \sum_i z_i C_i \tag{5.2}$$

Equation (5.1) shows how Poisson's equation relates the Laplacian of potential to free charge density, the permittivity of free space and the static polarization of surrounding molecules. This polarization of molecules causes an electric field that opposes an instigating electric field. It is generally accepted that Equation (5.1) can be applied to model electrolytes (Newman and Thomas-Alyea, 2004). However, in the application of Equation (5.1) an assumption is implicitly made that the only significant opposing electric field is due to the polarization of atoms and molecules. An equation describing the flux in an electrolyte (such as the Nernst-Planck equation) may predict charge

density due to the propensity for the flow of charge without considering the permittivity of free space or the polarization of molecules. Therefore, the relationships between the concentration and electric fields predicted by Poisson's equation and the Nernst-Planck equation, at steady-state, are examined. The Nernst-Planck equation is:

$$\mathbf{N} = -D_i \nabla C_i - \frac{z_i F}{RT} D_i C_i \nabla \Phi \tag{5.3}$$

Incorporating the Nernst-Einstein relation, multiplying by $z_i F$, and summing across all species:

$$\mathbf{i} = -F \sum_i \left(z_i D_i \nabla C_i \right) - \kappa \nabla \Phi \tag{5.4}$$

where the conductivity, κ, is:

$$\kappa = F^2 \sum_i z_i^2 u_i C_i \tag{5.5}$$

Taking the divergence of both sides of Equation (5.4):

$$\nabla \cdot \mathbf{i} = -F \nabla \cdot \sum_i \left(z_i D_i \nabla C_i \right) - \nabla \cdot \left(\kappa \nabla \Phi \right) \tag{5.6}$$

Rearranging Equation (5.6) and determining from Equation (2.19) that the divergence of current at steady-state is equal to zero:

$$\nabla \cdot \left(\kappa \nabla \Phi \right) = -F \nabla \cdot \sum_i \left(z_i D_i \nabla C_i \right) \tag{5.7}$$

For the special case where the diffusion coefficient and conductivity can be considered invariant:

$$\nabla^2 \Phi = -\frac{F}{\kappa} \sum_i \left(z_i D_i \nabla^2 C_i \right) \tag{5.8}$$

An initial comparison of Equation (5.2) with Equation (5.7) shows that these two equations are different. Equation (5.2) describes an electric field that is balanced with

the permittivity of free space and charge density created from the static polarization of surrounding atoms and molecules, and Equation (5.7) describes an electric field that is balanced with the propensity for transport of charge density. If an electrolyte of uniform initial composition in a finite container had a specified electric field imposed across it until steady-state, would Equation (5.2) or Equation (5.7) describe the charge density distribution? During the development of Poisson's equation from Maxwell's equations, no provision was made for the fact that charge density may be caused by phenomena other than the electric field, for example concentration gradients. Since Poisson's equation is founded on Maxwell's equations, a more detailed examination is required to resolve this question.

5.1.2 Apparent Displacement of Charge for Isotropic Media Conducting Electric Current

The Maxwell-Minkowski equations incorporate the Electric Displacement Field that is defined for a linear isotropic material in Equation (2.20). Equation (2.21) is an alternate representation of Equation (2.20) and includes the Polarization vector. These equations describe a displacement of charge as being independent of time. The displacement of any object can be described by time independent and time dependent terms in the following equation:

$$\mathbf{s} = \mathbf{s}_0 + \int \frac{d\mathbf{s}}{dt} dt \tag{5.9}$$

By replacing the displacement, $\mathbf{s}$, in Equation (5.9) with the electric displacement, $\mathbf{D}$, and assuming the time independent electric displacement shown on the RHS of Equation

(2.20) corresponds to the time independent electric displacement, $\mathbf{D}_0$, the following equation is obtained:

$$\mathbf{D} = \varepsilon_0 \mathbf{E} + \varepsilon_0 (\varepsilon_r - 1)\mathbf{E} + \int \frac{\partial \mathbf{D}}{\partial t} \partial t \tag{5.10}$$

The derivative of the electric displacement with time is the current density and the first three terms on the RHS can be simplified:

$$\mathbf{D} = \varepsilon \mathbf{E} + \int \mathbf{i} \partial t \tag{5.11}$$

Equation (5.11) describes a displacement that is equivalent to that described by Equation (2.23) at any instant in time. However, when applied over a time period a displacement due to current will be included in the calculation of the electric displacement field. When transport equations such as the Nernst-Planck equation or those described by dilute solution theory are applied over a time period to an electrolyte conducting electric current, the electric displacement as described by the second term on the RHS of Equation (5.11) will become significant when integrated over large time periods. In fact, when using a transport equation such as the Nernst-Planck equation the first term on the RHS of Equation (5.11) is zero because these macroscopic transport equations do not consider electric displacement due to the polarization of molecules nor the permittivity of free space. For a conductive linear isotropic material that obeys Ohm's Law, Equation (5.11) may be expressed as:

$$\mathbf{D} = \varepsilon \mathbf{E} + \int \kappa \mathbf{E} \partial t \tag{5.12}$$

Invoking Equation (2.17), combining with Equation (5.12) and applying over a time period during which the conductivity and potential field are constant over time, gives:

$$\nabla \cdot \mathbf{D} = \rho = \nabla \cdot (\varepsilon \mathbf{E}) + \nabla \cdot (\kappa \mathbf{E} \tau) \tag{5.13}$$

Equation (5.13) shows the relationship between charge density due to polarization and the permittivity of free space, electric current, and the applied electric field. For electrolytic systems, the permittivity of a typical moderately dilute electrolyte is approximately 10 magnitudes smaller than its conductivity. Therefore, if Equation (5.13) is applied over a time period of approximately 1×10^{-10} seconds the charge density due to polarization and the permittivity of free space is approximately equivalent to the charge density due to an electric current. In other words, over small time periods the first term on RHS of Equation (5.13) may approximate the second term on RHS of Equation (5.13). This is equivalent to saying that over extremely small time steps or periods the displacement of charge due to polarization (and the permittivity of free space) may be approximately the same as that due to current. However, macroscopic transport models, such as the Nernst-Planck equation or Dilute Solution Theory (Newman and Thomas-Alyea, 2004), do not predict the polarization of atoms and molecules, but instead calculate the transport of mass and charge, and thus current. Previous successes of Poisson's equation when coupled with transport equations (and the resulting very stiff equations), and applied over time, is likely due to the fact that the displacement accounted for in Poisson's equation approximates the displacement due to current at extremely small time steps in the discretized forms of these equations. At large time steps or periods the first term on the RHS of Equation (5.13) may be neglected and Equation (5.13) simplifies to:

$$\nabla\cdot\left(\kappa\tau\nabla\Phi\right)=-\rho \tag{5.14}$$

Equation (5.14) is also obtained from Equation (5.11) when the electric displacement described by the first term on the RHS of Equation (5.11) has been neglected, such as

when dilute solution theory is applied. Equation (5.14) relates the electric field with free charge density for an electrolyte conducting charge over a significant time period if Equation (2.24) is applicable. For electrolytes, charge density may be expressed in terms of concentrations and if the gradient of conductivity is negligible (as in an isotropic electrolyte), Equation (5.14) becomes:

$$\nabla^2 \Phi = -\frac{F}{\kappa\tau}\sum_i z_i C_i \tag{5.15}$$

Equation (5.15) describes the electric field caused by charge density due to electric current over a significant time period. Therefore, Equation (5.15) describes the relationship between the charge density and electric potential field that may be coupled with transport equations for an isotropic electrolyte conducting electric current over a period of time.

An equation similar to Equation (5.12) may be developed directly from the fundamental continuity equation (Equation (2.19)). Integrating Equation (2.19) over a time period and assuming Ohm's Law gives:

$$\nabla \cdot (\kappa\tau \mathbf{E}) + A = -\rho \tag{5.16}$$

Where A is the constant of integration. According to the theory developed in this chapter, the constant of integration corresponds to the time independent electric displacement shown on the RHS of Equation (2.20) for a linear isotropic material. Incorporating the definition of electric potential into Equation (5.16) and neglecting the time independent electric displacement:

$$\nabla \cdot (\kappa\tau \nabla\Phi) = \rho \tag{5.17}$$

Comparing Equation (5.17) with Equation (5.12) shows the only difference between the two equations to be a negative sign. This difference arises from the fact that

Equations (5.12) and (5.17) both describe a dynamic current associated with static charge, but in the derivation of Equation (5.12) it was assumed that the electric current was a result of the static charge, while in the derivation of Equation (5.17) it was assumed that the static charge was a result of the electric current. Equations (5.12) and (5.13) describe the electric field caused by mobile charge density due to an electric current if Equation (2.24) applies. However, for an electrolyte with significant concentration gradients Equation (5.12) is not applicable. In fact, significant electrical current caused by the diffusion of ions may occur due to the concentration field, when the electric field has negligible gradients. Therefore, a more complex relationship than expressed in Equation (2.24) may exist for a non-isotropic electrolyte.

5.1.3 Apparent Displacement of Charge for Non-Isotropic Media Conducting Electric Current

In Section 5.1.1 it was shown that Poisson's equation describes a different charge density distribution than that inherent in the Nernst-Planck equation at steady-state. In Section 5.1.2 the relationship between the electric displacement incorporated in Poisson's equation and due to an electric current was explored. Equation (5.12) describes the electric displacement due to permittivity of free space, polarization of atoms and molecules, and electric current, for linear isotropic conducting media. The electric current in Equation (5.12) is described by Ohm's Law, which may not hold for an electrolyte that is non-isotropic; in a non-isotropic electrolyte, fields other than the electric field, such as the concentration gradients, may produce an electric current. Diffusion due to the concentration gradient may cause a macroscopic displacement of ions that causes charge density not described by Poisson's equation (as shown in Section

5.1.1). This charge density will have an effect on the electric potential. Therefore, Equation (5.12) should be expanded to account for other electric displacements that may occur in a non-isotropic electrolyte. Hence, it is necessary to add a second time independent, concentration dependent, term to the definition of the electric displacement field for the case of a non-isotropic electrolyte that is conducting current:

$$\mathbf{D} = \varepsilon\mathbf{E} + \mathbf{D}_0(\mathbf{p}) + \int \kappa\mathbf{E}\partial t \tag{5.18}$$

The term, $\mathbf{D}_0(\mathbf{p})$, in Equation (5.18), represents electric displacement that is a function of the property, $(\mathbf{p})$, of the non-isotropic electrolyte. In Section 5.2 the properties that will be examined will be concentration gradients and convection. In an isotropic material the second term on the RHS of Equation (5.18) is zero, and Equation (5.12) would apply. Therefore, Equation (5.18) (and the theory presented in this section) solves the question presented in Section 5.1.1 of whether Equation (5.2) or Equation (5.7) describes the steady-state charge density distribution. The answer is that both equations are simultaneously correct, but one equation accounts for the effects of bound charge density and the other accounts for the effects of mobile charge density.

5.2 Describing the Electric Field Caused by a Non-Isotropic Electrolyte

In this section the electric field caused by a non-isotropic electrolyte is explored. In the Maxwell-Boffi equations (Boffi, 1957) it is assumed an applied electric field causes charge density due to the polarization of atoms and molecules. This charge density causes an electric field to set up in opposition to the applied electric field. In the development presented here this latter effect it is also assumed to occur; however, the

incorporated charge density is created by phenomena other than the polarization of atoms and molecules.

5.2.1 Development of an Equation for the Electric Potential Field Caused by an Electrolyte: The Inherent Charge Density Model

It has been firmly established in the open literature that the flux of species can be described according to moderately dilute solution theory (Newman and Thomas-Alyea, 2004):

$$\mathbf{N}_i = -z_i u_i F C_i \nabla \Phi - D_i \nabla C_i - D_i C_i \nabla \ln \gamma_i + C_i \mathbf{V} \tag{5.19}$$

and (Newman and Thomas-Alyea, 2004):

$$\frac{\partial C_i}{\partial t} = -\nabla \cdot \mathbf{N}_i + S_i \tag{5.20}$$

Multiplying Equation (5.20) by $z_i F$ and summing over all species gives:

$$\frac{\partial}{\partial t}\left(F \sum_i z_i C_i \right) = -\nabla \cdot \left(F \sum_i z_i \mathbf{N}_i \right) + F \sum_{\mathrm{i}} z_i S_i \tag{5.21}$$

Electric current is defined (Newman and Thomas-Alyea, 2004):

$$\mathbf{i} = F \sum_i z_i \mathbf{N}_i \tag{5.22}$$

Substituting Equation (5.22) into Equation (5.21) and rearranging gives:

$$\nabla \cdot \mathbf{i} = F \sum_i z_i S_i - \frac{\partial}{\partial t}\left(F \sum_i z_i C_i \right) \tag{5.23}$$

Equation (5.23) implies that the divergence of electric current is caused only by the charge created by electrochemical reactions and the accumulation of charge density. For the development presented here, the electrochemical reactions are assumed to consist of charge balanced but spatially separated anodic and cathodic reactions.

Multiplying Equation (5.19) by $z_i F$ and summing over all species gives the electric current:

$$\mathbf{i} = -F^2 \nabla\Phi \sum_i z_i^2 u_i C_i - F \sum_i z_i D_i \nabla C_i - F \sum_i z_i D_i C_i \nabla \ln \gamma_i + F\mathbf{v} \sum_i z_i C_i \tag{5.24}$$

Therefore, the divergence of current is:

$$\nabla \cdot \mathbf{i} = -\nabla \cdot \left(\kappa \nabla\Phi\right) - F\nabla \cdot \sum_i z_i D_i \nabla C_i - F\nabla \cdot \sum_i z_i D_i C_i \nabla \ln \gamma_i + F\nabla \cdot \mathbf{v} \sum_i z_i C_i \tag{5.25}$$

Substituting Equation (5.23) into Equation (5.25) and rearranging:

$$\begin{aligned} \nabla \cdot \left(\kappa \nabla\Phi\right) = -F\nabla \cdot \sum_i z_i D_i \nabla C_i - F\nabla \cdot \sum_i z_i D_i C_i \nabla \ln \gamma_i + F\nabla \cdot \mathbf{v} \sum_i z_i C_i \\ - F \sum_i z_i S_i + F \frac{\partial}{\partial t}\left(\sum_i z_i C_i \right) \end{aligned} \tag{5.26}$$

Expanding the left-hand-side of Equation (5.26) gives:

$$\begin{aligned} \nabla^2\Phi = -\frac{F}{\kappa}\nabla \cdot \sum_i z_i D_i \nabla C_i - \frac{F}{\kappa}\nabla \cdot \sum_i z_i D_i C_i \nabla \ln \gamma_i + \frac{F}{\kappa}\nabla \cdot \mathbf{v} \sum_i z_i C_i \\ - \frac{F}{\kappa} \sum_i z_i S_i + \frac{F}{\kappa} \frac{\partial}{\partial t}\left(\sum_i z_i C_i \right) - \frac{\nabla \kappa \nabla\Phi}{\kappa} \end{aligned} \tag{5.27}$$

Equation (5.27) describes the relationship between the electric potential and concentration fields from moderately dilute solution theory. In some situations the last term on the RHS of Equation (5.27) may be neglected.

A second method exists for deriving Equation (5.26) from Maxwell's Equations. The continuity equation (Equation (2.19)) can be derived from Ampere's law with Maxwell's correction (Equation (2.16)) (Siegel, 1991). If the definition of current density from moderately dilute solution theory (Equation (5.24)) is incorporated into Equation (2.19):

$$\nabla \cdot \left(\kappa \nabla \Phi\right) = -F\nabla \cdot \sum_i z_i D_i \nabla C_i - F\nabla \cdot \sum_i z_i D_i C_i \nabla \ln \gamma_i + F\nabla \cdot \mathbf{V} \sum_i z_i C_i + F\frac{\partial}{\partial t}\left(\sum_i z_i C_i\right) \tag{5.28}$$

The only difference between Equation (5.26) and Equation (5.28) is the absence of the term $-F\sum_i z_i S_i$ in Equation (5.28). However, this term may be considered to be only a special case of the term $F \cdot \partial / \partial t\left(\sum_i z_i C_i\right)$ that describes the accumulation of charge density. In Section 5.2.2 of this thesis, during the discretization over time of Equation (5.27), the sign of the time dependent charge density accumulation term will be explored to ensure that the predicted electric potential describes current caused by charge density and not the electric current that would cause charge density, as discussed in Section 5.1.2.

5.2.2 Discretization of the Inherent Charge Density Model

Equation (5.27) is discretized using the finite difference approximations. Discretized values of the electric potential field are found over the next time step using values of concentration of species calculated by a transport equation (such as the one discussed in Chapter 6 of this thesis) over the previous time step. Values of conductivities are calculated at each time step at each node using these values of concentrations and Equation (5.5). For the calculation of conductivities, mobilities were calculated from the corresponding diffusion coefficient using the Nernst-Einstein equation. This application of the Nernst-Einstein equation may be considered applicable only to infinitely dilute solutions; however, according to Newman and Thomas-Alyea, “its

failure is related to the approximate nature of the [dilute solution theory] flux equation" (20043). Since the theory presented in this chapter overcomes some limitations of dilute solution theory and the corresponding flux equation, limitations concerning the Nernst-Einstein equation may also be improved. When required, activity coefficients were calculated, via the Extended Debye-Hückel equation (Bockris, 1977) at each time step and assumed constant over each individual control volume.

As was shown in Section 5.1.2, there are two electric currents associated with charge density. There is the electric current that results in charge density and the electric current that eliminates charge density. These two electric currents oppose one another. Since a transport equation is used to predict transport and current (and charge density), Equation (5.27) must predict the electric potential that reduces charge density. This reduction will be ensured by the correct application of Equation (5.27). During discretization, Equation (5.27) will be projected over the next time step. This affects the second last term on RHS of Equation (5.27), which becomes:

$$\frac{F}{\kappa}\frac{\partial}{\partial t}\sum_i z_i C_i \cong \frac{F}{\kappa}\frac{\left[\left(\sum_i z_i C_i\right)^{t+1} - \left(\sum_i z_i C_i\right)^{t}\right]}{\Delta t} \tag{5.29}$$

where the superscript, t, indicates the time step. The value of future charge density is unknown, but Equation (5.29) should tend to promote electroneutrality at the next time step. Electroneutrality at the next time step is:

$$\left(\sum_i z_i C_i\right)^{t+1} = 0 \tag{5.30}$$

Equation (5.29) and Equation (5.30) are incorporated into Equation (5.27). This incorporation of Equation (5.30) does not mean that the model assumes

electroneutrality. Instead, the model calculates the electric field caused by a quantity of charge density different from electroneutrality. In other words, the reference value of zero volts for zero charge density is chosen. This development ensures that the resulting expression describes the electric field caused by the electrolyte and is not simply a rearrangement of the transport equation described by moderately dilute solution theory. The time discretized form of Equation (5.27) becomes:

$$\nabla^2\Phi = -\left[\frac{F}{\kappa}\sum_i z_i D_i \nabla^2 C_i\right]^t - \left[\frac{F}{\kappa}\sum_i z_i D_i \left(\nabla C_i \cdot \nabla \ln \gamma_i + C_i \nabla^2 \ln \gamma_i\right)\right]^t$$
$$-\left[\frac{F}{\kappa}\sum_i z_i S_i\right]^t + \left[\frac{F}{\kappa}\nabla \cdot \mathbf{V}\sum_i z_i C_i\right]^t - \left[\frac{F}{\kappa}\frac{\sum_i z_i C_i}{\Delta t}\right]^t - \left[\frac{\nabla\kappa\nabla\Phi}{\kappa}\right]^t \qquad (5.31)$$

The second last term on the RHS of Equation (5.31) is the same as the term on the RHS of Equation (5.15), which was developed from Maxwell's Electric Displacement Field. This last term is also equivalent, but of opposite sign, to the relationship developed from the continuity equation (Equation (2.19)), and implied in Equation (5.17). The first four terms, and the last term, on the right-hand-side of Equation (5.31) are dependent on the properties of the electrolyte. These first four terms represent the electric displacement, $\mathbf{D}_0(\mathbf{p})$, in Equation (5.18). The first term on RHS of Equation (5.31) is equivalent to the diffusion potential. This term causes potential due to the different diffusion rates. The second term on RHS describes the effects of activity gradients on the Laplacian of potential. If the activity coefficients are calculated using a model such as the Extended Debye- Hückel equation (Bockris, 1977), then some effects of charge density due to polarization of atoms and molecules are included in this term. The third term on RHS describes the effect of spatially separated sources and sinks of

charge on the Laplacian of potential. The fourth and last terms on RHS describes the effects of convection and conductivity, respectively.

Since the electric field calculated using Equation (5.27) considers the effects of all charged species on the electric field, and the effect of this electric field on the electro-migration is considered in the coupled transport equation, the electric interaction between charged species is thus incorporated into this model (and discussed in Chapter 6). Therefore, this model can simulate systems where the electric interaction between species is important, such as for liquid-junctions. Also, because Equation (5.27) considers the effects of charge density on the electric field and resulting transport, this model is not restricted to electrically neutral bulk electrolytes.

5.3 Conclusions

Charge density distribution may occur in a medium subjected to an electric field. In an electrolyte, charge density may occur due to the polarization of atoms and molecules and also due to other phenomena, such as the different rates of diffusion of ions. Transport equations, such as the Nernst-Planck equation, predict the charge density due to the flow of electric current, but do not predict the charge density due to the polarization of atoms and molecules. The Inherent Charge Density Model, developed in this chapter, relates the Laplacian of electric potential to the properties of a non-isotropic electrolyte that may be conducting an electric current. This model neither assumes electroneutrality nor does it directly incorporate Poisson's equation; however, Poisson's equation may be indirectly utilized through the calculation of activity coefficients, if applicable. The charge density considered by the Inherent Charge Density Model is the same charge density predicted by the transport equation developed from moderately

dilute solution theory. This is because the Inherent Charge Density Model is a manipulation of the transport equation described by moderately dilute solution theory. It was shown that the Inherent Charge Density Model can be developed strictly from moderately dilute solution theory, or it can be developed incorporating Ampere's law with Maxwell's correction. Also, the relationship between the model and Poisson's equation can be explained using Maxwell's concept of the Electric Displacement Field.

5.4 Recommendations

This chapter investigated the electric field coupled with a non-isotropic electrolyte that may be conducting an electric current. An equation (the Inherent Charge Density Model) was developed that characterizes this electric field and may be coupled with the transport equation described by dilute solution theory. It is recommended that a transport equation and suitable numerical method is developed for solving these equations. Coupling this transport equation with the Inherent Charge Density Model will allow for the simulation of many electrochemical systems. The use of Patankar's (1980) method to develop the electrochemical transport equation would guarantee conservation of charge and mass.

6. THE NEW GOVERNING EQUATIONS: A UNIVERSAL ELECTROLYTE MODEL

Chapters 3 and 4 presented numerical models for crevice corrosion that coupled a transport equation with a simple characterization of the electric field. Chapter 5 developed a comprehensive multi-dimensional characterization of the electric field (the Inherent Charge Density Model). This chapter couples the Inherent Charge Density Model with an electrolyte transport equation developed using the method of Patankar (1980). Subsequently, validations using this universal electrolyte model are presented.

6.1 Universal Model

The developments presented in this section are for an equation that may be combined with the Inherent Charge Density Model and result in a model that predicts electric and concentration fields. An important aspect of the overall development is the assumption that a transport equation, such as the Nernst-Plank equation, defines the relationship between concentration and electric potential fields and the inclusion of additional assumptions, such as Poisson's equation, are not essential. It was shown in Chapter 5 that this approach is consistent with Maxwell's equations.

The following development results in a model for multi-dimensional multi-component transport in an electrolyte, accounting for charge density, concentration gradients, convection, and spatially separated anodic and cathodic reactions. The

resulting model consists of two coupled equations: one equation for transport and one equation for the electric field. The development of the discretized transport model is shown in this chapter. The equation for the electric field (Inherent Charge Density Model) was developed in Chapter 5. However, the governing equations (transport and Inherent Charge Density Model) are:

$$\frac{\partial C_i}{\partial t} - \left(z_i u_i F \nabla\Phi + D_i \nabla \ln \gamma_i - \mathbf{V}\right) \cdot \nabla C_i = D_i \nabla^2 C_i + S_i \tag{6.1}$$

$$\begin{aligned} \nabla^2 \Phi = & -\frac{F}{\kappa} \nabla \cdot \sum_i z_i D_i \nabla C_i - \frac{F}{\kappa} \nabla \cdot \sum_i z_i D_i C_i \nabla \ln \gamma_i + \frac{F}{\kappa} \nabla \cdot \mathbf{V} \sum_i z_i C_i \\ & - \frac{F}{\kappa} \sum_i z_i S_i + \frac{F}{\kappa} \frac{\partial}{\partial t} \left(\sum_i z_i C_i \right) - \frac{\nabla \kappa \nabla \Phi}{\kappa} \end{aligned} \tag{6.2}$$

Equation (6.1) describing transport is developed using the Control Volume method (Patankar, 1980). Equation (6.1) considers the spatial profile of activity coefficients, transport due to electromigration, diffusion, and convection, and includes a term for reactions. Equation (6.1) treats the flow of species due to the electric field in the same way as it treats the flow of species due to the convection field. In the Control Volume method the flow of species across control volume boundaries is dealt with using a differencing scheme and Peclet number. Therefore, Equation (6.1) contains fewer terms than the transport equation developed to be approximated using the Finite Difference method. Equation (6.2) describes the electric potential field in an electrolyte. It has terms that represent the Laplacian of potential caused by diffusion potential, spatial profile of activity coefficients, charge balanced but spatially separated anodic and cathodic reactions, convection, charge density, and conductivity. When the spatial profile of the activity coefficient in solution is nearly uniform, or $\nabla \ln \gamma_i = 0$, Equations

(6.1) and (6.2) simplify to the equations developed using infinitely dilute solution theory (Kennell and Evitts, 2010a):

$$\frac{\partial C_i}{\partial t} - \left(z_i u_i F \nabla\Phi - \mathbf{V}\right)\cdot\nabla C_i = D_i \nabla^2 C_i + S_i \tag{6.3}$$

$$\begin{aligned}\nabla^2\Phi = -\frac{F}{\kappa}\sum_i z_i D_i \nabla^2 C_i - \frac{F}{\kappa}\sum_i z_i S_i + \frac{F}{\kappa}\nabla\cdot\mathbf{V}\sum_i z_i C_i \\ + \frac{F}{\kappa}\frac{\partial}{\partial t}\left(\sum_i z_i C_i\right) - \frac{\nabla\kappa\nabla\Phi}{\kappa}\end{aligned} \tag{6.4}$$

During the numerical solution of Equation (6.1) a differencing scheme is used, such as the Hybrid Scheme, the Power-law Scheme, or the Upwind Scheme (the Power-law Scheme was used for the simulations presented in this thesis). A Peclet number is defined:

$$P_x = \frac{\left(z_i u_i F \frac{\partial\Phi}{\partial \mathrm{x}} + D_i \frac{\partial \ln\gamma_i}{\partial x} - V\right)\Delta x}{D_i} \tag{6.5}$$

The use of this Peclet number is justified in Section 6.2.2 of this thesis.

6.2 Electrolytic Transport

6.2.1 Development of the discretized transport equation

The methods and nomenclature used in the development of the transport equation are those of Patankar (1980), and effort has been taken to present this development in a manner that is parallel to that, but with the introduction of electromigration. According to moderately dilute solution theory the flux of each dissolved species under the influence of an electric potential field is (Newman and Thomas-Alyea, 2004):

$$\mathbf{N}_i = -z_i u_i F C_i \nabla\Phi - D_i \nabla C_i - D_i C_i \nabla \ln\gamma_i + C_i \mathbf{V} \tag{6.6}$$

For clarity, the subscript, *i*, indicating an individual species, is dropped in the following development. However, each of the following equations in this section applies to one chemical species only. Also, for brevity, this development is conducted in two dimensions only. Manipulating Equation (6.6) for the flux across a control volume boundary:

$$J_x \equiv \left(U - zuF\frac{d\Phi}{dx} - D\frac{d\ln\gamma}{dx} \right) C - D\frac{dC}{dx} \tag{6.7}$$

$$J_y \equiv \left(V - zuF\frac{d\Phi}{dy} - D\frac{d\ln\gamma}{dy} \right) C - D\frac{dC}{dy} \tag{6.8}$$

where all of the values in parentheses will amount to a constant between each pair of adjacent nodes at each time step, and will henceforth be designated: "the modified flow field". The integration of Equation (6.6) gives:

$$\frac{\left(C_P - C_P^0\right)\Delta x\Delta y}{\Delta t} + J_n + J_e - J_s - J_w = \left(S_c + S_p C_P\right)\Delta x\Delta y \tag{6.9}$$

Equation (6.9) is the same as the equation developed by Patankar for convective-diffusive problems (1980). However, the fluxes in Equation (6.9) contain extra terms that account for electro-migration and activities included in the modified flow field. Therefore, as explained in Section 6.2.2, the numerical techniques that have evolved during the development of the Control Volume method may be used. Also, Equation (6.9) is the discretized form of Equation (6.1). In Patankar's development, the flow rate is dependent only on the flow field (convection) and control volume size. In this development the flow rate is dependent upon all constants that sum to make the modified flow field (as justified in Section 6.2.2) and control volume size:

$$f_n = \left(V - zuF\frac{d\Phi}{dy} - D\frac{d\ln\gamma}{dy} \right)_n \Delta x \tag{6.10}$$

$$f_s = \left(V - zuF\frac{d\Phi}{dy} - D\frac{d\ln\gamma}{dy} \right)_s \Delta x \tag{6.11}$$

$$f_e = \left(U - zuF\frac{d\Phi}{dx} - D\frac{d\ln\gamma}{dx} \right)_e \Delta y \tag{6.12}$$

$$f_w = \left(U - zuF\frac{d\Phi}{dx} - D\frac{d\ln\gamma}{dx} \right)_w \Delta y \tag{6.13}$$

For the case of an incompressible flow, Patankar assumes that the divergence of the flow field must be zero. However, the modified flow field presented here does not satisfy this assumption for the case of flow for a single species. The conservation of species, however, is assured in this model because any flux leaving a control volume is the flux entering a neighboring control volume. This is a property of the Control Volume technique. For the modified flow field that does not satisfy Patankar's assumption, Equation (6.9) can be manipulated to obtain, through Equations (6.14) and (6.15), Equation (6.16):

$$\begin{aligned} \frac{\left(C_P - C_P^0\right)\Delta x\Delta y}{\Delta t} + \left(f_n + f_e - f_s - f_w\right)C_P + \left(J_n - f_n C_P\right) + \left(J_e - f_e C_P\right) \\ - \left(J_s - f_s C_P\right) - \left(J_w - f_w C_P\right) = \left(S_c + S_p C_P\right)\Delta x\Delta y \end{aligned} \tag{6.14}$$

$$\begin{aligned} \frac{\left(C_P - C_P^0\right)\Delta x\Delta y}{\Delta t} + \left(f_n + f_e - f_s - f_w\right)C_P + a_N\left(C_P - C_N\right) + a_E\left(C_P - C_E\right) \\ - a_S\left(C_S - C_P\right) - a_W\left(C_W - C_P\right) = \left(S_c + S_p C_P\right)\Delta x\Delta y \end{aligned} \tag{6.15}$$

$$a_P C_P = a_N C_N + a_E C_E + a_S C_S + a_W C_W + b \tag{6.16}$$

where:

$$a_P = \left(\frac{\Delta x\Delta y}{\Delta t} + f_n + f_e - f_s - f_w + a_N + a_E - a_S - a_W + S_P\Delta x\Delta y \right) \tag{6.17}$$

$$a_N = D_n A\left(\left|P_n\right|\right) + [[-f_e, 0]] \tag{6.18}$$

$$a_E = D_e A\left(\left|P_e\right|\right) + [[-f_e, 0]] \tag{6.19}$$

$$a_S = D_s A\left(\left|P_s\right|\right) + [[f_s, 0]] \tag{6.20}$$

$$a_W = D_w A\left(\left|P_w\right|\right) + [[f_w, 0]] \tag{6.21}$$

$$b = \left(S_c + \frac{C_P^0}{\Delta t} \right) \Delta x \Delta \tag{6.22}$$

The function, $A\left(\left|P_n\right|\right)$, depends on the choice of differencing scheme, as indicated earlier in Section 6.1. Therefore, the previous development results in two main differences when compared with the development of Patankar: Equation (6.17) contains variables for the flow rate, f_n, f_e, f_s, f_w, that have not cancelled, as is the case when electromigration is considered, and the flow field has been modified to include electromigration and activity coefficients.

6.2.2 Peclet number and modified flow field

The Peclet number described by Equation (6.5) can be used during the numerical solution of Equation (6.1), because for each time step, at each node, each variable inside the brackets on the numerator of Equation (6.5) is constant. Since the Power-law Scheme is an empirical fit of the exact solution of the governing equation between a pair of nodes (Patankar, 1980):

$$\frac{\phi - \phi_0}{\phi_L - \phi_0} = \frac{\exp\left(Px / L\right) - 1}{\exp\left(P\right) - 1} \tag{6.23}$$

where the governing equation is (Patankar, 1980):

$$\frac{d}{dx}(\rho u \phi) = \frac{d}{dx}\left(D \frac{d\phi}{dx} \right) \tag{6.24}$$

Therefore, the Power-law Scheme will fit the solution of the governing equation where a new constant, instead of the flow field, is defined. Equation (6.23) is the exact solution of Equation (6.24) when ρu and D are constants, which will be true if the variable u is replaced by the new modified flow field term. Ramifications do arise due to the divergence of the modified flow field not being equal to zero, and these issues were dealt with in Section 6.2.1. Therefore, differencing schemes developed for solving the convection-diffusion problem can still be used with this Peclet number and modified flow field, providing the variable describing the flow field is replaced by the value for the new modified flow field at all stages in the numerical procedure.

6.3 Boundary Conditions and Numerical Methods

Boundary conditions for the coupled numerical solution of Equations (6.1) and (6.2) are needed. For any boundary where there is a solid barrier and no mass transfer, the boundary condition for Equation (6.1) is (shown in the *x*-dimension):

$$\frac{\partial C_i}{\partial x} = 0 \tag{6.25}$$

and for Equation (6.2):

$$\frac{\partial \Phi}{\partial x} = 0 \tag{6.26}$$

Therefore, Equation (6.26) is utilized if the solid boundary is an insulator or an electroactive surface. If the solid boundary is an insulator the use of Equation (6.26) as a boundary condition follows the same procedure as mass transport and current

distribution models described by Newman and Thomas-Alyea (2004) and Equation (2.10). Equation (6.26) can also be used as a boundary condition for Equation (6.2) at an electro-active surface by setting the value of the source terms in Equations (6.1) and (6.2) equal to the rate of dissolution or deposition. The use of a single simple boundary condition at all surfaces for Equation (6.2) is advantageous, since in other methods more complex treatments at boundary surfaces are required, as explained in Chapter 2.

Boundary conditions may also be utilized that specify electrolyte properties adjacent to the bulk electrolyte. For Equation (6.1):

$$C_i = A \tag{6.27}$$

and for Equation (14):

$$\Phi = B \tag{6.28}$$

For the results and validations presented in this thesis the ADI method was used to solve Equation (6.1) and Gauss' method was used to solve Equation (6.2) multi-dimensionally. When utilizing Gauss' method to solve for the electric potential, an arbitrary reference potential of zero volts was initially assumed over the entire electrolyte. Therefore, the predicted electric fields presented in this thesis show only gradients of potential and not absolute values. To calculate the absolute values the electric potential would need to be specified in one location in the field. When solving Equation (6.2) one-dimensionally an implicit method was used with a fictitious node located outside of the electrolyte. It was arbitrarily assumed that the reference potential at these fictitious nodes was zero volts.

6.4 Model Validation

6.4.1 Model Simplifications

In the simulations presented in this section convection was assumed to be absent. The terms from Equation (6.2) responsible for causing large potential gradients are two terms associated with charge density: $-F/\kappa\sum_i z_i S_i$ and $F/\kappa\cdot\partial/\partial t\left(\sum_i z_i C_i\right)$. In other words, large potential gradients are associated with the transport of charge density, and when large potential gradients are present these two terms dominate the other terms on the Right-Hand-Side (RHS) of Equation (6.2). Therefore, when there are significant gradients of potential all other terms on the RHS of Equation (6.2) are insignificant. However, when there are smaller potential gradients the diffusion potential term and activity terms may be significant, but the last term, $\nabla\kappa\nabla\Phi/\kappa$, approaches zero. This simplifies the numerical solution of Equation (6.2). In the solution procedure, conductivity was calculated as a function of concentration at each time step, at each node. The simplified equation (when convection is absent) for the electric potential field is:

$$\nabla^2\Phi = -\frac{F}{\kappa}\nabla\cdot\sum_i z_i D_i \nabla C_i - \frac{F}{\kappa}\nabla\cdot\sum_i z_i D_i C_i \nabla \ln\gamma_i - \frac{F}{\kappa}\sum_i z_i S_i + \frac{F}{\kappa}\frac{\partial}{\partial t}\left(\sum_i z_i C_i\right) \tag{6.29}$$

Equations (6.1) and (6.29) were solved to find the concentration and electric fields in several physical systems.

6.4.2 Results and discussion

Since the model presented in this chapter predicts both concentration and electric fields, validations against experimental data and comparisons against expected trends are presented as such. Firstly, in Section 6.4.2.1, predicted potential differences across one-dimensional liquid-junctions are compared with values calculated and experimentally determined by others. Then, in the remaining portion of Section 6.4.2.1, the electric and concentration gradients for a liquid-junction initially undergoing free diffusion and involving four different charged species will be analyzed, including two-dimensional predictions. In Section 6.4.2.2, predicted one-dimensional transport and concentration gradients are validated against experimental and computational work conducted by others for an engineered corroding crevice. Although these one-dimensional concentration gradients have been previously calculated by other models, the methods and theories utilized in this chapter are unique in that electric force interactions are predicted without the need to prescribe the current distribution and with a single transport property. In Section 6.4.2.3 a two-dimensional system is explored. In this system ionic transport occurs between two tubes of different diameters and across a moving liquid-junction and the transport of species is instigated by anodic and cathodic reactions occurring in spatially separated locations.

6.4.2.1 Liquid-junctions

When two electrolytes of varying composition are brought into contact with each other a tendency for the diffusion of species from areas of higher concentration into areas of lower concentration exists. Different ions diffuse (and migrate) at different rates, causing localized charge density. Thus, an electric field caused by diffusion potential, activities, and charge density may be present across the liquid-junction. This

electric field will have the effect of slowing down the faster moving species and speeding up the slower moving species. For a free diffusion liquid-junction (where the two electrolytes are brought into contact to form an initially sharp boundary in a long, vertical tube) the region of varying concentration increases with the square root of time, and the potential of such a junction should be independent of time (Newman and Thomas-Alyea, 2004). In this section it will be demonstrated that the model presented in this chapter predicts: the correct potential difference across a free diffusion liquid-junction; that this potential difference is constant over time; that the predicted thickness of the region with varying concentration increases proportionally to the square root of time; and charge density is confined to boundaries.

Predictions were conducted for different solutions containing liquid-junctions. Table 6.1 shows the predicted potential differences across various liquid-junctions compared with values presented by Newman and Thomas-Alyea (2004). Newman and Thomas-Alyea calculated the values of potential differences without including the effects of charge density. Later in this chapter it will be shown that inclusion of the effects of charge density in Equation (6.29) is beneficial. For the cases where the gradients of activity coefficients were assumed negligible, the only data used to predict the potential differences were the initial species concentrations and the diffusion coefficients for each species. Diffusion coefficients for all species involved in simulations presented in this chapter are shown in Table 6.2. Ion mobilities were calculated from diffusion coefficients using the Nernst-Einstein equation. For the case where the gradients of activity coefficients were assumed significant, the Extended Debye-Hückel equation (Bockris and Reddy , 1977) was utilized with the ionic sizes recommended by Kielland

(1937). The inclusion of these activity coefficients calculated with the Extended Debye-Hückel equation incorporates some electric effects due bound charge density described by Poisson's equation additional to the effects of charge density already described by Equation (6.29).

The values predicted by The Inherent Charge Density Model (shown in Table 6.1) correspond with values presented by Newman and Thomas-Alyea (2004). Interestingly, the potential differences calculated by Equation (6.29), when activity gradients are not neglected, are similar to the values predicted by the Equation (6.29) when activity gradients are neglected. These results show that Equation (6.29) can represent the electric field without inclusion of activity coefficients for some scenarios. In Chapter 5 it was shown how Equation (6.29) incorporates a different form of charge density to Poisson's equation. To clarify the following discussion, let the charge density incorporated in Poisson's equation be called the bound charge density and that incorporated in Equation (6.29) be called the mobile charge density. Since Poisson's equation was used in the derivation of the Extended Debye-Hückel equation to find the ionic distribution (Newman and Thomas-Alyea, 2004), activity coefficients account for some aspects of electric force interactions due to the bound charge density incorporated in Poisson's equation. Since the potential values from Table 6.1 calculated incorporating activity coefficients are similar to the values calculated without activities, it is demonstrated that the effects of bound charge density on the electric field is substantially less than that of mobile charge density, for the simulations presented.

Table 6.1. Free diffusion liquid-junction potentials (where values with an asterisk are for activity coefficients equal to one and the bold values were experimentally determined).

Mol/liter			Φ_1-Φ_2, mV	
Ion	Solution 1	Solution 2	Values Presented by Newman and Thomas-Alyea[1]	Values Predicted by The Inherent Charge Density Model
K^+	0	0.01	-33.50	-34.0
H^+	0.02	0	-34.67*	-34.5*
Cl^-	0.02	0.01		
K^+	0	0.1	-27.31 **(27.08[2])**	-27.1
H^+	0.1	0	**(-28.3[3])**	-27.3*
Cl^-	0.1	0.1	-26.69*	
K^+	0	0.05	-20.7	-18.5
H^+	0.02	0	-18.50*	-18.5*
Cl^-	0.02	0.05		
K^+	0.1	0.1	-0.157	0.2
NO_3^-	0.05	0	-0.423*	-0.2*
Cl^-	0.05	0.1		
Cu^{2+}	0	0.1	-6.22*	-6.2*
Ag^+	0.2	0		
NO_3^-	0.2	0		
ClO_4^-	0	0.2		

1. Newman and Thomas-Alyea (2003); 2. Chloupek et al. (1933); 3. Grahame and Cummings (1950).

Table 6.2. Diffusion coefficients.

Ion	Diffusion coefficient (10^{-5} cm^2s^{-1})
Ag^+	1.648
Cu^{2+}	0.714
H^+	9.311
K^+	1.957
NO_3^-	1.902
Cl^-	2.032
ClO_4^-	1.792

Lide (2010)

The potentials shown in Table 6.1 can be explored by examining the corresponding transport predictions. Figures 6.1 and 6.2 show the concentration gradients across the

liquid-junction after different periods of simulated time for the 0.1 M $Cu(ClO_4)_{2<aq>}$ - 0.2 M $AgNO_{3<aq>}$ liquid-junction. Figure 6.1 shows the initially sharp concentration gradients across the liquid-junction after 1 second. Figure 6.2 shows, that after a period of 130 minutes, species have been transported from regions of higher concentration to regions of lower concentration and the concentration gradients are subsequently less steep. It can also be seen that the concentration gradients in Figure 6.2 are different for each species. The concentration gradients shown in Figure 6.2 differ from those predicted by classical dilute solution theory where the electric interaction forces are not considered; Figure 6.2 shows that the concentration of nitrate ions is less than the concentration of silver ions on the left side of the intersection, and the concentration is greater on the right side. If classical dilute solution theory was used and the electric interaction between the silver and nitrate ions was not modeled, the nitrate ion concentration would be less than the silver ion concentration on both sides of the junction because nitrate ions diffuse more quickly.

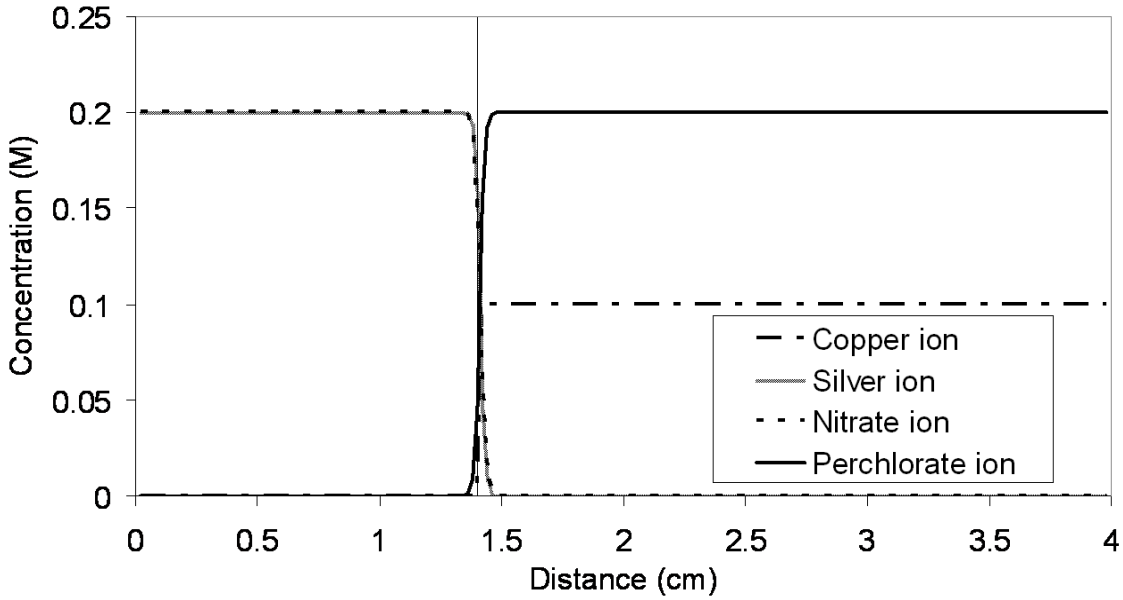

Figure 6.1. Predicted concentration gradients for 0.1 M $Cu(ClO_4)_2$ - 0.2 M $AgNO_3$ liquid junction after 1 second. The vertical line shows the position of the original junction between the two electrolytes at 1.4 cm.

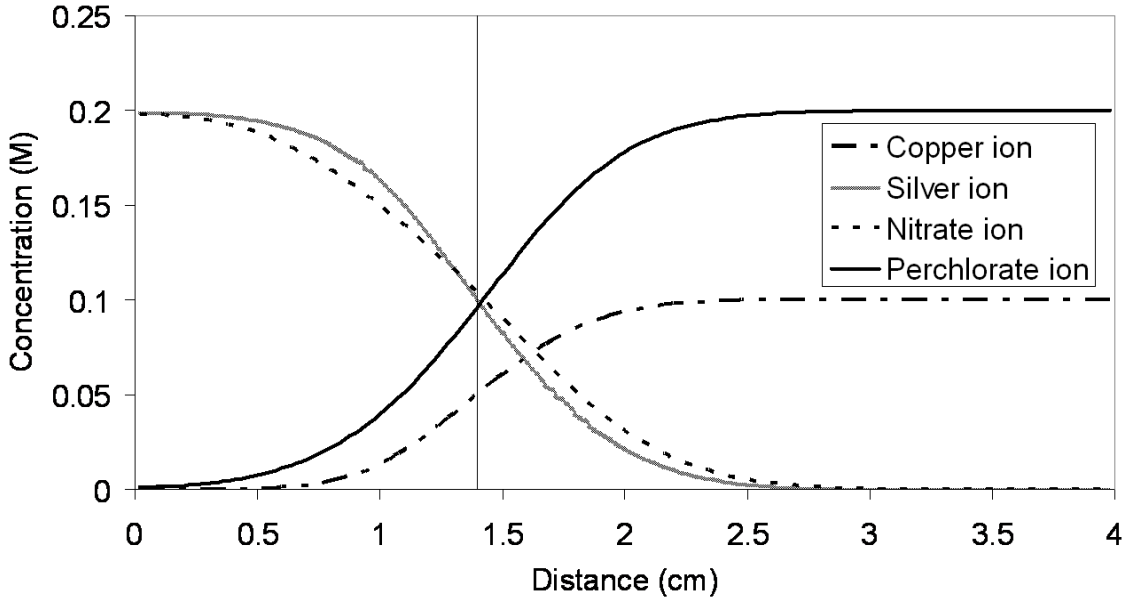

Figure 6.2. Predicted concentration gradients for 0.1 M $Cu(ClO_4)_2$ - 0.2 M $AgNO_3$ liquid junction after 130 mins. The vertical line shows the position of the original junction between the two electrolytes at 1.4 cm.

An additional validation of the model concerns the region of varying concentration. The region of varying concentration is the region where there are concentration gradients and can be seen in Figure 6.2 from approximately 0.25 cm to 2.7 cm. This region increases with time, and for a free diffusion liquid-junction it should increase proportionally to the square root of time. Figure 6.3 shows the predicted thickness of the region with varying concentration against the square root of time for the 0.1 M $Cu(ClO_4)_{2<aq>}$ - 0.2 M $AgNO_{3<aq>}$ junction. The best fit line to this data has a coefficient of determination of 0.9988.

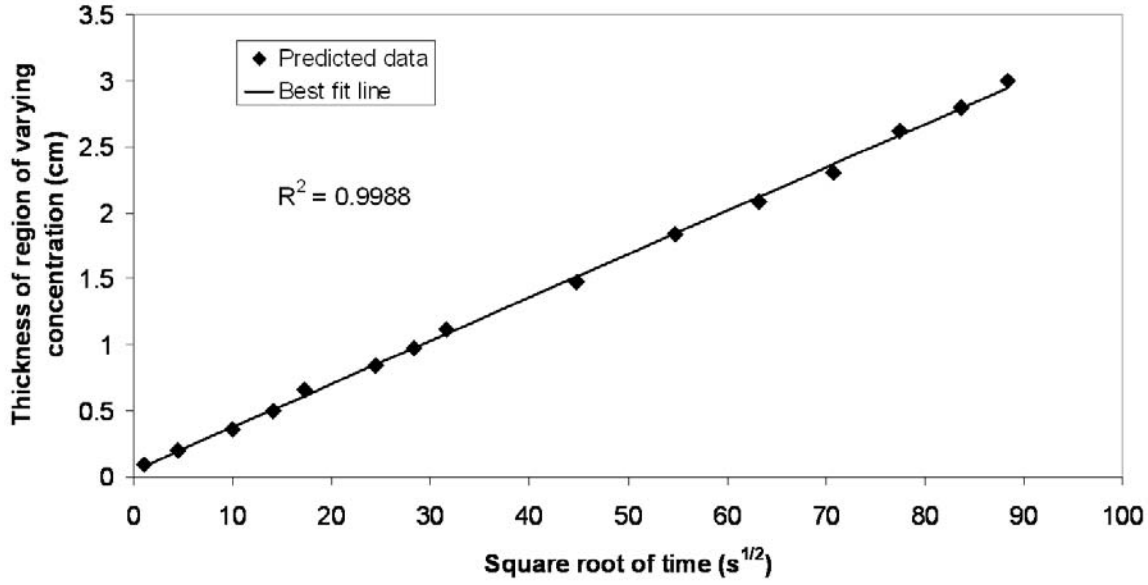

Figure 6.3. Predicted thickness of the region of varying concentration for 0.1 M $Cu(ClO_4)_2$- 0.2 M $AgNO_3$ liquid junction.

Figure 6.4 shows the predicted electric potential across the 0.1 M $Cu(ClO_4)_{2<aq>}$ - 0.2 M $AgNO_{3<aq>}$ liquid junction at different times. It can be seen that the predicted potential difference across the junction is constant at -6.2 mV for the entire period of

free diffusion. After approximately 2.5 hours, when the region of varying concentration expands to contact the solid boundary at the edge of the electrolyte, the junction is no longer considered to be a free diffusion liquid junction and the predicted electric potential difference is no longer constant.

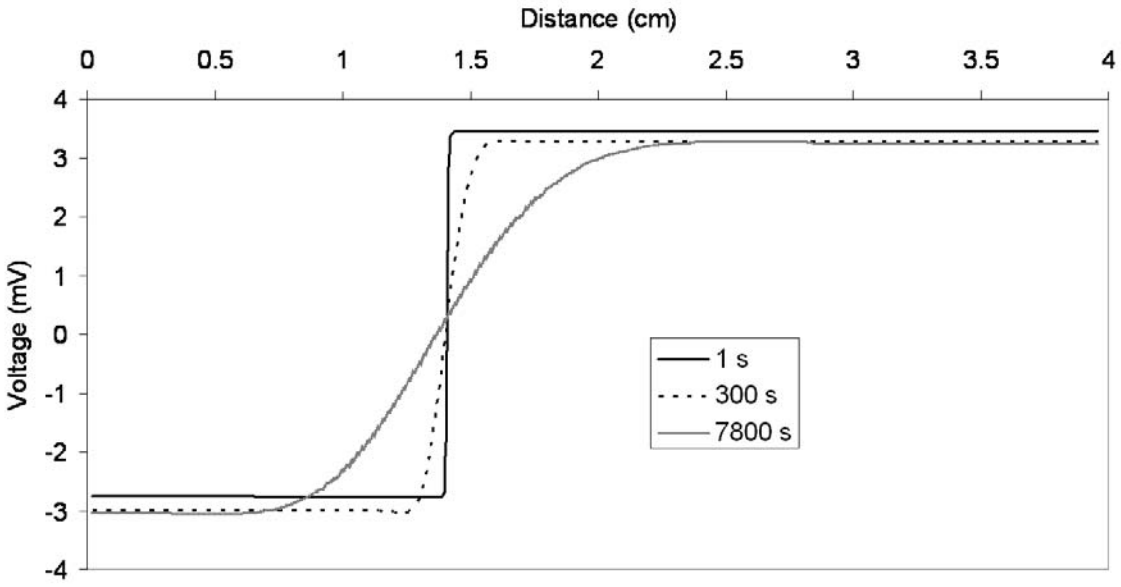

Figure 6.4. Electric potential distribution for 0.1 M $Cu(ClO_4)_2$- 0.2 M $AgNO_3$ liquid junction.

One of the novel aspects of the model is its ability to inherently balance the dynamic effects of charge density with mass transport and concentration gradients in the electrolyte while maintaining bulk electroneutrality. The model balances these effects during all simulations. Figure 6.5 shows the charge density in solution after 10 seconds of simulated contact for the 0.1 M $Cu(ClO_4)_{2<aq>}$ - 0.2 M $AgNO_{3<aq>}$ liquid-junction, and it can be seen that the charge density is located at electrolyte boundaries; the predicted

bulk electrolyte exhibits electroneutrality. This demonstrates that even though the electroneutrality assumption was not made, bulk electroneutrality is predicted.

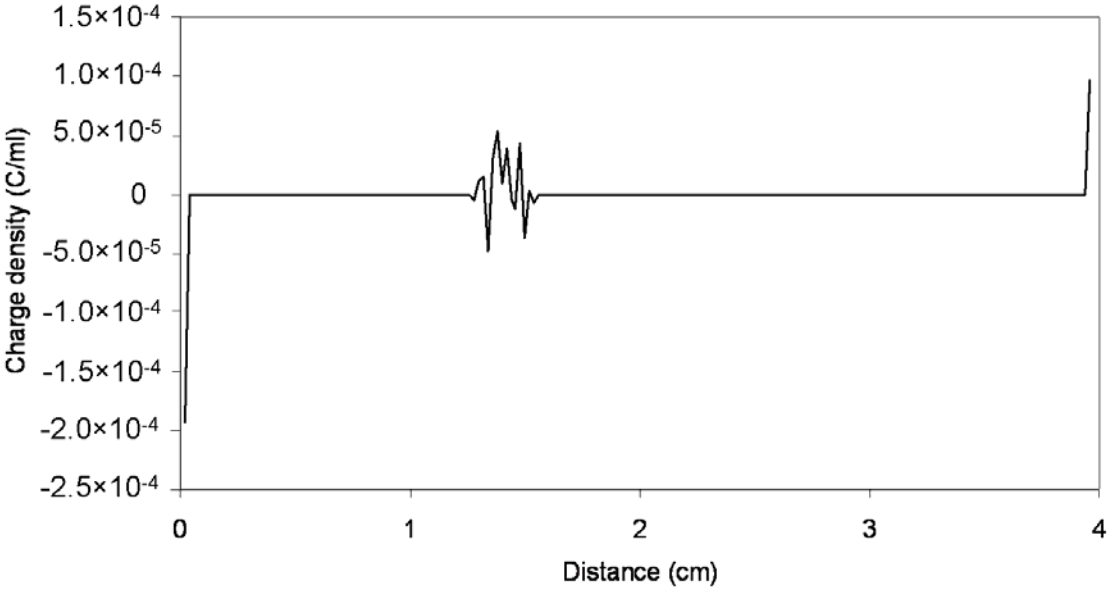

Figure 6.5. Charge density across 0.1 M $Cu(ClO_4)_2$- 0.2 M $AgNO_3$ liquid-junction after 10 seconds of simulated time.

This model is able to make predictions in more than one dimension, while considering electric force interactions, and without prescribing the current distribution. Figure 6.6 shows the predicted electric field for a two-dimensional container filled in three quadrants with 0.1 M $Cu(ClO_4)_{2<aq>}$ and one quadrant with 0.2 M $AgNO_{3<aq>}$. The $AgNO_3$ is in the quadrant on the right hand side of Figure 6.6. Figure 6.6 shows the electric field after one second of contact between the $Cu(ClO_4)_{2<aq>}$ and $AgNO_{3<aq>}$ solutions. The difference in potential measured across the junction between the two solutions, and shown in Figure 6.6, is 6.2 mV. This value is the same as the one-dimensional prediction. Figure 6.7 shows the electric field across the liquid-junction

after 45 minutes of simulated contact. The predicted potential difference evident in Figure 6.7 is 6.2 mV.

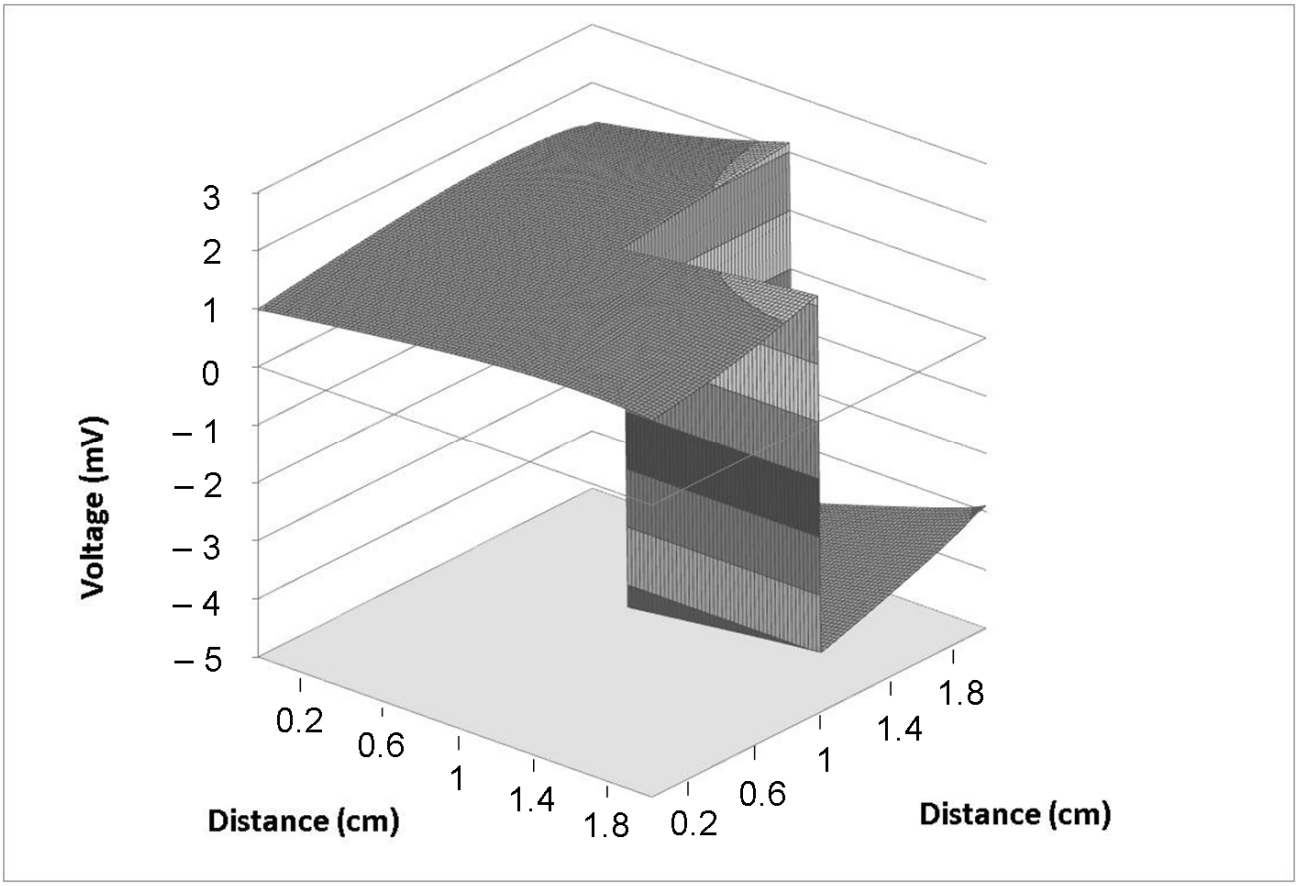

Figure 6.6. Electric potential field across a two-dimensional 0.1 M $Cu(ClO_4)_2$- 0.2 M $AgNO_3$ liquid-junction after 0.001 seconds.

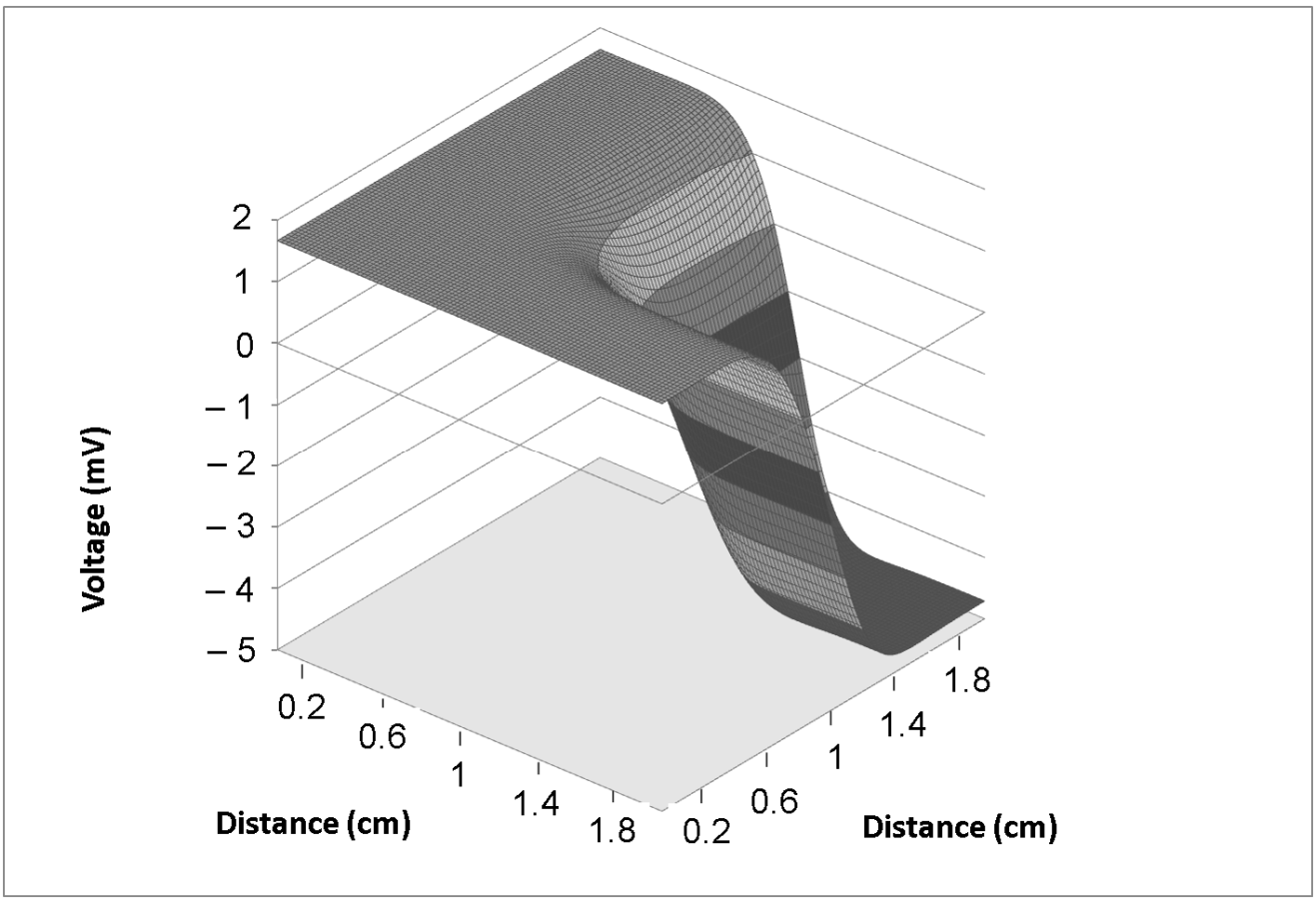

Figure 6.7. Electric potential field across a two-dimensional 0.1 M $Cu(ClO_4)_2$- 0.2 M $AgNO_3$ liquid-junction after 45 minutes.

This section has demonstrated distinct validations and expected trends: an accurate prediction of the electric potential differences across free diffusion liquid-junctions (compared with both experimental and simulated data), a prediction of a constant electric potential difference with time, the correct relationship between the thickness of the region of varying concentration with time, and charge density located only at electrolyte boundaries. However, this model is capable of modeling more advanced systems than shown above, while still considering charge density. Some of these will be explored in the next sections of this chapter.

6.4.2.2 One-dimensional transport

In Section 6.4.2.1 it was shown how there are interaction forces between charged species over liquid-junctions. In this section a more complex system, consisting of an engineered corroding crevice, will be analyzed. In this crevice there is an anode at one end of a glass tube containing an electrolyte and with a cathode located outside of the crevice. The anode instigates ionic transport through the electrolyte and thus the establishment of a liquid-junction that will move away from the anode. Figure 6.8 shows a schematic of this setup. In this figure the silver anode is connected to a power source and cathode via a wire. The silver anode is also immersed in an electrolyte inside tubes leading to a reservoir containing the cathode, thus completing an electrochemical circuit. The electrolyte is 0.1 M $KNO_{3<aq>}$. When an electrical current is applied, silver dissolves from the anode into the electrolyte. This dissolution causes localized charge density and the establishment of an electric field in the electrolyte that causes transport of cations away from the anode and anions towards the anode. Therefore, both K^+ and Ag^+ ions undergo net transport away from the anode, while NO_3^- undergoes net transport towards the anode. Since the diffusion coefficient (and thus mobility) is greater for K^+ than for Ag^+, K^+ ions are transported away from the anode more quickly than Ag^+ ions, causing a $AgNO_3 – KNO_3$ liquid junction (or boundary) to form. Once formed, the liquid junction will move down the tube and in practice this junction can be made visible by the addition of an insignificant amount of ascorbic acid (0.001 M). The model balances the dynamic concentration gradients across the liquid-junction and bulk electroneutrality with charge density located at the surface of the silver anode.

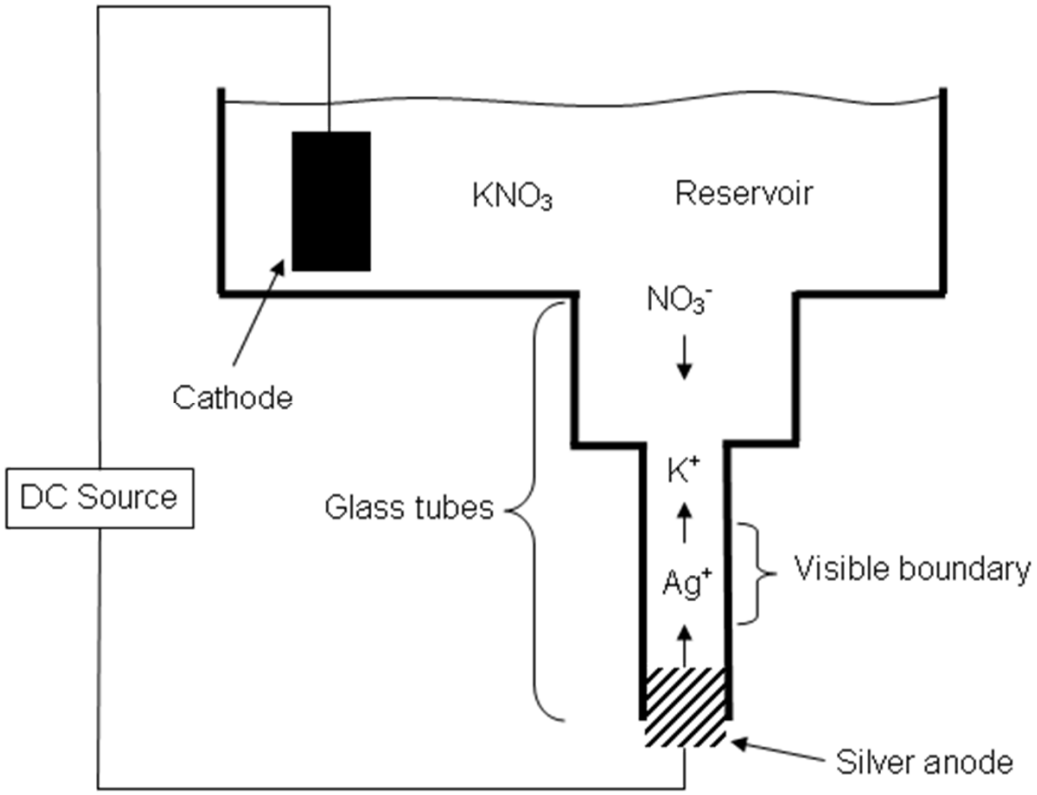

Figure 6.8. System for observing the movement of $AgNO_{3<aq>}$ – $KNO_{3<aq>}$ liquid junction.

Two simulations were conducted: one where the tubes connecting the anode to the reservoir were of two different internal diameters (discussed in Section 6.4.2.3), and one where a single tube of uniform diameter connected the anode to the reservoir. This second simulation corresponds to the experiment and simulation conducted by Fu and Chan (1984), where the inside diameter of the tube was 2 mm and a current of 1 mA was applied to the anode. Figure 6.9 shows the position of the liquid-junction as predicted by the model presented in this chapter and as experimentally measured by Fu and Chan (1984). Figure 6.9 shows an excellent correspondence between the predicted and experimentally determined data.

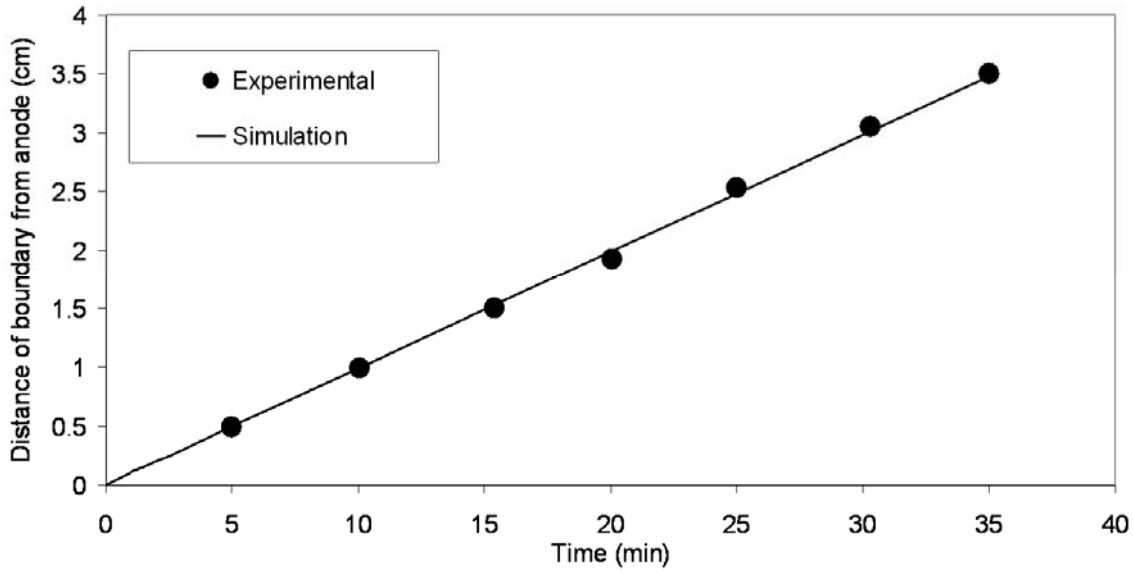

Figure 6.9. Experimental data of Fu and Chan (1984) (circles) and data simulated using model presented in this chapter.

Figure 6.10 shows the concentration profiles of Ag^+, K^+, and NO_3^- after a ten minute period predicted by the present model and the one-dimensional Fu and Chan model. The concentrations predicted by this model are represented by solid lines and those predicted by Fu and Chan by the dashed lines. Both models predict concentrations of Ag^+ in excess of 0.3 M near to the silver anode. The concentration of NO_3^- is predicted to be equal to the sum of cation concentrations by both models, indicating bulk electroneutrality. The predicted concentration profiles are similar for both models; however, the model of Fu and Chan predicts slightly steeper concentration gradients, both at the liquid-junction and closer to the silver anode. The present model predicts concentration gradients similar to those predicted by the one-dimensional model of Heppner (2006), shown in Figure 6.11. Figure 6.11 shows the concentration gradients of Ag^+ and K^+ after 20 minutes of simulating the Fu and Chan experiment.

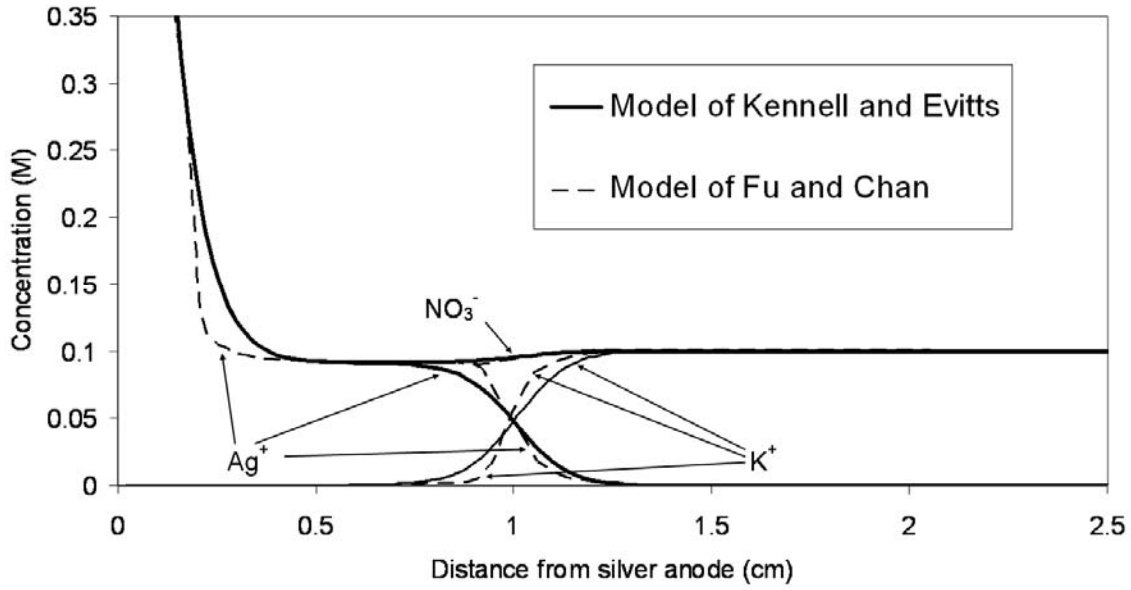

Figure 6.10. Concentration profiles of Ag^+, NO_3^- and K^+ after 10 minutes of current simulated by the current model and Fu and Chan (1984).

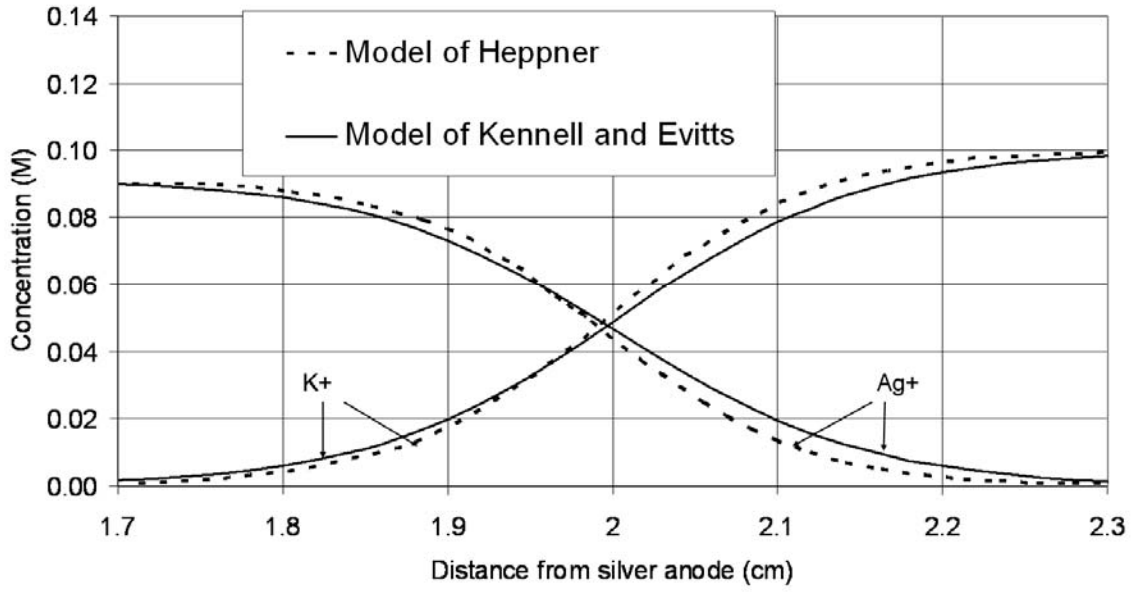

Figure 6.11. Concentration profiles of Ag^+ and K^+ after 20 minutes of current simulated by the current model and Heppner (2006).

The model presented in this chapter predicts similar concentration gradients to the other models, but unlike these one-dimensional models, no current distribution is assumed. Instead, a source term equivalent to the dissolution rate of silver ions is implemented at the crevice tip. Therefore, transport along the tube is caused by the electric field initially established by the charge density from the dissolution, not by a prescription of the electric current vector. This ability to model without assuming a current distribution is an important step towards modeling multi-dimensional systems.

6.4.2.3 Multi-dimensional current distributions

Simulations were also conducted for a second moving boundary scenario where the capillary between the anode and the reservoir was comprised of glass tubes with two different internal diameters, as shown in Figure 6.8. The solution and electrodes were the same as that used by Fu and Chan (1984). Since current passing through the tubes must now experience a sudden expansion, significant current must flow both in the axial and radial directions. An experiment was conducted to validate the results of this simulation. This experiment is described in greater detail in Appendix A. The smaller and larger glass tubes had inside diameters of 2.9 mm and 6.9 mm, respectively. The predicted movement of the liquid-junction was found to match that experimentally measured in the same manner as that shown in Figure 6.9 (see Appendix A).

Figure 6.12 shows the electric field predicted ten seconds after the start of current flow for the multi-dimensional case described above. Figure 6.12 shows the electric potential field along the smaller diameter tube, from 0 cm to 3.65 cm from the anode, and the larger diameter tube, from 3.65 cm to 5 cm from the anode. From Figure 6.12, it can be seen that the predicted electric potential gradient is significantly steeper along the

length of the smaller tube than along the length of the larger diameter tube, as would be expected due a lower flux of charge passing through the larger diameter tube. Figure 6.12 shows a total potential gradient across the first 5 cm of tubing to be approximately 4.5 V after ten seconds of current flow. The predicted electric potential difference across the computation domain remained relatively constant with time for the entire simulation; however, small changes to the shape of the field did occur, corresponding with the movement of the liquid-junction down the tubes. The potential difference along the first five centimeters of the tube was not experimentally measured; however, the potential difference along the entire tube length (10 cm) was measured at 10.2 V. This voltage also remained relatively constant with time (±0.2 V).

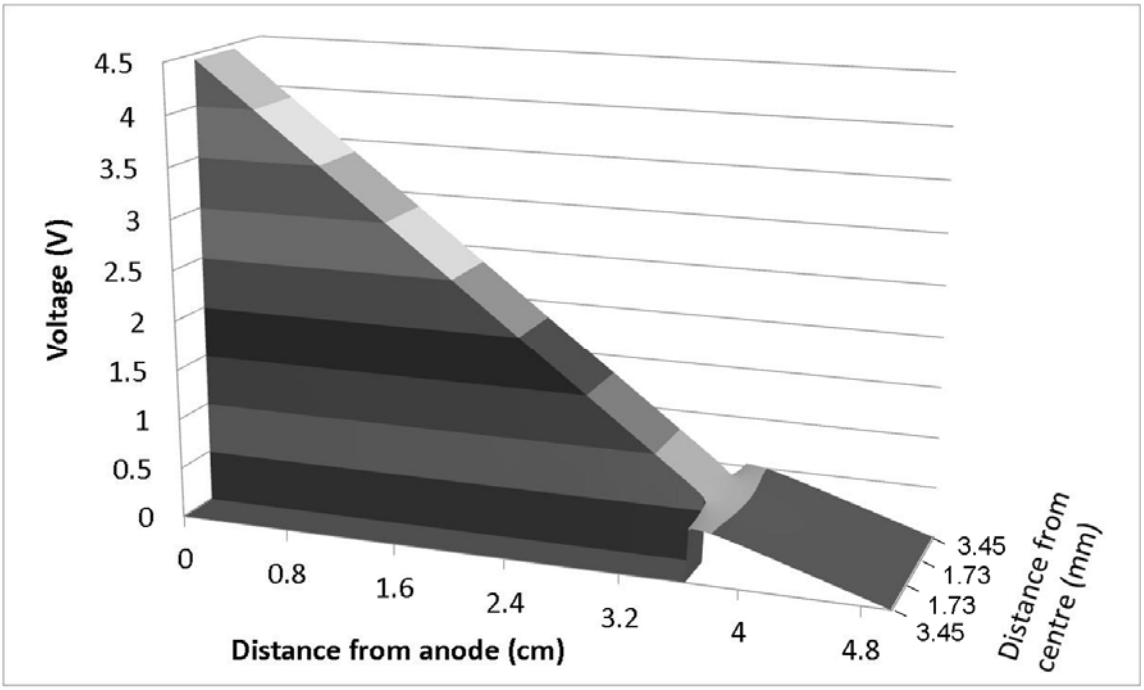

Figure 6.12. Electric field present in a current conducting electrolyte contained in two tubes of different internal diameters after 10 seconds of current.

Figure 6.12 also shows the electric field across the intersection between the two tubes. Figure 6.13 shows an enlarged view of this electric field across the intersection. It can be seen that the electric field in both the smaller and larger diameter tubes is uniform across the diameter at distances of approximately 3 mm from their intersection. At distances closer to the intersection of tubes, the electric potential shows significant gradients both along the length and radius of the tubes. An important aspect of these predictions is that this electric potential field across the intersection of the tubes, along the tubes, and across the liquid-junction, is predicted to maintain electroneutrality at all locations except at those areas immediately adjacent to the anode (the control volumes which encompass source terms). This prediction is obtained with the relatively simple boundary conditions, when compared with the boundary conditions required for conventional dilute solution theory.

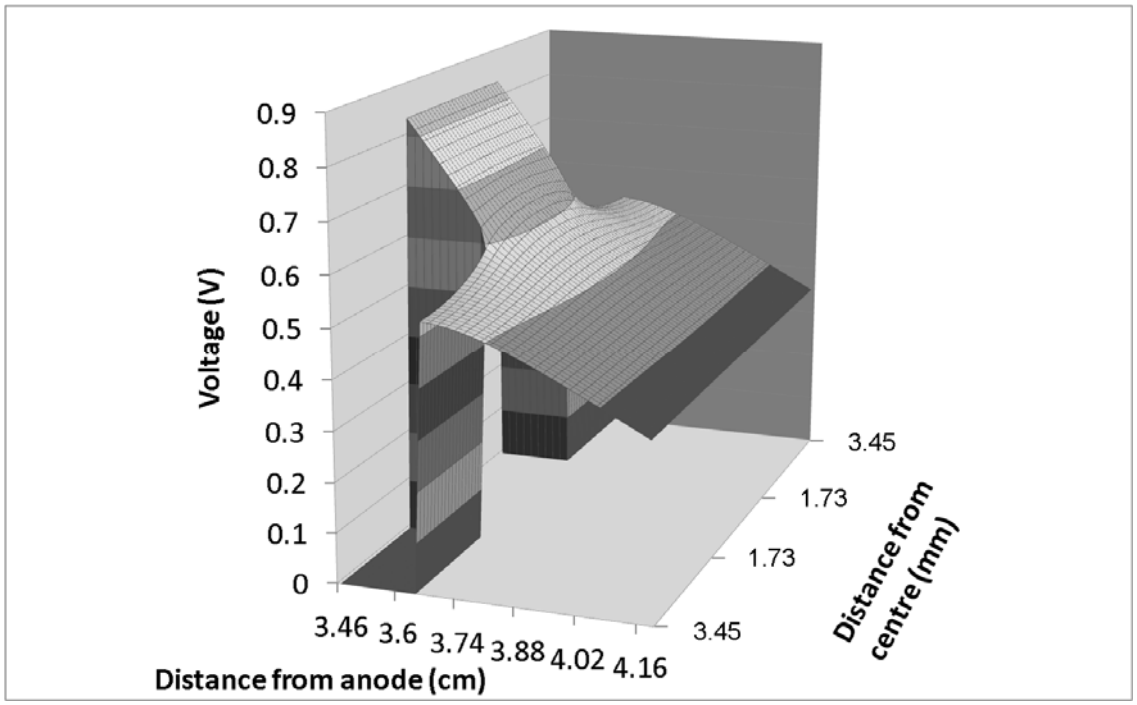

Figure 6.13. Electric potential field across the intersection of the smaller and larger diameter tubes after ten seconds of current.

Equations (6.1) and (6.29) also predict current distributions. For the case discussed above, the predicted current distribution across the intersection between the two tubes is displayed in Figure 6.14. In Figure 6.14 the direction of the overall current through the electrolyte is displayed by the direction arrows located at various positions throughout the electrolyte. The magnitude of the overall electric current at the origin of each arrow is proportional to the length of the arrow.

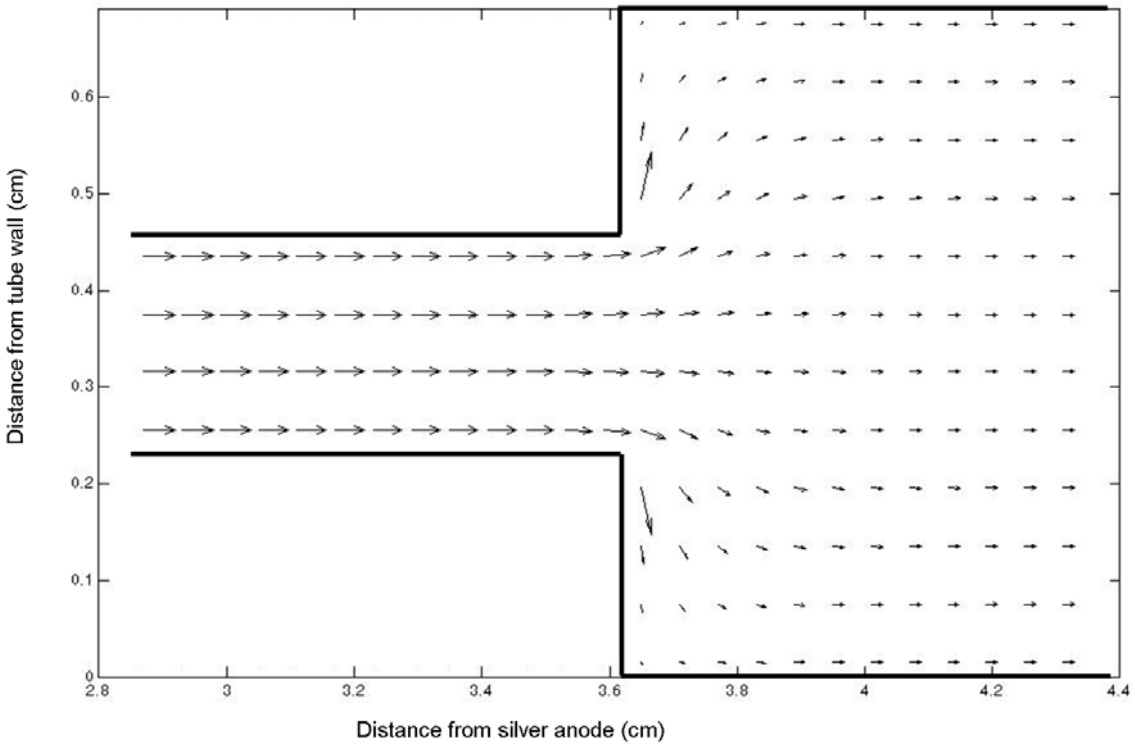

Figure 6.14. Electric current distribution predicted across the intersection between the larger and smaller diameter tubes.

6.5 Model Advantages

Several benefits to using the model presented in this chapter exist. As demonstrated in the results and discussion, this model does not require the prescription of current distributions. Instead, the model is capable of predicting multi-dimensional current distributions due to the composition of the electrolyte, electrochemical reactions and the electric field. In Section 6.3 the simple boundary conditions needed to solve Equation (6.2) multi-dimensionally were presented. The more complex boundary conditions for use with classical dilute solution theory, and the need to balance these boundary conditions with the current distribution, were presented in Section 2.3. Furthermore,

Equation (6.2) does not assume insignificant concentration gradients, as does Laplace's equation (Equation (2.9)). In fact, it was demonstrated in this chapter that Equation (6.2) predicts the electric fields across liquid-junctions where concentration gradients are very significant. The model presented here predicts electric and concentration fields across multi-dimensional liquid-junctions using a single transport property for each dissolved species (the diffusion coefficient), unlike concentrated solution theory which needs three properties, as described in Section 2.3. It was also demonstrated in this chapter, that with the prescription of a single transport property, Equation (6.2) models the electric force interactions between species without utilizing Poisson's equation. Modeling charge density without Poisson's equation has one main benefit: Equation (6.2) is not numerically stiff. The applicability of Poisson's to the case of mobile charge density was examined in Chapter 5 and will be reexamined in Chapter 9.

6.6 Conclusions

A new model describing the electric field and its interaction with electrolytic transport was presented. The benefits of this model were also discussed. The model was validated for different systems, including a multi-dimensional artificially corroding crevice containing a moving liquid-junction. For each system the model predictions fit the experimental data of others, the simulated data of others, and the expected trends. These validations confirm that this new model can predict multi-dimensional current distributions while considering concentration fields, charge density, activities, electric force interactions, and spatially separated anodic and cathodic reactions (significant migration). This model only requires a single transport property for each dissolved species and utilizes simple boundary conditions.

6.7 Recommendations

Because the model presented in this chapter has been shown to correctly predict concentration and electric fields for electrolytes where electric force interactions and spatially separated anodic and cathodic reactions may occur, the model should be applied to additional electrochemical systems where these combined criteria are important. Additionally, because this model makes fewer assumptions than classical dilute solution theory, it should be examined whether or not this model can correctly predict experimentally observed phenomena that classical dilute solution theory does not. One example of this is the large potential drops due to the extension of the cathode in a charging lithium-ion cell.

7. APPLICATION OF THE NEW THEORY – PART I: CHARGE DENSITY IN NON-ISOTROPIC ELECTROLYTES CONDUCTING CURRENT

Sections 7.1 through 7.4 of this chapter constitute a reproduction from The Canadian Journal of Chemical Engineering, of the paper in press: Glyn F. Kennell, Richard W. Evitts, "Charge Density in Non-isotropic Electrolytes Conducting Current", In Press (2011a).The author of this thesis contributed to this paper in the following capacities: main investigator, conducted numerical modeling, analyzed results, wrote initial drafts of manuscript, corresponding author, and corrected drafts with editorial contributions made by Prof. Evitts.

The universal electrolyte model was validated in Chapter 6. This chapter applies the universal electrolyte model to two systems and investigates the advantages of including the effects of charge density and concentration gradients on the simulation of the electric potential field. It is found that phenomena previously unreported by models based on conventional methods (but experimentally observed) are simulated by the new universal electrolyte model.

7.1 Introduction

A theory commonly used as a foundation for electrochemical models is dilute solution theory (Newman and Thomas-Alyea, 2004). Dilute solution theory assumes

bulk electroneutrality and often further assumptions, such as uniform electrolyte concentration, are required to model multi-dimensional current distributions and mass transfer. Instead, the model presented in this chapter uses aspects of dilute solution theory but does not make assumptions of electroneutrality nor uniform electrolyte concentrations. Predictions made by this model demonstrate the benefits of not making these assumptions. Simulations presented in this chapter show how the inclusion of the effects of charge density allows for the simulation of a liquid-junction using a single transport property for each dissolved species: the diffusion coefficient. Simulations also demonstrate how the absence of these assumptions allow for the modeling of phenomenon experimentally observed in lithium-ion cells but not previously successfully modeled with dilute solution theory.

West et al. (1982) presented a model accounting for the coupled transport in the electrolyte and electrode phases of a cell with porous insertion electrodes and a liquid electrolyte. The system was modeled one-dimensionally using infinitely dilute solution theory. Some assumptions made included: electroneutrality, very high conductivity in the electrode phase, a mono-valent electrolyte salt, and negligible flow due to concentration gradients or solid matrix expansion. Simulations demonstrated how electrolyte depletion was the principal factor limiting the discharge capacity of the system. Doyle et al. (1993) presented a model for a lithium-ion cell based on concentrated solution theory that was implemented considering one-dimensional transport for a galvanostatic current. The cell was comprised of a lithium foil anode, a polymer electrolyte and composite cathode. The model was used to simulate concentration gradients across the system. It was found that the decreased lithium

concentration in the composite cathode (below one molar) illustrated the need for higher lithium concentrations to maintain adequate conductivity. This model was expanded by Fuller et al. (1994) who considered a porous insertion anode instead of a lithium foil anode. This composite electrode consisted of an inert conducting material, the electrolyte, and the solid active insertion particles. Transport was considered one-dimensionally through the solid electrode via diffusion and through the electrolyte via concentrated solution theory. Arora et al. (1999) used the macroscopic model of Fuller et al. (1994) for one-dimensional lithium-ion battery predictions. The influence of lithium deposition on the charging and overcharging of intercalation electrodes was examined. It was observed that lithium deposition was predicted for cells with lower excess negative electrode capacity and no deposition was predicted for cells with higher excess negative capacity.

There are a limited number of published works pertaining to the multi-dimensional current distributions concerned with edge effects in lithium-ion cells. Scott et al. (2003a) presented an argument for the need for multi-dimensional lithium-ion cell modeling due to experimentally observed anomalous potentials attributed to edge effects and cathode extensions. In lithium-ion cells, the cathode may be extended past the edge of the anode to avoid lithium deposition that may occur preferentially at electrode edges, even when average conditions do not favor lithium deposition. Scott et al. found that after 90 seconds of charging their lithium-ion cell a potential difference of approximately 1 V was seen between the center of their cell coil and a region near to the cathode edge. This cathode edge was extended past the anode and adjacent to the bare current collector. Scott et al. concluded that this large potential difference exceeded that

which could be explained by ohmic drops in the current collector or concentration induced shifts in the reference potential. Instead, they concluded that this potential drop was consistent with an iR induced potential gradient in the electrolyte in a direction parallel to the plane of the electrodes. The driving force behind this iR drop was determined to originate from a local galvanic cell in the negative electrode. The galvanic cell was deemed to occur because of a lithium-ion gradient within the electrolyte associated with the cathode extension.

Tang et al. (2009) used the experimental studies of Scot et al. (described above) to justify the need for their two-dimensional lithium-ion cell model based on dilute solution theory. Using this model Tang et al. investigated the deposition of lithium during charging for a cell that had similarities with the cell used in the experimental work of Scot et al. The modeled lithium-ion cell contained an anode comprised of Li_yCoO_2, a cathode of Li_xC_6, and an electrolyte of 1.2 M $LiPF_6$ in EC:2DMC. Phenomena that were predicted by the model included the possibility for lithium deposition near the edge region for electrodes that were of equal length due to greater accessibility of the cathode edge. This deposition was predicted to occur towards the end of the cell charging period, minutes before the cutoff potential for the overall cell was reached. Further predictions demonstrated that extending the cathode past the edge of the anode reduced the possibility for this phenomenon. Tang et al. did not report any of the anomalous large potentials seen during early charging of the cell and reported by Scott et al. This chapter will discuss how, by neither making assumptions of electroneutrality nor uniform concentrations, both the phenomenon predicted by Tang et al. and the phenomenon experimentally observed by Scott et al. may be predicted.

7.2 Theory

Two cases are numerically simulated in this chapter. Both cases use the same governing equations. The first case simulated is a liquid-junction and the second a lithium-ion cell. The two governing equations used to model transport and the resultant dynamic electric fields for both cases are (Kennell and Evitts, 2010b):

$$\frac{\partial C_i}{\partial t} - \left(z_i u_i F \nabla \Phi - \mathbf{V}\right) \cdot \nabla C_i = D_i \nabla^2 C_i + S_i \tag{7.1}$$

$$\nabla^2 \Phi = -\frac{F}{\kappa} \nabla \cdot \sum_i z_i D_i^{eff} \nabla C_i + \frac{F}{\kappa} \nabla \cdot \mathbf{V} \sum_i z_i C_i - \frac{F}{\kappa} \sum_i z_i S_i + \frac{F}{\kappa} \frac{\partial}{\partial t} \left(\sum_i z_i C_i \right) \tag{7.2}$$

Equation (7.1) is used to model electrolytic transport. Equation (7.1) was developed using Patankar's Control Volume method (1980), and as such, contains one less term than a similar equation developed for finite difference or finite element discretization. This is because the terms inside the parenthesis in Equation (7.1) are combined into a flow field that is balanced with diffusion via the Power-law Scheme (Patankar, 1980). Utilizing Patankar's method in this way ensures the conservation of charge and mass. Equation (7.2) was developed from Maxwell's equations and Maxwell's concept of the electric displacement field and is projected forward in time. Equation (7.1) was solved using the ADI method and Equation (7.2) was solved using Gauss' method. When solving Equation (7.2) for the electric field an arbitrary reference potential of zero volts was used over the entire electrolyte domain. Therefore, the electrolyte electric potentials predicted in this chapter do not represent absolute values, but differences. To obtain actual values of electric potential the potential must be prescribed at some point within the predicted field. The electric field and coupled transport predictions showed no signs of instability or oscillation for the time step of 0.001 seconds used in all of the

simulations presented in this chapter. The distance between nodes was varied from 1×10^{-6} m to 0.01 m in the final simulation presented in this chapter that used a non-uniform cluster of nodes. The combined application of Equations (7.1) and (7.2) were validated against different sources of experimental and numerical data (Kennell and Evitts, 2010b) and presented in Chapter 6 of this thesis. These equations do not assume electroneutrality; instead, these equations account for the effects of charge density without directly incorporating Poisson's equation. Benefits of using Equation (7.2) instead of Poisson's equation include: Equation (7.2) is not numerically stiff when compared to equations incorporating Poisson's equation; and Poisson's equation incorporates a bound charge density that is different from the mobile charge density associated with conduction in non-isotropic electrolytes (Kennell and Evitts, 2010b). Conductivity was assumed to be non-uniform with time and position:

$$\kappa = F^2 \sum_i z_i^2 u_i C_i \tag{7.3}$$

The Bruggeman formula was used to modify diffusion coefficients for the porosity of the liquid electrolyte phase within the plasticized phase (Tang et al., 2009):

$$D^{eff} = D\beta^{1.5} \tag{7.4}$$

For the case of a solid electrode into which lithium is inserted via an electrochemical reaction, Equation (7.1) reduces to Equation (7.5) because charged species are assumed absent from the solid film electrodes:

$$\frac{\partial C_s}{\partial t} = D_j \nabla^2 C_s + S_s \tag{7.5}$$

In Equation (7.5) the diffusion coefficient, D_j, depends on the material from which the electrode is constructed. These and other values are given in Table 7.1. Therefore, the

simulation domain is comprised of three sub-domains: the anode, the cathode, and the electrolyte. These sub-domains are illustrated in Figure 7.1. Figure 7.1 also shows the dimensions that were modified between simulations.

Table 7.1. Model parameters

Electrode parameters	**Li_xC_6**	**Li_xCoO_2**
Reaction rate constant k, $m^{2.5}mol^{-0.5}s^{-1}$	4.9×10^{-11} [1]	2.8×10^{-10} [2]
Initial stoichiometric coefficient	0.01[3]	1[3]
Maximum concentration, mol m^{-3}	30540[3]	56250[3]
Diffusion coefficients, m^2s^{-1}	5.5×10^{-14} [2]	1.0×10^{-11} [2]
Transfer coefficients (α_a, α_c)	0.5[3]	0.5[3]
Electrolyte parameters		
Volume fraction	0.55[4]	
$LiPF_6$ initial concentration, mol m^{-3}	1200[3]	
Li^+ diffusion coefficient in liquid phase, m^2s^{-1}	8.39×10^{-11} [5]	

1. Arora et al., (1999); 2. Doyle and Fuentes (2003); 3. Tang et al., (2009);
4. Christensen et al., (2006); 5. Stewart and Newman, (2008)

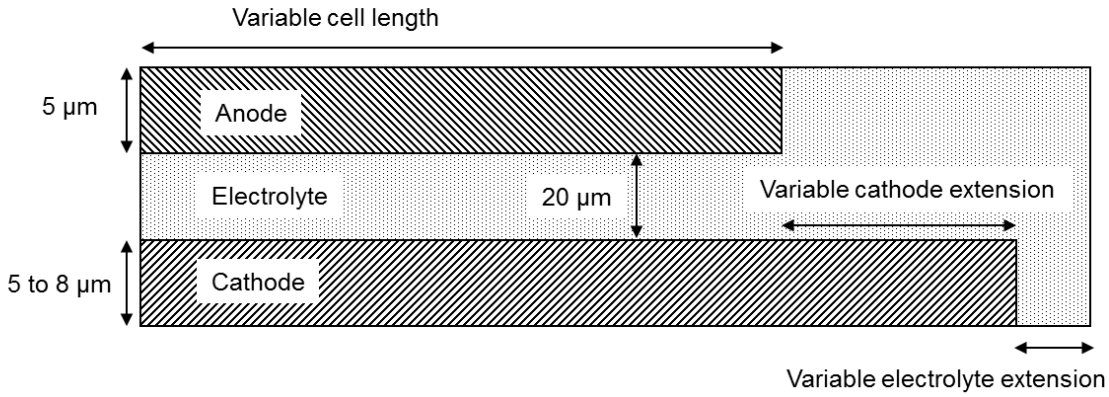

Figure 7.1. Lithium-ion cell (not to scale).

During charging of the lithium-ion cell electrochemical reactions cause the insertion of lithium from the electrolyte into the cathode and lithium from the anode is released into the electrolyte. These electrochemical reactions are assumed to follow Tafel kinetics:

$$i_a = i_{o,a} \exp\left(\frac{\alpha_{a,k} F}{RT} \left(\Phi_a - \Phi_e - U_a \right) \right) \tag{7.6}$$

In Equation (7.6), Φ_a represents the value of the uniform applied electric potential field in the anode, Φ_e represents the value of the electric potential in the electrolyte adjacent to the anode which is a function of time and space and calculated via Equation (7.2), and U_a represents the equilibrium potential of lithium in the anode. The insertion reaction for lithium into the cathode is also described using Tafel kinetics:

$$i_c = -i_{o,c} \exp\left(-\frac{\alpha_{c,k} F}{RT} \left(\Phi_c - \Phi_e - U_c \right) \right) \tag{7.7}$$

In Equation (7.7) the potentials, Φ_c and U_c, describe the applied electric potential of the cathode and the equilibrium potential of lithium in the cathode, respectively, and Φ_e represents the value of the electric potential in the electrolyte adjacent to the cathode. The equilibrium potentials of lithium in the electrodes are described as a function of lithium concentration. The equilibrium potential of lithium in the anode is described (Doyle and Fuentes, 2003):

$$U_a = 3.8552 + 1.2473\left[1-\left(\frac{C_s}{C_{t,a}}\right)\right] - 11.152\left[1-\left(\frac{C_s}{C_{t,a}}\right)\right]^2 + 42.8185\left[1-\left(\frac{C_s}{C_{t,a}}\right)\right]^3 - 67.711\left[1-\left(\frac{C_s}{C_t}\right)\right]^4 + 42.508\left[1-\left(\frac{C_s}{C_{t,a}}\right)\right]^5 - 6.132\times10^{-4}\exp\left[7.657\left(\frac{C_s}{C_{t,a}}\right)^{115}\right] \tag{7.8}$$

The equilibrium potential of lithium in the cathode is calculated (Arora et al., 1999):

$$U_c = 0.7222 + 0.13868\left(\frac{C_s}{C_t}\right) + 0.028952\left(\frac{C_s}{C_t}\right)^{0.5} - 0.017189\left(\frac{C_s}{C_t}\right)^{-1} + 0.0019144\left(\frac{C_s}{C_t}\right)^{-1.5} + 0.28082\exp\left\{15\left[0.06-\left(\frac{C_s}{C_t}\right)\right]\right\} - 0.79844\exp\left\{0.44649\left[\left(\frac{C_s}{C_t}\right)-0.92\right]\right\} \tag{7.9}$$

The exchange current density is calculated (Tang et al., 2009):

$$i_o = Fk\left(C_t - C_s\right)^{\alpha_j}\left(C_s\right)^{\alpha_c}\left(C\right)^{\alpha_a} \tag{7.10}$$

For both anode and cathode the applied electric potential fields, Φ_a and Φ_c, were determined such that:

$$\oint_{electrode} i_{Li}\,ds = I_{set}\,l_{electrode} \tag{7.11}$$

This ensures that equivalent amounts of Lithium ions are inserted and withdrawn from the electrolyte ensuring overall electroneutrality of the electrolyte; however, this approach allows for non-uniform charge density as a function of time and position within the electrolyte. The overall potential of the cell is calculated:

$$V_{cell} = \Phi_a - \Phi_c \tag{7.12}$$

Assumptions that were not made during the development of this model include: uniform electrolyte concentration, electroneutrality, uniform concentration in anode or cathode, nor linearized electrochemical reaction kinetics. Also, the potential along the edge of the electrodes is not assumed constant with time nor with position. Some of the assumptions made during model development are shown in Table 7.2.

Table 7.2. Assumptions made in model

1.	Solid film electrodes
2.	Tafel kinetics
3.	Irreversible capacity loss on first cycle neglected
4.	Film resistances on electrodes neglected
5.	Isothermal

7.3 Results and Discussion

7.3.1 Liquid-junctions

Although many approaches to modeling electrochemical systems are based on dilute solution theory and the assumption of bulk electroneutrality, the model presented in this chapter does not make this assumption. Instead, the effects of a non-isotropic electrolyte (including concentration gradients and charge density) on the electric field are accounted for. Evidence of this can be seen in Figures 7.2 and 7.3 showing electric potential gradients and electric potential fields. Figure 7.2 shows the predicted electric gradient across a one-dimensional 0.1 M $HCl_{<aq>}$ – $KCl_{<aq>}$ liquid-junction after one second of contact between the two electrolytes. The junction between the two electrolytes was simulated to be 1.4 cm from the left electrolyte boundary. The difference in electric potential across the junction in Figure 7.2 is -27.3 mV. Newman and Thomas-Alyea (2004) presented this value to be -27.31 mV as calculated using concentrated solution theory. Furthermore, this value from Figure 7.2 corresponds well with experimentally determined values: -27.08 mV (Chloupek et al., 1933) and -28.3 (Grahame and Cummings, 1950). An additional benefit to using Equation (7.2) to model the electric field is the ability for complex multi-dimensional predictions over large or small time periods involving charge density. Figure 7.3 shows the predicted electric field across a two-dimensional 0.1 M $HCl_{<aq>}$ – $KCl_{<aq>}$ liquid-junction after 0.01 seconds. For the simulation of Figure 7.3, one quadrant on the right contains 0.1 M $HCl_{<aq>}$ and the remaining three quadrants contain 0.1 M $KCl_{<aq>}$. The resulting dynamic electric field shows a -27 mV difference along the interface between the two electrolytes.

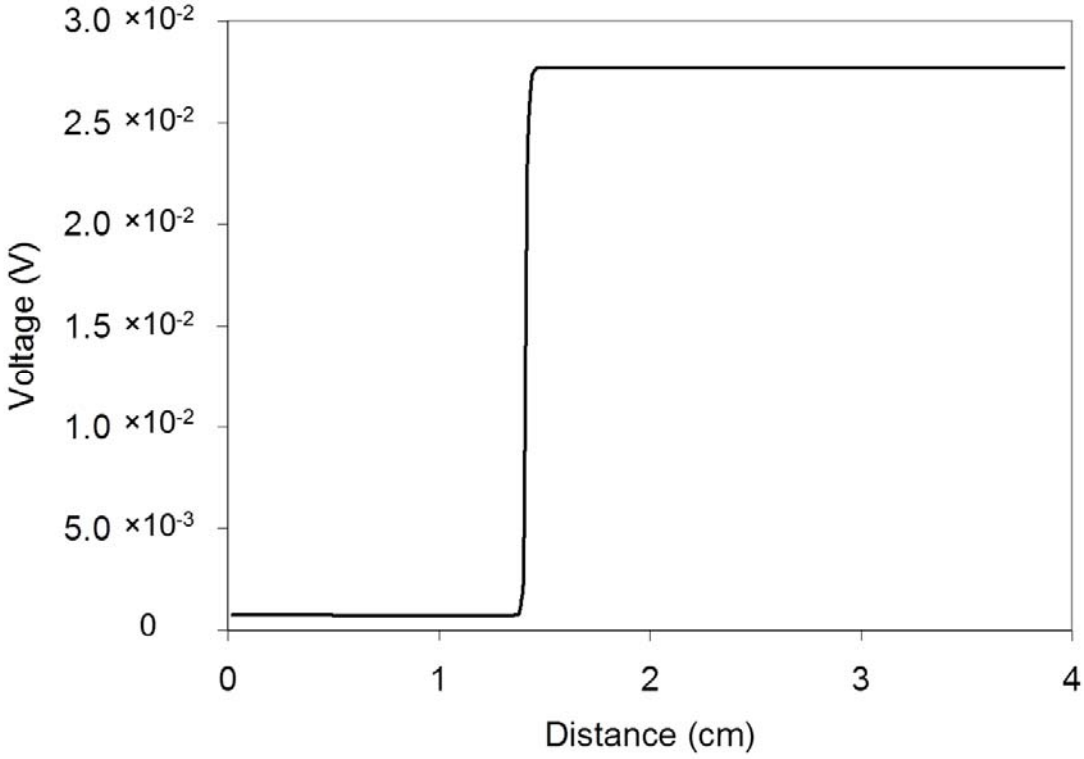

Figure 7.2. Electric potential across one-dimensional 0.1 M $HCl_{<aq>}$ – $KCl_{<aq>}$ liquid-junction after one second of contact.

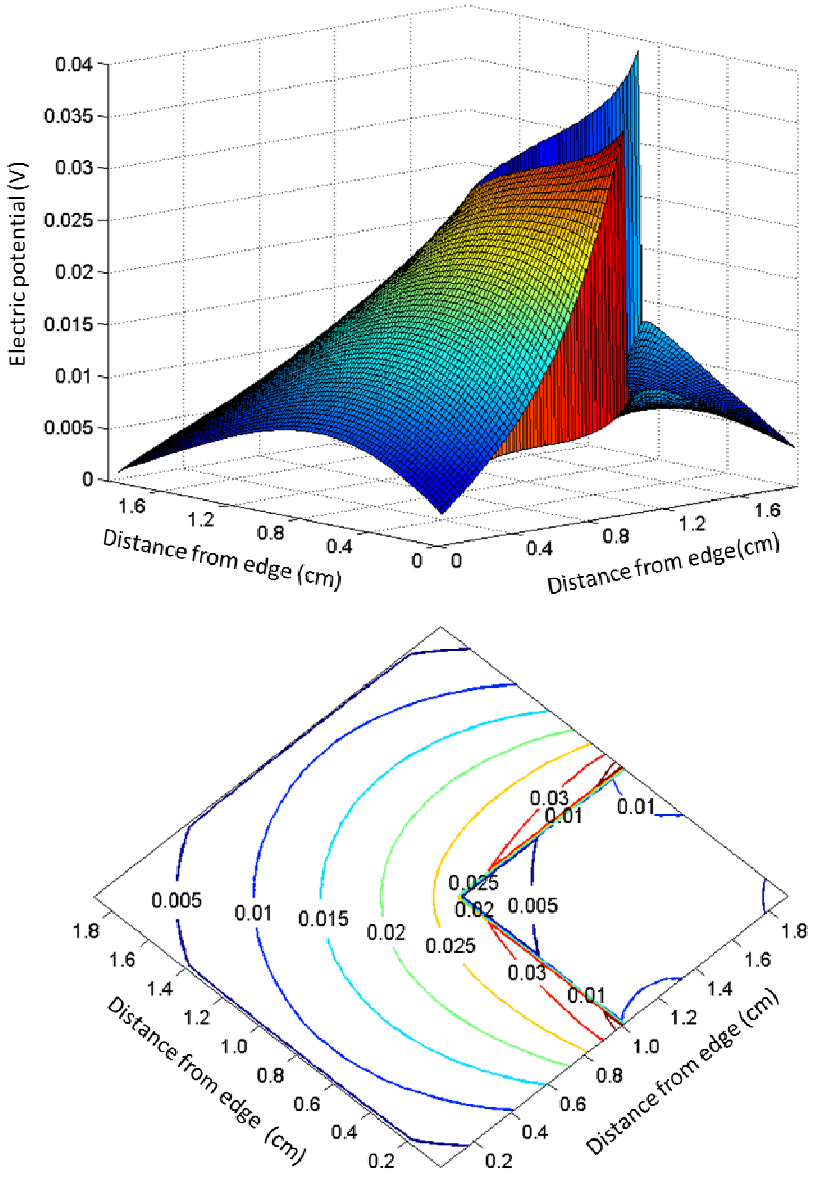

Figure 7.3. Electric potential across two-dimensional 0.1 M $HCl_{<aq>}$ – $KCl_{<aq>}$ liquid-junction after 0.01 seconds of contact.

Charge density is an important aspect of the simulations presented in this chapter. Equation (7.2) accounts for the effects of localized charge density on the overall electric field. During the simulation of Figure 7.2, charge density was predicted that caused the

one-dimensional electric potential gradient seen in Figure 7.2. This charge density, after one second of contact, is shown in Figure 7.4. Figure 7.4 shows significant charge density located at electrolyte boundaries only. The bulk electrolyte demonstrates electroneutrality, as expected, even though no assumption of bulk electroneutrality was made during model development.

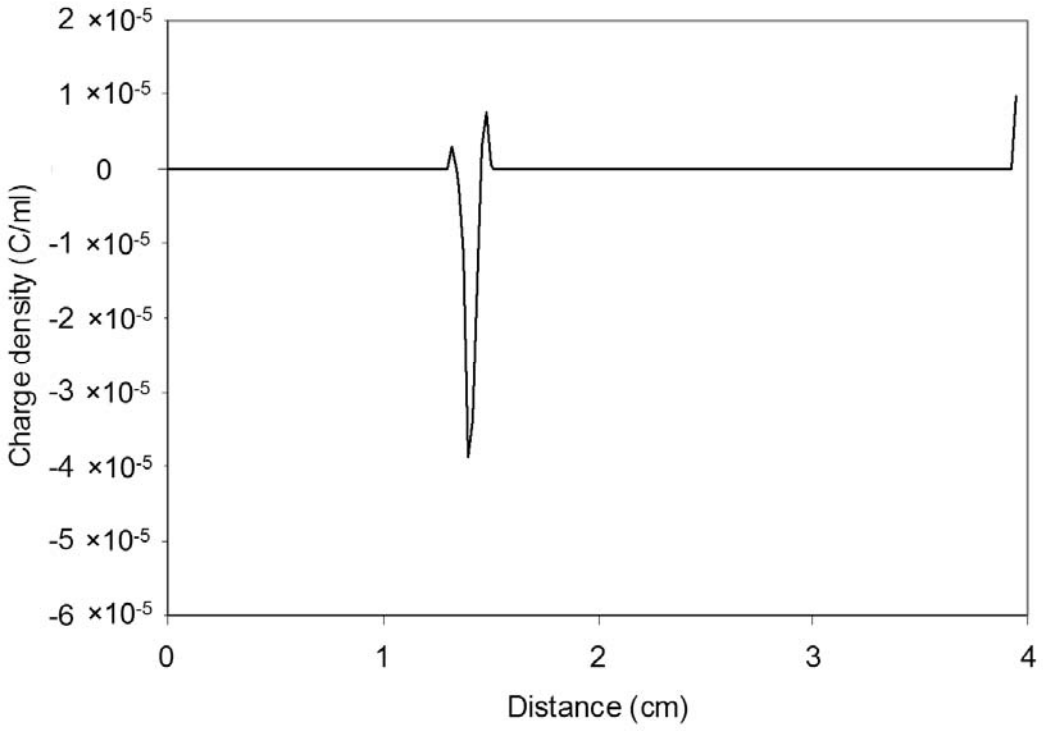

Figure 7.4. Charge density distribution across one-dimensional 0.1 M HCl<aq> – KCl<aq> liquid-junction after one second of contact.

7.3.2 Lithium-ion Cell with Equal Anode and Cathode Length

The previous results demonstrated that the governing equations presented in this Chapter account for the multi-dimensional electric interactions between charged species when concentration gradients are the main instigator of transport. The following results

demonstrate that these governing equations also prove beneficial for the case of spatially separated electrodes. Simulations were conducted for a lithium-ion cell geometry shown in Figure 7.1 where the cathode extension and the electrolyte extension were equal to zero. In other words, the lengths of the anode, cathode, and electrolyte were equivalent. This results in a cell where transport of Li^+ occurs in one dimension only, directly from the anode to the cathode, and in the electrodes themselves due to diffusion. A potential difference between the electrodes is expected that is uniform with length along the electrodes. The simulated electric potential field is shown in Figure 7.5. Figure 7.5 shows a steady-state electric field that was predicted at times greater than 5000 seconds during charging at 4.37 Am^{-2} (1 C). For the simulation presented in Figure 7.5, the anode and cathode widths were 5 μm. This corresponds to simulations conducted by Tang et al. (2009).

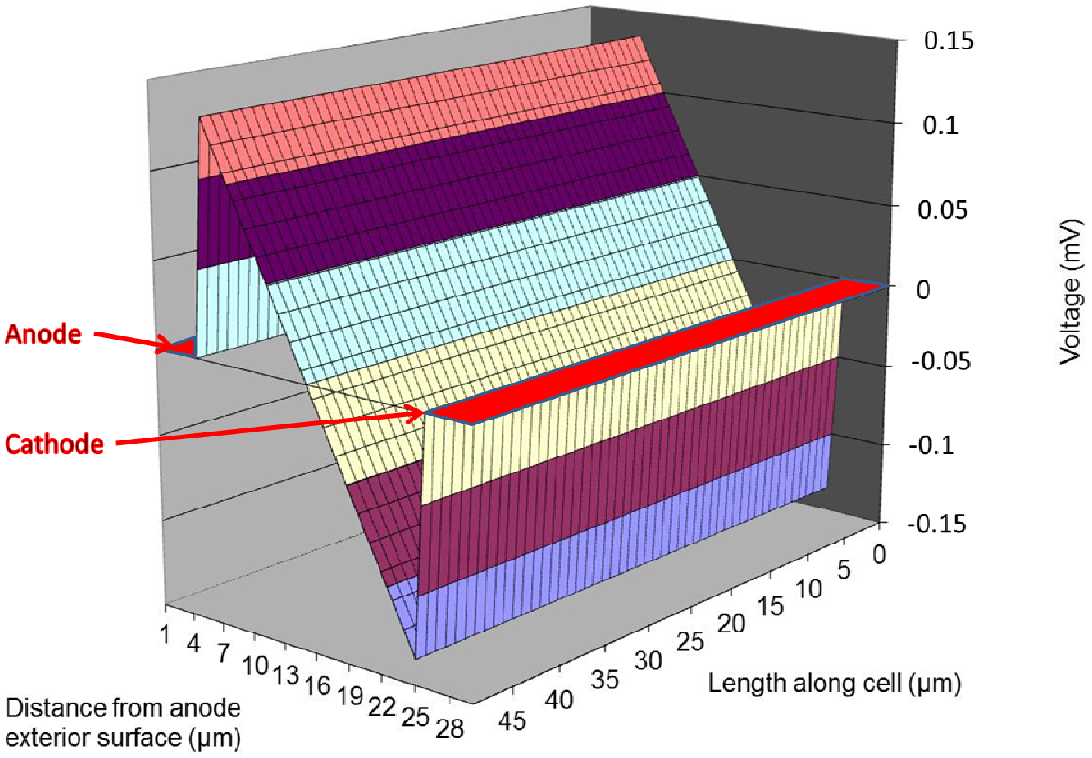

Figure 7.5. Potential field through the electrolyte of a lithium-ion cell with equal electrode and electrolyte lengths after steady-state was achieved. The width of the electrodes was 5 µm.

Figure 7.6 shows a comparison of the cell potential for the equal electrode length simulation presented in Figure 7.5 compared with the cell potential predicted by the model of Tang et al. for a cell of a similar geometry (except for edge effects). Figure 7.6 shows a reasonable correlation between the two predicted potentials. However, the model from this chapter predicts the cut-off potential of 4.2 volts is reached 42 seconds before the model of Tang et al. (2009). One possible reason for this is that although the geometries and currents investigated by the two model are similar, the geometry investigated by Tang et al. included edge effects of the electrodes. These edge effects may impact the overall cell potentials slightly. The model presented in this chapter will

also be used to investigate edge subsequently. It will be shown that the inclusion of the effects of charge density and non-uniform electrolyte composition allow for the prediction of an experimentally observed phenomenon that was not reported in the predictions of Tang et al. The simulation of this phenomenon is possible because assumptions of electroneutrality and uniform concentrations were not made. Figure 7.7 shows the one-dimensional charge density distribution across the electrolyte from the anode interior surface to the cathode interior surface as predicted for the simulation of Figures 7.5 and 7.6. Figure 7.7 shows a charge density distribution that (when coupled with the concentration gradient effects and the effects of electrochemical reactions) causes the steady-state electric potential gradient seen in Figure 7.5. It should be noted that the nodes closest to the electrode edges are greatly affected by the electrochemical reactions occurring on electrode surfaces. This is the reason why these nodes display a charge density of opposite sign to adjacent nodes.

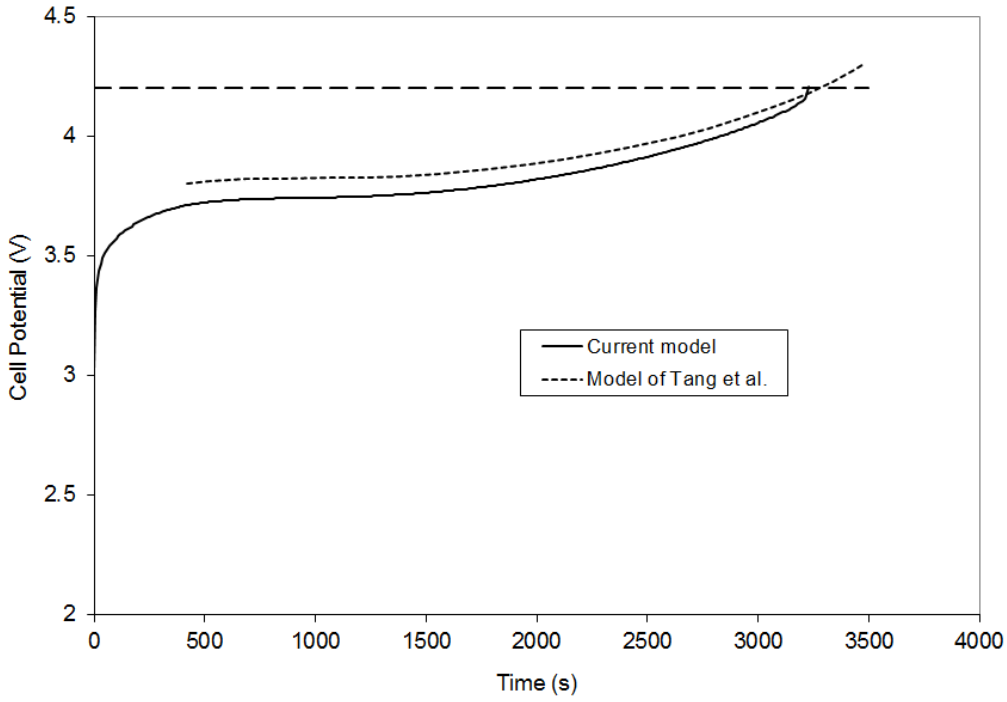

Figure 7.6. Predicted cell voltage for lithium-ion cell with equal electrode and electrolyte lengths, and electrode widths of 5 μm.

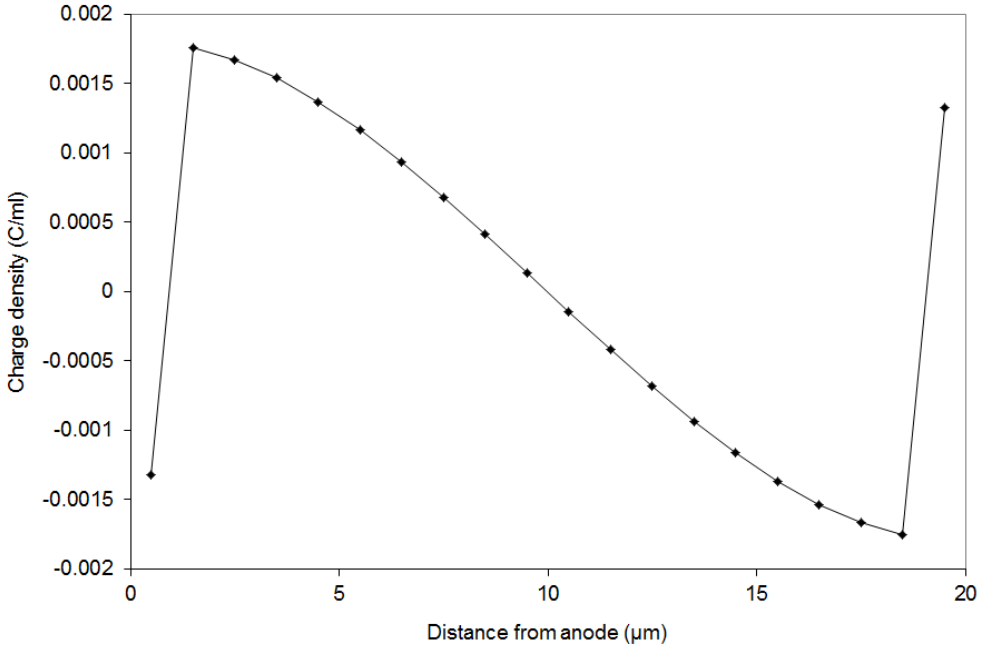

Figure 7.7. Steady-state charge density distribution across the electrolyte in a lithium-ion cell with equal electrode and electrolyte lengths, and electrode widths of 5 μm.

7.3.3 Lithium-ion Cell with Edge Effects (Flooded Cell)

The model presented in this chapter may also simulate a lithium-ion cell where edge effects are present. Figure 7.8 shows the electric field for the case of a lithium-ion cell with electrodes of equal length and the flooded electrolyte is extended 10 μm past the end of the electrodes after 140 seconds. The cell current was prescribed to be 4.37 Am^{-2} and the width of the cathode was 6 μm. Figure 7.8 shows how an electric field is created that causes the transport of lithium ions from the anode to the cathode. It can also be seen that the electric field along the face of the electrodes is affected by the electrode edges; along the face, near to the edge, the electric field is no longer uniform with cell length. In fact, the slight gradients along the cell length will cause the transport of lithium towards the cell edges. It was seen during this simulation that the greater accessibility of the cathode edge, and the higher surface area associated with the edge, caused a higher concentration of lithium in the cathode at the edge. This higher concentration caused a situation where lithium deposition was more likely at the cathode edge, especially near the end of the charge cycle just before the overall cell cutoff potential was reached. This simulated phenomenon is similar to the phenomenon simulated by Tang et al. (2009) and will therefore not be explored in this chapter. Instead, the phenomenon of anomalous potentials at the start of cell charging not reported by Tang et al. and experimentally observed by Scott et al. (2003a) will be explored.

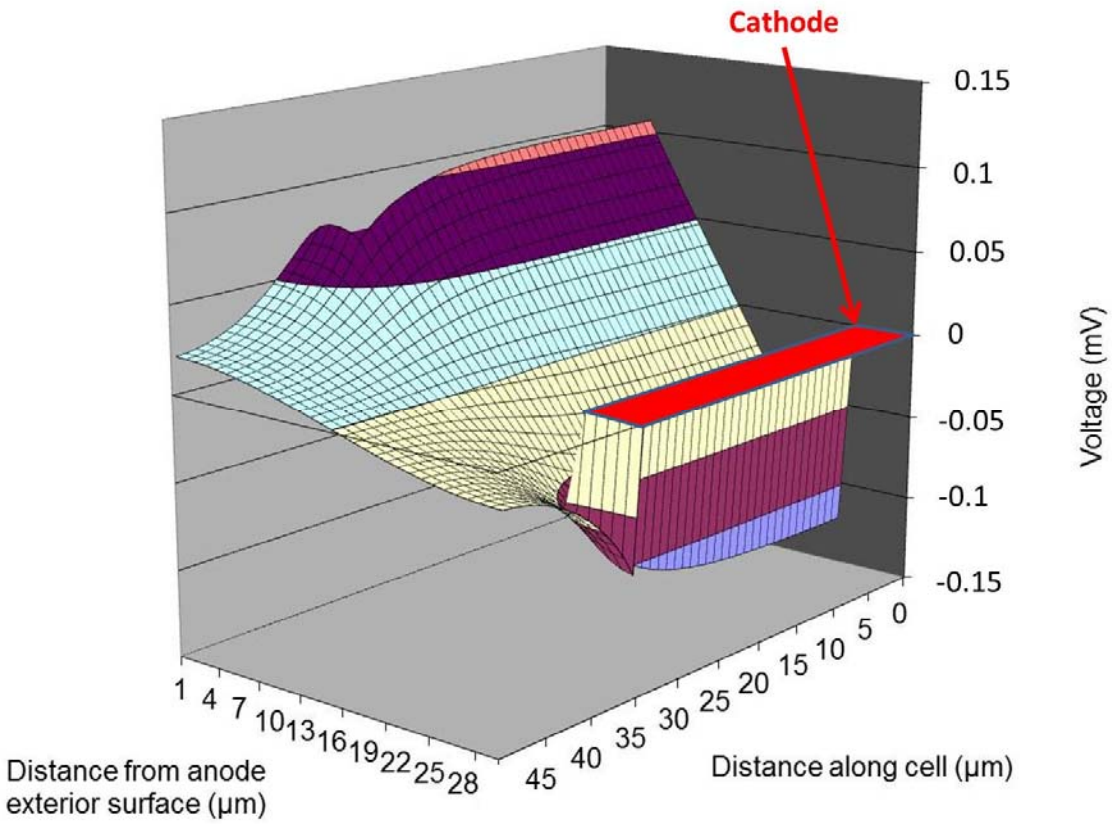

Figure 7.8. Electric potential field across the electrolyte in a lithium-ion cell after 140 seconds where the electrolyte is extended 10 μm past the equal length electrodes. The width of the cathode was 6 μm.

7.3.4 Lithium-ion Cell with Cathode Extension

The effect of current and potential drops parallel to electrodes is greatly increased if the length of the cathode is increased significantly beyond the edge of the anode, as is common during lithium-ion cell preparation (Scott et al., 2003b). This extension has been seen to reduce the chance of lithium deposition towards the end of the cell charging period (Tang et al., 2009), but it may have other side-effects (Scott et al., 2003a). Figure 7.9 shows the simulated potential field after 80 seconds corresponding to the case where the cathode (8 μm thickness) is extended 30 μm past the anode edge and the anode undergoes 1 C charging (4.37 Am^{-2}). Figure 7.9 shows an electric field

that will transport a significant quantity of lithium-ions from the part of the cell with an adjacent anode through the electrolyte towards the part of the cell with extended cathode and no adjacent anode. The electric field causes this transport via migration. However, lithium-ions are also transported through the electrolyte towards the extended cathode via diffusion. Figure 7.10 shows the concentration field of lithium-ions for the case presented in Figure 7.9. Figure 7.10 shows that the absence of an adjacent anode parallel to the extended cathode causes the lithium-ion concentration in this region to be reduced. This is because lithium-ions in this region are consumed from the electrolyte via insertion into the cathode without the accompanying dissolution from an adjacent anode. Instead, lithium-ions must diffuse and migrate from accessible regions of the anode. The electric field associated with the migration of lithium-ions towards the edge is shown in Figure 7.9 and is lower towards the cathode edge. Interestingly, this lower electrolyte potential adjacent to the cathode edge, Φ_e, causes the rate of electrochemical insertion of lithium into the cathode to be reduced towards the cathode edge (Equation (7.7)). Therefore, it is expected that as the length of the cathode extension is increased, the potential gradient needed to transport lithium-ion towards the edge will increase (because of the iR drop), and the rate of lithium insertion towards the edge will decrease. This decrease in lithium insertion along the extended cathode causes a localized galvanic cell and concentration gradients within the cathode, driven by the electric field associated with lithium-ion concentration gradients in the electrolyte. These concentration gradients within the cathode support the electric field in the electrolyte. Essentially, these multiple phenomena occur simultaneously and one symptom is the large electric potential drop in the electrolyte. This phenomenon has

been seen experimentally (Scott et al., 2003a), but has not previously been successfully modeled.

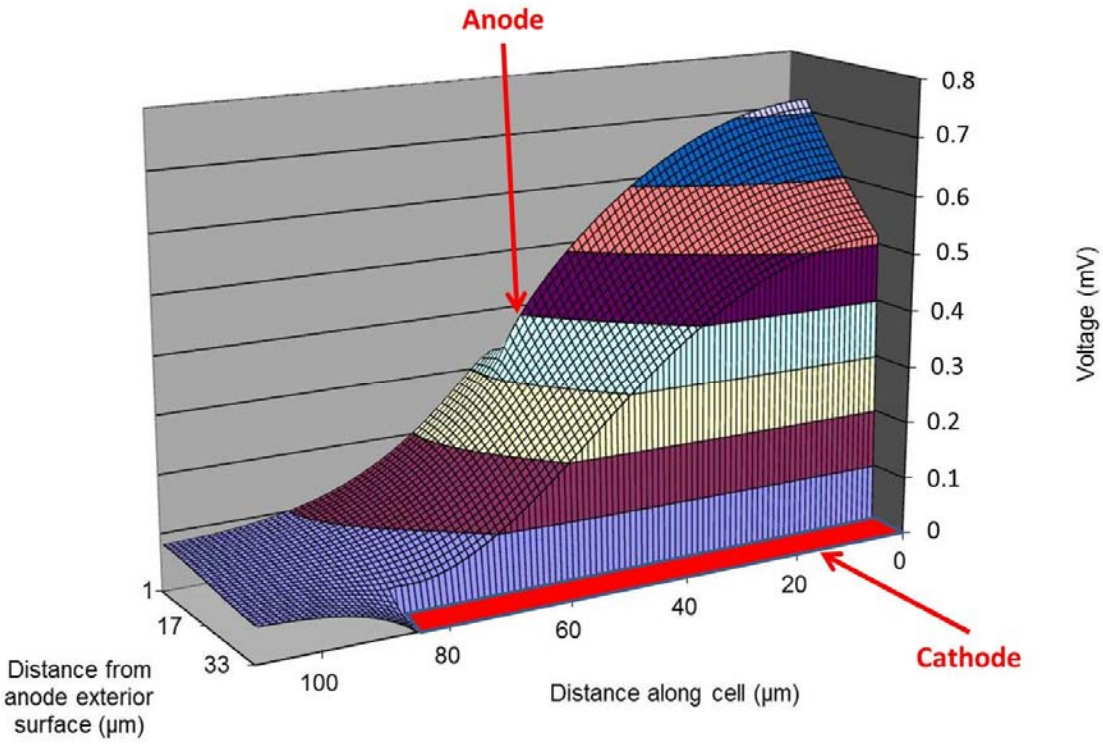

Figure 7.9. Electric potential field after 80 seconds for the situation where the cathode is extended 30 µm past the anode edge. A uniform mesh was used and a cathode thickness of 8 µm.

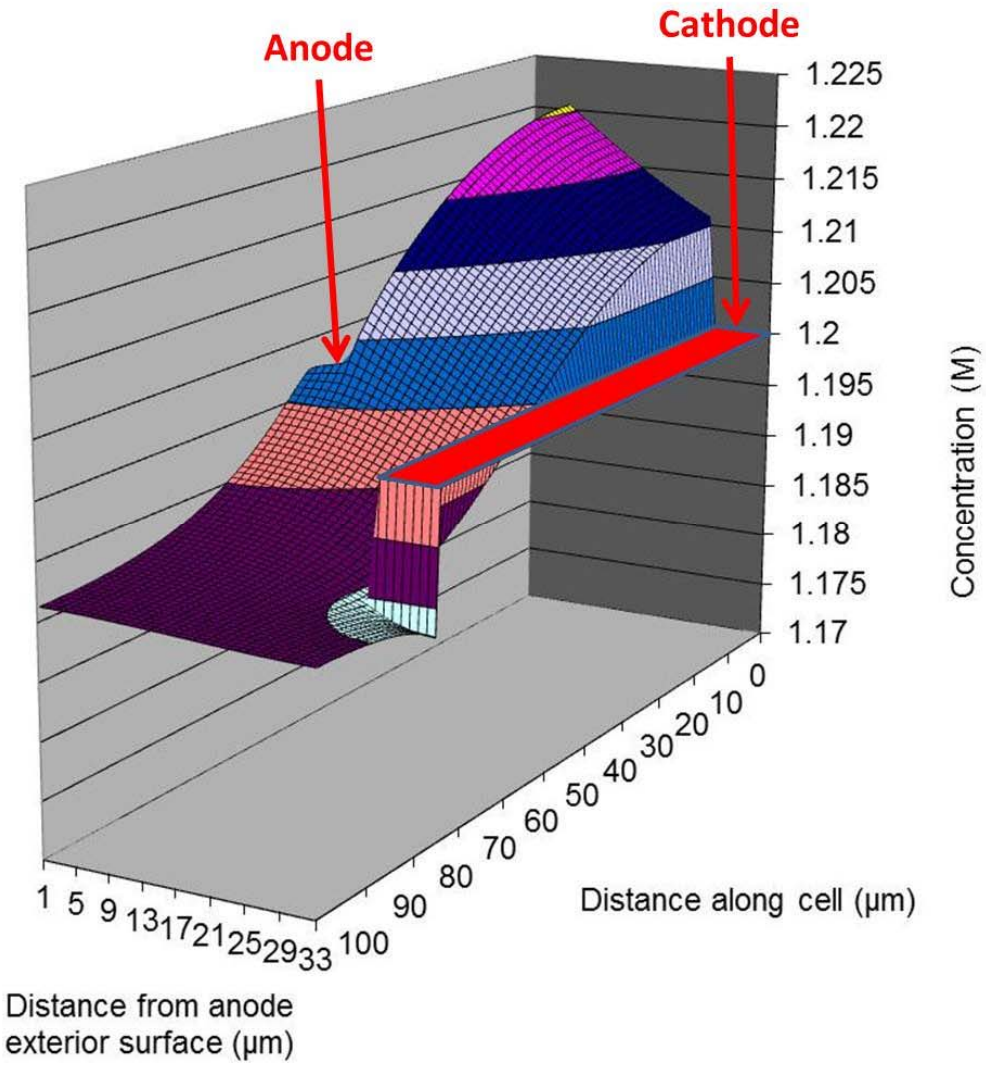

Figure 7.10. Li concentration after 80 seconds for the situation where the cathode is extended 30 µm past the anode edge. A uniform mesh was used and a cathode thickness of 8 µm.

To further model the effects of extending the cathode past the anode a non-uniform mesh was used. This allowed for a cluster of nodes in areas of significant multi-dimensional currents and a more sparse arrangement in areas where the electric current was mainly in one-dimension. In this manner, the length of the cell being modeled was

increased to 25 cm. The extension of the cathode past the anode was increased to 2.5 mm, and the extension of the electrolyte past the edge of the cathode was increased to 1 mm. A galvanic cell, iR drop through the electrolyte, and other phenomena similar to the case for a 30 μm cathode extension were predicted. However, because of the greater cathodic extension, the magnitude of these predicted phenomena was greater. Figure 7.11 shows the predicted potential drop along the center of the electrolyte with distance along the cell length. Since the electric potential difference through the electrolyte perpendicular to the electrodes was only approximately 3 mV, these potential gradients were excluded in a one-dimensional plot. Figure 7.11 shows a difference in electric potential between the cathode edge and the main portion of the cell of approximately 0.45 V, about half of the maximum value seen experimentally by Scott et al. (2003a). However some dimensions and properties associated with the experimental lithium-ion cell of Scott et al. (2003) were unknown. Since simulation parameters and properties were not exactly matched with those of Scott et al., this simulation does not represent a validation of the model. Instead, this simulation demonstrates that the model presented in this chapter is able to model the phenomenon seen experimentally, due to the cathode extension in a lithium-ion cell, for the first time.

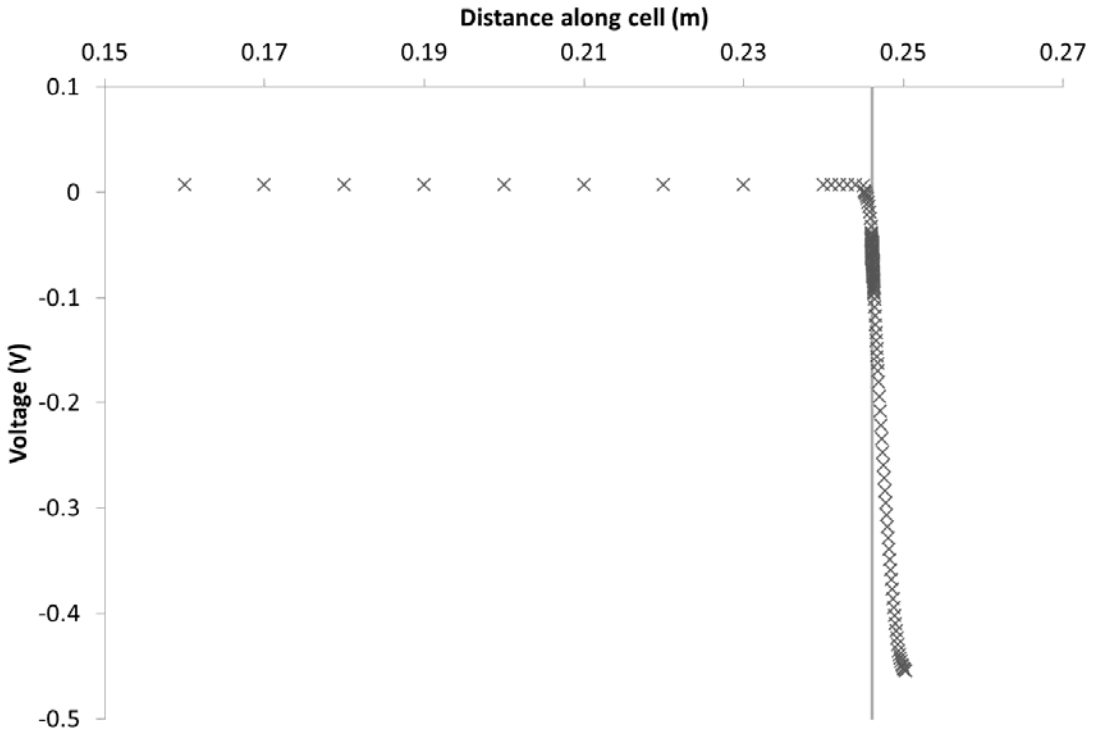

Figure 7.11. Electric potential drop along the center of the electrolyte for a lithium-ion cell with cathode extended 2.5 mm past the anode after 400 seconds. The electrolyte width was 20 µm and the electrolyte was extended 1 mm past the cathode edge. The anode and cathode widths were 5 µm and 8 µm, respectively. The position of the anode edge is demarked by the vertical line.

7.4 Conclusions

Benefits of assuming neither electroneutrality nor uniform concentration gradients are presented by investigating predictions made for two systems. The first system investigated was that of a 0.1 M $HCl_{<aq>}$ – $KCl_{<aq>}$ liquid-junction. It was shown how the electric field balanced with charge density at electrolyte boundaries corresponded well with values calculated and experimentally measured by other researchers. It was also shown how this model is able to extend such successful simulations into two-dimensions whilst only using a single prescribed transport property for each dissolved species: the diffusion coefficient.

The second system investigated in this chapter was that of a charging lithium-ion cell. It was shown how inclusion of concentration and charge density effects allowed for the prediction of a phenomenon experimentally seen early during cell charging. This phenomenon is associated with edge effects and the extension of the cathode past the edge of the anode. Although simulation parameters were not exactly matched with the unreported parameters of the experiment, a potential drop about half of the maximum experimental potential drop was predicted.

7.5 Recommendations

Since the results presented in this chapter demonstrate the Inherent Charge Density Model can simulate the phenomenon causing the large potential drops along the length of the electrolyte in a charging lithium-ion cell with extended cathode, it would be beneficial to predict the dependence of current distributions and electric fields on the stoichiometric coefficient of lithium inserted into electrodes.

8. APPLICATION OF THE NEW THEORY – PART II: TWO-DIMENSIONAL LITHIUM-ION BATTERY MODELING AND ELECTRODE CONCENTRATION GRADIENT EFFECTS ON THE ELECTRIC FIELD IN THE ELECTROLYTE

The universal electrolyte model developed in Chapter 6 and applied in Chapter 7 is further applied to the case of a charging lithium-ion cell to investigate the effects of gradients of lithium concentrations within electrodes. The gradients of lithium concentrations within electrodes are affected by the cell geometry. Different geometries are investigated, including extending the electrolyte past the edges of the electrodes and extending the cathode past the edge of the anode. It is found that the electrolyte extension has little impact on the behavior of the electrodes, although it does increase the effective conductivity towards the electrode edges by a small amount. However, the extension of the cathode past the edge of the anode, and the existence of electrochemical reactions on the flooded edges of the electrodes, are both found to impact the concentration gradients of lithium in electrodes and the current distribution within the electrolyte.

8.1 Introduction

Lithium-ion cells store and release energy via the emission, transport and insertion of lithium-ions from/into electrode materials at different electrochemical potentials. This difference in potential may be because the electrodes are comprised of different materials, because of an externally applied electric potential, and/or may also be because

of the stoichiometric coefficient of lithium already present in the electrodes. At the ends of electrodes are edges. Lithium-ions may be produced and consumed at these edge regions if they are in contact with the electrolyte, such as when the electrolyte is flooded. At flooded electrode edges the properties of the edges may cause multi-dimensional effects, such as concentration gradients in the electrolyte and the electrodes, and also electric potential gradients in the electrolyte.

It has previously been found that negative consequences to the cell performance may arise due to the concentration gradients associated with the flooded electrode edges. These negative consequences include the increased risk for lithium deposition at the cathode edge region. Therefore, the cathode edge may be extended past the anode edge to reduce the likelihood of lithium deposition at the cathode edge region; however, this may result in a new set of negative consequences. Some of these consequences were experimentally observed by Scott et al. (2003a, 2003b), and include the observation of a relatively large electric potential drop through the electrolyte, parallel to the electrodes, and associated with the extended cathode edge.

A number of mathematical models have been used to model lithium-ion cells where transport is modeled one-dimensionally between the bulk anode and cathode and were reviewed in Chapter 7. These one-dimensional models are not able to model the multi-dimensional edge effects. Tang et al. (2009) presented a two-dimensional model for the investigation of lithium deposition. They utilized a COMSOL Multiphysics model (based on dilute solution theory) to explain why extending the cathode edge may decrease the tendency for lithium deposition during cell charging. Some of the assumptions made by Tang et al. were: constant and uniform electrolyte concentrations

and conductivity, uniform anode concentration with respect to position, linearized Tafel kinetics, solid film electrodes, and electrolyte electroneutrality. Tang et al. showed that for their assumptions, a cathodic extension of 0.4 mm is sufficient to prevent the onset of lithium deposition. Eberman et al. (2010) used a two-dimensional model based on concentrated solution theory to model the effects of a cathode under-lap (the opposite to a cathode extension). Eberman et al. used this model to conduct a sensitivity analysis of various factors on the risk for lithium deposition. They found the three most significant factors affecting the risk of deposition to be: the open-circuit potential, the size of the underlap, and the charge rate. Kennell and Evitts (2011) (Chapter 7) presented a two-dimensional model for the concentrations, current distributions, and electric field as a function of time, in a lithium-ion cell. Kennell and Evitts demonstrated that, by neglecting few properties, it was possible to predict not only the lithium deposition at the cathode edge at later charging times, but also the large electric gradients experimentally seen along the electrolyte by Scott et al. (2003a, 2003b) during early charging. These large electric gradients during early cell charging were not presented for previous two-dimensional lithium-ion battery models. The model of Kennell and Evitts made a number of assumptions similar to Tang et al. (2009), however, the following assumptions were not made: constant and uniform electrolyte concentrations and conductivity, uniform anode concentration with respect to position, nor electrolyte electroneutrality. Instead, electrolyte concentrations and conductivities were predicted dependent on time and position, and anodic lithium concentrations were predicted dependent on time and position. Kennell and Evitts demonstrated how not making the electroneutrality assumption was beneficial to different simulations, including those

pertaining to a lithium-ion cell (2011). This paper further explains the model of Kennell and Evitts and uses the model to investigate the effects of electrode concentration gradients associated with equal and extended edges.

8.2 Theory

Lithium-ion cells are modeled using two governing equations where fluid bulk velocity has been neglected (Kennell and Evitts, 2010b):

$$\frac{\partial C_i}{\partial t} - \left(z_i u_i F \nabla \Phi\right) \cdot \nabla C_i = D_i \nabla^2 C_i + S_i \tag{8.1}$$

$$\nabla^2 \Phi = -\frac{F}{\kappa} \nabla \cdot \sum_i z_i D_i^{eff} \nabla C_i - \frac{F}{\kappa} \sum_i z_i S_i + \frac{F}{\kappa} \frac{\partial}{\partial t} \left(\sum_i z_i C_i \right) \tag{8.2}$$

Equation (8.1) may be used to describe the transport of species due to diffusion and migration. Equation (8.1) also contains a term for the source or sink of species due to reactions. Because Equation (8.1) was developed for discretization using the Control Volume technique, and an up-winding scheme, it omits one term that would be present in an equation developed for use with alternative methods: $-\left(z_i u_i F \nabla^2 \Phi\right) C_i$. This application of Equation (8.1), using the Control Volume technique, also ensures the conservation of charge and mass due to transport. Equation (8.2) describes the Laplacian of potential due to diffusion potential, spatially separated anodic and cathodic reactions, and charge density. When this equation is applied over a time interval the sign of the last term is changed and a system of i+1 equations are available for solving for i species concentrations and the electric field. This system of equations is advantageous when compared to equation sets containing Poisson's equation,

$\nabla \cdot (\varepsilon \nabla \Phi) = -F \sum_i z_i C_i$, because it is not numerically stiff. The effective diffusion coefficient was calculated:

$$D^{eff} = D\beta^{1.5} \tag{8.3}$$

Values for diffusion coefficients and other model parameters are the same as those presented in Table 7.1. Conductivity was assumed non-uniform with time and position:

$$\kappa = F^2 \sum_i z_i^2 u_i C_i \tag{8.4}$$

The calculation of conductivity requires the species mobility. For the calculation of species mobilities the Nernst-Einstein equation was used:

$$D_i = RTu_i \tag{8.5}$$

The lithium-ion cell was assumed to consist of a plasticized electrolyte sandwiched between two solid electrodes. Figure 8.1 shows the cell geometry and the aspects that were modified between simulations; the extension of the cathode edge beyond the anode edge, and the electrolyte edge beyond the cathode edge, were varied. This allowed for the numerical domain to be split into three parts: the cathode, the anode, and the electrolyte. These three domains were solved concurrently, where charged species were assumed to exist in the plastic electrolyte, but not in the solid electrodes. This allowed for the simplification of Equation (8.1) inside the electrodes:

$$\frac{\partial C_i}{\partial t} = D_i \nabla^2 C_i + S_i \tag{8.6}$$

where the electric potential field inside each electrode was assumed to be uniform and equal to an applied value, Φ_a or Φ_c, depending on the electrode. The boundary

condition used for all boundaries of each of the three numerical domains for Equation (8.1) or (8.6) was:

$$\frac{\partial C_i}{\partial x} = 0 \tag{8.7}$$

and the boundary condition used for Equation (8.2) at all electrolyte boundaries was:

$$\frac{\partial \Phi}{\partial x} = 0 \tag{8.8}$$

During charge and discharge, charge and mass are transported between the three numerical domains via the source terms in Equations (8.1), (8.2), and (8.6). The following development will describe how the source terms are calculated as being dependent on electrochemical reactions, how charge and mass are conserved, and how the overall cell potential is determined.

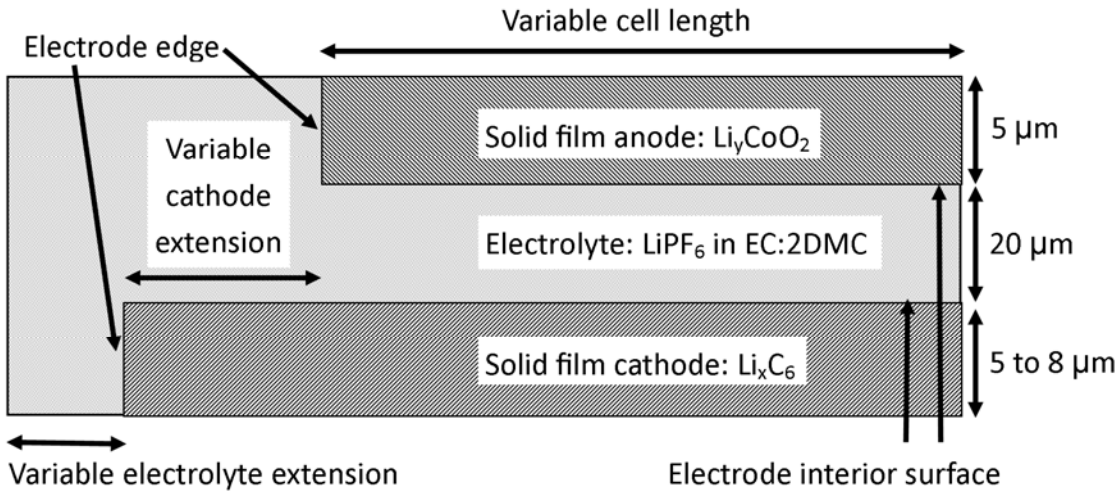

Figure 8.1. Cell configuration (not to scale).

The rates of electrochemical reactions are assumed to follow Tafel kinetics for the anode and cathode:

$$i_a = i_{o,a} \exp\left(\frac{\alpha_{a,k} F}{RT}\left(\Phi_a - \Phi_e - U_a\right)\right) \tag{8.9}$$

$$i_c = -i_{o,c} \exp\left(-\frac{\alpha_{c,k} F}{RT}\left(\Phi_c - \Phi_e - U_c\right)\right) \tag{8.10}$$

where Φ_e represents the electric potential of the electrolyte adjacent to the electrode. Φ_e is calculated from Equation (8.2), and is considered non-uniform with time and position. U_a and U_c represent the equilibrium potential of the anode and cathode respectively, as a function of lithium stoichiometric coefficient. The equilibrium potential in the anode is calculated (Doyle and Fuentes, 2003):

$$\begin{aligned} U_a = {} & 3.8552 + 1.2473\left[1 - \left(\frac{C_s}{C_{t,a}}\right)\right] - 11.152\left[1 - \left(\frac{C_s}{C_{t,a}}\right)\right]^2 + 42.8185\left[1 - \left(\frac{C_s}{C_{t,a}}\right)\right]^3 \\ & - 67.711\left[1 - \left(\frac{C_s}{C_t}\right)\right]^4 + 42.508\left[1 - \left(\frac{C_s}{C_{t,a}}\right)\right]^5 - 6.132 \times 10^{-4} \exp\left[7.657\left(\frac{C_s}{C_{t,a}}\right)^{115}\right] \end{aligned} \tag{8.11}$$

The equilibrium potential in the cathode is calculated (Arora et al., 1999):

$$\begin{aligned} U_c = {} & 0.7222 + 0.13868\left(\frac{C_s}{C_t}\right) + 0.028952\left(\frac{C_s}{C_t}\right)^{0.5} - 0.017189\left(\frac{C_s}{C_t}\right)^{-1} \\ & + 0.0019144\left(\frac{C_s}{C_t}\right)^{-1.5} + 0.28082 \exp\left\{15\left[0.06 - \left(\frac{C_s}{C_t}\right)\right]\right\} \\ & - 0.79844 \exp\left\{0.44649\left[\left(\frac{C_s}{C_t}\right) - 0.92\right]\right\} \end{aligned} \tag{8.12}$$

The exchange current density from Equations (8.9) and (8.10) is calculated (Tang et al., 2009):

$$i_o = Fk\left(C_t - C_s\right)^{\alpha_j}\left(C_s\right)^{\alpha_c}\left(C\right)^{\alpha_a} \tag{8.13}$$

Figure 8.2 shows the equilibrium potentials of the electrodes described by Equations (8.11) and (8.12) where the anode is fabricated from Li_yCo_2 and the cathode from Li_xC_6. The solid lines in Figure 8.2 represent the portion of the equilibrium potentials that correspond to the stoichiometric coefficient likely to exist in a lithium-ion cell. In other words, the solid part of the line for Li_yCo_2 corresponds to the stoichiometric coefficient of between 0.99 and 0.58 (in the anode) and the solid part of the line for Li_xC_6 corresponds to the stoichiometric coefficient of between 0.01 and 1 (in the cathode).

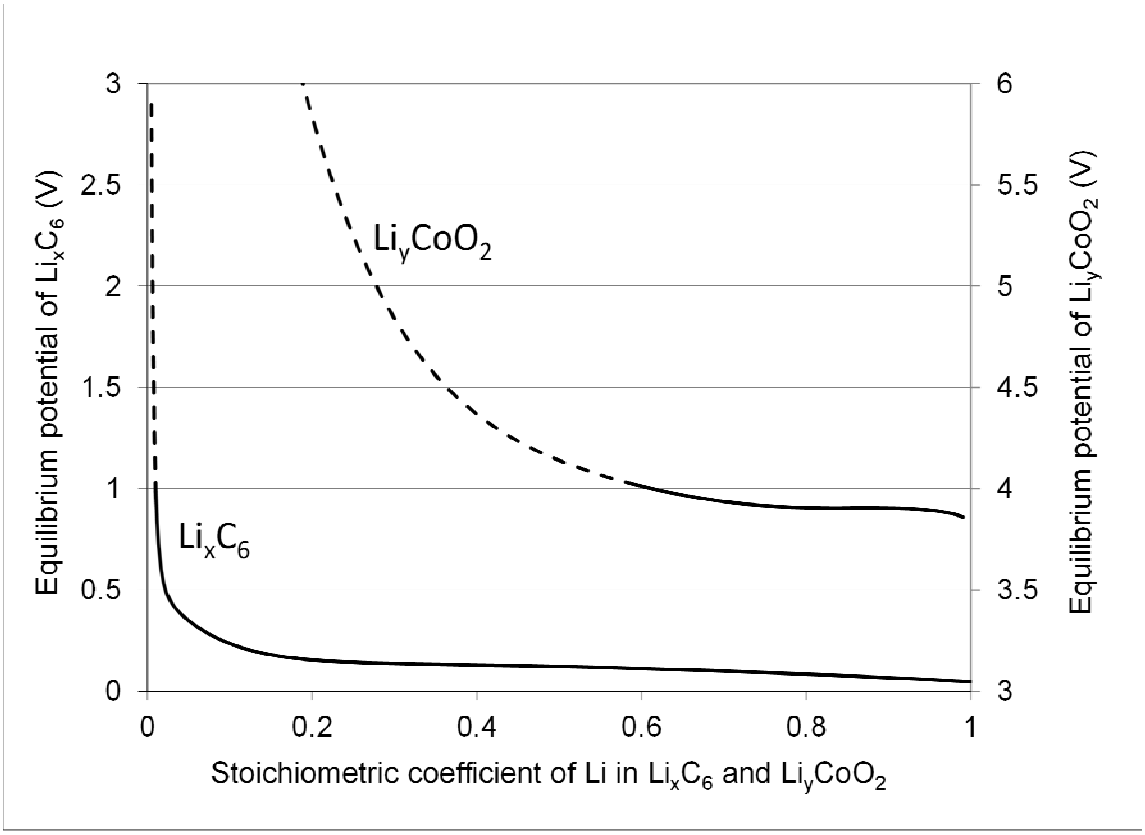

Figure 8.2. Equilibrium potential of electrode as a function of stoichiometric coefficient.

The rates of electrochemical reactions are converted into source terms. If it is assumed that at the surface of the electrode the currents described by Equations (8.9) and (8.10) are perpendicular to the electrode surface, the current vector describing the electrochemical reaction rate, $\mathbf{i}_i$, is produced. This current vector is converted into a source term for use with Equations (8.1), (8.2), and (8.6):

$$S_i = \frac{\nabla \cdot \mathbf{i}_i}{z_i F} \tag{8.13}$$

Therefore, the species produced by electrochemical reactions are introduced into the numerical procedure via the source terms in Equations (8.1), (8.2) and (8.6), and the simple boundary conditions shown as Equations (8.7) and (8.8) are used at all boundaries. The conservation of charge and mass across numerical boundaries is guaranteed by ensuring the sum of each electrochemical reaction along the length of the electroactive surface is equal to a prescribed current:

$$\oint_{electrode} i_{Li} ds = I_{set} l_{electrode} \tag{8.14}$$

Equation (8.14) is satisfied by modifying the rates of electrochemical reactions by varying the applied electric potentials, Φ_a and Φ_c. Then, the overall cell potential may be calculated:

$$V_{cell} = \Phi_a - \Phi_c \tag{8.15}$$

It should be noted that the model presented in this chapter does not assume insignificant concentration gradients in either the electrodes or the electrolyte. The model also does not assume electroneutrality, although overall cell electroneutrality is maintained through equal but opposite sums of electrochemical reactions occurring on the surfaces of electrodes.

8.3 Results and Discussion

Lithium-ion cells depend upon the transport of Li^+. Li^+ may be transported through an electrolyte because of different equilibrium potentials of electrodes. Different equilibrium potentials may be caused by different electrode materials and equilibrium potentials are also dependent on the stoichiometric coefficient of inserted lithium. The different electrode materials investigated in this paper are Li_yCoO_2 and Li_xC_6. The equilibrium potentials corresponding to different stoichiometric coefficients in each of these materials were presented in Figure 8.2. Simulations presented in this paper investigate not only the electric potentials established between the anode and cathode of a lithium-ion cell, but also the electric potentials that may exist parallel to the electrodes and caused by gradients of stoichiometric coefficients within the electrodes, as seen experimentally by Scott et al. (2003a, 2003b). The cell geometries investigated in the simulations presented in this paper are shown in Figure 8.1. The electrodes are considered solid film electrodes and the separator a plasticized 1.2 M $LiPF_6$ in EC:2DMC electrolyte. Further details are given in Table 1, including the locations of electrode edges and interior surfaces.

8.3.1 Equal length electrodes without edge reactions

Figure 8.3 shows the predicted electric field for the case where the anode and cathode are of equal length and the electrolyte is extended past the edges of the electrodes by 25 μm and the cell undergoes 4.37 Am^{-2} charging for 60 seconds. However, the simulation presented in this figure assumes that only the interior surfaces of the electrodes are electroactive. In other words, the edges of the electrodes do not emit or insert any

lithium-ions. This means that the increased surface area due to electrode edges does not have an impact on the overall rate of electrochemical reactions around the edge. Therefore, in this case, the main edge effect is the greater effective conductivity of the electrolyte towards the edge, caused by the electrolyte extension. The effect of this electrolyte extension on the predicted electric current distribution can be seen in Figure 8.4. This figure demonstrates how the electric current tends to move across the electrolyte directly from the anode to the cathode in the bulk interior of the cell (at larger distances from the edge); however, in the electrolyte nearer the edges of the electrodes it can be seen from Figure 8.4 that the electric current does not go directly from the anode to cathode. Instead, the current tends to spread out into the extended electrolyte region that would otherwise contain no current density. In other words, the extended electrolyte region has the effect of increasing the effective conductivity of this area. This increase in effective conductivity and reduced current densities near the edge region leads to a lower electric potential gradient, as seen in Figure 8.3.

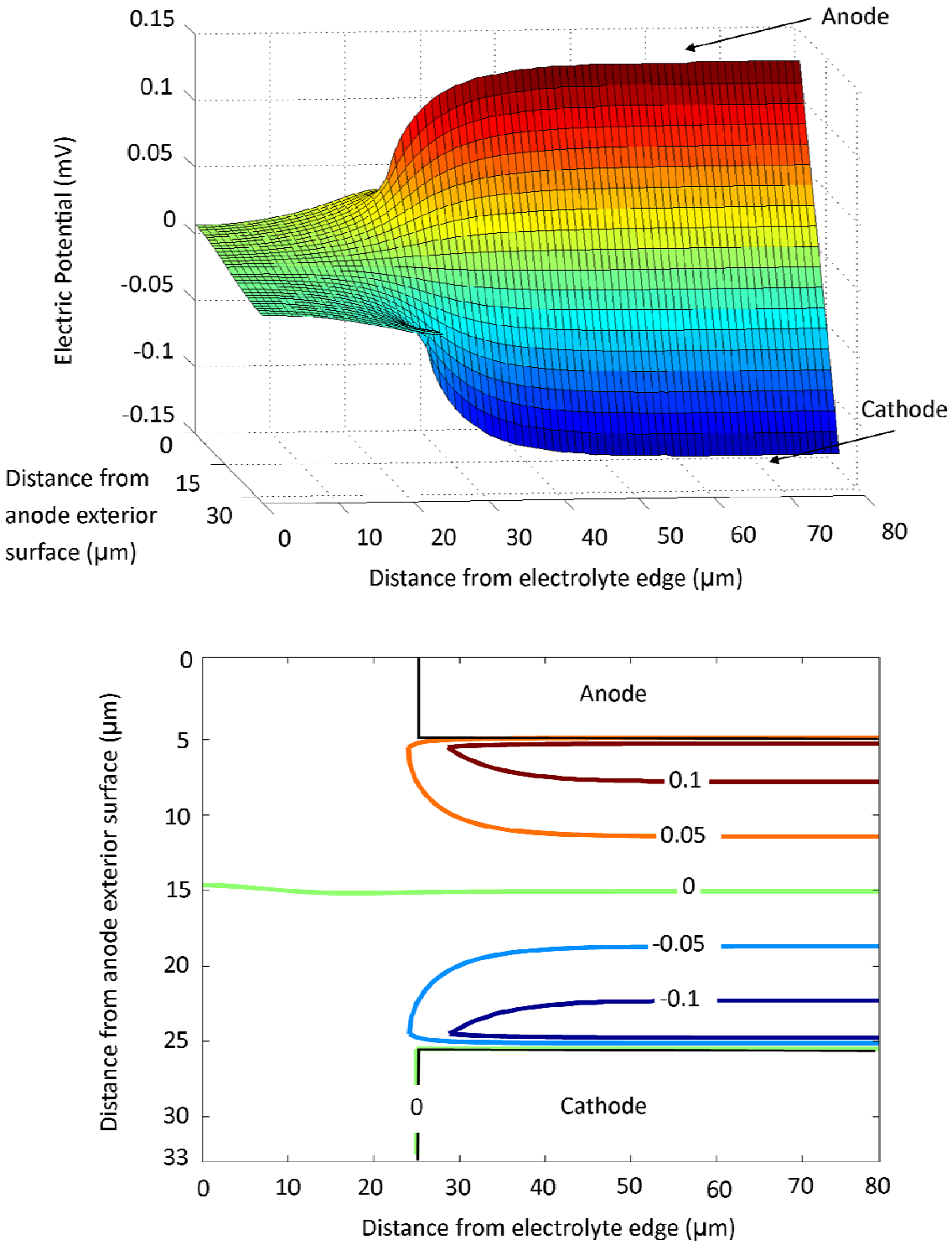

Figure 8.3. Electric potential field (mV) for flooded electrodes without edge reactions after 60 seconds. The width of the cathode is 8 μm.

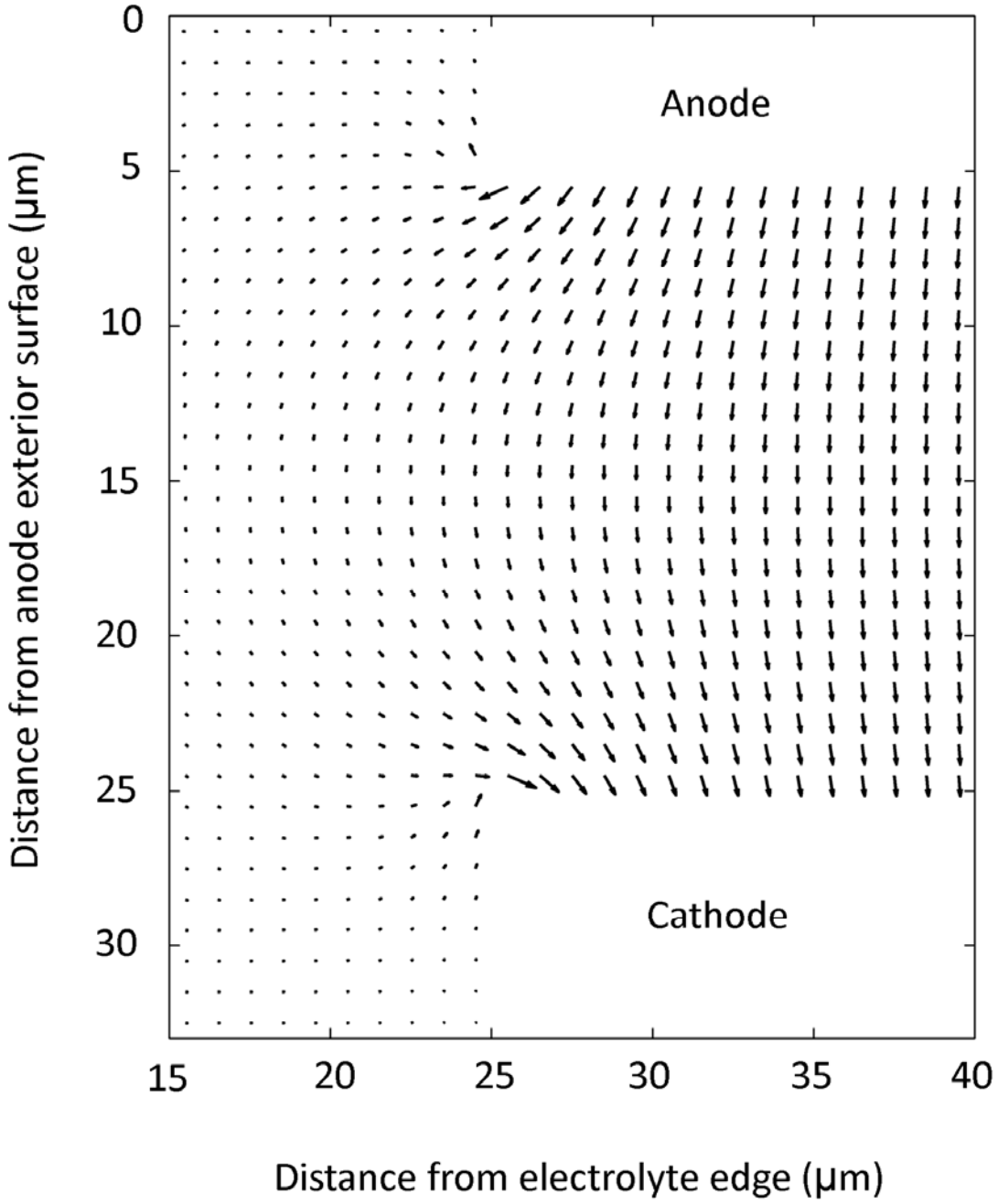

Figure 8.4. Electric current distribution near electrode edges for equal electrode length lithium-ion cell without edge reactions after 60 seconds.

Figures 8.3 and 8.4 represent the case where no electrochemical reactions occur on electrode edges. Because the edges are electrochemically inactive, lithium stoichiometric gradients may only be caused by the electrochemical reactions along the interior electrode surfaces. The rates of these electrochemical reactions (Equations (8.9) and (8.10)) depend upon the electric potential adjacent to the electrode, Φ_e. Figure 8.3 shows how the electric potential adjacent to the electrodes is reduced at the edge region, including on the interior electrode surfaces, due to the increased effective conductivity of the extended electrolyte. In other words, the increased effective conductivity of the extended electrolyte may decrease the potential gradient across the electrolyte and this may cause an increase in electrochemical reaction rates on the interior surface near the electrode edges. This effect was seen in the simulations. However, this effect was extremely small, as can be seen in Figure 8.5, showing the concentration of lithium inserted into the cathode after a full hour of 1 C charging. Figure 8.5 shows that the increase in lithium concentration near the cathode edge/tip is so small that it is unobservable in this figure. From this analysis it can be concluded that the effect of the electrolyte extension does not have a perceivable effect on electrode concentrations at the conditions examined, but it does increase the effective conductivity near the edge region.

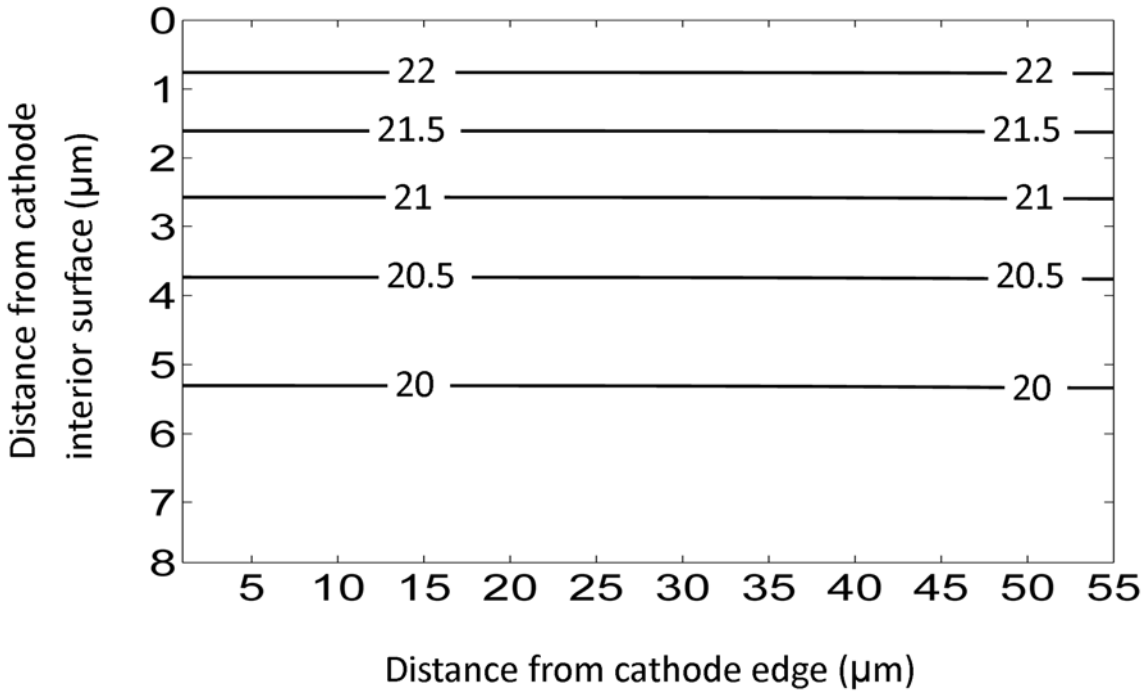

Figure 8.5. Cathode concentration for a cathode width of 8 µm and equal electrode lengths in a lithium-ion cell after 1 hour of charging and no edge reactions.

8.3.2 Equal length electrodes with edge reactions

Figure 8.6 shows the predicted electric field for the case of two equal width electrodes (5 µm) and equal length electrodes with an electrolyte extension of 25 µm after 60 seconds of 4.37 Am^{-2} charging. In this simulation it was assumed that the electrochemical reactions occurred along the complete surfaces of the electrodes in contact with the electrolyte, including the electrode interior surfaces and electrode edges. It is important to note that for clarity and in order to present the complete data set, the length axis in Figure 8.6 is non-uniform from a distance of more than 40 µm from the electrolyte edge. Therefore, Figure 8.6 allows the analysis of data from the uniform mesh close to the electrode edges coupled with the bulk/interior of the lithium cell where electric current moves uniformly from anode to cathode. Figure 8.6 shows

that the effect of the edge reactions (when the width of both electrodes is 5 μm) is to raise the electric potential near the edges above that seen in the bulk region. The reason for this increase in electrolyte potentials towards the electrode edges is associated with gradients of lithium stoichiometric coefficient in the electrodes towards the edges. This phenomenon will be explained below.

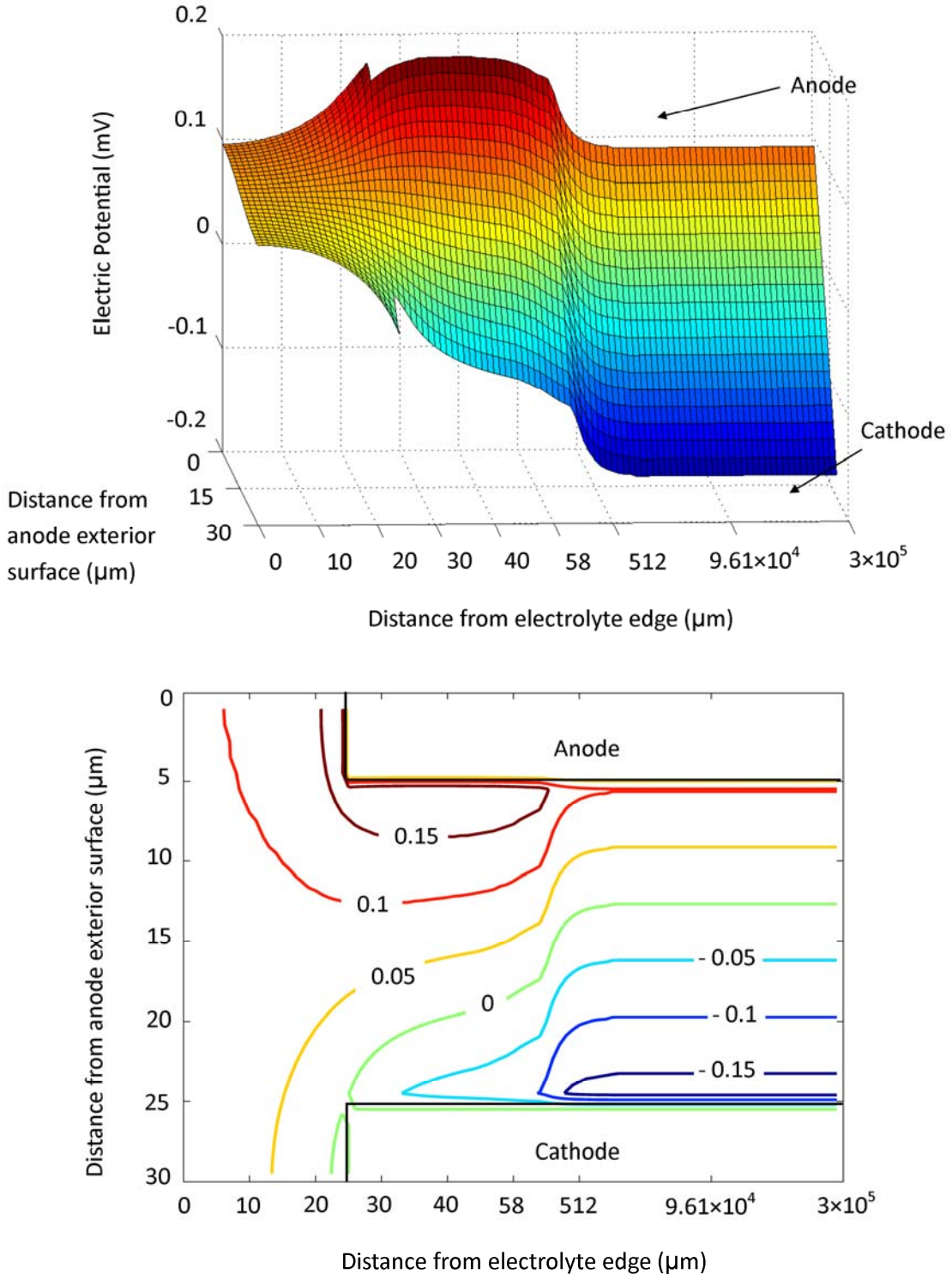

Figure 8.6. Predicted electric potential (mV) from equal length flooded electrodes with edge reactions after 60 s of charging. The widths of the anode and cathode were 5 μm.

Figure 8.6 displays an electric potential field that is elevated above bulk values towards the edges of the electrodes for the case of equal width electrodes. The electric potential is elevated towards the electrode edges because the overall rate of anodic half reactions in this region is greater than the overall rate of cathodic reactions, occurring on their respective electrodes. In other words, in this edge region, the anode is producing more electric current than the cathode is consuming. This electric current must then migrate along the electrolyte, parallel to the electrodes, towards the bulk cell. This predicted electric current distribution is shown in Figure 8.7. Figure 8.7 shows electric current emanating from the anode interior surface and the anode edge. A significant portion of this electric current flows into the extended electrolyte region, taking advantage of the increased effective conductivity in this area. This electric current flows towards the cathode interior surface and edge, where lithium is inserted into the cathode. The relative magnitudes of the currents associated with the tips of the anode and cathode edges can also be compared from Figure 8.7. The arrow depicting the current flowing/inserting into the cathode tip is approximately half of the size of the arrow depicting the current flowing/emanating out of the anode. The difference in magnitude of these two currents is due to the dependence of the rates of electrochemical reactions on the equilibrium potentials, U_a and U_c (as shown in Equations (8.9) and (8.10)). When the charging of the cell is started, the stoichiometric coefficient of lithium in the anode is very close to 1 and is represented by the right-hand portion of the solid line in Figure 8.2. This solid portion of the line only has a slight gradient of potential for a change in stoichiometric coefficient. In other words, this equilibrium potential does not change significantly for a concentration gradient inside the electrode, and

electrochemical reaction rates will not change drastically for such a gradient. Therefore, for the case presented in Figures 8.6 and 8.7, an elevated quantity of current will emanate from the anode tip that is more affected by the increased tip surface area, and less affected by the resulting concentration gradient within the electrode. The opposite is true of the cathode tip. At the start of cell charging the stoichiometric coefficient inside the cathode will be represented by the left side of the corresponding solid line in Figure 8.2. As is evident, there is a very large gradient of potential associated with a small change in stoichiometric coefficient in this region. Therefore, the rate of electrochemical reactions (as described by Equation (8.10)) will be very much affected by a gradient of lithium concentration in the electrode. So, although the larger surface area at the cathode tip may promote an increased rate of lithium insertion into the tip area, the large change in equilibrium potential that this would cause is prohibitive. Instead, the extra current produced at the anode tip and edge must migrate elsewhere, along the electrolyte adjacent to the cathode, in a manner that balances transport and concentration gradients in the electrolyte with concentration and equilibrium potentials in the electrodes. The resulting concentration gradients within electrodes are discussed below.

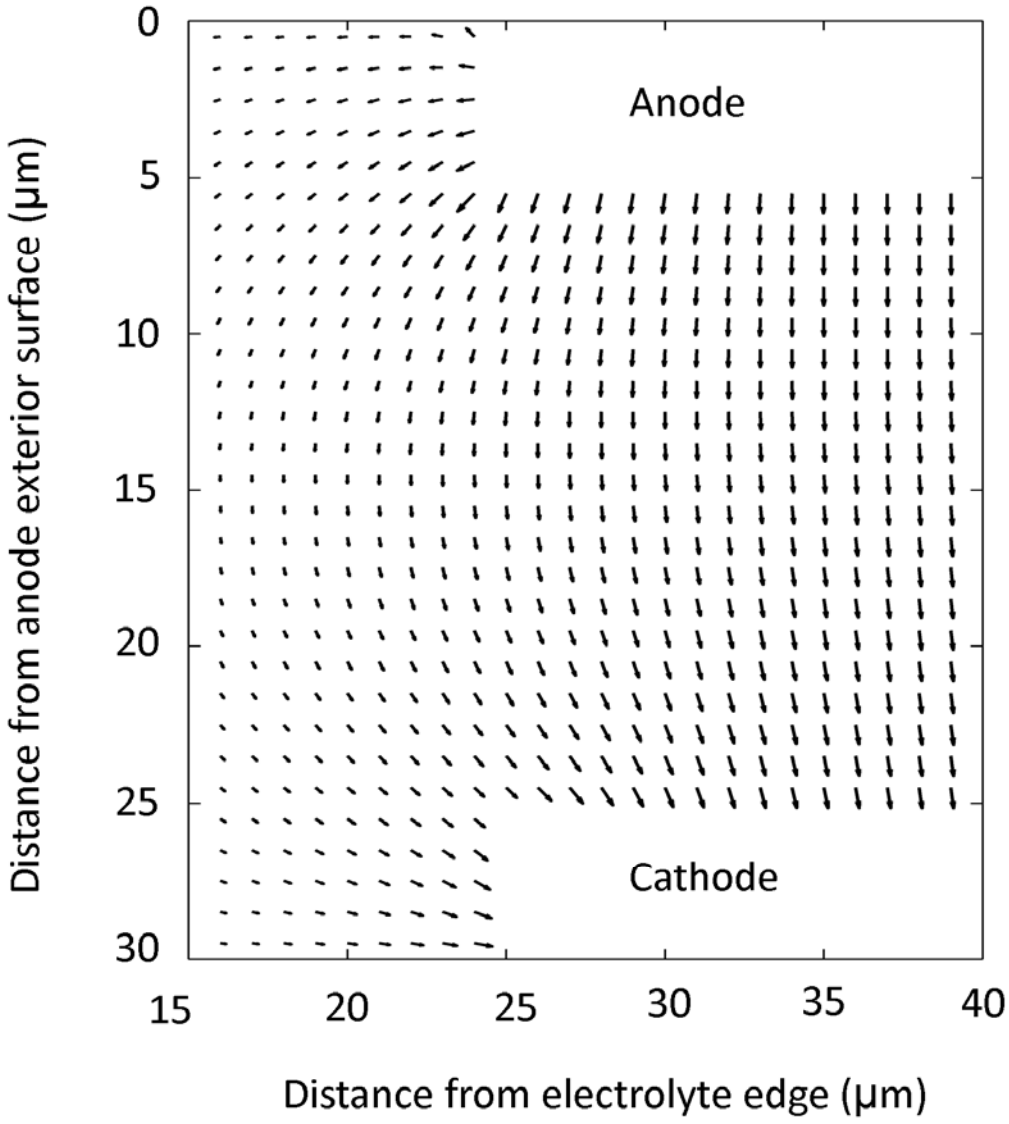

Figure 8.7. Electric currents for the equal length (5 μm width) electrodes after 60 seconds simulated charging.

Figure 8.8 shows the concentration gradients towards the cathode edge after 60 seconds of cell charging. The lengthwise gradients are restricted to within 5 μm of the edge. This is a smaller region than for the gradients in the anode, shown in Figure 8.9, where the lengthwise gradients extend 25 μm from the anode edge. This reinforces the

concept that stoichiometric gradients are allowed in the anode during early cell charging, but not in the cathode because of the large gradients in equilibrium potential that this would cause. In other words, the electrochemical reaction rate of lithium emanating from the anode is not greatly affected by the anodic lithium stoichiometric coefficient; however, the opposite is true of the cathode (during early charging). Because the numerical model used a non-uniform mesh, the length of the bulk cell was of sufficient length such that the microscopic phenomena occurring at the electrode edges did not have a significant effect on the macroscopic bulk cell and overall cell potential. In this manner, the numerical model predicts where the excess current from the anode edge is inserted into the cathode. Figure 8.10 shows the current density of the electrochemical reactions occurring on the surfaces of both the anode and cathode. The current densities are shown as a function of distance from the electrode edge. The positive distances from the electrode edge correspond to locations on the electrode interior surface, away from the edge, and those negative distances correspond to distances away from the electrode tip, along the electrode edge itself. Figure 8.10 shows a drastic reduction in the cathodic reaction rate at the electrode tip (of approximately 65% from bulk values) that is necessary in order to avoid large stoichiometric lithium gradients in the cathode. The anodic reaction rate suffers only a mild reduction at the tip, as shown in Figure 8.10. However, since the overall production and consumption of Li^+ must be equal along the entire cell, this excess Li^+ produced at the electrode edges must be consumed elsewhere. Figure 8.10 shows at distances of approximately 0.01 mm to 0.02 mm from the edge the anodic reaction rate is less than the cathodic reaction rate. Therefore, it is in this region that the excess current from the edge region is

inserted into the cathode. This spreading out of the excess lithium avoids steep lithium concentration gradients towards the cathode edge, and instead balances these gradients with iR drops and concentration effects in the electrolyte.

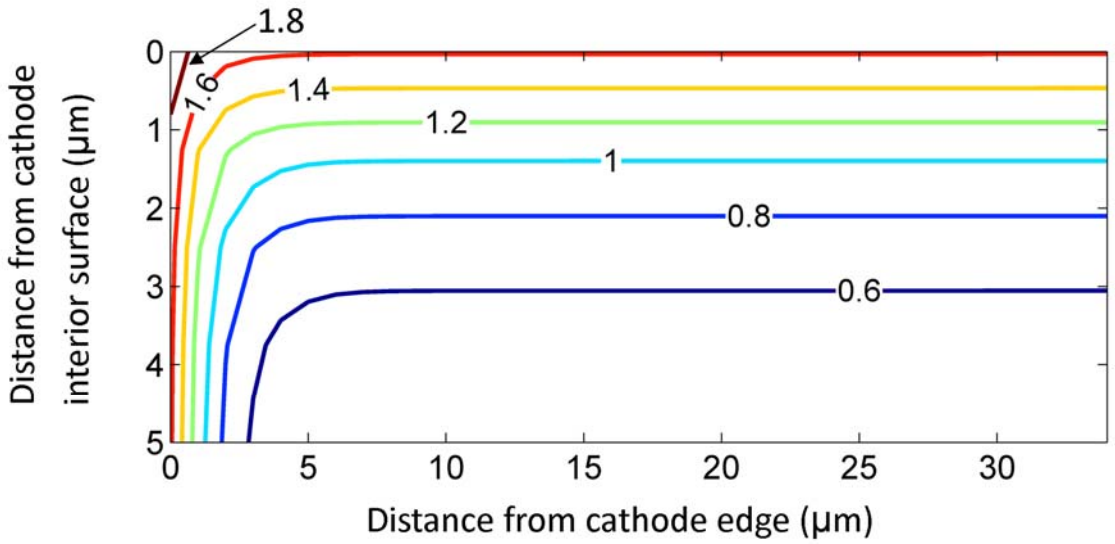

Figure 8.8. Predicted lithium concentration (M) in cathode from equal length flooded electrode cell with edge reactions after 60 seconds of charging.

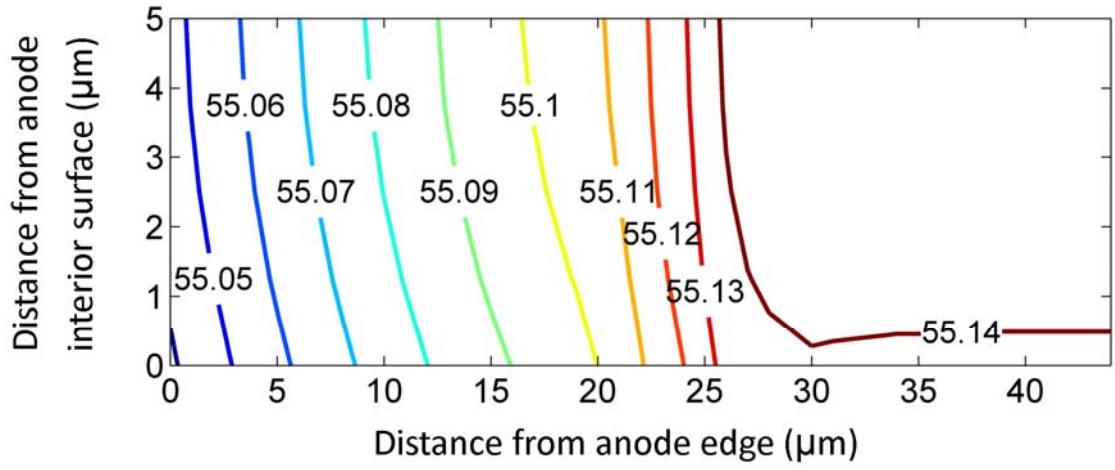

Figure 8.9. Predicted lithium concentration (M) in anode from equal length flooded electrode cell with edge reactions after 60 seconds of charging.

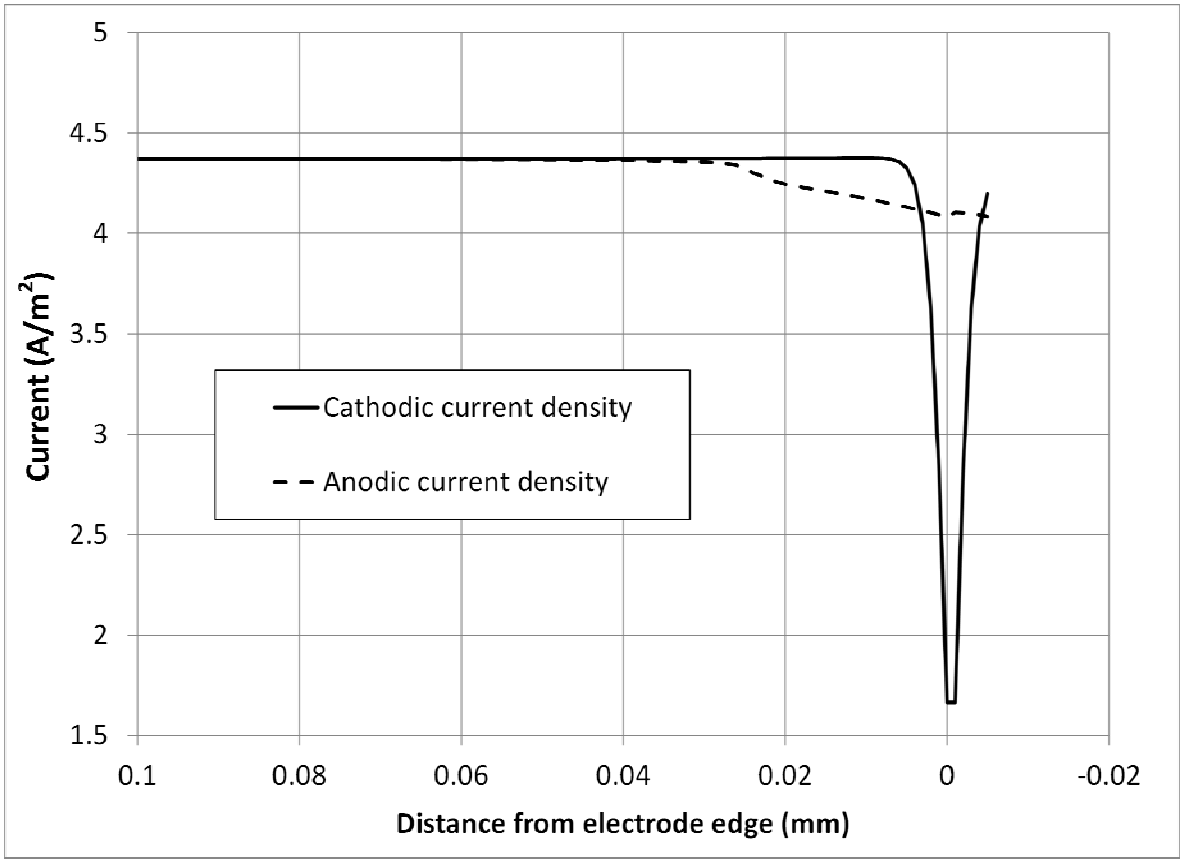

Figure 8.10. Electrochemical reaction rate of lithium dissolution or insertion along surface of electrodes.

If a cell geometry similar to the one used in the predictions from Figures 8.6 to 8.10 was altered, such that the width of the cathode was increased from 5 μm to 8 μm, but all other initial parameters were maintained, this would increase the cathodic surface area on the cathode edge. This increase in cathode width would also decrease the concentration gradients within the cathode caused by lithium diffusion from the interior surface. However, the predicted data shown in Figure 8.11 illustrates that this increase in cathode width decreases the values of electric potential towards the electrode edges, after 60 seconds of charging. Figure 8.12 shows the electric current distribution for the case of the 8 μm cathode width. Figure 8.12 displays the extra current that is drawn

parallel to the electrodes into the edge area to compensate for the additional lithium being inserted into the cathode in this area. Therefore, the preceding predictions show that the rate of lithium insertion into the cathode is primarily determined by the concentration gradients within the cathode, and the rate of lithium emission from the anode is determined by anode surface area and electrolyte potential gradients, during early cell charging.

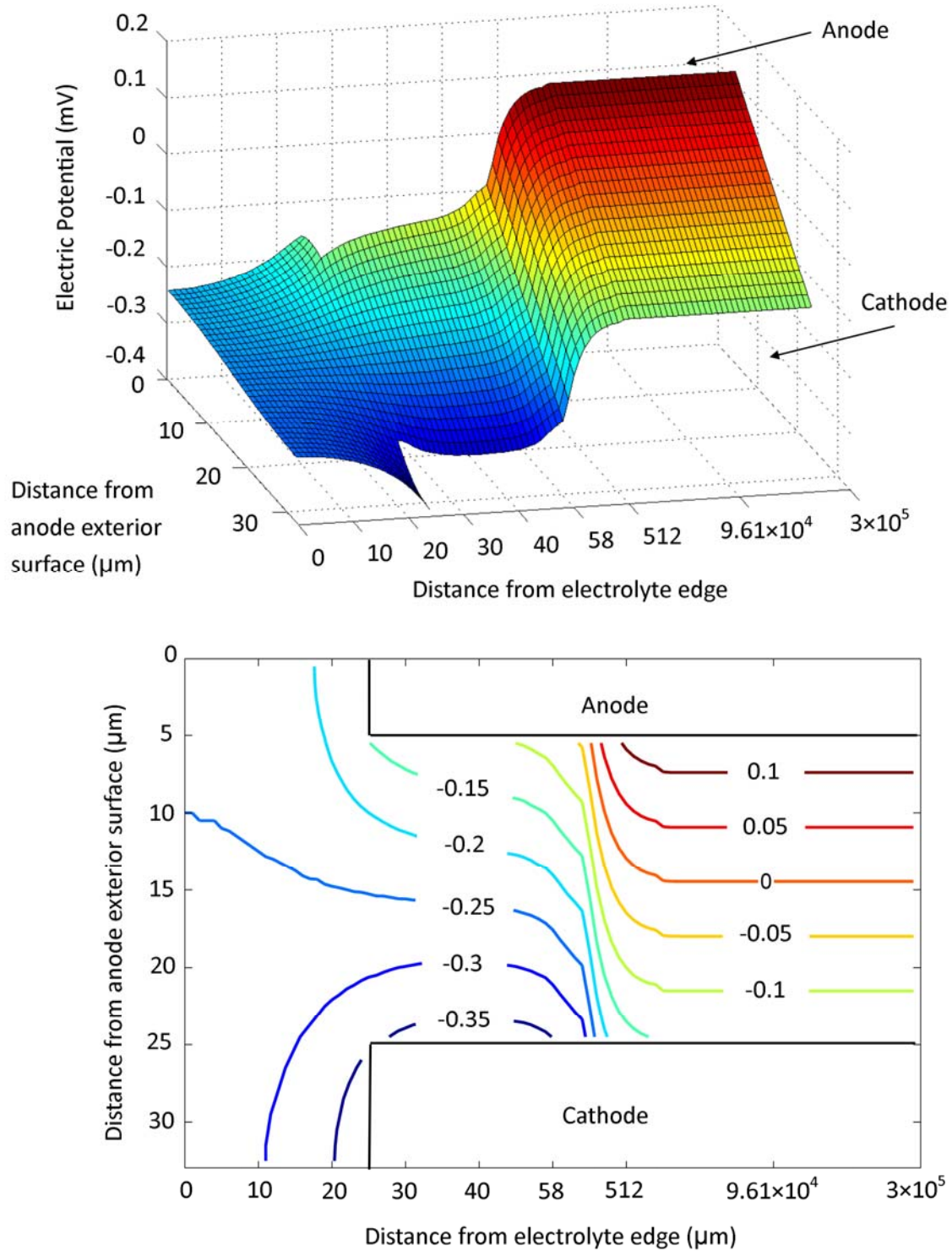

Figure 8.11. Predicted electric potential (mV) from equal length flooded electrodes with edge reactions after 60 s of charging. The width of the cathode was 8 μm.

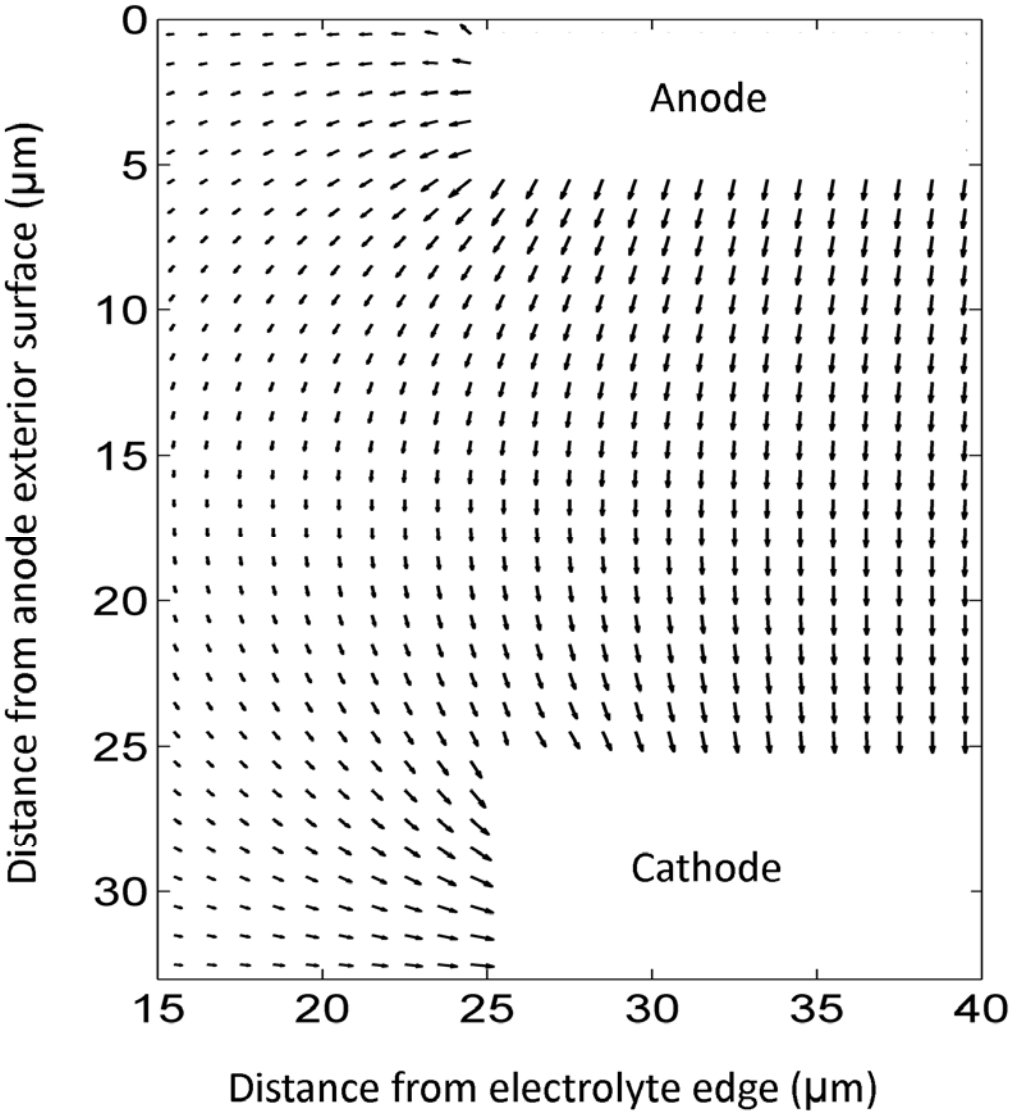

Figure 8.12. Electric currents for the equal length electrodes after 60 seconds simulated charging. The width of the anode is 5 μm and the cathode width is 8 μm.

8.3.3 Extended cathodes

Large potential drops due to concentration gradients within the cathode have been seen experimentally when the cathode edge is extended significantly past the anode edge (Scott et al, 2003a,b). The cathode edge may be extended in order to prevent higher

levels of lithium concentration at the tip/edge that may be detrimental to the cell. The model presented in this paper does predict these damaging levels of lithium concentration, and the resulting lithium deposition, at the cathode tip/edge; however, these high levels of lithium are more likely to occur in the cathode towards the end of cell charging when the stoichiometric coefficient of lithium in Li_xC_6 is almost 1. The relationship between the equilibrium potential and stoichiometric coefficient of lithium in Li_xC_6 of an almost completely charged cell is represented by the right-hand-side of the solid line in Figure 8.2. The gradient of this portion of the line is much less steep than the gradient for the uncharged cathode (Li_xC_6), represented by the left-hand-side of the solid line. These different gradients of equilibrium potential for an uncharged and charged cathode result in the possibility for larger lithium concentration gradients in a cathode approaching a full charge. In other words, if the spatial difference in stoichiometric coefficient of lithium in an electrode causes a large gradient of equilibrium potential, a large gradient of electric potential may be apparent in the electrolyte, as seen by Scott et al. (2003a,b). If the cell is in a state of charge whereby a large difference in stoichiometric coefficient (with position) does not cause a large gradient of equilibrium potential, then large gradients of electric potential may not be seen in the electrolyte, however, large concentration gradients in the electrode may be possible, along with electrode over saturation and lithium deposition at regions of high surface area, as seen in the numerical simulations of Tang et al. (2009). The model presented in this paper predicts both such phenomena. For example, Figure 8.13 shows the concentration profile for the cathode of 6 μm width and equal electrode length cell having undergone 4.37 Am^{-2} charging for one hour. Figure 8.13 shows that although

much of the cathode concentration is significantly below the maximum concentration of 30.5 M, the tip region is above this concentration and lithium deposition here is likely.

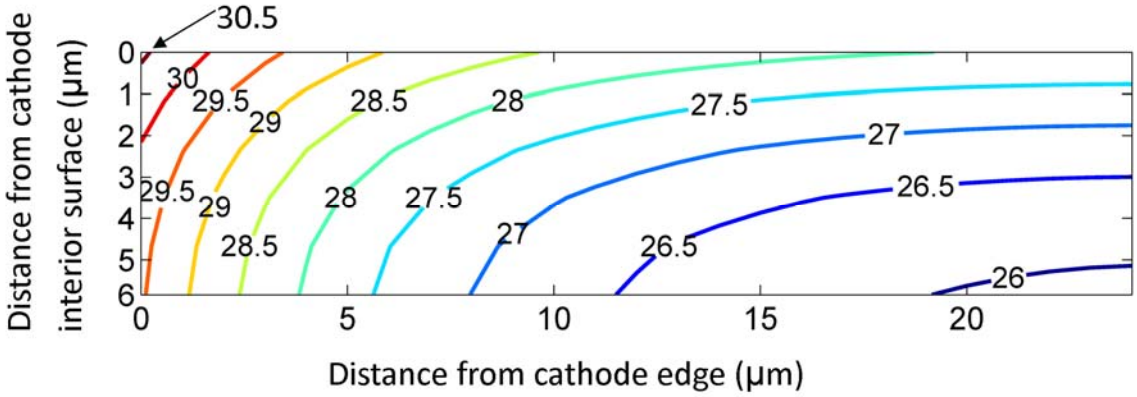

Figure 8.13. Cathode lithium concentration (M) from equal length flooded electrodes with edge reactions after 1 hour of 4.37 Am-2 charging. Cathode width is 6 μm.

Figure 8.14 shows the predicted electric field for the case where the cathode is extended past the edge of the anode by 1.75 cm, after 100 seconds of charging at 2 Am^{-2}, corresponding to the current density utilized by Scott et al. (2003a). The width of the cathode was 8 μm and the initial stoichiometric coefficient in the cathode was 0.0025. Figure 8.14 shows a predicted electric field that has a minimum of approximately -0.4 V with respect to the bulk values. This is about half of the maximum experimental value seen by Scott et al. (2003a) after 90 seconds for a lithium ion cell with a cathode extension undergoing charging of a similar current density. However, many cell parameters were unpublished by Scott et al. and the predictions given here are for solid electrodes, not porous ones. Of interest in this case is not a direct comparison with experimental data, but instead, the trends caused by lithium gradients in the electrodes and resulting effects are examined below.

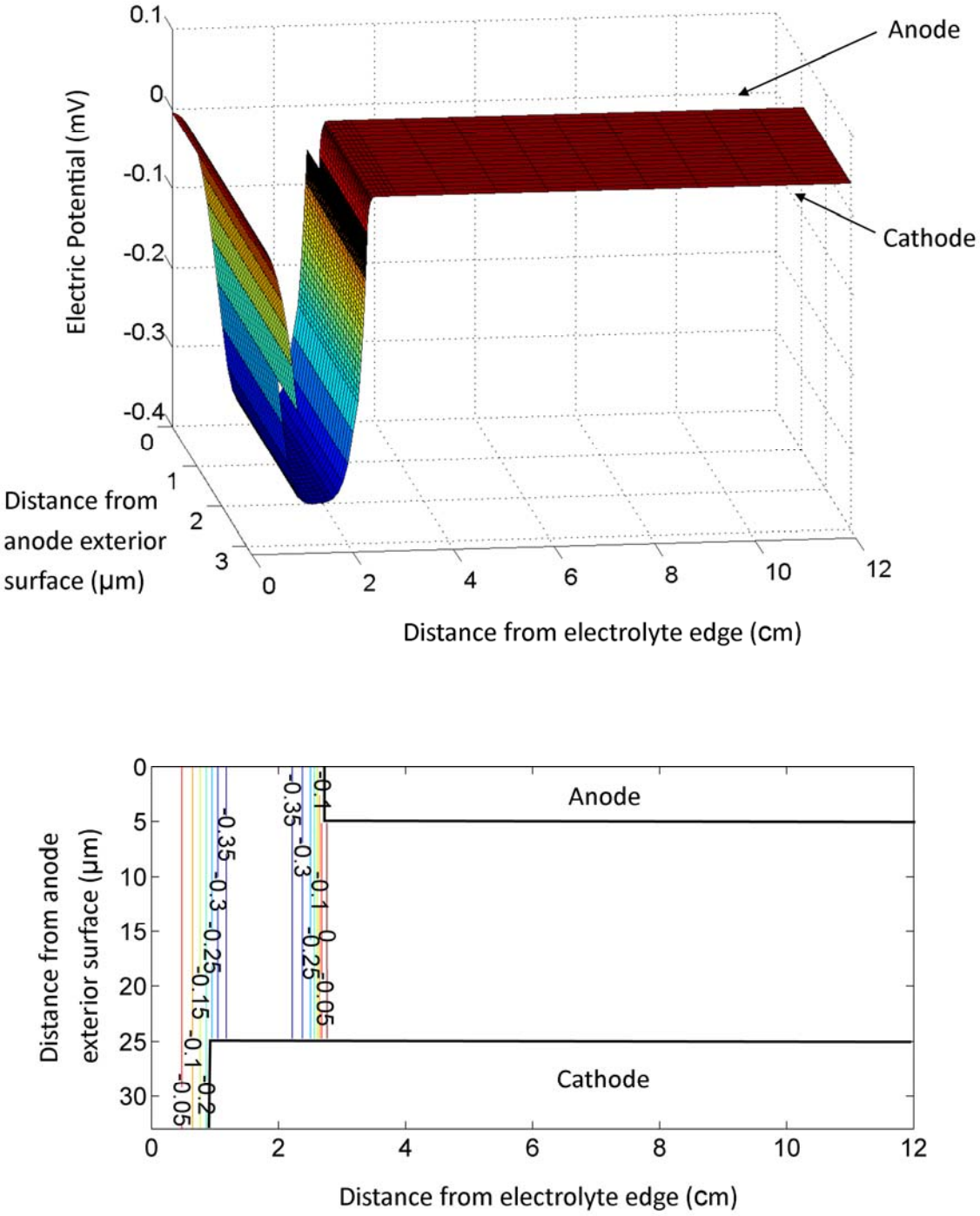

Figure 8.14. Electric potential field for electrodes of non-equal length after 100 seconds of simulated charging. The cathode width is 8 μm and the anode width is 5 μm. The cathode edge is extended past the anode edge by 1.75 cm and the initial stoichiometric coefficient for Li was assumed to be 0.0025% of the maximum value for this simulation only.

For the simulation presented in Figure 8.14 the concentration of lithium in both electrodes changes with position and time. Because the concentration of lithium is non-uniform with position, potential gradients are evident in the electrolyte. The effect of the lithium electrode gradients on the cell will be investigated through an examination of the rates of electrochemical reactions occurring on electrode surfaces. Figure 8.15 shows the rate of anodic currents emanating from the anode from the simulation presented in Figure 8.14 as a function of position at different times. Positive distance values represent the interior surface of the anode and negative values the small edge region. Because at larger distances from the anode edge the current was predicted to remain constant, this data was not presented as part of this figure. Figure 8.15 shows that at early charging times (100 s and 500 s) the highest rates of current are drawn from regions close to the anode edge. The anode emanates current from this region for two reasons: this region is the closest to the extended cathode and this region has a greater surface area due to the anode edge. Also, by observing the right-hand-side of the anodic curve in Figure 8.2, it is evident that significant concentration gradients are possible in the initially charging anode without significant gradients of equilibrium potential. Figure 8.16 shows a figure similar to Figure 8.15, but describing the current inserted into the cathode. At the early charging times of 100 s and 500 s Figure 8.16 shows that current densities of approximately 0.4 and 0.2 A/m^2 were inserted along the extended region of the cathode, respectively. It is expected that at early charging times the gradient of lithium in the cathode causes significant gradients of equilibrium potential which provide the driving force behind the large potential drop in the electrolyte (shown in Figure 8.14), and allows these significant cathodic reaction rates. Over an initial

period of time, small levels of lithium are inserted into the extended cathode region and the concentration of lithium in the extended cathode region will increase such that a large difference in equilibrium potential no longer exists between the edge region and the bulk cell region. This is displayed in Figure 8.2 because the gradient of equilibrium potential decreases with increasing stoichiometric coefficient. This decrease in the difference in equilibrium potential decreases the available driving force for the migration and insertion of lithium along the extended cathode and is visible in Figure 16 that shows how the current drawn by the extended cathode decreases for times of 1000 s and later. This decrease in current drawn by the extended cathode also affects the current emanating from the anode. Figure 8.15 shows that after 1000 s the excess current being drawn from the region towards the edge of the anode has decreased and some other effects are visible as the "hook" shape in the reaction rates towards the edge region. This "hook" shape is likely because of the decreased current being drawn towards the extended cathode and the decreased iR drop in the electrolyte making it more possible for current to be drawn from the anode surface further into the cell. This current drawn from the anode further into the cell takes advantage of the fact that the anode edge became more depleted of lithium during the early charging when the extended cathode was drawing significant quantities of current. Figure 8.15 shows that as time progresses further, less and less excess current is produced towards the anode edge region, and instead, because the extended cathode is no longer drawing significant current, the concentration gradients previously established in the anode become the dominant phenomenon impacting the rate of anodic reaction. This is because, as the cell becomes more charged and the stoichiometric coefficient in the anode decreases, a slight

gradient in electrochemical potential is evident towards the left of the corresponding solid line in Figure 8.2. This significant gradient of lithium concentration in the anode after 1 hour is shown in Figure 8.17. Figure 8.18 shows the concentration gradient of lithium in the cathode after 1 hour. It can be seen that the concentration of lithium in the extended region is approximately one tenth of the maximum value seen in the bulk cell.

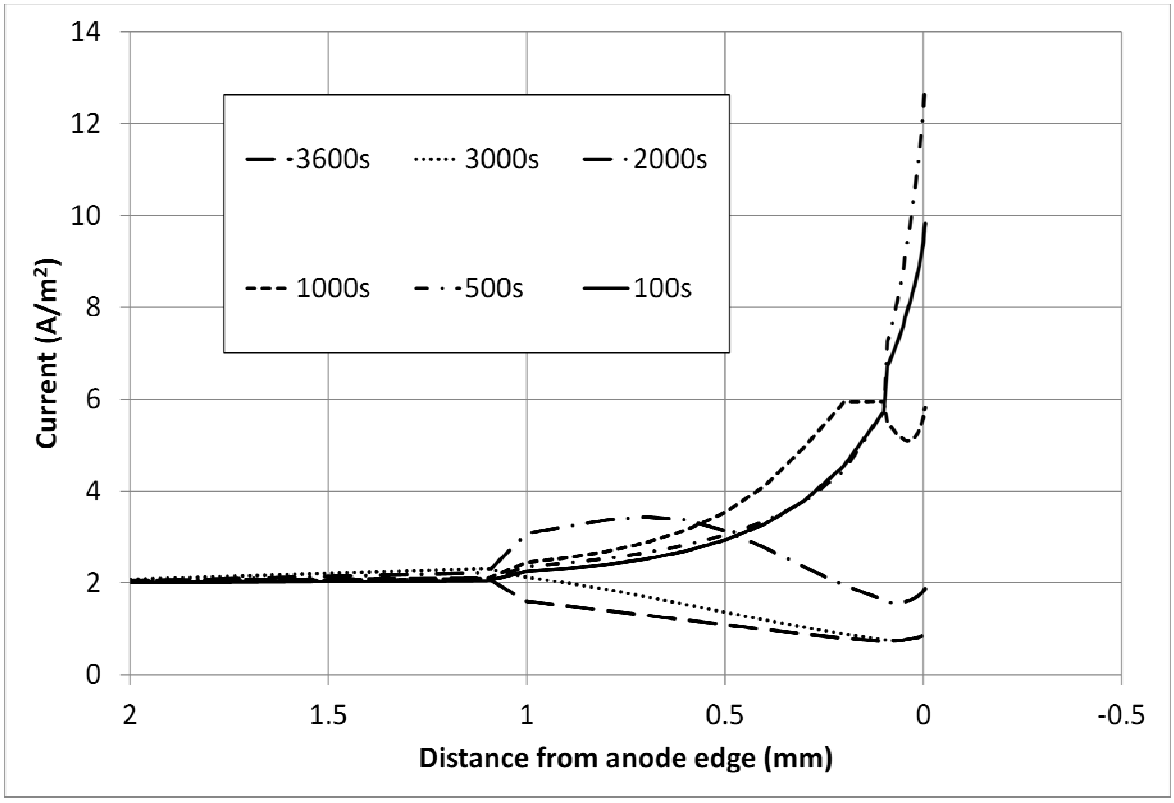

Figure 8.15. Electric current emanating from anode surface at different times. Positive distance values represent the interior anode surface and negative distance values represent the distance along the anode edge itself, away from the anode tip.

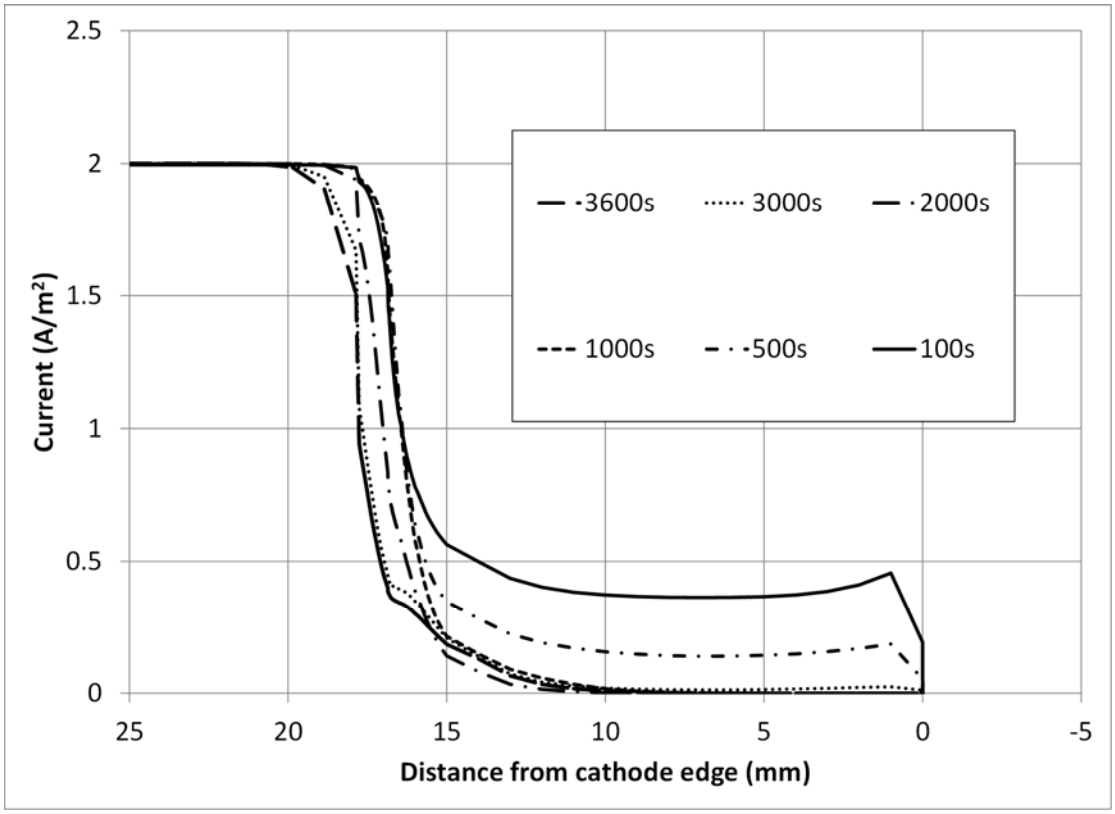

Figure 8.16. Electric current inserted into cathode surface at different times. Positive distance values represent the interior cathode surface and negative distance values represent the distance along the cathode edge itself, away from the cathode tip

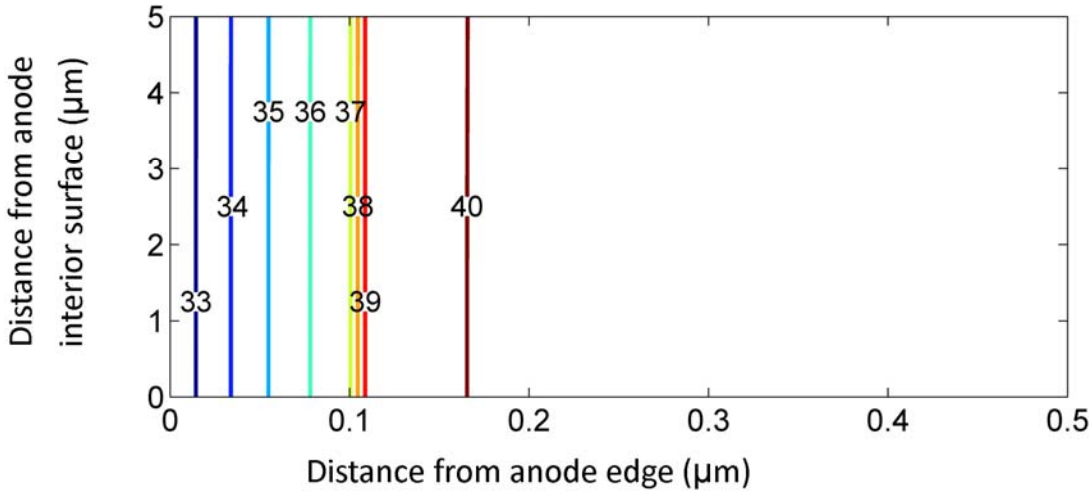

Figure 8.17. Predicted anode lithium concentration (M) showing depleted area towards anode tip after 1 hour of charging at 2 A/m^2.

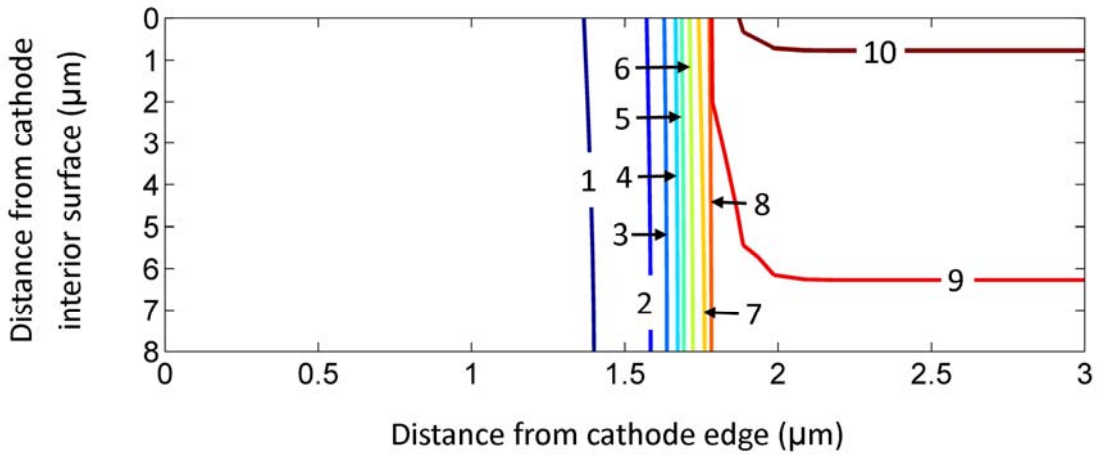

Figure 8.18. Predicted cathode lithium concentration (M) for the extended cathode after 1 hour of charging at 2 A/m^2.

8.4 Conclusions

This chapter explored the edge effects of electrodes in lithium-ion cells undergoing charging, and the effects of stoichiometric coefficient gradients within electrodes. It was found that the increase in effective conductivity associated with a flooded electrolyte extended past the electrode edges does not have an appreciable effect on the rates of anodic or cathodic reactions near the edge regions. However, it was found that lithium concentration gradients inside the cathode impacted the rate of cathodic reactions significantly and concentration gradients inside the anode did not significantly impact the rate of anodic reactions, during early cell charging. Instead, the rates of anodic reactions were significantly affected by the surface area of the anode contacting the electrolyte, and not the concentration gradient of lithium in the anode. It was also found that during later stages of cell charging, when the gradient of equilibrium potential due to a gradient in cathodic stoichiometric coefficient was less steep,

concentration gradients within the cathode were more likely and might lead to a possibility for lithium deposition at the edge region.

Simulations were conducted for the case where the cathode edge was extended past the anode edge to reduce the possibility for lithium deposition at the cathode edge. The simulations indicated that the stoichiometric coefficient of lithium in an extended cathode edge would be reduced; however, this extension may cause alternative negative consequences that have been experimentally observed by others. These negative consequences include a large electric potential drop along the electrolyte and caused by the gradient of lithium stoichiometric coefficient in the extended cathode edge. The lithium stoichiometric coefficient gradient inside the cathode causes a large potential drop in the electrolyte during early cell charging when a gradient in the cathodic stoichiometric coefficient causes a large gradient in equilibrium potential. It was observed that this gradient in equilibrium potential would decrease as charging of the cell proceeded, causing a reduction in the rate of cathodic reactions occurring along the extended cathode region. The behavior of the cell due to these varying rates was also examined.

9. AN EXTENSION AND RAMIFICATIONS OF THE NEW THEORY

This thesis started with a review of classical electrochemical theory. Then, models of crevice corrosion and electrolytic transport were presented that led to a new theory. Applications and validations of numerical models based on this new theory were also presented. This chapter will build on this new theory in a way that explains and clarifies the concept of the electric field: *the propensity for charge density*.

9.1 Propensity for Charge Density

Figure 9.1 shows two spheres connected by a linear elastic spring at steady-state. There is one exterior force acting on these spheres, shown in Figure 9.1 as F and the solid double headed arrow, and the force of gravity is absent. There is a displacement between the spheres because of the exterior applied force. Additional to the exterior force ($\mathbf{F}$) acting on the spheres and pushing them apart there is a force within the spring that acts equally and opposite to the exterior force and keeps the spheres from separating further.

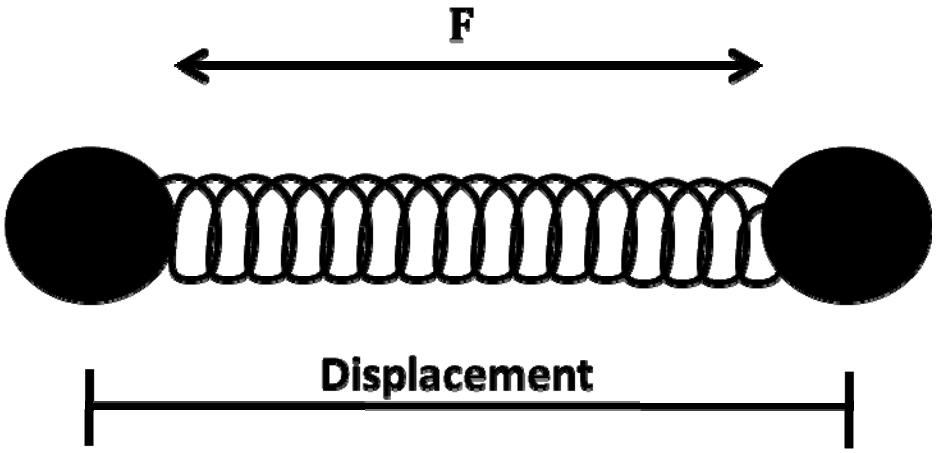

Figure 9.1. Displacement between spheres connected with a spring.

If the applied force from Figure 9.1 was part of a larger system in which forces must be balanced, then the force acting between the spheres must be calculated. If the only system properties known are the displacement between the spheres and the constant of elasticity of the spring, the force acting between the spheres may be calculated via Hooke's Law:

$$\mathbf{F} = -k\mathbf{s} \tag{9.1}$$

It is important to note from the previous example that for the same force acting on the spheres, different displacements may exist depending on the value of the constant of elasticity of the spring. The previous example is similar to two steady-state bound charged spheres undergoing an external electric potential, shown in Figure 9.2. Figure 9.2 shows an external applied electric potential (E) acting on the spheres as the solid double headed arrow. Figure 9.2 also shows a second attraction occurring between the two spheres because of their different charges, as the dashed double headed arrow. This example is reminiscent of the bound charge densities created by an applied electric field in a linear isotropic material. As presented in Equation (2.23), for bound charge density

in a linear isotropic material the electric displacement is described in a manner similar to Hooke's Law. Rearranging Equation (2.23) gives:

$$\mathbf{E} = \varepsilon^{-1}\mathbf{D} \tag{9.2}$$

Therefore, it is a simple conclusion that the applied electric field may cause different electric displacements in a linear isotropic material, depending on the value of its dielectric constant. In other words, for the same electric field, a larger electric displacement will be caused by a larger dielectric constant.

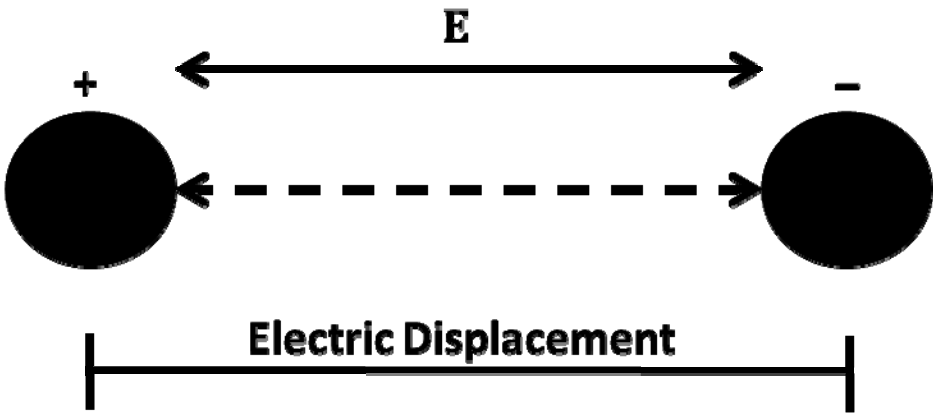

Figure 9.2. Displacement between charged spheres.

Poisson's equation was given as Equation (2.27). Another form of Poisson's equation for a linear isotropic material with a uniform permittivity is:

$$\nabla \cdot \mathbf{E} = \varepsilon^{-1}\nabla \cdot \mathbf{D} \tag{9.3}$$

where, according to (2.17), $\nabla \cdot \mathbf{D} = \rho$. Therefore, for a given electric field an infinite number of possible values for charge density and electric displacement exist, dependent upon the value of the constant of permittivity. As Hooke's Law is simply one way in

which the exterior applied force can be determined from an empirical understanding of a spring, so is Equation (9.3) one way of determining the electric field from a similar empirical understanding. The important conclusion to be drawn from this line of reasoning is that if the electric field is to be determined from a known quantity of charge density, it is important to have an understanding of the phenomena that caused this charge density in the first place. In other words, the electric field is not balanced with charge density, but the electric field is balanced with the strength of the phenomenon causing the charge density. Therefore, if mobile charge density is created due to electrolytic transport, the proportionality constant in Equation (9.3) will not be the dielectric constant, but the propensity for the transport of charge, as explained in Chapter 5. This line of reasoning differs from the open literature where it is commonly assumed that the relationship between any charge density and the electric field may be described via Poisson's equation.

The following discussion will highlight many things that may cause charge density. Because this thesis presents the idea that the electric field is a measure of the strength of the phenomena causing charge density, and not a measure of the charge density itself, and because many things may cause charge density, the name of this strength will be given: *the propensity for charge density*. One thing that causes a propensity for charge density has already been discussed: the electric field itself; when an electric field is applied to a linear non-isotropic material a bound charge density is created that opposes the applied electric field via the polarization or reorganization of atoms and molecules. This bound charge density is represented as the second term on the RHS of Equation (2.20). Empty space also causes an apparent charge density, represented as the first

term on RHS of Equation (2.20). For the subsequent analysis, because the electric displacement resulting from these two phenomena is assumed to be time independent, these types of charge density will be incorporated in a static charge density, ρ_S. The proportionality for this static charge density in a linear material is the dielectric constant.

Other things may have a tendency to cause charge density in an electrolyte. Concentration fields may have a tendency to cause ions to be transported at different rates, such as across a liquid junction, causing a charge density that is dependent upon the non-isotropic properties of the electrolyte. The electric field due to charge density created in such a manner is not calculated via Poisson's equation, because that would assume the charge density was formed due to the time independent phenomena incorporated in Poisson's equation, and not the amount of time dependent electrolytic transport. Instead, the propensity for different rates of ionic transport correctly describe the propensity for charge density. This was demonstrated in Chapter 5.

A further example of a phenomenon causing a propensity for charge density may be given for the case of the surface overpotential, or the double layer. As described in Section 2.2, an electric double layer may be associated with a surface overpotential. Different ions have tendencies to be located closer or further away from an interface. If the interface is electrically charged, this charge may also affect the tendencies for where ions are located. The tendencies for ions to be located closer or further from an interface may again be described as a propensity for charge density, and this phenomenon will be balanced by the electric field. In fact, by using the concept of the "propensity for charge density" a macroscopic phenomenon that causes an electric field may be balanced with microscopic phenomena, via the electric field, regardless of

whether the phenomena cause an electric displacement, are caused by an electric current or spatially distinct electrochemical reactions, are due to the microscopic polarization or rearrangement of atoms and molecules, are caused by an inherent property of the medium, or are a direct response of the medium to the applied electric field. As long as the propensity for charge density from each phenomenon is correctly described, all of the phenomena will be correctly balanced via the electric field.

As shown in Chapter 3 and Chapter 4, rates of electrochemical reactions may be calculated from predictions of electric gradients caused by ionic transport through the electrolyte. This was accomplished by assuming an electrochemical circuit and that the electric gradient through the substrate was negligible (see Figure 3.4). Electrochemical reaction rates were then calculated dependent upon the difference in electric potentials between the substrate and adjacent electrolyte. In other words, the electrochemical reaction rates described one propensity for charge density, and the ionic transport described another propensity for charge density. This concept was further expanded multi-dimensionally for the new theory and applications presented in Chapters 5 to 8. In these chapters the concept of the propensity for charge density was applied multi-dimensionally and found capable of predicting the electric field across the entire cell.

9.2 A New Form of Maxwell's Equations

This section will present a new form of Maxwell's equations that accounts for the advances in understanding presented in this thesis. In Chapter 5, it was shown how the electric displacement field for a non-isotropic electrolyte includes terms for time independent, time dependent, and medium dependent terms, in Equation (4.18).

Expressing Equation (4.18) without the assumption of Ohm's law or the assumption of a linear isotropic medium gives:

$$\mathbf{D} = \mathbf{D}_0 + \mathbf{D}_0(\mathbf{p}) + \int \mathbf{i}\partial t \tag{9.4}$$

According to Section 9.1, there are multiple forms of charge density that may be present in a medium, depending on the phenomenon that caused the charge density. If each of the terms on the RHS of Equation (9.4) is allocated a different form of charge density, three forms exist:

$$\nabla \cdot \mathbf{D}_0 = \rho_{\mathbf{S}} \tag{9.5}$$

$$\nabla \cdot \mathbf{D}_0(\mathbf{p}) = \rho_N \tag{9.6}$$

$$\nabla \cdot \int \mathbf{i}\partial t = \rho_M \tag{9.7}$$

and the sum of all of these forms of charge density would be:

$$\rho_T = \rho_S + \rho_N + \rho_M \tag{9.8}$$

Theory from this thesis explains that an electric displacement might be associated with an electric current applied over a time period. For this reason, the electric current should be incorporated into the definition of the Electric Displacement Field and Maxwell's equations would take the form:

$$\nabla \times \mathbf{E} = -\frac{\partial}{\partial t}\mathbf{B} \tag{9.9}$$

$$\nabla \times \mathbf{H} = \frac{\partial}{\partial t}\mathbf{D} \tag{9.10}$$

$$\nabla \cdot \mathbf{D} = \rho_T \tag{9.11}$$

$$\nabla \cdot \mathbf{B} = 0 \tag{9.12}$$

One of the great accomplishments of Maxwell's equations is the ability to derive the continuity equation (Equation (2.19)) from Ampere's law with Maxwell's correction. Therefore, it must also be possible to accomplish this derivation using this new arrangement of the equations. If the divergence of both sides of Equation (9.10) is taken:

$$\nabla \cdot \nabla \times \mathbf{H} = \nabla \cdot \frac{\partial}{\partial t}\mathbf{D} \tag{9.13}$$

The left-hand-side of Equation (9.13) is zero. Rearranging Equation (9.13) and incorporating Equation (9.11) gives:

$$0 = \frac{\partial}{\partial t}\rho_T \tag{9.14}$$

Substituting the definition of the total charge density, given in Equation (9.8) into Equation (9.14) and rearranging gives:

$$0 = \frac{\partial}{\partial t}\left(\rho_S + \rho_N + \rho_M\right) \tag{9.15}$$

Equation (9.15) is interesting because it shows that all of the phenomena associated with the creation of an electric field may be represented as charge density. Equation (9.15) balances all of the propensities for charge density and can be considered a property that will ensure an overall electric potential drop of zero around an electrochemical circuit. Incorporating Equation (9.7) into Equation (9.15) and rearranging gives:

$$\nabla \cdot \mathbf{i} = -\frac{\partial}{\partial t}\left(\rho_S + \rho_N\right) \tag{9.16}$$

Equation (9.16) is a continuity equation similar to Equation (2.19), but where the charge density has been separated into different components dependent upon the forces that caused the charge density in the first place. This is consistent with the original version

of Maxwell's equations that incorporated a charge density and an electric displacement due to the permittivity of free space that was neither a true electric displacement nor a real charge density. Instead, Maxwell's equations should balance the strengths of the things that cause charge density; in other words, the propensity for charge density should be balanced.

10. CONCLUSIONS AND RECOMMENDATIONS

This thesis presents a development of ideas and numerical models that corroborate each other. The development commences with an examination of crevice corrosion using a model consisting of a transport equation based on dilute solution theory coupled with a characterization of the electric field also developed from dilute solution theory. This model provides some evidence that the electric field may be characterized through a rearrangement of the transport equation from dilute solution theory. This model also illuminates phenomena occurring during crevice corrosion. In the subsequent work presented in this thesis, the concept that 'the electric field may be characterized through a rearrangement of the transport equation described by dilute solution theory' is further expanded through a rearrangement of this transport equation without neglecting any phenomena. Also, an analysis of Maxwell's equations shows how to apply this equation and shows that this equation is not a simplification of Poisson's equation, but instead incorporates the effects of different forms of charge density from those in Poisson's equation. This expanded characterization of the electric field is coupled with a multi-dimensional transport model, validated, and applied to lithium-ion batteries. During this application, it is demonstrated that the new model predicts experimentally observed phenomena that were not previously predicted using conventional dilute solution theory. Finally, this thesis concludes with a rearrangement of Maxwell's fundamental equations

to incorporate the situation where multiple forms of charge density may simultaneously exist, such as within a non-isotropic electrolyte conducting electric current. The following important general conclusions may be drawn from this thesis:

1. Different forms of charge density may exist in an electrolyte. For example, charge density may be caused through a time independent polarization of atoms and molecules that is caused by an applied electric field, or charge density may be caused by the time dependent different rates of ionic diffusion and caused by concentration gradients. Other fields and phenomena may also cause charge density, such as spatially distinct anodic and cathodic reactions.

2. The property that should be balanced in an electrochemical system is not the quantity of charge density, but the strengths of the phenomena causing the charge density. If the type of charge density is known, then the strengths of the phenomena may be calculated via empirical values, such as the permittivity or the conductivity. This conclusion allows for the advancement of dilute solution theory to incorporate previously neglected phenomena, such as charge density.

3. Since this thesis suggests many fields or phenomena may cause or be in balance with charge density, and that charge density also interacts with the electric field, a name is suggested for the property that should be balanced in an electrochemical system: the propensity for charge density.

4. A rearrangement of Maxwell's fundamental equations allows for the inclusion of systems where multiple forms of charge density exist. This new form of Maxwell's equations is presented in Section 9.2.

5. From this understanding of Maxwell's equations, and through a rearrangement of the transport equation from dilute solution theory (that incorporates those phenomena significant in electrolytes), the first general characterization of the electric field coupled with an electrolyte may be developed. This equation is named the Inherent Charge Density Model. Its development and application are presented in Chapter 5.

6. Poisson's equation may be successful in modeling the charge density caused by ionic transport when it is applied over a suitable time step, even though Poisson's equation incorporates a time independent form of charge density. This is because the electric displacement caused by ionic transport approaches the time independent electric displacement incorporated in Poisson's equation at extremely small time steps.

7. The transport equation from dilute solution theory not only describes transport, but it also describes the electric field if the composition of the electrolyte is known.

Important conclusions concerning crevice corrosion and numerical models of crevice corrosion presented in this thesis include:

1. Regions of net cathodic activity may occur towards the tip of a corroding crevice. The possibility exists for both the evolution of hydrogen and the net deposition of metal in these regions. This discovery may also explain some experimentally observed phenomena.

2. The possibility for regions of net cathodic activity, caused by a combination of Ohmic potential drops and concentration gradient effects, may also be responsible for the initiation of the Reverse Crevice Corrosion of Copper. A possible mechanism describing regions of net cathodic activity was presented in Chapter 4.

3. It was found that cathodic reactions became more prominent inside the crevice after a significant electric potential drop was caused by ionic transport and the corresponding Ohmic considerations. It was also found, for the cases examined, some cathodic reactions could be neglected until the onset of active crevice corrosion and the accompanying Ohmic potential drops within the crevice.

4. It was shown how the two schools of theory describing crevice corrosion, the iR Drop Theory and the Critical Crevice Solution Theory, could be combined to successfully model crevice corrosion. Both theories contribute important effects to the understanding of crevice corrosion.

5. It can be concluded that, for the stainless steel crevice investigated, the correct scaling law should be L^2/G. This scaling law correctly fit the numerical data for the case where L^2/G=401 cm for all of the crevice aspect rations examined.

6. Three phases of crevice corrosion were numerically observed: the total corrosion phase, the dynamic corrosion phase, and the quasi-steady state phase. These three phases describe the process through which a crevice in incubation changes from experiencing a uniform passive current along the length of the crevice to an actively corroding crevice with regions of high active corrosion near the crevice mouth and regions with negligible corrosion occurring deeper into the crevice.

Some important conclusions may be drawn from the numerical work conducted on charging lithium-ion cells. The following conclusions may be drawn:

1. Charge density effects may be important in the modeling of lithium-ion batteries, as well as other systems. Because neither the assumption of electroneutrality nor Poisson's equation was made, significant charge density was predicted for the situation where one-dimensional transport was occurring between the electrodes of a charging cell. This charge density affected the electric field across the separator between the charging electrodes.

2. The universal electrolyte model used to simulate the charging cell was found to be beneficial over other approaches because it neglects no phenomena already incorporated in the flux equation of dilute solution theory. Unlike conventional electrolyte modeling (described in Section 2.3), the assumption of insignificant concentration gradients in the electrolyte was not made. It was shown how the universal model was able to predict phenomena previously experimentally

observed but not previously reported for models based on conventional dilute solution theory.

3. It was found that significant concentration gradients within the cathode of a charging cell, caused by an extension of the cathode past the anode, were responsible for the relatively large potential drop along the length of a lithium-ion cell electrolyte. These concentration gradients within the cathode caused gradients in equilibrium potentials along the surface of the cathode and thus a driving force for lithium transport and an Ohmic potential drop through the electrolyte was formed.

4. The extension of the electrolyte past the edges of the electrodes was not found to have a significant effect on either electrode; however a slight increase in the effective conductivity in the region of the extension was numerically observed.

5. The inclusion of the effects of reactions occurring on the flooded electrode edges was found to be significant. Electrochemical reactions occurring on flooded electrode edges were found to cause significant concentration gradients within the electrodes. These concentration gradients within the electrodes caused local changes in the equilibrium potential of the electrodes. Also, the edge reactions may cause a net electric current towards the electrode edges or away from the electrode edges, depending on the size and nature of the edges.

6. The rate of lithium insertion into the cathode is primarily determined by the concentration gradients within the cathode, and the rate of lithium emission from

the anode is determined by anode surface area and electrolyte potential gradients, during early cell charging.

Final conclusions may be made concerning the universal electrolyte model: this model may be applied to different complex electrochemical systems undergoing multiple phenomena using the same boundary conditions; and the only prescribed quantities required are the initial concentrations and diffusion coefficients, system geometry, and the positions and rates of spatially distinct anodic and cathodic reactions.

The theory and universal model presented in this thesis present a foundation for future work. The following recommendations are made for future work:

1. The universal model should be applied to further electrochemical systems and the model for a lithium-cell should be further developed. The universal model should be very suitable to the case of the porous electrode lithium-ion cell because of the manner in which electric current is introduced into the numerical solution domain. In the universal electrolyte model, electric current is introduced into the numerical solution domain via the source terms in the two coupled equations. Therefore, it is relatively simple to convert the source terms to represent current emanating from a porous electrode instead of a solid film electrode. This conversion would be simple when compared with the model needed for conventional dilute solution theory where the electric current must be introduced via boundary conditions and is relatively complex to apply to the porous electrode situation.

2. As well as engineered systems, the universal electrolyte model should be applied more extensively to the case of charge density in electrolytes. One case that requires more attention is that of the liquid-junction. The distribution of mobile charge density across liquid-junctions should be examined at different time intervals, including very shortly after contact between the two different electrolytes.

3. The ramifications of reorganizing Maxwell's equations should be investigated. This reorganization of Maxwell's equations may be beneficial for fields of study other than electrochemistry. This fundamental reorganization likely has other impacts than those studied in this thesis.

REFERENCES

Alavi, A., R.A. Cottis, "The Determination of pH, Potential and Chloride Concentration in Corroding Crevices on 304 Stainless Steels and 7475 Aluminium Alloy", Corrosion Science 27, (1987) 443-451.

Al-Zahrani, A.M., H.W. Pickering, "IR Voltage Switch in Delayed Crevice Corrosion and Active Peak Formation Detected using a Repassivation-Type Scan", Electrochim. Acta 50, (2005) 3420.

Arora, P., M. Doyle, R.E. White, "Mathematical Modeling of the Lithium Deposition Overcharge Reaction in Lithium-Ion Batteries Using Carbon-Based Negative Electrodes", J. Electrochem. Soc. 146, (1999) 3543-3553.

Bockris, J., A. Reddy, "Modern Electrochemistry", (Oxford: Plenum Press, 1977), p251.

Boffi, L., "Electrodynamics of Moving Media", ScD Thesis, Massachusetts Institute of Technology, Cambridge (1957).

Chloupek, J.B., V.Z. Kanes, B.A. Danesova, Collection of Czechoslovak Chemical Communications, 5, 1933 p469-527.

Christensen, J., V. Srinivasan, J. Newman, “Optimization of Lithium-Titanate Electrodes for High-power Cells”, J. Electrochem. Soc. 153, A560 (2006).

Cui, F., F. Presuel-Moreno, R. Kelly, “Computational Modelling of Cathodic Limitations on Localized Corrosion of Wetted SS 316L at Room Temperature”, Corrosion Science 47, (2005) 2987-3005.

Doyle, M., J. Newman, “Comparison of Modeling Predictions with Experimental Data from Plastic Lithium Ion Cells”, J. Elecctrochem. Soc. 143, (1996) 1890.

Doyle, M, T.F. Fuller, J. Newman, “Modeling of Galvanostatic Charge and Discharge of the Lithium/Polymer/Insertion Cell”, J. Electrochem. Soc., 140, (1993) 1526 – 1533.

Doyle, M, Y Fuentes, “Computer Simulations of a Lithium-ion Polymer Battery and Implications for Higher Capacity Next-generation Battery Designs”, J. Electrochem Soc., 150, A706-A713 (2003).

Eberman, K., P.M. Gomadam, G. Jain, E. Scott, “Material and Design Options for Avoiding Lithium-plating during Charging”, ECS Transactions, 25 (2010), 47-58.

Engelhardt, G.R., D.D. MacDonald, P.J. Millett, "Transport Processes in Steam Generator Crevices-I. General Corrosion Model", Corrosion Sci. 41, (1999) 2165 – 2190.

Evitts, R.W. "Modelling of Crevice Corrosion", Ph.D. Thesis, University of Saskatchewan, Saskatoon, SK (1997).

Fu, J.W., S.K. Chan, "A Finite Element Method for Modelling Localized Corrosion Cells", Corrosion 40, (1984): p540.

Fuller, T. F., M. Doyle, J. Newman, "Simulation and Optimization of the Dual Lithium Ion Insertion Cell", J. Electrochem. Soc. 141, (1994) 1 – 10.

Galvele, J.R., "Transport Processes and the Mechanism of Pitting of Metals", J. Electrochem. Soc. 124, (1976) 464 – 474.

Galvele, J.R., "Transport Processes in Passivity Breakdown-II. Full Hydrolysis of the Metal Ions", Corrosion Science 21, (1981) 551 – 579.

Galvele, J.R., J.R. Gravano, "Transport Processes in Passivity Breakdown-III. Full Hydrolysis Plus Ion Migration Plus Buffers", Corrosion Science 24, (1984) 517 – 534.

Grahame, D.C., J.I. Cummings, Office of Naval Research Technical Report 5, (1950).

Heppner, K.L., "Development of Predictive Models of Flow Induced and Localized Corrosion", Ph.D. Thesis, University of Saskatchewan, Saskatoon, SK (2006).

Heppner, K.L., R.W. Evitts, "A Hybrid Differencing Scheme for Mass Transport in Electrochemical Systems", International Journal of Numerical Methods for Heat & Fluid Flow 15(8), (2005) 842-862.

Heppner, K.L., R.W. Evitts, "New Method for Calculating Charge Density in Electrochemical Systems", Corrosion Engineering, Science and Technology, (2006) 110 – 121.

Heppner, K.L., R.W. Evitts, "New Method for Calculating Charge Density in Electrochemical Systems", Corr. Eng., Science and Technology, (2006) 110-121.

Heppner, K.L., R.W. Evitts, J. Postlethwaite, "Prediction of the Crevice Corrosion Incubation Period of Passive Metals at Elevated Temperatures: Part I – Mathematical Model", Can. J. of Chem. Eng. 80, (2002a) 849 – 856.

Heppner, K.L., R.W. Evitts, J. Postlethwaite, “Prediction of the Crevice Corrosion Incubation Period of Passive Metals at Elevated Temperatures: Part II – Model Verification and Simulation”, Can. J. of Chem. Eng. 80, (2002b) 857 – 864.

Kennell, G.F., R.W. Evitts, K.L. Heppner, “A Critical Crevice Solution and iR Drop Crevice Corrosion Model”, Corrosion Sci. 50, (2008) 1716.

Kennell, G.F., R.W. Evitts, “A Universal Multi-dimensional Charge and Mass Transfer Model”, Advances in Fluid Mechanics 8, (2010a) 181 – 192.

Kennell, G.F., R.W. Evitts, “Charge Density in Non-isotropic Electrolytes Conducting Current”, Canadian J. of Chem. Eng. (2011a) (In Press)

Kennell, G.F., R.W. Evitts, “Crevice Corrosion Cathodic Reactions and Crevice Scaling Laws”, Electrochimica Acta. 54: (2009a) 4696-4703.

Kennell, G.F., R.W. Evitts, “Extinct Regions in a Corroding Crevice”, proceedings of NACE Northern Area Western Conference 2009, Victoria, BC, February 9th – 12th, (2009b).

Kennell, G.F.S., R.W. Evitts, “Multi-component Multi-dimensional Transport of Charge and Mass with Corresponding Electric Field,” Abs # 1267, presented at 218th ECS Meeting, in Las Vegas, USA, 10th – 15th October, (2010b).

Kielland, J., “Individual Activity Coefficients of Ions in Aqueous Solutions”, J. Am. Chem. Soc. 59, (1937): p1675-1678.

D.R. Lide, CRC Handbook of Chemistry and Physics, 90th Ed. (CRC Press, 2010): p5-76.

Majidi, A.P., M.A. Streicher, “The Double Loop Reactivation Method for Detecting Sensitization in AISI 304 stainless steels”, Corrosion 40, (1984) 584 – 593.

Matsushima, I., J. Sakai, K. Masamura, “Mechanism of Crevice Corrosion”, in “Proc. 7th International Congress on Metallic Corrosion,” Rio De Janeiro, Brasil, October 4 – 11 (1978).

Maxwell, J., “A Dynamical Theory of the Electromagnetic Field”, Royal Society Transactions, vol. CLV, reprinted in Simpson, T., Maxwell on the Electromagnetic Field, Rutgers University Press, New Brunswick, NJ (1997).

Newman, J.S., “Electrochemical Systems”, 1st Ed, Prentice Hall, Toronto, (1973).

Newman, J.S., K.E. Thomas-Alyea, “Electrochemical Systems”, 3rd Ed, John Wiley & Sons, NJ (2004).

Oldfield, J.A., “Crevice Corrosion of Stainless Steels – the importance of crevice geometry and alloy composition”, Bulletin du Cercle d’études des métaux 14.9, (1980) 19.1 – 19.11.

Oldfield, J.W., W.H. Sutton, “Crevice Corrosion of Stainless Steels I. A Mathematical Model”, British Corrosion Journal 13, (1978) 13-22.

Patankar, S.V., “Numerical Heat Transfer and Fluid Flow”, (NY: Hemisphere, 1980), p1-194.

Pickering, H.W., “On the Roles of Corrosion Products in Local Cell Processes”, Corrosion 42, (1986) 125.

Rothwell, E.J., M.J. Cloud, “Electromagnetics”, CRC Press, Boca Raton (2009).

Scott, E., G. Tam, B. Anderson, C. Schmidt, “Anomalous Potentials in Lithium Ion Cells: Making the Case for 3-D Modeling of 3-D Systems”, Paper 1282 presented at the Electrochemical Society Meeting, Orlando, FL, Oct 13th 2003, (2003a).

Scott, E., G. Tam, C. Schmidt, “Observation and Mechanism of Anomalous Local Potentials during Charging of Lithium Ion Cells”, Paper 193 presented at the Electrochemical Society Meeting, Paris, France, April 29th 2003, (2003b).

Sharland, S.M., "A Mathematical Model of the Initiation of Crevice Corrosion in Metals", Corrosion Science 33, (1988) 183 – 201.

Sharland, S.M., P.W. Tasker, "A Mathematical Model of Crevice and pitting Corrosion-I. The Physical Model", Corrosion Science 28, (1988) 603 – 620.

Shrier, L.L., Corrosion, Vols I and II, Newness Butterworth, London, 1979.

Shreir, L.L., R.A. Jarman, G.T. Burstein, Corrosion, 3rd ed., Butterworth-Heinemann, Oxford, (1994).

Siegel, D.M., "Innovation in Maxwell's Electromagnetic Theory", Cambridge University Press, New York, (1991).

Sridhar, N., D.S. Dunn, "Effect of Applied Potential on Changes in Solution Chemistry Inside Crevices on Type 304L Stainless Steel and Alloy 825", in "Proc. Corrosion 94," Paper No. 347, 1994, NACE International, Houston, TX (1994).

Stewart, S.G., J. Newman, "The use of UV/vis Absorption to Measure Diffusion Coefficients in $LiPF_6$ Electrolytic Solutions", J. of Electrochem. Soc., 155, (2008), F13-F16.

Tang, M., Albertus, P., Newman, J., "Two-dimensional Modelling of Lithium Deposition during Cell Charging," Journal of the Electrochemical Society, 156 (2009), A390-A399.

Turnbull, A., D.H. Ferriss, "Mathematical Modelling of the Electrochemistry in Corrosion Fatigue Cracks in Structural Steel Cathodically Protected in Sea Water", Corrosion Science 26, (1986) 601 – 628.

Turnbull, A., J.G.N. Thomas, J. Electrochem. Soc 129, (1982) 1412.

Walton, J.C., G. Cragnolino, S.K. Kalandros, "A Numerical Model of Crevice Corrosion for Passive and Active Metals," Corrosion Sci. **38**, (1996) 1 - 18.

Watson, M.K, J. Postlethwaite, "Numerical Simulation of Crevice Corrosion of Stainless Steels and Nickel Alloys in Chloride Solutions", Corrosion 46, (1990a) 522 – 529.

Watson, M.K., J. Postlethwaite, "Numerical Simulation of Crevice Corrosion", in "Proc. Corrosion/90", Las Vegas, NV, April 23-27, 1990, NACE International, Houston, TX, (1990b) 156:1 – 156:19.

Watson, M.K., J. Postlethwaite, "Numerical Simulation of Crevice Corrosion: The Effect of the Crevice Gap Profile", Corrosion Sci. 32, (1991) 1253 – 1262.

West, K., T. Jacobsen, S. Atlung, “Modeling of Porous Insertion Electrodes with Liquid Electrolyte”, J. Electrochem. Soc. 129, (1982) 1480 – 1485.

White, S.P., G.J. Weir, N.J. Laycock, “Calculating Chemical Concentrations During the Initiation of Crevice Corrosion”, Corrosion Science 42, (2000) 605 – 629.

Xu, Y., H.W. Pickering, “A Model of the Potential and Current Distributions within Crevices and its Application to the Iron – Ammoniacal System”, Proceedings 92. Proc. Symp. Crit. Factors Localized Corros., 1991 (1992), 389 – 406.

Xu, Y., H.W. Pickering, “The Initial Potential and Current Distributions of the Crevice Corrosion Process”, J. of Electrochem. Soc. 140, (1993) 658-668.

APPENDIX A. MOVING BOUNDARY EXPERIMENT FOR A GLASS TUBE WITH A SUDDEN EXPANSION

An experiment measuring the movement of a liquid-junction, or boundary, down a glass tube was conducted. This experiment was similar to the experiment of Fu and Chan (1984); however a glass tube with different internal diameters and a sudden expansion was used instead of the single 2 mm internal diameter glass tube used by Fu and Chan. The experimental setup is portrayed in Figure 6.8. The internal diameter of the smaller tube was 2.9 mm and that of the larger tube was 6.9 mm. The current applied to the silver anode was 1 mA. The electrolyte inside the glass tube and reservoir consisted of a 0.1 M KNO_3 solution. Similar to the experiment of Fu and Chan, a small quantity of ascorbic acid (0.001 M) was used to reduce Ag^+ to visible Ag particles suspended in solution. Figure A.1 shows the visible $AgNO_{3<aq>} - KNO_{3<aq>}$ liquid junction inside the glass tubes with a sudden expansion and plugged with a silver anode. Teflon tape was used to seal around the anode and region of sudden expansion.

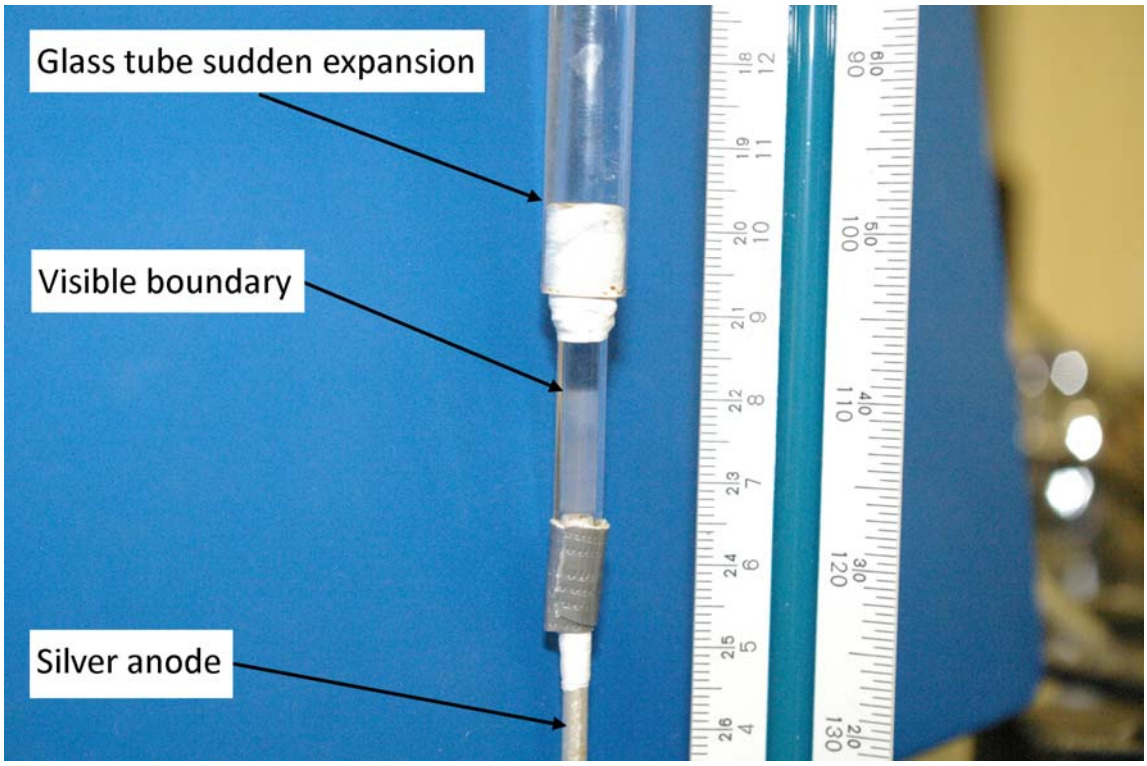

Figure A.1. Apparatus for experimentally determining movement of liquid-junction.

It was possible to visually measure the rate of movement of the liquid-junction down the smaller 2.9 mm internal diameter tube. In the smaller diameter tube the boundary/liquid-junction was observed to be flat at all times; however, it was assumed that this boundary would not be flat upon emergence from the smaller diameter tube into the larger diameter tube at the region of sudden expansion. To measure this non-flat boundary, a digital camera was used to take photographs of the boundary at different times. These photographs were then expanded and digitized to compare with the dynamic boundary profile as numerically predicted using the Universal Electrolyte model presented in Chapter 6. Predicted data is compared with the experimentally observed movement of the boundary down the smaller tube in Figure A.2. Figure A.2 shows a good correlation between these data sets similar to the correlation in Figure 6.9.

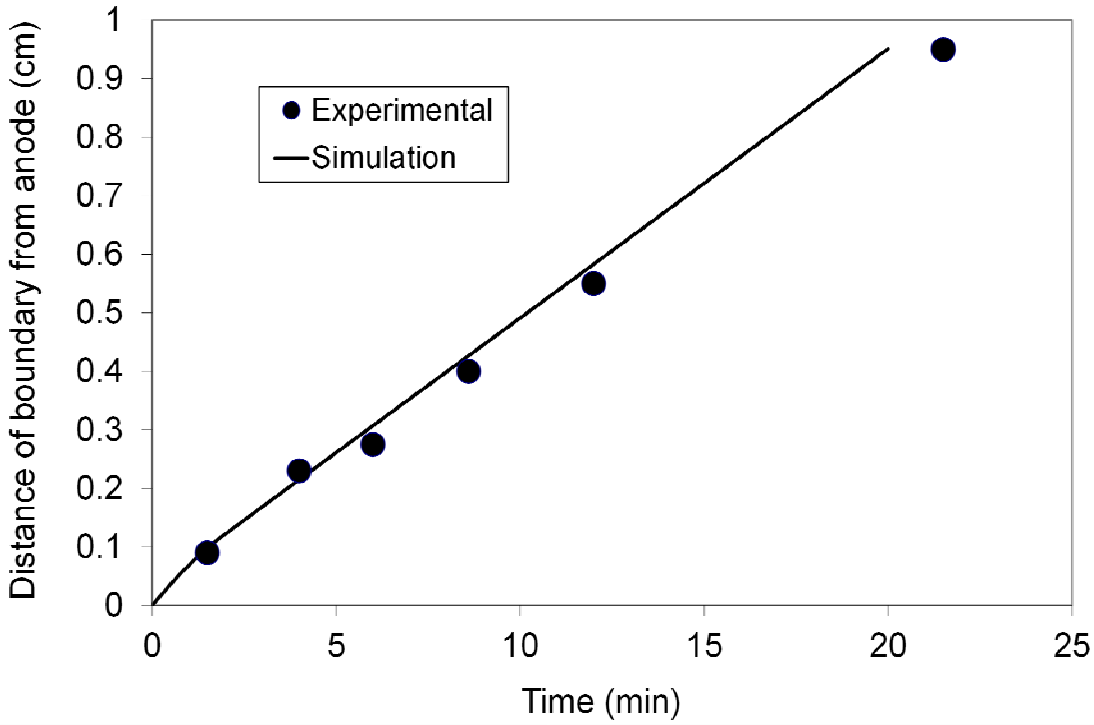

Figure A.2. Experimental data (circles) and data simulated using the model presented in Chapter 6 (line).

Also compared were the experimentally determined and numerically predicted boundaries at different times after the movement of the liquid-junction through the sudden expansion from the 2.9 mm diameter tube to the 6.9 mm diameter tube. Figures A3 to A6 shows these boundaries. It appears that the simulated profile fits that seen experimentally at the early times shown in Figures A3 and A4; however, these profiles do not correspond very well at the later times displayed in Figures A5 and A6. It was concluded that the difference in density between the suspended metallic Ag particles and the electrolyte were affecting the experimentally observed boundary profile, especially at later times.

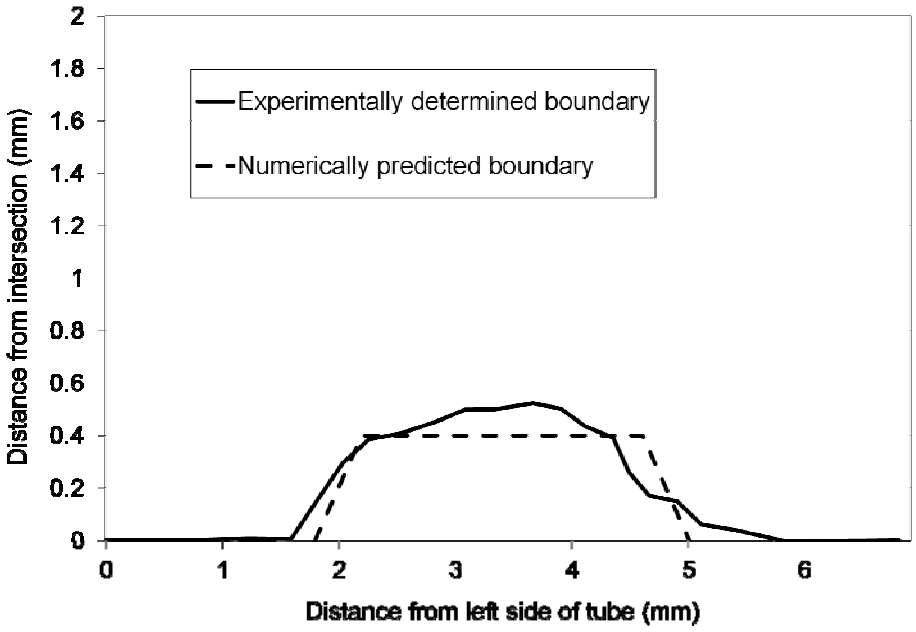

Figure A.3. Visible boundary between $AgNO_{3<aq>}$ and $KNO_{3<aq>}$ solutions 1 minute after passing the sudden expansion with an applied current of 1 mA.

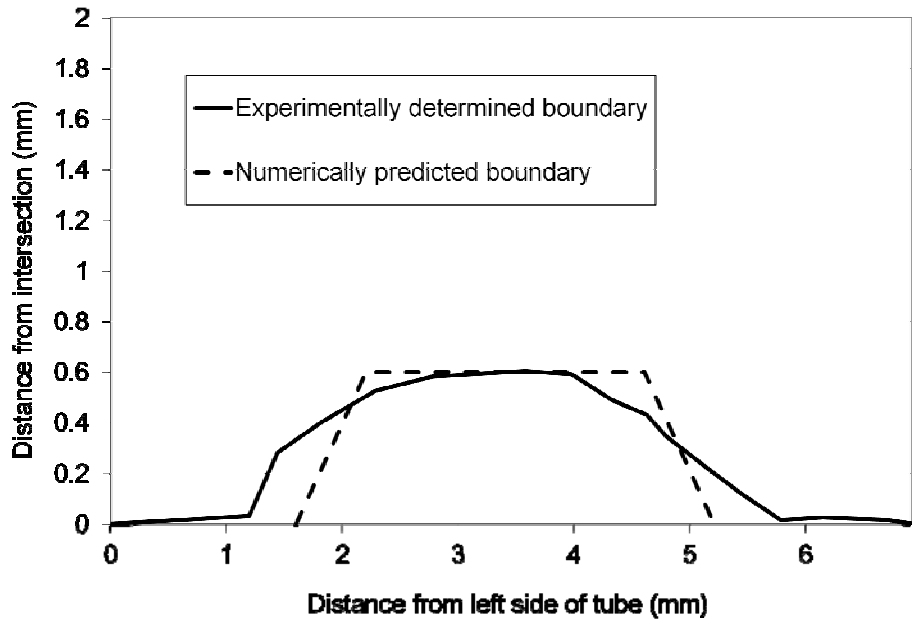

Figure A.4. Visible boundary between $AgNO_{3<aq>}$ and $KNO_{3<aq>}$ solutions 1 minute and 40 seconds after passing the sudden expansion with an applied current of 1 mA.

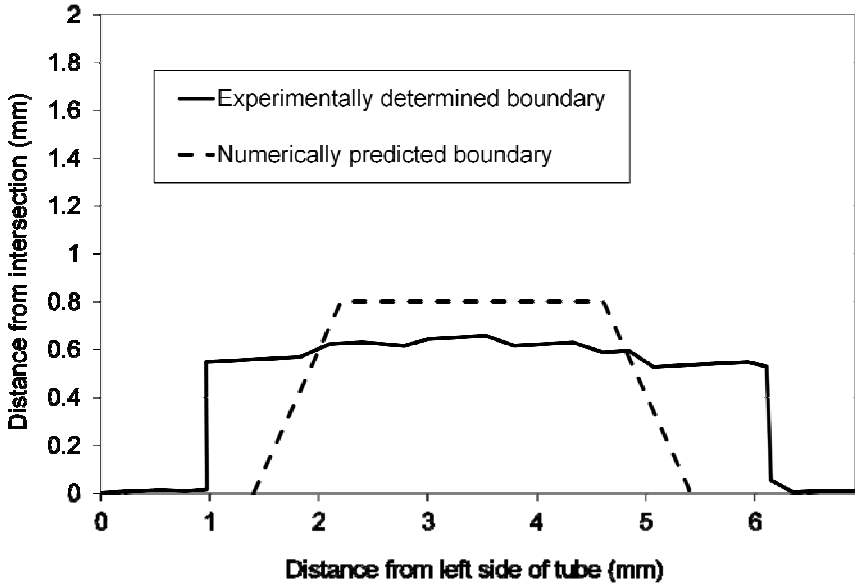

Figure A.5. Visible boundary between $AgNO_{3<aq>}$ and $KNO_{3<aq>}$ solutions 2 minutes and 30 seconds after passing the sudden expansion with an applied current of 1 mA.

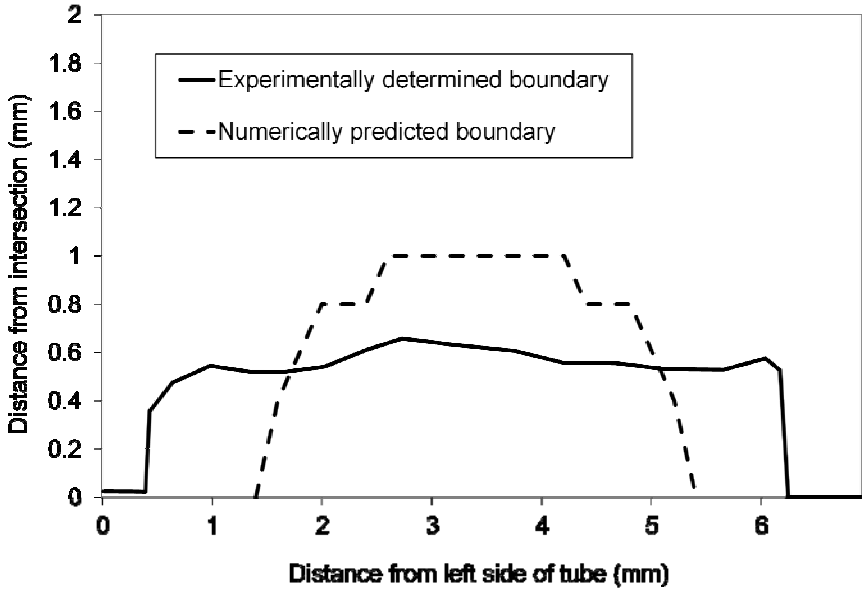

Figure A.6. Visible boundary between $AgNO_{3<aq>}$ and $KNO_{3<aq>}$ solutions 3 minutes after passing the sudden expansion with an applied current of 1 mA.